

Faculty of Engineering and Science

**Laminar Forced Convective Heat Transfer Studies in Circular and Non-circular
Ducts with Polyacrylamide Additives in Water-based Al₂O₃ Nanofluid**

Angnes Tiong Ngieng Tze

**This report is presented for the Degree of
Doctor of Philosophy in Chemical Engineering
of
Curtin University**

September 2017

DECLARATION

To the best of my knowledge and belief, this thesis contains no material previously published by any other person except where due acknowledgment has been made.

This thesis contains no material which has been accepted for the award of any other degree or diploma in any university.

Signature:

Date: ..10th September 2017...

ACKNOWLEDGEMENT

It is my pleasure to acknowledge the many people who made this thesis possible.

I would like to extend my first and foremost gratitude to the Almighty God for giving me the strength and blessings so that I can accomplish this research in the best possible way.

I am profoundly grateful to my supervisors, Associate Professor Dr. Perumal Kumar and Dr Agus Saptoro for giving me the opportunity to work under them. I appreciate their endless guidance, motivation and patience through my PhD journey. They have provided me with helpful advice and assistance which have critically improved the quality of my research.

My heartfelt thanks to the lab technicians Ms Magdalene, Mr Marconi and Mr Michael Ding for their help and support in the preparation of my experimental works. I also like to remember my HDR friends for their love and kind support.

I am indebted to my lovely parents and siblings for being caring and generous enough to stand by me to achieve whatever I have today. I am also grateful to my husband, Ryan Lau for always being there to join in all my difficult times.

Last but not the least, I sincerely acknowledge the financial support from the Ministry of Higher Education (MOHE) Malaysia under the Exploratory Research Grant Scheme (ERGS) ERGS/1/2012/TK05/CURTIN/02/1.

PUBLICATION LIST**Journal paper:**

1. Tiong, N.T.A., Saptoro, A., Kumar, P. 2017. "Numerical studies on the laminar thermal-hydraulic efficiency of water-based Al₂O₃ nanofluid in circular and non-circular ducts." In press, DOI: <https://doi.org/10.1515/cppm-2017-0019> (SCOPUS cited journal).
2. Tiong, N.T.A., Kumar, P., Saptoro, A. 2015. "Reviews on Drag Reducing Polymers." *The Korean Journal of Chemical Engineering* 32 (8): 1455-1476. (Thomson Reuters Web of Science cited publication, 2016 Impact Factor: 2.007).

Conference presentation:

1. Tiong, N.T.A., Saptoro, A., Kumar, P., Numerical studies on the laminar thermal-hydraulic efficiency of water-based Al₂O₃ nanofluid in circular and non-circular ducts, 29th Symposium of Malaysian Chemical Engineers, Miri, Malaysia, 1 – 3 December 2016.
2. Tiong, N.T.A., Kumar, P., Saptoro, A., CFD Studies on the laminar heat transfer and flow behaviour of polyacrylamide solution and nanofluid in circular and non-circular ducts, 3rd International Workshop on Heat Transfer Advances for Energy Conservation and Pollution Control, Taipei, Taiwan, 16-19 October 2015.

ABSTRACT

The conventional heat transfer fluids have low thermal performance. In view of this issue, nanofluid has emerged as a promising solution owing to its heat transfer enhancement (HTE) ability. Nanofluid is a suspension of nano-sized particles in a base fluid. Nonetheless, the HTE of nanofluid is achieved at the expense of a higher pressure drop, resulting in low thermal-hydraulic efficiency. It is crucial to improve the efficiency of nanofluid to make its application beneficial. This study addresses the problem of low thermal-hydraulic efficiency of nanofluid in the circular and non-circular ducts by adding polymer additives in it. Polymer solution is reported to increase the heat transfer in the laminar regime.

In the literature, the addition of surfactant additives, a type of solution having similar flow characteristic as the polymer additives, into nanofluids for turbulent circular flow had been investigated. However, studies on the effect of polymer additives on the laminar heat transfer and flow behaviour of nanofluids in the circular and non-circular ducts are very limited and these become research needs. Therefore, this study aims to (1) examine the effect of polymer additives on the rheology, heat transfer and flow behaviour of nanofluid for the laminar circular and non-circular flow, (2) evaluate the thermal-hydraulic efficiency of this new hybrid fluid known as poly-nanofluid, (3) find an optimum concentration of poly-nanofluid for the best efficiency and (4) propose correlations to predict the Nusselt number and friction factor of poly-nanofluid in the pipe flow.

The nanofluid and polymer considered in this research were Al_2O_3 based nanofluid and polyacrylamide (PAA), respectively. This research was conducted in three main stages: rheology measurements, heat transfer and flow studies. The rheology of PAA solution and poly-nanofluid were measured using Rheometer AR-1500ex. Furthermore, the heat transfer studies were carried out through experimental works in a double pipe heat exchanger and Computational Fluid Dynamics (CFD) modelling of the same. The CFD modelling was performed using ANSYS FLUENT Version 15.0. The CFD model was validated against the experimental results and data from the existing literature.

Meanwhile, for the flow studies, the numerical values of pressure drop obtained were compared and verified with the analytical predictions. The validated CFD model was then employed to evaluate the thermal-hydraulic efficiency of Al_2O_3 nanofluid with and without PAA additives in the circular, square, 2:1 rectangular and 4:1 rectangular ducts. The viscosity of PAA solution and poly-nanofluid from the rheology measurements served as input for the simulations.

The rheology results indicated that the addition of PAA additives changed the rheology of nanofluid from Newtonian to non-Newtonian shear-thinning behaviour. The viscosity of poly-nanofluid was well-fitted with the Carreau model which was functions of shear rate and temperature. On the other hand, from the analysis of thermal-hydraulic efficiency in this present study, the use of nanofluid did not show advantages over that of water. When PAA additives were added to nanofluid, the heat transfer of nanofluid is further augmented, but the pressure drop also increases. The HTE of poly-nanofluid in the circular pipe (including double pipe heat exchanger) was attributed to the increased thermal conductivity and shear-thinning characteristic of the solution; while the presence of secondary flow was responsible for the HTE in the non-circular ducts. Besides, the increased pressure drop was due to the increased viscosity of the solution.

The HTE achieved in the circular duct was weaker compared to that of the non-circular ducts while the pressure drop in all the geometries was comparable. The HTE of poly-nanofluid in the circular pipe (including the double pipe heat exchanger) was not attractive as the efficiency was poor. Therefore, it was not beneficial to add PAA additives to nanofluid for the circular pipe flow. In contrast, the thermal-hydraulic efficiency of poly-nanofluid in the non-circular ducts were better than those of water and pure nanofluid. The optimum concentration was found to be 50 ppm PAA added to 4% Al_2O_3 nanofluid, with the best average efficiency of 1.667 obtained in the square duct. The flow of poly-nanofluid was most efficient in the square duct because the HTE obtained was the highest with the lowest pressure drop increment. In addition, correlations were proposed for the Nusselt number and friction factor of poly-nanofluid in the pipe flow.

The main contributions of this present study are such that (1) it provides a better understanding of the rheology behaviour of the new hybrid fluid – poly-nanofluid, (2) the effect of PAA additives on the heat transfer and flow behaviour of nanofluid is known and (3) the Nusselt number and friction factor correlations are proposed for the first time for poly-nanofluid in the pipe flow. Significantly, the second contribution helps to extend the heat transfer application of nanofluid by improving its efficiency and it paves way for new heat transfer applications in the future. It is recommended to extend this study to turbulent regime for future work. Moreover, it is also proposed to include the measurement of thermal properties of poly-nanofluid for future research.

TABLE OF CONTENTS

ACKNOWLEDGEMENT	I
PUBLICATION LIST	II
ABSTRACT	III
NOMENCLATURE	X
LIST OF ABBREVIATIONS	XV
LIST OF FIGURES	XVI
LIST OF TABLES	XXIII
CHAPTER 1: INTRODUCTION	
1.1 Background of the study	1
1.2 Scope of the study	4
1.3 Significance of the study	5
1.4 Thesis organization	6
CHAPTER 2: LITERATURE REVIEW	
2.1 Nanofluid	8
2.1.1 Studies on heat transfer performance of nanofluids	8
2.1.2 Proposed HTE mechanisms for nanofluids	11
2.1.3 Experimental studies on both heat transfer and flow behaviour of nanofluids	12
2.1.4 Numerical studies on both heat transfer and flow behaviour of nanofluids	19
2.2 Polymer	26
2.2.1 Experiments on laminar heat transfer and flow characteristics of polymer solutions in non-circular ducts	26
2.2.2 Experiments on laminar heat transfer and flow characteristics of polymer solutions in circular ducts	29
2.2.3 Numerical studies on laminar heat transfer and flow characteristics of polymer solutions	30
2.2.4 Studies on turbulent heat transfer and flow characteristics of polymer solutions in circular ducts	36
2.2.5 Studies on turbulent heat transfer and flow characteristics of polymer solutions in non-circular ducts	39
2.3 Addition of additives to nanofluid	39
2.4 Summary and research gaps	44
2.5 Identified problem statement and research questions of the study	45
2.6 Aim and objectives of the study	46

CHAPTER 3: RESEARCH METHODOLOGY

3.1 Rheology measurement.....	48
3.1.1 Experimental setup.....	48
3.1.2 Preparation of test fluids	49
3.1.3 Experimental procedures	50
3.2 Heat transfer experimental studies.....	51
3.2.1 Experimental setup.....	51
3.2.2 Preparation of test fluids	54
3.2.3 Experimental procedures	54
3.3 Uncertainty Analysis.....	55
3.4 Simulation works	58
3.4.1 Geometry creation.....	58
3.4.2 Meshing.....	59
3.4.3 Governing equations	60
3.4.3.1 Single-phase model	60
3.4.3.2 Two-phase mixture model.....	61
3.4.3.3 Two-phase Eulerian model.....	63
3.4.3.4 Two-phase VOF model	66
3.4.3.5 Viscoelastic property	67
3.4.4 Thermo-physical properties	69
3.4.4.1 Water	70
3.4.4.2 Al ₂ O ₃ nanofluid	71
3.4.4.3 PAA solution	74
3.4.4.4 Poly-nanofluid	74
3.4.5 Boundary conditions	75
3.4.6 Numerical solution strategy.....	76
3.4.7 Grid independence study.....	78
3.5 Data reduction.....	81

CHAPTER 4: RHEOLOGICAL STUDY

4.1 Introduction.....	84
4.2 Rheology of PAA solution.....	84
4.3 Rheology of poly-nanofluid.....	86
4.4 Curve fitting for PAA solution and poly-nanofluid	87
4.5 Summary.....	91

**CHAPTER 5: HEAT TRANSFER PERFORMANCE OF NANOFLUID,
POLYMER AND POLY-NANOFLUID**

5.1 Introduction.....	92
5.2 Result validation	92
5.2.1 Water.....	92

5.2.2 Al ₂ O ₃ nanofluid.....	94
5.2.3 PAA solution.....	96
5.2.4 Poly-nanofluid.....	99
5.3 Heat transfer characteristic of Al ₂ O ₃ nanofluid	102
5.3.1 Single-phase modelling in double pipe heat exchanger.....	102
5.3.2 Single-phase modelling in circular and non-circular ducts.....	105
5.3.3 Two-phase modelling in different geometries	112
5.3.4 Comparison of results from single- and two-phase models.....	117
5.4 Heat transfer characteristic of PAA solution	120
5.4.1 Double pipe heat exchanger.....	120
5.4.2 Circular and non-circular ducts.....	122
5.5 Heat transfer characteristic of poly-nanofluid	127
5.5.1 Double pipe heat exchanger.....	127
5.5.2 Circular and non-circular ducts.....	129
5.6 Correlation to predict the Nusselt number of poly-nanofluid in circular and non-circular ducts.....	140
5.7 Summary	144

CHAPTER 6: FLOW FEATURE OF NANOFLUID, POLYMER AND POLY-NANOFLUID

6.1 Introduction.....	147
6.2 Result validation	147
6.2.1 Water.....	147
6.2.2 Al ₂ O ₃ nanofluid.....	149
6.2.3 PAA solution.....	151
6.3 Flow feature of Al ₂ O ₃ nanofluid	153
6.3.1 Pressure drop in double pipe heat exchanger (single-phase modelling).....	153
6.3.2 Pressure drop in circular and non-circular ducts (single-phase modelling).....	156
6.3.3 Pressure drop in different geometries (two-phase modelling).....	162
6.3.4 Comparison of results from single- and two-phase models.....	164
6.3.5 Friction factor for different geometries.....	166
6.4 Flow feature of PAA solution	168
6.4.1 Pressure drop in double pipe heat exchanger.....	168
6.4.2 Pressure drop in circular and non-circular ducts.....	169
6.4.3 Friction factor for different geometries.....	172
6.5 Flow feature of poly-nanofluid	174
6.5.1 Pressure drop in double pipe heat exchanger.....	174
6.5.2 Pressure drop in circular and non-circular ducts.....	176
6.5.3 Friction factor for different geometries.....	182

6.6 Correlation to predict the friction factor of poly-nanofluid	184
6.7 Summary	185
CHAPTER 7: THERMAL-HYDRAULIC EFFICIENCY OF NANOFLUID, POLYMER AND POLY-NANOFLUID	
7.1 Introduction	187
7.2 Thermal-hydraulic efficiency of Al ₂ O ₃ nanofluid	187
7.2.1 Double pipe heat exchanger	187
7.2.2 Circular and non-circular ducts	188
7.3 Thermal-hydraulic efficiency of PAA solution	190
7.3.1 Double pipe heat exchanger	190
7.3.2 Circular and non-circular ducts	192
7.4 Thermal-hydraulic efficiency of poly-nanofluid	193
7.4.1 Double pipe heat exchanger	193
7.4.2 Circular and non-circular ducts	194
7.5 Optimum concentration	196
7.6 Summary	197
CHAPTER 8: CONCLUSIONS AND RECOMMENDATIONS	
8.1 Conclusions	199
8.2 Recommendations	203
REFERENCES	205
APPENDICES	
Appendix A	217
Appendix B	224
Appendix C	227
Appendix D	232
Appendix E	233
Appendix F	237
Appendix G	241
Appendix H	246
Appendix I	247

NOMENCLATURE

A_c	cross-sectional area (m ²)
A_i	interfacial area concentration (1/m)
A_t	total heat transfer area (m ²)
\vec{A}	face normal vectors
$B_{\bar{r}}$	bias limit
C_D	drag coefficient
C_p	heat capacity (J/kg K)
\vec{c}	vectors from the cell centroid to the centroid of the adjacent cells
D	diameter (m)
D_h	hydraulic diameter (m)
D_i	annulus inner diameter (m)
D_o	annulus outer diameter (m)
d_i	tube inner diameter (m)
d_o	tube outer diameter (m)
d_p	diameter of the nanoparticles (nm)
E	energy (J)
\vec{F}_{lift}	lift force (N)
f	friction factor
f_{drag}	drag
\vec{f}	vectors from the cell centroid to the centroid of the adjacent faces
\vec{g}	gravitational acceleration (m/s ²)
H	height (m)
h	convective heat transfer coefficient (W/m ² K)
h_{av}	average heat transfer coefficient (W/m ² K)
h_e	sensible enthalpy (J)
h_i	inside fluid film coefficient (W/m ² K)
h_{id}	inside dirt coefficient (W/m ² K)
h_{od}	outside dirt coefficient (fouling factor) (W/m ² K)

h_s	outside fluid film coefficient (W/m ² K)
J	number of variable
K	consistency index (Pa s ⁿ)
K_{pq}	interphase momentum exchange coefficient
k	thermal conductivity (W/m K)
k_{eff}	effective thermal conductivity (W/m K)
k_t	turbulent thermal conductivity (W/m K)
k_w	thermal conductivity of the material for tube wall (W/m K)
L	number of correlated bias error sources
l	length (m)
M	number of measurements taken for a variable
m	mass flow rate (kg/s)
N	physical property
N_1	first normal stress difference (Pa)
N_2	second normal stress difference (Pa)
Nu	Nusselt number
Nu_{av}	average Nusselt number
n	power law exponent
n'	rate index
P	static pressure (Pa)
$P_{\bar{r}}$	precision limit
Pe	Peclet number
Pr	Prandtl number
ΔP	pressure drop (Pa)
p	wetted perimeter of the cross-section (m)
Q	heat transfer rate (J/s)
Q_c	cold volume flow rate (L/min)
Q_h	hot volume flow rate (L/min)
q''	heat flux (W/m ²)
\vec{R}_{pq}	interaction force (N)

Re	Reynolds number
Re^+	Generalized Reynolds number shown in Figure 2.9
Re'	Kozicki's generalized Reynolds number as defined in Equation 3.94
Re^*	Kozicki's generalized Reynolds number as defined in Equation 3.95
Re_p	relative Reynolds number
\bar{r}	averaged result of a variable
$S_{\bar{r}}$	standard deviation of an averaged result
s	nanoparticle size (nm)
T	temperature (K)
T_b	bulk temperature (K)
$T_{c,i}$	cold inlet temperature (K)
$T_{c,o}$	cold outlet temperature (K)
$T_{h,i}$	hot inlet temperature (K)
$T_{h,o}$	hot outlet temperature (K)
T_w	wall temperature (K)
ΔT_{LMTD}	logarithmic mean temperature difference (K)
t	time (s)
t_c	coverage factor
U	overall heat transfer coefficient ($W/m^2 K$)
$U_{\bar{r}}$	total uncertainty
u	velocity in x direction (m/s)
v	fluid velocity or velocity in y direction (m/s)
\vec{v}	velocity vectors (m/s)
\vec{v}_{dr}	drift velocity (m/s)
$\vec{v}_{p,bf}$	slip velocity (m/s)
∇v	velocity gradient
$(\nabla v)^T$	transpose of velocity gradient
W	width (m)
w	velocity in z direction (m/s)
w_w	weight fraction

X	variable
x	pipe axial distance (m)
z	axial coordinate shown in Figure 2.4 (m)

Greek symbols

α	cone angle of the rheometer ($^{\circ}$)
η	thermal-hydraulic efficiency
$\eta(\dot{\gamma})$	non-Newtonian viscosity (Pa s)
η_{∞}	infinite-rate viscosity (Pa s)
η_0	zero-rate viscosity (Pa s)
θ	sensitivity coefficient
\emptyset	thermo-physical properties
φ	volume fraction
ρ	density (kg/m^3)
μ	viscosity (Pa s)
ψ_1	first normal stress coefficient (Pa s^2)
ψ_2	second normal stress coefficient (Pa s^2)
τ	shear stress (Pa)
$\bar{\tau}$	viscous stress tensor or stress-strain tensor
$\bar{\tau}^P$	polymeric stress tensor
τ_p	particulate relaxation time (s)
$\dot{\gamma}$	shear rate or scalar rate-of-deformation tensor (1/s)
$\underline{\dot{\gamma}}$	rate-of-deformation tensor
$\underline{\dot{\gamma}}_2$	second rate-of-deformation tensor
λ	characteristic time (s)

Subscripts

av	average
bf	base fluid
i	inner or inside
m	mixture
nf	nanofluid

<i>o</i>	outlet or outside
<i>p</i>	nanoparticles
<i>poly-nf</i>	poly-nanofluid
<i>tf</i>	test fluid
<i>w</i>	wall

LIST OF ABBREVIATIONS

AC	Amorphous carbonic
CEF	Criminale-Ericksen-Filbey
CFD	Computational fluid dynamics
CMC	Carboxymethylcellulose
CNTs	Carbon nanotubes
CTAC	Cetyltrimethyl ammonium chloride
DR	Drag reduction
EG	Ethylene glycol
FENE-P	Finitely Extensible Nonlinear Elastic- Peterlin
HTAC	Hexadecyl trimethyl ammonium chloride
HTE	Heat transfer enhancement
HTR	Heat transfer reduction
H2	Heat transfer under both circumferential and axial constant heat flux
MUSCL	Third-order Monotonic Upstream-Centered Scheme for Conservation Laws
PAA	Polyacrylamide
PEO	Polyethylene oxide
PRESTO	Pressure Staggering Option
PTT	Phan-Thien-Tanner
QUICK	Quadratic Upwind Interpolation for Convective Kinetics
SIMPLE	Semi Implicit Method for Pressure Linked Equations
TNT	Titanate nanotubes
UDF	User-defined function
VBF	Viscoelastic-Based-Fluid
VFBN	Viscoelastic-Fluid-Based Nanofluid
VOF	Volume of fluid
XG	Xanthan gum

LIST OF FIGURES

Figure 1.1: The overview of the chapters in this thesis.	7
Figure 2.1: The ratio of heat transfer coefficient for Al ₂ O ₃ and CuO nanofluids to that of distilled water at different Peclet number (Nassan, Heris, and Noie 2010).....	10
Figure 2.2: (a) Thermal conductivity enhancement and (b) viscosity increment of water-based Al ₂ O ₃ nanofluid (Ghanbarpour, Haghigi, and Khodabandeh 2014).....	15
Figure 2.3: Viscosity of CuO and Al ₂ O ₃ nanofluids (Heris, Etemad, and Esfahany 2006).	16
Figure 2.4: Shear stress ratio of Al ₂ O ₃ nanofluid at the Reynolds number of 20000 (Bianco, Manca, and Nardini 2011).....	22
Figure 2.5: Pumping power of Al ₂ O ₃ nanofluid (Zhao et al. 2016).....	22
Figure 2.6: Secondary flow pattern of a viscoelastic solution in a non-circular duct (Semjonow 1967).....	27
Figure 2.7: Heat transfer coefficient increment of a rectangular duct when compared to a circular pipe (Mena et al. 1978).	28
Figure 2.8: Effect of second normal stress coefficient on maximum velocity of vortexes (Norouzi, Kayhani, and Nobari 2009).....	32
Figure 2.9: Dimensionless axial velocity in a cross-section of a square duct (Gao and Hartnett 1993).	34
Figure 2.10: Schematic of pipeline turbulent flow regions (Abubakar et al. 2014).	37
Figure 2.11: Influence of temperature on the convective heat transfer coefficient for 1200 ppm (a) VBF and (b) VBFN (Yang et al. 2013).	42
Figure 2.12: Variation of pressure drop per unit length as a function of velocity at different VBF and VBFN concentration (Yang et al. 2013).....	43
Figure 3.1: Flow chart showing the research methodology of this study.....	47
Figure 3.2: (a) Cone-and-plate geometry (Zhang, Wang, and Chen 2009) and (b) rheometer AR-1500ex.	48
Figure 3.3: Shear stress versus shear rate plot for water at 298.15 K.....	50
Figure 3.4: Viscosity versus shear rate plot for water at 298.15 K.....	51
Figure 3.5: Continuous flow step applied for the rheology measurement.	51
Figure 3.6: Schematic of the heat exchanger apparatus.....	52
Figure 3.7: Schematic diagram of the double pipe heat exchanger.	53
Figure 3.8: Computation grids for (a) circular, (b) square, (c) 4:1 rectangular, (d) 2:1 rectangular ducts, and (e) double pipe heat exchanger.	59
Figure 3.9: (a) Density, (b) heat capacity, (c) thermal conductivity, and (d) viscosity of water with the fitted trendline for each case.....	71

Figure 3.10: Variations of (a) Nusselt number and (b) friction factor of the grids from the chosen grid (%) for circular pipe.....	79
Figure 3.11: Vectors used to compute the orthogonal quality (<i>Ansys Fluent 15.0 User's Guide</i> 2013).....	80
Figure 4.1: Viscosity of PAA solution at 298.15 K.....	85
Figure 4.2: Viscosity of 1000 ppm PAA solution.....	85
Figure 4.3: Viscosity of poly-nanofluid at 298.15 K.....	86
Figure 4.4: Comparison of the viscosity of PAA solution and poly-nanofluid at 298.15 K.....	87
Figure 4.5: Comparison of the viscosity obtained from the experiments with that of the Carreau model for (a) 1000 ppm PAA and (b) 10 ppm PAA in 4% Al ₂ O ₃ nanofluid.....	88
Figure 4.6: Comparison between experimental viscosity and predicted viscosity from Carreau model using Equations 4.1 to 4.4 for (a) 1000 ppm PAA and (b) 10 ppm PAA in 4% nanofluid.....	90
Figure 4.7: First normal stress coefficient of 1000 ppm PAA solution.....	91
Figure 5.1: Overall heat transfer coefficient of water in double pipe heat exchanger at hot inlet temperatures of (a) 313.15 K and (b) 323.15 K.....	93
Figure 5.2: Overall heat transfer coefficient of 0.10% nanofluid at hot inlet temperatures of (a) 313.15 K, (b) 318.15 K and (c) 323.15 K.....	96
Figure 5.3: Comparison between the experimental and numerical overall heat transfer coefficient of 1000 ppm PAA solution at (a) 313.15 K, (b) 318.15 K and (c) 323.15 K.....	97
Figure 5.4: Comparison between the numerical local Nusselt number with the experimental values of Hartnett and Kostic (1985) for 1000 ppm PAA solution in the 2:1 rectangular duct ($Re^*=1368$).....	99
Figure 5.5: Comparison between the experimental and numerical overall heat transfer coefficient of 10 ppm PAA in 0.10% nanofluid at hot inlet temperatures of (a) 313.15 K, (b) 318.15 K and (c) 323.15 K.....	100
Figure 5.6: Comparison between the experimental and numerical overall heat transfer coefficient of 1000 ppm PAA in 0.10% nanofluid at hot inlet temperatures of (a) 313.15 K, (b) 318.15 K and (c) 323.15 K.....	101
Figure 5.7: Enhancement in overall heat transfer coefficient of Al ₂ O ₃ nanofluid with comparison to pure water at hot inlet temperature of 323.15 K.....	103
Figure 5.8: (a) Heat transfer rate and (b) overall heat transfer coefficient of 4% Al ₂ O ₃ nanofluid at different hot inlet temperatures.....	104
Figure 5.9: (a) Heat transfer coefficient and (b) Nusselt number of 4% Al ₂ O ₃ nanofluid (from temperature-dependent approach).....	106
Figure 5.10: <i>Nu</i> enhancement of 4% nanofluid for temperature-dependent approach.....	109

Figure 5.11: Temperature profile at the outlet of (a) circular and (b) 4:1 rectangular ducts (for temperature-dependent properties and $Re=2000$).....	110
Figure 5.12: Nusselt number of 1% and 4% Al_2O_3 nanofluid.	111
Figure 5.13: Local Nusselt number of 1% Al_2O_3 nanofluid.....	112
Figure 5.14: Overall heat transfer coefficient of 0.01% and 4% nanofluid obtained using two-phase models at the hot inlet temperatures of (a) 313.15 K and (b) 323.15 K.	113
Figure 5.15: Nusselt number of 0.01% and 4% Al_2O_3 nanofluid obtained from two-phase models for (a) circular pipe and (b) square duct.....	114
Figure 5.16: Overall heat transfer coefficient of nanofluid obtained using the mixture model at the hot inlet temperature of 323.15 K.....	115
Figure 5.17: Nusselt number of 4% nanofluid obtained from the mixture model.....	115
Figure 5.18: Nusselt number of 1% nanofluid at x/D_h of 116.	116
Figure 5.19: Overall heat transfer coefficient of nanofluid from the single and two-phase models at the hot inlet temperature of 313.15 K.	117
Figure 5.20: Comparison of the Nusselt number obtained from different models for (a) 0.01% and (b) 4% Al_2O_3 nanofluid in circular pipe.	119
Figure 5.21: Overall heat transfer coefficient of PAA solution in the double pipe heat exchanger at hot inlet temperature of 323.15 K.	121
Figure 5.22: Overall heat transfer coefficient of 1000 ppm PAA solution at different hot inlet temperatures.	121
Figure 5.23: Ratio of overall heat transfer coefficient of PAA solution to that of water at hot inlet temperature of 323.15 K.	122
Figure 5.24: Nusselt number of PAA solution in (a) circular and (b) 4:1 rectangular ducts.	123
Figure 5.25: Velocity contour (m/s) of secondary flow for 1000 ppm PAA solution at the outlet cross-section of (a) 4:1 rectangular, (b) 2:1 rectangular and (c) square ducts ($Re^*=1000$).	125
Figure 5.26: Radial velocity vector (m/s) of 1000 ppm PAA solution at the outlet cross-section of circular pipe.	125
Figure 5.27: Nusselt number ratio of 1000 ppm PAA solution to that of water.....	126
Figure 5.28: Overall heat transfer coefficient of 1000 ppm PAA in nanofluid for double pipe heat exchanger.....	127
Figure 5.29: Overall heat transfer coefficient of PAA in 4% Al_2O_3 nanofluid for double pipe heat exchanger.....	128
Figure 5.30: Overall heat transfer coefficient of 1000 ppm PAA in 4% Al_2O_3 nanofluid at different hot inlet temperatures.....	128
Figure 5.31: Heat transfer coefficient of PAA in 4% Al_2O_3 nanofluid for (a) circular and (b) square ducts.....	130

Figure 5.32: Heat transfer coefficient of 10 ppm PAA in nanofluid for (a) circular and (b) square ducts.....	131
Figure 5.33: Nusselt number of 10 ppm PAA in nanofluid for (a) circular and (b) square ducts.....	132
Figure 5.34: Nusselt number ratio of 1000 ppm PAA in 0.13% nanofluid to that of 0.13% nanofluid.....	133
Figure 5.35: Temperature contour (K) of (a) 4% Al ₂ O ₃ nanofluid, (b) 10 ppm PAA in 0.13% nanofluid, (c) 10 ppm PAA in 4% nanofluid and (d) 1000 ppm PAA in 4% nanofluid at the outlet cross-section of the square duct ($Re^*=250$).....	134
Figure 5.36: Velocity contour and vector (m/s) of secondary flow for 1000 ppm PAA in 4% nanofluid at the outlet cross-section of (a) 4:1 rectangular, (b) 2:1 rectangular and (c) square ducts ($Re^*=250$).....	136
Figure 5.37: Temperature contour (K) of 1000 ppm PAA in 4% nanofluid at the outlet cross-section of (a) square, (b) 2:1 rectangular and (c) 4:1 rectangular ducts ($Re^*=250$).....	138
Figure 5.38: Comparison of numerical and predicted Nusselt number of poly-nanofluid (circular pipe) based on Equations 5.1 to 5.4.....	141
Figure 5.39: Comparison of numerical and predicted Nusselt number of poly-nanofluid in circular pipe based on new correlation (Equation 5.5).	142
Figure 5.40: Comparison of numerical and predicted Nusselt number of poly-nanofluid in square duct based on new correlation (Equation 5.6).	143
Figure 5.41: Comparison of numerical and predicted Nusselt number of poly-nanofluid in 2:1 rectangular duct based on new correlation (Equation 5.7).	143
Figure 5.42: Comparison of numerical and predicted Nusselt number of poly-nanofluid in 4:1 rectangular duct based on new correlation (Equation 5.8).	144
Figure 6.1: Pressure drop of water in the double pipe heat exchanger at hot inlet temperatures of (a) 313.15 K and (b) 323.15 K.....	148
Figure 6.2: Friction factor for water in (a) circular and (b) 2:1 rectangular ducts for temperature-independent and temperature-dependent properties.	149
Figure 6.3: Pressure drop of 0.10% nanofluid at hot inlet temperatures of (a) 313.15 K, (b) 318.15 K and (c) 323.15 K.....	151
Figure 6.4: Comparison of friction factor for 1000 ppm PAA at the hot inlet temperatures of (a) 313.15 K and (b) 323.15 K.	152
Figure 6.5: Pressure drop of nanofluid at hot inlet temperature of 323.15 K.	153
Figure 6.6: Wall shear stress of nanofluid at hot inlet temperature of 323.15 K.....	154

Figure 6.7: Pressure drop of 4% nanofluid at different hot inlet temperatures.....	155
Figure 6.8: Magnitude of ΔP increment at Reynolds number of 1300.	155
Figure 6.9: Pressure drop variation with nanoparticle concentration in the circular pipe for the cases of (a) temperature-independent and (b) temperature-dependent properties.	157
Figure 6.10: Effect of nanofluid concentration on velocity profile at the outlet of (a) circular and (b) 4:1 rectangular ducts (temperature-dependent properties, $Re=2000$).	158
Figure 6.11: Effect of Reynolds number on velocity profile along the horizontal direction of outlet cross-section of circular pipe (temperature-dependent properties).	159
Figure 6.12: Pressure drop of 4% nanofluid for temperature-dependent approach.	161
Figure 6.13: Pressure drop of 0.01% and 4% nanofluid obtained using two-phase models at the hot inlet temperatures of (a) 313.15 K and (b) 323.15 K.	163
Figure 6.14: Pressure drop of 4% Al_2O_3 nanofluid obtained from two-phase models for circular pipe.	163
Figure 6.15: Pressure drop of nanofluid obtained in the double pipe heat exchanger using the mixture model at hot inlet temperature of 313.15 K.	164
Figure 6.16: Pressure drop obtained from different models for (a) 1% and (b) 4% nanofluid in double pipe heat exchanger at hot inlet temperature of 313.15 K.	165
Figure 6.17: Comparison of pressure drop obtained from different models for 4% nanofluid in circular pipe.	166
Figure 6.18: Friction factor of nanofluid at hot inlet temperature of 323.15 K.	167
Figure 6.19: Friction factor of 4% nanofluid (temperature-dependent approach).	167
Figure 6.20: Pressure drop of PAA solution in double pipe heat exchanger at hot inlet temperature of 323.15 K.	168
Figure 6.21: Pressure drop of 1000 ppm PAA solution at different hot inlet temperatures.	169
Figure 6.22: Pressure drop of (a) 10 and (b) 1000 ppm PAA solution.	170
Figure 6.23: Pressure drop ratio of 1000 ppm PAA solution to that of water.	171
Figure 6.24: Pressure drop ratio of PAA solution to that of water for square duct.	172
Figure 6.25: Friction factor of PAA solution in (a) double pipe heat exchanger (hot inlet temperature of 313.15 K), (b) circular and (c) square ducts.	174
Figure 6.26: Pressure drop of 10 ppm PAA in nanofluid for double pipe heat exchanger at hot inlet temperature of 313.15 K.	175
Figure 6.27: Pressure drop of PAA in 4% Al_2O_3 nanofluid for double pipe heat exchanger at hot inlet temperature of 313.15 K.	175

Figure 6.28: Pressure drop ratio of 1000 ppm PAA in 4% nanofluid to 4% nanofluid for double pipe heat exchanger.....	176
Figure 6.29: Pressure drop of 10 ppm PAA in nanofluid for (a) circular and (b) square ducts.....	177
Figure 6.30: Pressure drop of PAA in 4% Al ₂ O ₃ nanofluid for (a) circular and (b) square ducts.....	178
Figure 6.31: Pressure drop of 1000 ppm PAA in 4% Al ₂ O ₃ nanofluid.....	181
Figure 6.32: Friction factor of poly-nanofluid in (a) double pipe heat exchanger (temperature of 313.15 K), (b) circular and (c) square ducts.....	183
Figure 6.33: Comparison of numerical and predicted friction factor of poly-nanofluid based on the new correlation (Equation 6.1).....	184
Figure A.1: Error propagation into the experimental results (Stern et al. 1999).....	217
Figure D.1: Two algorithms available for the pressure-based solver (<i>Ansys Fluent 15.0 User's Guide</i> 2013).....	232
Figure F.1: Variations of (a) Nusselt number and (b) friction factor of the grids from the chosen grid (%) for 2:1 rectangular duct.....	237
Figure F.2: Variations of (a) Nusselt number and (b) friction factor of the grids from the chosen grid (%) for 4:1 rectangular duct.....	238
Figure F.3: Variations of (a) Nusselt number and (b) friction factor of the grids from the chosen grid (%) for square duct.....	239
Figure F.4: Variations of (a) Nusselt number and (b) friction factor of the grids from the chosen grid (%) for double pipe heat exchanger.....	240
Figure H.1: Friction factor for water in (a) 4:1 rectangular and (b) square ducts for temperature-independent and temperature-dependent properties.....	246
Figure I.1: Overall heat transfer coefficient of (a) 0.01% and (b) 1% Al ₂ O ₃ nanofluid at different hot inlet temperatures.....	247
Figure I.2: Comparison of Nusselt number obtained from different models for 4% Al ₂ O ₃ nanofluid in (a) 2:1 rectangular, (b) 4:1 rectangular and (c) square ducts.....	250
Figure I.3: Pressure drop of nanofluid in 2:1 rectangular duct for the cases of (a) temperature-independent and (b) temperature-dependent properties.....	251
Figure I.4: Pressure drop of nanofluid in 4:1 rectangular duct for the cases of (a) temperature-independent and (b) temperature-dependent properties.....	252
Figure I.5: Pressure drop of nanofluid in square duct for the cases of (a) temperature-independent and (b) temperature-dependent properties.....	253
Figure I.6: Pressure drop of 0.10% Al ₂ O ₃ nanofluid for temperature-dependent approach.....	255
Figure I.7: Pressure drop of 4% Al ₂ O ₃ nanofluid for temperature-independent approach.....	256

Figure I.8: Pressure drop of 1% nanofluid obtained from two-phase models for circular pipe.	256
Figure I.9: Pressure drop of 4% nanofluid obtained from two-phase models for 2:1 rectangular duct.....	257
Figure I.10: Pressure drop of 4% nanofluid obtained from two-phase models for 4:1 rectangular duct.	257
Figure I.11: Pressure drop of 4% nanofluid obtained from two-phase models for square duct.....	258
Figure I.12: Comparison of pressure drop obtained from different models for 4% Al ₂ O ₃ nanofluid in (a) square and (b) 4:1 rectangular ducts.....	259
Figure I.13: Friction factor of PAA solution in (a) 2:1 and (b) 4:1 rectangular ducts.....	260
Figure I.14: Heat transfer coefficient of 10 ppm PAA in nanofluid in (a) 4:1 and (b) 2:1 rectangular ducts.	261
Figure I.15: Heat transfer coefficient of PAA in 4% Al ₂ O ₃ nanofluid in (a) 4:1 and (b) 2:1 rectangular ducts.	262
Figure I.16: Pressure drop of 10 ppm PAA in nanofluid for (a) 4:1 and (b) 2:1 rectangular ducts.....	266
Figure I.17: Pressure drop of PAA in 4% Al ₂ O ₃ nanofluid for (a) 4:1 and (b) 2:1 rectangular ducts.....	267
Figure I.18: Friction factor of poly-nanofluid in (a) 2:1 and (b) 4:1 rectangular ducts.....	270

LIST OF TABLES

Table 2.1: Summary of experimental and numerical studies on heat transfer and flow behaviour of different nanofluids.	23
Table 2.2: Summary of numerical studies on the flow of polymeric solution in non-circular ducts.	35
Table 3.1: Solutions used for rheology measurement.	49
Table 3.2: Specifications of the double pipe heat exchanger.	53
Table 3.3: Specifications of the hot and cold circuits.	53
Table 3.4: The bias limits for different individual variables.	57
Table 3.5: The results of uncertainty analysis.	57
Table 3.6: Dimensions of the simulated circular and non-circular ducts.	58
Table 3.7: Temperature-independent thermo-physical properties of water used.	70
Table 3.8: Temperature-dependent properties of water.	70
Table 3.9: Thermo-physical properties of the nanoparticles used in this study.	72
Table 3.10: Temperature-independent thermo-physical properties of nanofluid.	72
Table 3.11: Coefficients for Equation 3.73.	73
Table 3.12: Mesh quality of different geometries.	80
Table 3.13: Value of constants in Equation 3.95.	83
Table 5.1: Comparison of numerical Nu_{H_2} of water with the theoretical value ($Re=250$).	94
Table 5.2: h enhancement (%) of nanofluid in circular pipe.	106
Table 5.3: Nu enhancement (%) of nanofluid in circular pipe.	107
Table 5.4: $Nu_{poly-nf}/Nu_{nf}$ for square duct.	139
Table 5.5: $Nu_{poly-nf}/Nu_{PAA}$ for square duct.	140
Table 6.1: τ_w increment (%) of Al_2O_3 nanofluid in the circular pipe.	160
Table 6.2: ΔP increment (%) of Al_2O_3 nanofluid in the circular pipe.	160
Table 6.3: $\Delta P_{poly-nf}/\Delta P_{nf}$ for circular pipe.	179
Table 6.4: $\Delta P_{poly-nf}/\Delta P_{nf}$ for square duct.	179
Table 6.5: $\Delta P_{poly-nf}/\Delta P_{PAA}$ for circular pipe.	180
Table 6.6: $\Delta P_{poly-nf}/\Delta P_{PAA}$ for square duct.	181
Table 7.1: Thermal-hydraulic efficiency of nanofluid in double pipe heat exchanger.	188
Table 7.2: Thermal-hydraulic efficiency of nanofluid in circular pipe.	189
Table 7.3: Thermal-hydraulic efficiency of PAA solution in double pipe heat exchanger.	191

Table 7.4: Thermal-hydraulic efficiency of PAA solution in different geometries.	192
Table 7.5: Thermal-hydraulic efficiency of poly-nanofluid in double pipe heat exchanger at hot inlet temperature of 313.15 K.	194
Table 7.6: Thermal-hydraulic efficiency of poly-nanofluid in circular pipe.	195
Table 7.7: Thermal-hydraulic efficiency of poly-nanofluid in square duct.	195
Table 7.8: Average thermal-hydraulic efficiency of poly-nanofluid.	197
Table A.1: Values of variables in Equation 3.7.	218
Table A.2: Values of variables in Equation 3.8.	221
Table A.3: Values of variables in Equation 3.9.	222
Table E.1: Solution method for the modelling of test fluids in circular and non-circular ducts (except for two-phase nanofluid modelling).	233
Table E.2: Solution method for the modelling of nanofluid in circular and non-circular ducts under the mixture and VOF models.	233
Table E.3: Solution method for the modelling of nanofluid in circular and non-circular ducts under the Eulerian model.	233
Table E.4: Solution method for the modelling of test fluids in double pipe heat exchanger (except for two-phase nanofluid modelling).	233
Table E.5: Solution method for the modelling of nanofluid in double pipe heat exchanger under the mixture model.	234
Table E.6: Under-relaxation factors for numerical studies of water and nanofluid in circular and non-circular ducts (except for the two-phase nanofluid modelling).	234
Table E.7: Under-relaxation factors for numerical studies of nanofluid in circular and non-circular ducts under the mixture model.	234
Table E.8: Under-relaxation factors for numerical studies of nanofluid in circular and non-circular ducts under the Eulerian model.	234
Table E.9: Under-relaxation factors for numerical studies of nanofluid in circular and non-circular ducts under the VOF model.	235
Table E.10: Under-relaxation factors for numerical studies of PAA solution and poly-nanofluid in circular pipe.	235
Table E.11: Under-relaxation factors for numerical studies of PAA solution and poly-nanofluid in non-circular ducts.	235
Table E.12: Under-relaxation factors for numerical studies of test fluids in double pipe heat exchanger (except for two-phase nanofluid modelling).	235
Table E.13: Under-relaxation factors for numerical studies of nanofluid in double pipe heat exchanger under the mixture model.	236
Table G.1: The values of constants for η_{∞} in Equation 4.1.	241

Table G.2: The values of constants for η_o in Equation 4.2.....	242
Table G.3: The values of constants for λ in Equation 4.3.	242
Table G.4: The values of constants for n' in Equation 4.4.	243
Table G.5: Constants for a in Equation 4.6.	243
Table G.6: Constants for b in Equation 4.7.	244
Table G.7: Constants for c in Equation 4.8.....	244
Table G.8: Constants for d in Equation 4.9.	245
Table G.9: Constants for Equation 4.10.....	245
Table I.1: h enhancement (%) of nanofluid in 2:1 rectangular duct.....	248
Table I.2: Nu enhancement (%) of nanofluid in 2:1 rectangular duct.....	248
Table I.3: h enhancement (%) of nanofluid in 4:1 rectangular duct.	248
Table I.4: Nu enhancement (%) of nanofluid in 4:1 rectangular duct.....	249
Table I.5: h enhancement (%) of nanofluid in square duct.	249
Table I.6: Nu enhancement (%) of nanofluid in square duct.	249
Table I.7: τ_w increment (%) of Al_2O_3 nanofluid in 2:1 rectangular duct.	254
Table I.8: ΔP increment (%) of Al_2O_3 nanofluid in 2:1 rectangular duct.....	254
Table I.9: ΔP increment (%) of Al_2O_3 nanofluid in 4:1 rectangular duct.....	254
Table I.10: ΔP increment (%) of Al_2O_3 nanofluid in square duct.....	255
Table I.11: $Nu_{poly-nf}/Nu_{nf}$ for circular pipe.....	263
Table I.12: $Nu_{poly-nf}/Nu_{nf}$ for 4:1 rectangular duct.	263
Table I.13: $Nu_{poly-nf}/Nu_{nf}$ for 2:1 rectangular duct.	264
Table I.14: $Nu_{poly-nf}/Nu_{PAA}$ for 4:1 rectangular duct.	264
Table I.15: $Nu_{poly-nf}/Nu_{PAA}$ for 2:1 rectangular duct.	265
Table I.16: $\Delta P_{poly-nf}/\Delta P_{nf}$ for 2:1 rectangular duct.....	268
Table I.17: $\Delta P_{poly-nf}/\Delta P_{nf}$ for 4:1 rectangular duct.....	268
Table I.18: $\Delta P_{poly-nf}/\Delta P_{PAA}$ for 2:1 rectangular duct.....	269
Table I.19: $\Delta P_{poly-nf}/\Delta P_{PAA}$ for 4:1 rectangular duct.....	269
Table I.20: Thermal-hydraulic efficiency of nanofluid in square duct.	271
Table I.21: Thermal-hydraulic efficiency of nanofluid in 2:1 rectangular duct.	271
Table I.22: Thermal-hydraulic efficiency of nanofluid in 4:1 rectangular duct.	271
Table I.23: Thermal-hydraulic efficiency of poly-nanofluid in double pipe heat exchanger at hot inlet temperature of 318.15 K.....	272
Table I.24: Thermal-hydraulic efficiency of poly-nanofluid in double pipe heat exchanger at hot inlet temperature of 323.15 K.....	272
Table I.25: Thermal-hydraulic efficiency of poly-nanofluid in 4:1 rectangular duct.....	273
Table I.26: Thermal-hydraulic efficiency of poly-nanofluid in 2:1 rectangular duct.....	273

CHAPTER 1: INTRODUCTION

1.1 Background of the study

Heat transfer can be regarded as one of the most essential industrial processes. Heat needs to be added or removed from process streams in industries such as power generation, transportation, electronics and chemical production. In these industrial applications, heat transfer is achieved through heat exchangers, evaporators and condensers. It is desirable to increase the heat transfer efficiency in these devices. The heat transfer efficiency can be attained using heat transfer enhancement (HTE) techniques which are classified into active and passive methods (Shahmohammadi and Jafari 2014). The active methods involve the usage of external force like stirring to enhance heat transfer rate while no external power is applied for the passive methods. Examples of passive techniques are inserting baffles in the flow path or approaches to improve the thermal properties of the heat transfer fluids.

The development of advanced heat transfer fluids with better heat transfer performance is in great demand. This is because the thermal performance of the conventional heat transfer fluids like water, oil and ethylene glycol is poor, owing to their low thermal conductivity (Choi and Eastman 1995). The use of small solid particles as the suspended additives in the heat transfer fluids is an effective way to augment the thermal conductivity of the fluids. Early researches focused on the milli- or micrometer-sized solid particles and this approach has been well known for more than 100 years (Lotfi, Saboohi, and Rashidi 2010). Nonetheless, the milli- or micro-sized solid particles are not industrially attractive because their suspension induce high penalty of pressure drop, poor suspension stability, sedimentation, erosion, fouling and channel clogging due to their high density and big size (Wang and Mujumdar 2007). Since the fluids with milli- or micrometer-sized particles are not effective enough to outweigh the drawbacks related to their application, the research focus is then dedicated to nano-sized particles. Study in the use of nano-sized particles has become more popular as the advancement in the material technology makes their fabrication easier.

The suspension of these nano-sized particles in the base fluid can change the thermal and transport characteristics of the fluid. They are found to have superior properties and stability compared to the milli- or micrometer-sized particles due to their greater surface area to volume ratio. In addition, nanoparticles can fluidize in the base fluid easily due to their small size, hence preventing the problems of channel clogging and erosion of the channel wall. Dispersants can be added to enhance the stability of the suspension to avoid sedimentation of the nanoparticles (Choi and Eastman 1995; Wang and Mujumdar 2007; Lotfi, Saboohi, and Rashidi 2010; Chinnaraj 2011). The suspension of nano-sized particles in a base fluid is termed as nanofluid. Choi and Eastman (1995) were the first to use this term and they proposed the nanofluid as a potential replacement of the conventional heat transfer fluids.

Nanofluids can be categorized according to their base fluid, type of material, particle size, shape, and concentration. Base fluids that are commonly used for the preparation of nanofluids are the conventional heat transfer fluids. The materials of the nanoparticles are divided into metallic, metal-oxide, chalcogenides and other particles such as carbon nanotubes (CNTs) (Stroder 2011). The widely utilized nanoparticles include Al_2O_3 , CuO , TiO_2 , Ag , Cu , Fe , and CNTs. It is observed from literature that the size of nanoparticles generally varies from 20 nm to 100 nm (Ozerinc 2010). Nanofluids have been applied as the coolants in electronic and refrigeration devices, automotives, and power generators. Besides, nanofluids can be used in the solar energy systems, thermal management system for vehicles, machining processes, heat exchangers and transformers (Goktepe, Atalik, and Erturk 2014; Kakac and Pramuanjaroenkij 2016).

It is evident that nanofluids offer exciting new possibilities for HTE. Nevertheless, this HTE is achieved at the expense of a higher pressure drop, particularly for higher nanoparticle concentrations. The increased pressure drop is ascribed to the viscosity increment induced by the presence of the nanoparticles (Heris, Etemad, and Esfahany 2006; Hwang, Jang, and Choi 2009; Esfe et al. 2014). This increased pressure drop is the main concern for the application of nanofluids as the heat transfer fluids. Hence, the use of nanofluids is economical only if their thermal-hydraulic efficiency is enhanced.

Polymers might be useful in improving the thermal-hydraulic efficiency of the nanofluids. Generally used polymers are normally long-chained with high molecular weight (ranging from 1 to 10 million). These polymers include polyacrylamide (PAA), polyethylene oxide (PEO), polyacrylic acid (Carbopol), carboxymethylcellulose (CMC), and hydroxyethylcellulose (Natrosol) (Peysner 1973; Berman 1978; Kostic 1994; Lin, Ko, and Tsou 1996). Polymers are proposed for wide applications such as oil field operations, slurry or hydraulic capsule pipeline transportation, suppression of atherosclerosis, prevention of lethality from hemorrhagic shock, increment of water flow and water jet focusing in fire-fighting equipment, prevention of overflow in sewage systems, hydropower and irrigation systems, and as an anti-misting agent in jet fuel (Wang et al. 2011).

For laminar regime, polymers are reported to be viscoelastic in non-circular ducts (Gupta, Metzner, and Hartnett 1967; Oliver and Karim 1971; Mena et al. 1978; Hartnett and Kostic 1985). (Viscoelastic material exhibits both viscous and elastic behaviour simultaneously). With this viscoelastic characteristic, polymers can give significant heat transfer argumentation without inducing higher fluid friction. On the other hand, polymer additives are able to reduce fluid friction for both internal and external turbulent flow. For a pipe flow, the reduction in the fluid friction is, however, always accompanied by a great amount of heat transfer performance deterioration. Some researchers had reported that the heat transfer reduction (HTR) can be higher than the friction reduction (Gupta, Metzner, and Hartnett 1967; Poreh and Paz 1968; Kwack and Hartnett 1983; Hartnett and Kwack 1986).

The term “poly-nanofluid” can be employed to describe the solution formed when the polymer additives are added into the nanofluid. Kostic (2013) suggested the development of poly-nanofluid as one of the potential researches which can open up many more unprecedented applications in the future. Therefore, research studying the heat transfer performance, pressure drop and thermal-hydraulic efficiency of the poly-nanofluid is of paramount importance and desirable.

1.2 Scope of the study

The present study focuses on the thermal-hydraulic efficiency investigation of the nanofluid, polymer and poly-nanofluid in circular and non-circular ducts for the laminar regime. The Reynolds number covered in this research ranges from 250 to 2000. This research is performed through experiments and Computational Fluid Dynamics (CFD) simulations. The experimental work is divided into the rheological measurement and heat transfer study. The examination of the rheological behaviour of polymer and poly-nanofluid is carried out using a rheometer AR-1500ex (TA Instruments). In addition, the heat transfer experiments are conducted using a double pipe heat exchanger, representing the circular duct. Besides, simulations are executed using ANSYS FLUENT software Version 15.0 to obtain the heat transfer performance and pressure drop of nanofluid, polymer and poly-nanofluid in the circular and non-circular ducts. The thermal-hydraulic efficiency is evaluated using the heat transfer and pressure drop data obtained.

Numerical studies are selected as parts of the research methods since they are cost- and time-effective. Simulations have been widely applied to study the dynamics of the fluid flow. Furthermore, the images or contours obtained from the simulations are capable of providing better understanding on the heat transfer and fluid flow performance of the fluids studied. Integrated experimental studies with CFD works can aid in developing a reliable theoretical framework for the poly-nanofluid.

The non-circular ducts, especially rectangular ducts, have been widely employed in the development of liquid cooling modules for electronic packaging and many other industrial applications. Besides, the non-circular ducts have the advantage of lower pressure drop compared to the circular ducts (Hartnett and Kostic 1989; Gao and Hartnett 1992; Gingrich, Cho, and Shyy 1992b; Shin and Cho 1994; Nassan, Heris, and Noie 2010). The non-circular ducts studied are square, 4:1 rectangular and 2:1 rectangular ducts.

The nanoparticles and polymer additives used in this present study are Al_2O_3 nanoparticles and PAA, respectively. Water is the base fluid. Poly-nanofluid is the

mixture of water- Al_2O_3 nanofluid and PAA additives with different concentrations. Al_2O_3 nanofluid is selected because it is a very common nanofluid which is studied extensively in the research field. Furthermore, Al_2O_3 nanofluid is safe and it is physically and chemically stable. In addition, it is also cheaper compared to the other types of nanofluids (Sonawane, Khedkar, and Wasewar 2013). For the case of polymer, PAA is considered because it is a well-known polymer solution that exhibits substantial heat transfer augmentation in the laminar regime (Shin and Cho 1993). Besides, it is water-soluble, non-toxic and biodegradable. It has more resistance to mechanical degradation as well (Abubakar et al. 2014). The range of Al_2O_3 nanofluid and PAA studied are 0.01–4.00 vol% and 10–1000 ppm, respectively. These low to high concentration ranges are chosen because they are the general ranges used for research (Hartnett and Kostic 1985; Bschorer and Brunn 1996; Escudier, Presti, and Smith 1998; Kumar and Ganesan 2012; Yang et al. 2017).

1.3 Significance of the study

The research significances of this study can be viewed in two aspects. This first aspect is the theoretical contribution. This research helps in better understanding of the rheological behaviour of the new hybrid fluid – poly-nanofluid. The effect of polymer additives on the heat transfer performance and pressure drop of nanofluid can also be known. Using the obtained data, the correlations for the Nusselt number and friction factor are proposed to predict the heat transfer performance and flow characteristic of poly-nanofluid.

The second aspect of the significance is the practical applications. This study helps to extend the heat transfer applications of nanofluid by improving its thermal-hydraulic efficiency through adding polymer additives in it. Additionally, this research in the discovery of the new hybrid fluid can pave ways for new heat transfer applications. By obtaining the optimum concentration for the poly-nanofluid, it will open up opportunities for high thermal and hydraulic efficient systems.

1.4 Thesis organization

This thesis consists of eight chapters, including introduction, conclusion and recommendations. Chapter 2 is a review of the experimental and numerical investigations for the nanofluid and polymer solution. The laminar and turbulent heat transfer and flow behaviour of nanofluid and polymer in the circular and non-circular channels are inspected. Recent studies related to the addition of additives to nanofluid are also discussed. The research gap and problem statement are also emphasized. The aim and objectives of the study are given at the end of Chapter 2.

Chapter 3 describes the research methodology used to achieve the objectives of this study. In this chapter, the methods utilized for the rheology and heat transfer experiments are provided. Apart from this, the setup for simulations, governing equations, boundary conditions and solution strategy employed to solve the heat transfer and flow behaviour of the test fluids are also outlined. Data reduction is presented at the end of the chapter.

Chapters 4, 5, 6 and 7 present the results and discussion. Chapter 4 discusses the rheological behaviour of PAA solution and poly-nanofluid. Curve fitting for the solutions are also addressed. Chapter 5 shows the experimental and numerical heat transfer results obtained for nanofluid, PAA and poly-nanofluid. The heat transfer performances of these solutions in different geometries are compared. Chapter 6 describes the pressure drop and friction factor attained by these solutions in different ducts. The final result and discussion chapter, Chapter 7, links Chapters 5 and 6 together to evaluate the thermal-hydraulic efficiency of nanofluid, PAA and poly-nanofluid. Furthermore, Chapter 7 gives the optimum concentration of poly-nanofluid for the best thermal-hydraulic performance.

Chapter 8 presents a summary and conclusion of the work done in this study. The main findings are highlighted. Scopes of future work in poly-nanofluid are recommended in the last section of this thesis. The organization of the thesis and the link between the chapters is depicted in Figure 1.1.

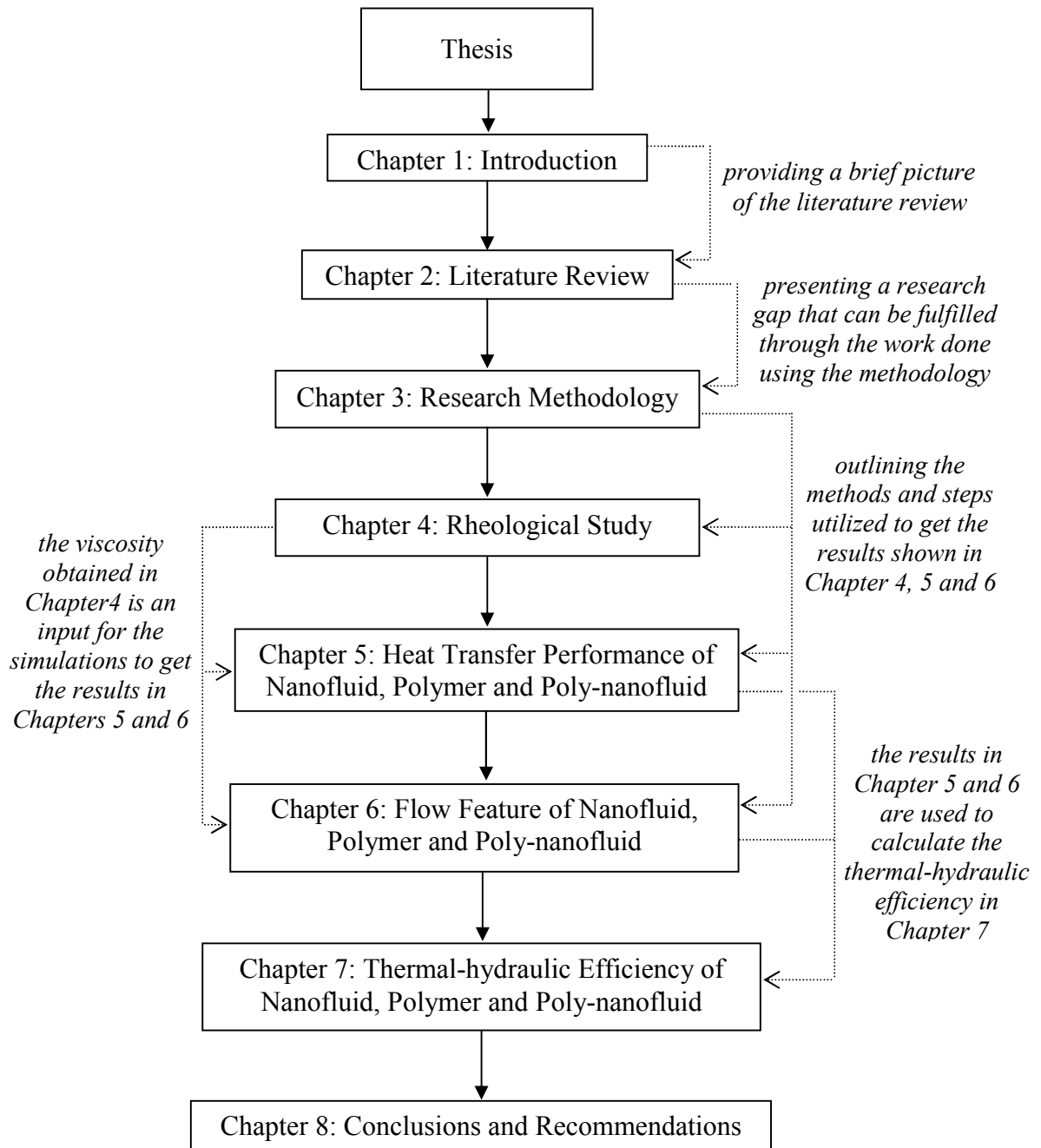


Figure 1.1: The overview of the chapters in this thesis.

CHAPTER 2: LITERATURE REVIEW

2.1 Nanofluid

After Choi and Eastman (1995) identified nanofluid as a promising alternative to the conventional heat transfer fluids, its suitability had been assessed extensively in the literature. Generally, research on the nanofluids can be divided into two categories. The first majority group focuses exclusively on the heat transfer performance of the nanofluids while the second group also examines the viscosity and the pressure drop of the nanofluid systems.

2.1.1 Studies on heat transfer performance of nanofluids

Early finding on nanofluid was made by Choi and Eastman (1995). They reported that by adding 5% and 20% Cu nanoparticles (with sphericity of 0.3) into water, the thermal conductivity of water could be augmented by a factor of 1.5 and 3.5, respectively. Lee et al. (1999) expressed that the dispersion of 4% CuO nanoparticles (35 nm) in ethylene glycol had remarkably improved the thermal conductivity by 20%. Hwang et al. (2006) observed that with 1% CNTs in water, the thermal conductivity could be increased up to 11.3%. Das (2017) and Leong et al. (2017) reviewed the thermal conductivity of hybrid nanofluids (nanofluids formed by dispersing two different nanoparticles into the base fluid) and deduced that the hybrid nanofluids also exhibited better thermal conductivity when compared to that of the base fluid.

Besides the thermal conductivity, research was also done on the heat transfer coefficient of nanofluids. Wen and Ding (2004) investigated the laminar convective heat transfer of Al_2O_3 nanoparticles in de-ionized water and concluded that greater HTE was encountered in the entrance region. Their results revealed that the heat transfer coefficient enhancement was much higher than that of the thermal conductivity for a circular pipe. The maximum thermal conductivity enhancement was approximately 10%, while the maximum convective heat transfer coefficient enhancement was more than 30%.

Lotfi, Saboohi, and Rashidi (2010) employed single-phase, two-phase mixture and Eulerian models to simulate a forced convective nanofluid flow in a circular tube with constant heat flux boundary condition. The mixture model was identified to be more precise in predicting the Nusselt number of nanofluid compared to the other two models. In addition, their results showed that the rate of HTE decreased with the increasing nanoparticle concentration. Akbari, Galanis, and Behzadmehr (2011) inspected the laminar mixed convection of alumina nanofluid in a circular tube using the same models as Lotfi, Saboohi, and Rashidi (2010). They also considered the volume of fluid (VOF) model in their work. They validated their numerical results against the experimental values of Wen and Ding (2004). The hydrodynamic fields estimated from the single-phase and two-phase models were found to be similar, but not for the thermal ones. All the three two-phase models gave similar results for the heat transfer coefficient.

Moraveji and Esmaili (2012) also employed the single-phase and discrete phase (two-phase) models for the investigation of water-based Al_2O_3 nanofluid in a circular tube. They stated that the average heat transfer coefficient enhancement obtained from the single-phase and discrete phase models were approximately 26.32% and 19.30% with respect to water, respectively, at the constant heat flux of $10,000 \text{ W/m}^2$. Furthermore, Fard, Esfahany, and Talaie (2010) reported that the heat transfer coefficient of 3% nanofluid computed using the two-phase model was 1.54 times the value of water at the Peclet number of 6500. Other research on the single-phase and two-phase simulations of nanofluids was reviewed in detail by Kakac and Pramuanjaroenkij (2016).

Lelea and Nisulescu (2011) numerically studied the heat transfer of water-based Al_2O_3 nanofluid in a micro-channel. The local heat transfer coefficient of nanofluid was found to increase with the increasing concentration. At the fixed pumping power of 0.13 W, the maximum HTE recorded was 37% for 9% nanofluid. Besides, Sonawane, Khedkar, and Wasewar (2013) utilized water-based Al_2O_3 nanofluid as the cooling medium in a concentric tube heat exchanger. They reported that the maximum enhancement of 47.36% in the overall heat transfer coefficient could be achieved with 3% nanofluid.

Heat transfer analysis using the nanofluids has also been performed in a circular pipe with helical inserts. Pathipakka and Sivashanmugam (2010) numerically examined the

heat transfer behaviour of Al_2O_3 nanofluid in a circular pipe with helical inserts. For the Reynolds number of 2039 and twist ratio of 2.93, the Nusselt number increment was 1.11, 1.21 and 1.33 times relative to the base fluid for 0.5%, 1.0% and 1.5% nanofluid, respectively. Comparing the plain tube and the tube fitted with helical inserts, the Nusselt number of the latter was higher compared to the former. However, the degree of Nusselt number increment was similar for both of the tubes.

Apart from circular pipe, the non-circular ducts also gained popularity due to the increasing demands for these sorts of geometries in many heat transfer applications, especially in the compact heat exchangers (Nassan, Heris, and Noie 2010). Nassan, Heris, and Noie (2010) used the water-based Al_2O_3 and CuO nanofluids in order to improve the thermal efficiency of a square duct. Their experimental results showed that the heat transfer coefficient in the square duct was enhanced by 18 and 21% with 1.5% Al_2O_3 and CuO nanofluids, respectively (Figure 2.1). Similar to the circular flow, the heat transfer performance of nanofluid in the square duct increased with the increasing nanoparticle loading, Reynolds number and Peclet number.

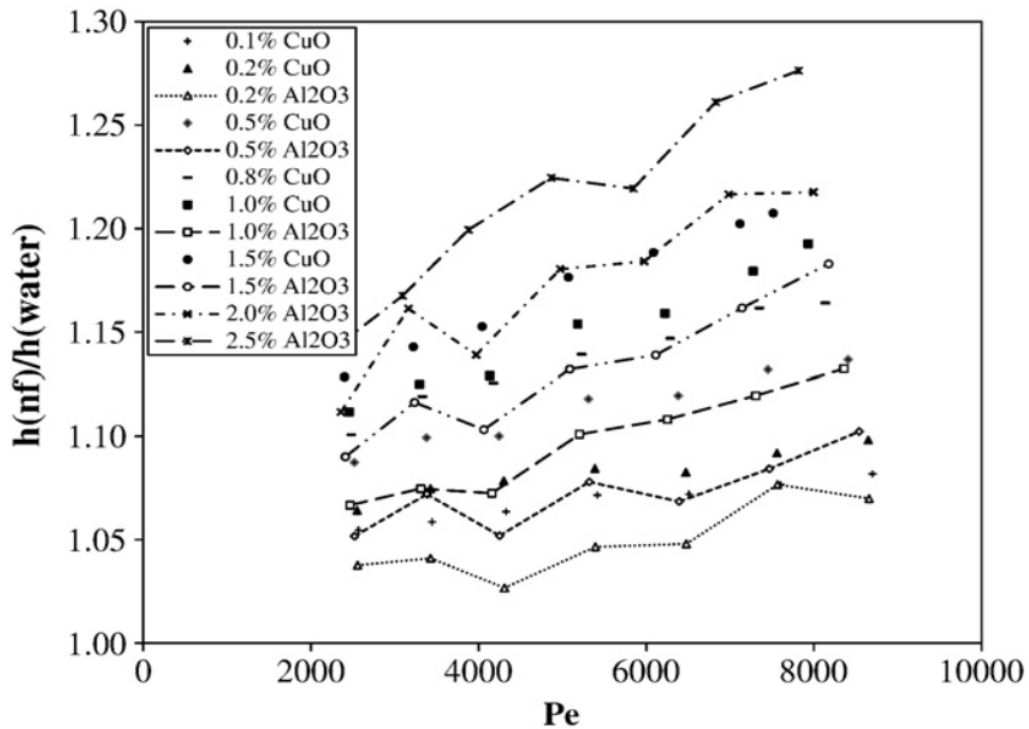


Figure 2.1: The ratio of heat transfer coefficient for Al_2O_3 and CuO nanofluids to that of distilled water at different Peclet number (Nassan, Heris, and Noie 2010).

Moreover, Heris et al. (2013) investigated the laminar heat transfer behaviour in a square duct using 2.5% nanofluid. They discovered that lower heat transfer rate experienced by the conventional heat transfer fluid in the square duct was basically due to the presence of some static sections for fluid near the corners of the duct. The nanoparticles helped to reduce these static sections, thus overcoming this poor heat transfer performance. The heat transfer coefficient was augmented up to 27.6% compared to that of the base fluid. The results of Heris et al. (2012) indicated that the Nusselt number enhancement of 59%, 68% and 77% were obtained by 4% water-based Al_2O_3 , CuO and Cu nanofluids, respectively.

2.1.2 Proposed HTE mechanisms for nanofluids

Some researchers observed higher enhancement in the heat transfer coefficient compared to that of the thermal conductivity (Hwang, Jang, and Choi 2009; Heris et al. 2013; Heyhat et al. 2013; Wang et al. 2013; Esfe et al. 2014), so the thermal conductivity enhancement could not be the sole reason for the convective heat transfer augmentation (Wen and Ding 2004; Nassan, Heris, and Noie 2010; Heris et al. 2013; Heyhat et al. 2013; Wang et al. 2013). Wen and Ding (2004) claimed that besides the thermal conductivity increment, the convective HTE for the laminar regime was also presumably attributed to particle migration. The particle migration evoked disturbance in the thermal boundary layer, leading to non-uniform distribution of the thermal conductivity and viscosity of the nanofluid systems. This reduced the thermal boundary layer thickness, hence, the heat transfer rate was improved. Chun, Kang, and Kim (2008) believed that the particles migration brought a high amount of nanoparticles to the near-wall thermal boundary layer and increased the thermal energy exchange rate. Similar remarks as Wen and Ding (2004) and Chun, Kang, and Kim (2008) were made by D. Kim et al. (2009), Heris, Etemad, and Esfahany (2006), Rashmi et al. (2013), and Wang et al. (2013). Wang, Xu, and Choi (1999) disclosed that besides a decrease in the thermal boundary layer thickness, conduction between nanoparticles and the duct wall, as well as promotion of turbulence were also responsible for the HTE. Rashmi et al. (2013) also pointed out that the HTE was ascribed to the presence of higher surface area for heat transfer by the nanoparticles. Other possible reasons for HTE might be the

bridging between nanoparticles and the interaction of solid-solid particles to solid-liquid molecules (Sonawane, Khedkar, and Wasewar 2013).

On the other hand, Hwang, Jang, and Choi (2009) stated that flattening of the velocity profile could increase the heat transfer coefficient. This velocity profile flattening was induced by the high gradients in the bulk properties, such as the nanoparticle concentration, thermal conductivity and viscosity, leading to the increase of temperature gradient at the wall region. In addition, Nassan, Heris, and Noie (2010) proposed that the laminar convective HTE of nanofluids was also due to the Brownian motion and nanoparticles dispersion. Nanoparticles dispersion and their interaction with the duct wall increased the heat transfer rate. Heris et al. (2013), Dawood, Mohammed, and Munisamy (2014) and Ganvir, Walke, and Kriplani (2017) agreed with Nassan, Heris, and Noie (2010) on the reasons behind the HTE of nanofluids.

2.1.3 Experimental studies on both heat transfer and flow behaviour of nanofluids

According to the research done by the authors (Choi and Eastman 1995; Lee et al. 1999; Wen and Ding 2004; Hwang et al. 2006; Fard, Esfahany, and Talaie 2010; Lotfi, Saboohi, and Rashidi 2010; Nassan, Heris, and Noie 2010; Pathipakka and Sivashanmugam 2010; Akbari, Galanis, and Behzadmehr 2011; Lelea and Nisulescu 2011; Moraveji and Esmaeili 2012; Heris et al. 2013; Sonawane, Khedkar, and Wasewar 2013) mentioned in Section 2.1.1, the HTE of nanofluids increases with the increasing of both nanoparticle loading and Reynolds number. However, the viscosity also increases with the nanofluid concentration as the fluid internal shear stress increases (Wang, Xu, and Choi 1999; Heris, Etemad, and Esfahany 2006; Chevalier, Tillement, and Ayela 2007; He et al. 2007; Lee et al. 2007; Namburu et al. 2007; Nguyen et al. 2007; Murshed, Leong, and Yang 2008; Nguyen et al. 2008; Chen et al. 2009; Duangthongsuk and Wongwises 2009b; Hwang, Jang, and Choi 2009; Rea et al. 2009; Chandrasekar, Suresh, and Bose 2010; Duangthongsuk and Wongwises 2010; Kole and Dey 2010; Vajjha, Das, and Kulkarni 2010; Lee et al. 2011; Phuoc, Massoudi, and Chen 2011; Mashaei, Hosseinalipour, and Bahiraei 2012; Heyhat et al. 2013; Rashin and Hemalatha 2013; Sundar, Singh, and Sousa 2013; Yiamsawas et al. 2013; Esfe et al. 2014; Ghanbarpour, Haghigi, and Khodabandeh 2014; Halelfadl, Estelle, and Mare 2014;

Azmi et al. 2016). These authors (Choi and Eastman 1995; Lee et al. 1999; Wen and Ding 2004; Hwang et al. 2006; Fard, Esfahany, and Talaie 2010; Lotfi, Saboohi, and Rashidi 2010; Nassan, Heris, and Noie 2010; Pathipakka and Sivashanmugam 2010; Akbari, Galanis, and Behzadmehr 2011; Lelea and Nisulescu 2011; Moraveji and Esmaeili 2012; Heris et al. 2013; Sonawane, Khedkar, and Wasewar 2013) did not take the viscosity or flow resistance into consideration in their studies. Many researchers emphasized the importance of taking viscosity or rheological behaviour of nanofluids into account for the heat transfer analysis. It is conceded that the viscosity is as significant as the thermal conductivity and heat transfer coefficient in the thermal operations that involve fluid flow because it measures the internal resistance of the flow. The internal resistance of the fluid flow is directly related to the required pumping power of the system (Wang, Xu, and Choi 1999; Keblinski, Eastman, and Cahill 2005; Nguyen et al. 2007; Mare et al. 2011; Aladag et al. 2012). Therefore, it is essential to investigate the viscosity (or pressure drop) in order to assess the practical applicability of nanofluids.

Many experiments were conducted on nanofluids. Namburu et al. (2007) determined the viscosity of 1%–6.12% CuO nanoparticles in ethylene glycol and water mixture for a wide range of temperature from -35°C to 50°C. At -35°C, the viscosity of 6.12% CuO nanofluid was approximately 4 times higher than that of the base fluid. Nguyen et al. (2008) inspected the viscosity of 36 nm and 47 nm Al₂O₃ nanoparticles in water. The measurement indicated that the relative viscosity (ratio of the viscosity of nanofluid to that of water) for 13% of 36 nm and 47 nm Al₂O₃ nanoparticles in water were 4.3 and 5.4, respectively.

Furthermore, Kole and Dey (2010) examined the viscosity of a car engine coolant based Al₂O₃ nanofluid and affirmed that the viscosity of nanofluid was always higher than that of base fluid. Rashin and Hemalatha (2013) stated that with the presence of only 0.5 wt% CuO nanoparticles in coconut oil, the viscosity was increased by 5% at 308 K and shear rate of 3.67/s. An increase in the CuO nanoparticle concentration up to 5 times could increase the viscosity by approximately 27.6%. Yiamsawas et al. (2013) studied the viscosity of TiO₂ and Al₂O₃ nanoparticles in ethylene glycol and water mixture in the

temperature range of 15–60°C. The viscosity measured for TiO₂ and Al₂O₃ nanofluids were approximately 1.55 and 3.4 times higher than the viscosity of the base fluid, respectively. Similar observation with Namburu et al. (2007) that the viscosity of nanofluid decreased with the increasing temperature was made.

Wang, Xu, and Choi (1999) claimed that the viscosity increment came along with the thermal conductivity enhancement. The viscosity of 5% Al₂O₃ nanofluid was 85% higher relative to that of pure water. Chen et al. (2009) checked the thermal conductivity and viscosity for the suspensions of TiO₂ nanoparticles and titanate nanotubes in both water and ethylene glycol. From their experiments, it was observed that although the degree of thermal conductivity enhancement varied with different types of nanofluids, it was always accompanied by the increase in viscosity.

Lee et al. (2007), Murshed, Leong, and Yang (2008), Duangthongsuk and Wongwises (2009b), Chandrasekar, Suresh, and Bose (2010), Sundar, Singh, and Sousa (2013), Ghanbarpour, Haghigi, and Khodabandeh (2014), and Lee et al. (2011) concluded that the viscosity increment of nanofluids was substantially greater than the thermal conductivity augmentation. Lee et al. (2007) employed 2% Al₂O₃ nanofluid to study the convective heat transfer in a micro-channel. They pointed out that the thermal conductivity of the nanofluid was enhanced by solely 4–5%, but its viscosity was 12% higher in relation to the base fluid. Duangthongsuk and Wongwises (2009b) reported that the maximum achievable thermal conductivity by TiO₂ nanofluid was 6–8%, but with the penalty of increased viscosity around 7–17%. A viscosity increment of 136% along with a 9.7% increase in the thermal conductivity was noticed by Chandrasekar, Suresh, and Bose (2010) for their water-based Al₂O₃ nanofluid.

Additionally, Sundar, Singh, and Sousa (2013) observed in their experiment using Fe₃O₄ nanofluid that the thermal conductivity and viscosity were 48% and 196% higher than the base fluid, respectively. According to Ghanbarpour, Haghigi, and Khodabandeh (2014), with the concentration of Al₂O₃ nanoparticles ranging from 3–50 wt%, the thermal conductivity and viscosity were larger by 1.1 – 87% and 18.1 – 300%, respectively (Figure 2.2). Moreover, it was noted from Lee et al. (2011)'s experiments

that the thermal conductivity and viscosity obtained for 3% SiC nanofluid were increased by 7.2% and 102%, respectively. They believed that viscosity increment reduced the promising benefit of nanofluid for the heat transfer.

Besides experiments done merely on the thermal conductivity and viscosity analysis, experiments determining the other heat transfer behaviour together with the viscosity (or pressure drop) of nanofluids were also carried out. Heris, Etemad, and Esfahany (2006) ran an experiment with CuO and Al₂O₃ nanofluids in an annular tube under constant wall temperature boundary condition. The augmentation in the heat transfer coefficient of 3% CuO nanofluid was 23%, while it was 29% for Al₂O₃ nanofluid with the same concentration. They increased the nanofluid loading from 1–3% during their rheology measurement and identified that the viscosity was increased by 20–78% (Figure 2.3). Hwang, Jang, and Choi (2009) conducted experiments with water-based Al₂O₃ nanofluid in a fully developed laminar regime. Their results revealed that even with the low nanoparticle concentration of 0.3%, the convective heat transfer coefficient was raised by 8% in conjunction with 2.9% viscosity increment.

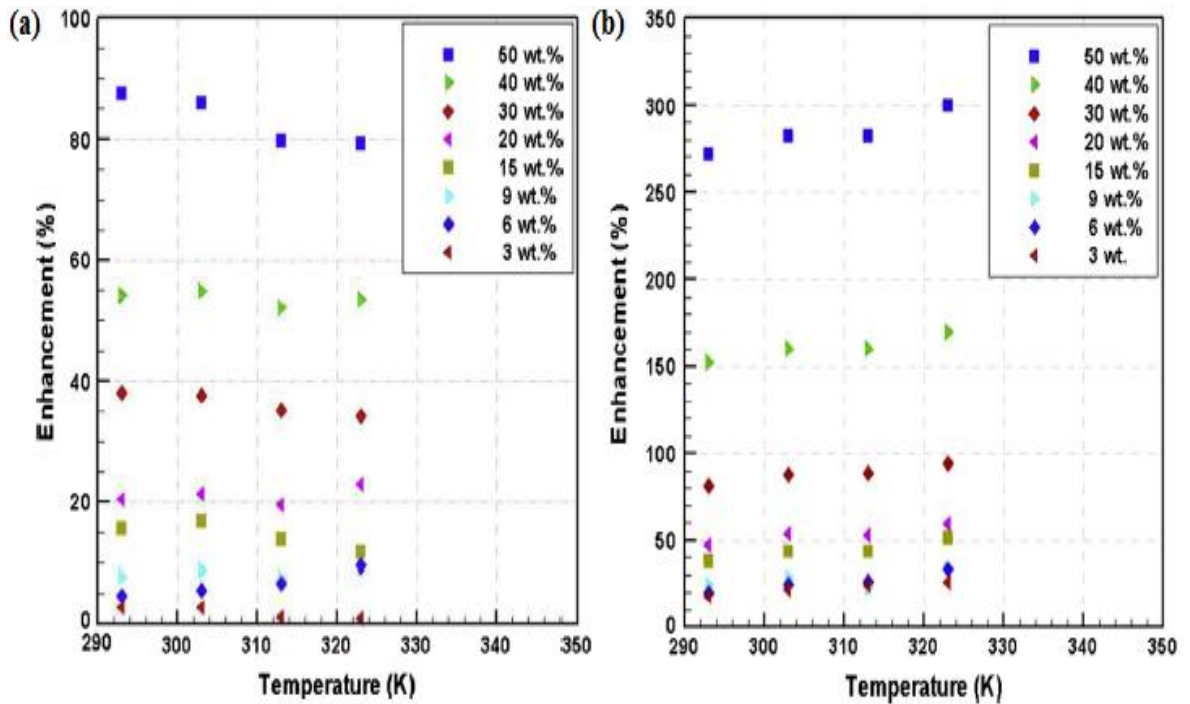


Figure 2.2: (a) Thermal conductivity enhancement and (b) viscosity increment of water-based Al₂O₃ nanofluid (Ghanbarpour, Haghigi, and Khodabandeh 2014).

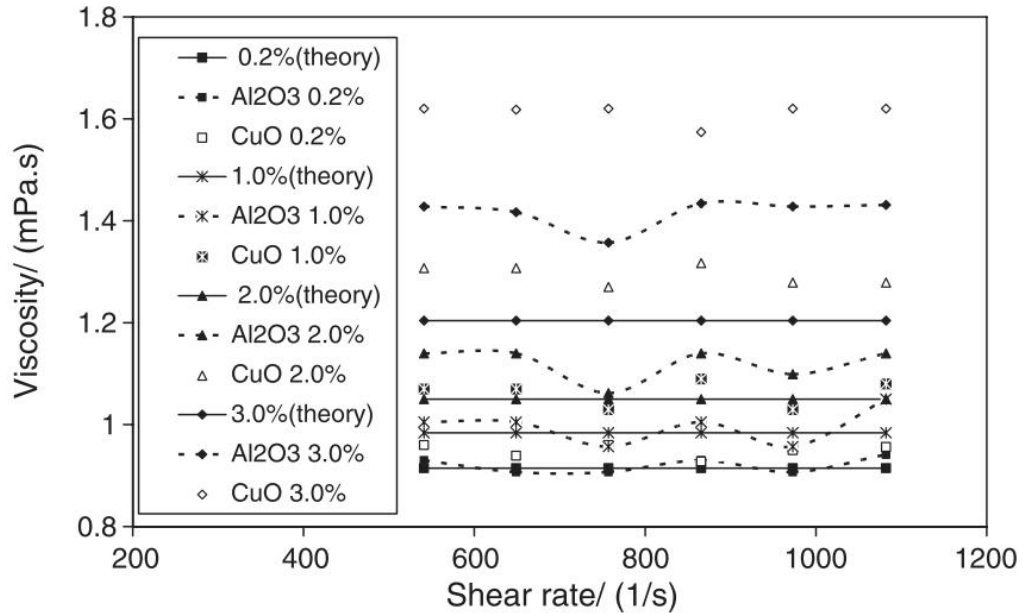


Figure 2.3: Viscosity of CuO and Al₂O₃ nanofluids (Heris, Etemad, and Esfahany 2006).

Halefadi, Estelle, and Mare (2014) prepared CNTs using different base fluids and tested them in a coaxial heat exchanger. They learned that the laminar thermal conductivity and heat transfer coefficient of nanofluids increased regardless of the type of base fluids used. The maximum increment in the thermal conductivity and heat transfer coefficient were both 15.4%. In contrast, the viscosity of CNTs was dependent on the type of base fluids. For example, the viscosity of the water-based CNTs was similar to the viscosity of pure water. However, the addition of 0.026% CNTs into water and ethylene glycol mixture increased the viscosity of the base fluid by 10%. The reason for no viscosity increment of water-based CNTs was due to the low CNTs concentration added. Higher concentration was expected to increase the viscosity of the nanofluid. Wang et al. (2013) addressed that the viscosity of 1.27% CNTs was comparatively five times greater than that of water. Their heat transfer coefficient of 0.05% and 0.24% nanofluids were enhanced by 70% and 190%, respectively, but the augmentation for 1.27% nanofluid was not presented. Furthermore, it was discerned that the friction factor of CNTs was similar to the value of water. Little penalty in the pumping power was incurred.

The results of Rea et al. (2009) demonstrated that the HTE of 6% Al₂O₃ nanofluid was 27% larger than water at the entrance region of a vertical heated tube. Its viscosity was 7.2 times higher than that of the base fluid. Besides, virtually the same increment in the

pressure drop was encountered. Heyhat et al. (2013) perceived from their experiments that for 2% water-based Al_2O_3 nanofluid in a circular pipe, the thermal conductivity and heat transfer coefficient could be augmented up to 18% and 32%, respectively. The maximum pressure drop of 5.7 times higher than that of the base fluid was experienced at the maximum concentration of 2%.

The experimental data of D. Kim et al. (2009) showed that the thermal conductivity was increased by 11% for 3% Al_2O_3 nanofluid. On the other hand, the heat transfer coefficient was enhanced by 15% and 20% for laminar and turbulent circular flow, respectively. Nevertheless, the viscosity of 3% Al_2O_3 nanofluid was increased to approximately 11% compared to that of pure water. The viscosity increment of 3% Al_2O_3 nanofluid acquired by D. Kim et al. (2009) was much smaller than the one obtained by Heris, Etemad, and Esfahany (2006). This could be due to the difference in the nanoparticle size considered. The nanoparticle size used by Heris, Etemad, and Esfahany (2006) was 20 nm, while the size range used by D. Kim et al. (2009) was 20–50 nm.

He et al. (2007) examined the heat transfer and flow characteristics of water-based TiO_2 nanofluid flowing upward through a vertical pipe for both laminar and turbulent regimes. The viscosity increment of 10.5% was incurred for 1.1% nanofluid. Moreover, the heat transfer coefficient was enhanced by 12% and more than 40% for the Reynolds number of 1500 and 5900, respectively. In addition, the effect of nanoparticles volume fraction on the heat transfer coefficient was more significant for the turbulent regime. From their experiments, the authors ascertained that the positive effect of thermal conductivity enhancement still outweighed the negative effect of viscosity increment.

Some experimental works were done for nanofluids in the turbulent regime as well (Xuan and Li 2003; Duangthongsuk and Wongwises 2009a, 2010; Fotukian and Esfahany 2010; Sundar and Sharma 2010; Vajjha, Das, and Kulkarni 2010; Esfe et al. 2014; Reddy and Rao 2014). Xuan and Li (2003) investigated the convective heat transfer by adding 2% Cu nanoparticles in water and found out that the heat transfer

coefficient of nanofluid was 60% higher than that of the pure water. Additionally, there was no extra penalty in the pressure drop for nanofluid.

Vajjha, Das, and Kulkarni (2010) evaluated the convective heat transfer of Al_2O_3 nanoparticles in a mixture of 60% ethylene glycol and 40% water. At the Reynolds number of 6000, the pressure loss of 6% Al_2O_3 nanofluid was approximately 3 times higher than the pressure loss of the base fluid. Nonetheless, its heat transfer coefficient enhancement was merely 80% with respect to the base fluid. Furthermore, the pressure drop was larger at higher nanofluid concentration because the higher concentration induced higher viscosity. Furthermore, Fotukian and Esfahany (2010) performed experiments in a circular tube using dilute CuO nanofluid (0.015–0.236%). The average turbulent heat transfer coefficient enhancement of 25% was observed with 20% increment in the pressure drop. Since the dilute nanofluid increased the pumping power, they suggested finding an optimum concentration in order to achieve better thermal-hydraulic efficiency. Sundar and Sharma (2010) studied the convective heat transfer in a tube with twisted tape insert by using water-based Al_2O_3 nanofluid. It was determined that for the Reynolds number of 22,000 and twist ratio of 5, 0.5% nanofluid could increase the heat transfer coefficient by 42.17%. Under the same condition, the friction factor was 1.27 times greater than that of pure water.

Duangthongsuk and Wongwises (2009a) revealed that the convective heat transfer coefficient of 0.2% water-based TiO_2 nanofluid in a double-tube heat exchanger was slightly higher than the value of pure water, which was in the range of 6–11%. Their conclusion for the pressure loss of nanofluid system was similar to the case of Xuan and Li (2003). On the other hand, although the nanofluid concentration utilized by Fotukian and Esfahany (2010) and Duangthongsuk and Wongwises (2009a) was similar, their observations on the pressure drop varied. The deviation in their results could be caused by the differences in the nanoparticles and experimental setup considered. Duangthongsuk and Wongwises (2010) then inspected nanofluid with higher concentrations. The heat transfer coefficient enhancement was 26% for 1% TiO_2 nanofluid. However, the heat transfer coefficient was 14% lower than the value of water

when the concentration was raised to 2%. This reduction in the heat transfer coefficient was attributed to the viscosity increment as the nanoparticle concentration got larger.

Esfe et al. (2014) reported that the maximum enhancement in the heat transfer coefficient and Nusselt number of 1% CNTs in a double tube heat exchanger were 83.29% and 40.67%, respectively. The HTE came along with 37% increment in the pressure drop. This 37% pressure drop increment was ascribed to the increased viscosity. The viscosity of 1% CNTs was approximately 1.48 times larger than the value of water. Moreover, Reddy and Rao (2014) claimed that with the presence of only 0.02% TiO₂ nanofluid flowing in a double tube heat exchanger, the heat transfer coefficient was enhanced by 10.73%. At the same time, the friction factor was increased by 8.73% when compared to the base fluid (ethylene glycol and water mixture).

2.1.4 Numerical studies on both heat transfer and flow behaviour of nanofluids

In addition to the experimental works mentioned in Section 2.1.3, some numerical studies on nanofluids had also been carried out. Rashmi et al. (2013) studied experimentally and numerically the laminar heat transfer characteristic of 0.01 wt% CNTs in a concentric tube heat exchanger. The thermal conductivity and Nusselt number enhancement of approximately 125.6% and 68.6% were achieved, respectively. Their numerical results under-estimated the heat transfer rate in comparison to their experimental data. This variation was owing to the application of constant thermal properties for their simulations. On the other hand, their experimental results showed that at room temperature, the viscosity of nanofluid was around 30% higher in relation to the base fluid. Dawood, Mohammed, and Munisamy (2014) investigated the effect of nanoparticle loading on the laminar heat transfer in an elliptic annulus. According to their results, 4% water-based SiO₂ nanofluid could increase the Nusselt number to more than 80% relative to the base fluid at the Reynolds number of 1000. Although the viscosity of the nanofluid was not being examined, the authors believed that the increased nanofluid concentration would impose a penalty on the wall shear stress.

Bianco et al. (2009) adopted the single-phase and two-phase discrete particle models considering both temperature-independent and temperature-dependent properties in

modelling the laminar forced convection of Al_2O_3 nanofluid in a circular duct. Good agreement with maximum deviation of 11% was obtained in the comparison between the results from the single- and two-phase models. For the Reynolds number of 250 and heat flux of 10000 W/m^2 , the convective heat transfer coefficient of 4% Al_2O_3 nanofluid was 1.180, 1.209, 1.205 and 1.183 times higher than that of water for temperature-independent and temperature-dependent properties of single-phase and two-phase models, respectively. They also reported an increase in the wall shear stress due to the increase in the nanofluid viscosity. The maximum increment in wall shear stress was as high as 2.135 times the value of water. Similar results were acquired by Maiga et al. (2005) for laminar forced convective flow in a circular tube. The wall shear stress and viscosity of 7.5% Al_2O_3 nanofluid were found to be quadrupled and doubled in comparison to that of the base fluid, respectively.

Bianco, Manca, and Nardini (2011) analyzed the behaviour of Al_2O_3 nanofluid in the turbulent flow. The shear stress which was a pressure drop indicator increased with the increasing nanoparticle concentration. For example, when the concentration varied from 1% to 4% and then to 6%, the shear stress increased by 10%, 200% and 300%, respectively (Figure 2.4). Thus, in the shear stress point of view, application of nanofluid was useful only at the lower concentration range. Bianco et al. (2008) and Namburu et al. (2009) also observed a trend of higher wall shear stress for higher nanofluid concentration, which in turn induced higher pressure drop for the nanofluid.

Mashaei, Hosseinalipour, and Bahiraei (2012) examined the laminar flow of Al_2O_3 nanofluid in a channel with discrete heat sources. The nanofluid was simulated as an incompressible fluid having temperature-dependent properties. The heat transfer coefficient enhancement achievable was 38%. Nevertheless, the drawback of using Al_2O_3 nanofluid for their heat transfer studies was the undesirable pressure drop increment up to 68%, caused by the increased viscosity. Kumar and Ganesan (2012) surveyed the turbulent heat transfer performance of dilute and concentrated Al_2O_3 nanofluid in a pipe flow under constant wall temperature condition. With the presence of low concentration of 0.02% Al_2O_3 nanoparticles in the base fluid, the Nusselt number was raised by 0.5%. However, the pressure drop accession became accentuated at high

volume fraction (particularly above 1%). Esfandiary, Habibzadeh, and Sayehvand (2016) agreed with Kumar and Ganesan (2012) that the pressure drop increased drastically for concentrated nanofluids over that of the dilute nanofluids, especially for turbulent flow. They noticed that at the Reynolds number of 4000, the pressure drop of 1% Al_2O_3 nanofluid was 1 kPa. When the concentration was further increased to 5.1%, the pressure drop was raised to more than 10 kPa. This pressure drop difference increased when the Reynolds number increased.

Zhao et al. (2016) studied the laminar flow of Al_2O_3 nanofluid in an offset strip fins channel and noted a maximum heat transfer coefficient enhancement of 26.69% (at the Reynolds number of 1000). Nonetheless, at the same Reynolds number, the ratio of the pressure drop of nanofluid to that of water was 1.157 and 2.097 for 1% and 4% nanofluid, respectively. This correlated to the pumping power increment of 22.86% and 188.94% for 1% and 4% nanofluid, respectively (Figure 2.5). They also evaluated the thermal-hydraulic performance of nanofluid under the constant heat transfer rate condition and concluded that the nanofluid had no benefit over the base fluid when the concentration was beyond 3%. Mashaei, Hosseinalipour, and Muslmani (2014) deduced that the thermal-hydraulic efficiency of Al_2O_3 nanofluid in a serpentine microchannel decreased when the Reynolds number increased. Moreover, the thermal-hydraulic efficiency was higher at higher heat flux because at higher temperature, the thermal conductivity increased while the viscosity decreased.

Moreover, Ahmad et al. (2017) investigated the laminar heat transfer and pressure drop of Al_2O_3 nanofluid in a rectangular duct. They reported that the thermal conductivity and pressure drop of 2.5% nanofluid were approximately 7.33% and 6.31% higher than that of water, respectively. Heris et al. (2015) who inspected the thermal-hydraulic index of Al_2O_3 and CuO nanofluids flowing through the square and triangular ducts revealed that nanofluids were practically applicable as the performance index for all the runs were greater than 1.0. A brief summary of the review on nanofluids is presented in Table 2.1.

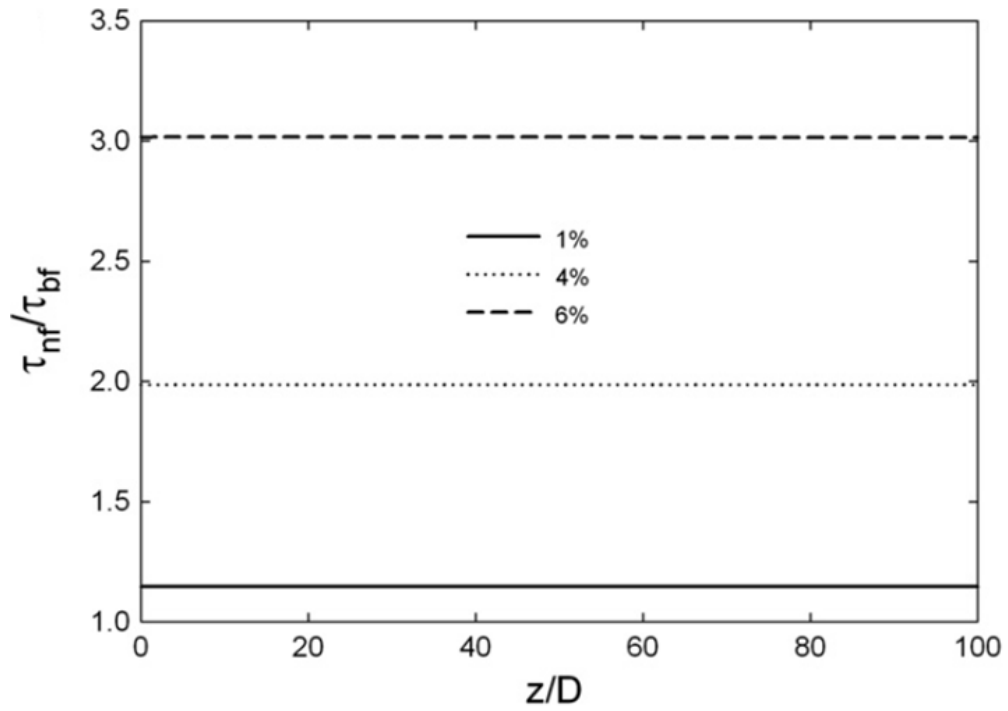


Figure 2.4: Shear stress ratio of Al₂O₃ nanofluid at the Reynolds number of 20000 (Bianco, Manca, and Nardini 2011).

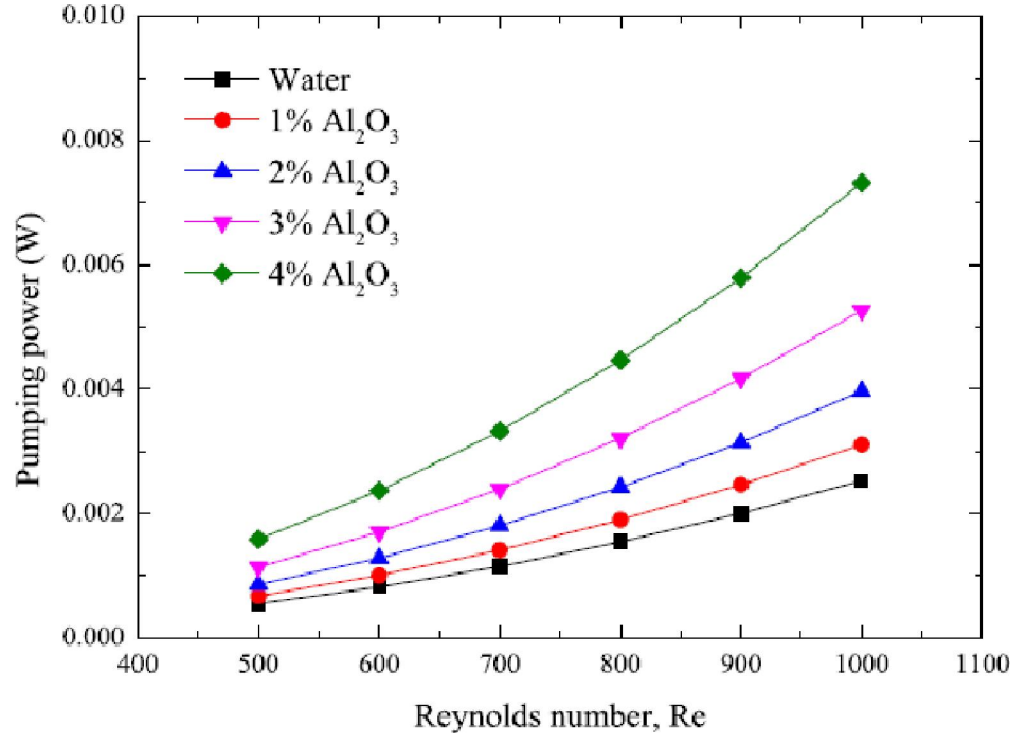


Figure 2.5: Pumping power of Al₂O₃ nanofluid (Zhao et al. 2016).

Table 2.1: Summary of experimental and numerical studies on heat transfer and flow behaviour of different nanofluids.

Nanoparticle type/ Base fluid	Nanoparticles concentration ^A (%)	Geometry	Maximum thermal conductivity (k), heat transfer coefficient (h) or Nusselt number (Nu) enhancement (%)	Maximum viscosity (μ) or pressure drop (ΔP) increment (%)	Reference
<i>Thermal conductivity or/and viscosity measurement</i>					
Al ₂ O ₃ /Water	3–5.5		k : 16		
Al ₂ O ₃ /EG	2.5–8	-	k : 41	μ (5% Al ₂ O ₃ /Water): 85	(Wang, Xu, and Choi 1999)
CuO/Water	4.5–9.5		k : 34	μ (3.5% Al ₂ O ₃ /EG): 38	
CuO/EG	6.25–14.75		k : 54		
CuO/(60:40 EG- water mixture)	1–6.12	-	-	μ : 300	(Namburu et al. 2007)
Al ₂ O ₃ (36 nm)/Water	0.15–13	-	-	μ : 330	(Nguyen et al. 2008)
Al ₂ O ₃ (47 nm)/Water				μ : 440	
Al ₂ O ₃ /Engine coolant	0.1–1.5	-	-	μ : 113	(Kole and Dey 2010)
CuO/Coconut oil	0.5–2.5 wt%	-	-	μ : 27.6	(Rashin and Hemalatha 2013)
Al ₂ O ₃ /(20:80 EG- water mixture)	1–4	-	-	μ : 240	(Yiamsawas et al. 2013)
TiO ₂ /(20:80 EG- water mixture)				μ : 55	
TiO ₂ /Water	0.1–1.8	-	k (1.2% TiO ₂ /Water) \approx 6	μ (1.2% TiO ₂ /Water) \approx 10	(Chen et al. 2009)
TiO ₂ /EG			k (1.8% TiO ₂ /EG) \approx 14.5	μ (1.8% TiO ₂ /EG) \approx 22	
TNT/Water			k (0.6% TNT/Water) \approx 3.8	μ (0.6% TNT/Water) \approx 82	
TNT/EG			k (1.8% TNT/EG) \approx 13.1	μ (1.8% TNT/EG) \approx 70	
Al ₂ O ₃ /Water	0.5–5	-	k (0.5% Al ₂ O ₃ /EG): 4.5	μ : 82	(Murshed, Leong, and Yang 2008)
Al ₂ O ₃ /EG			k (5% TiO ₂ /EG): 18	μ : 83	
TiO ₂ /Water			k (1% Al ₂ O ₃ (80 nm)/water) \approx 12		
TiO ₂ /EG			k (1% Al ₂ O ₃ (150 nm)/water) \approx 10.8		
TiO ₂ /Water	0.2–2	-	$k \approx$ 8	μ : 17	(Duangthongsuk and Wongwises 2009b)
Al ₂ O ₃ /Water	0.33–5	-	k (3% Al ₂ O ₃ /Water): 9.7	μ (5% Al ₂ O ₃ /Water): 136	(Chandrasekar, Suresh, and Bose 2010)
Fe ₃ O ₄ /Water	0.2–2	-	k : 48	μ : 196	(Sundar, Singh, and Sousa 2013)

Table 2.1: (Continued)

Nanoparticle type/ Base fluid	Nanoparticles concentration ^A (%)	Geometry	Maximum thermal conductivity (k), heat transfer coefficient (h) or Nusselt number (Nu) enhancement (%)	Maximum viscosity (μ) or pressure drop (ΔP) increment (%)	Reference
Al ₂ O ₃ /Water	3–50 wt%	-	k : 87	μ : 300	(Ghanbarpour, Haghigi, and Khodabandeh 2014)
SiC/Water	0.001–3	-	k : 7.2	μ : 102	(Lee et al. 2011)
Laminar flow					
Al ₂ O ₃ /Water CuO/Water	0.2–3	Annular tube	h : 29 h : 23	$\mu \approx 56$ $\mu \approx 78$	(Heris, Etemad, and Esfahany 2006)
Al ₂ O ₃ /Water	0.01–0.3	Circular tube	h : 8	μ : 2.9	(Hwang, Jang, and Choi 2009)
CNTs/Water	0.05–1.27	Circular tube	h (0.24% CNTs/Water): 190	μ : 400	(Wang et al. 2013)
Al ₂ O ₃ /Water	0.1–2	Circular tube	k : 18 h : 32	μ : 60 ΔP : 470	(Heyhat et al. 2013)
CNTs/(50:50 EG- water mixture)	0.026	Coaxial heat exchanger	k : 15.4	μ : 10	(Halelfadl, Estelle, and Mare 2014)
Al ₂ O ₃ /Water	0.6–6	Circular tube	h : 27	μ : 620	(Rea et al. 2009)
Al ₂ O ₃ /Water	1–4	Flow channel with discrete heat sources	h : 38	ΔP : 68	(Mashaei, Hosseinalipour, and Bahiraei 2012)
Al ₂ O ₃ /Water	2–8	Serpentine microchannel	h : 51	ΔP : 520	(Mashaei, Hosseinalipour, and Muslmani 2014)
Al ₂ O ₃ /Water CuO/Water	0.5–2	Square and triangular ducts	<u>Square duct:</u> $Nu \approx 48.43$ $Nu \approx 66.67$ <u>Triangular duct:</u> $Nu \approx 54.38$ $Nu \approx 56.52$	<u>Square duct:</u> $\Delta P \approx 12.54$ $\Delta P \approx 18.21$ <u>Triangular duct:</u> $\Delta P \approx 10.24$ $\Delta P \approx 10.51$	(Heris et al. 2015)
CNTs/Water	0.01 wt%	Concentric tube heat exchanger	k : 125.6 Nu : 68.6	$\mu \approx 30$	(Rashmi et al. 2013)

Table 2.1: (Continued)

Nanoparticle type/ Base fluid	Nanoparticles concentration ^A (%)	Geometry	Maximum thermal conductivity (k), heat transfer coefficient (h) or Nusselt number (Nu) enhancement (%)	Maximum viscosity (μ) or pressure drop (ΔP) increment (%)	Reference
Al ₂ O ₃ /Water	1–4	Offset strip fins channel	h : 26.69 Nu : 6.98	ΔP : 109.7	(Zhao et al. 2016)
Al ₂ O ₃ /Water	0.5–2.5	Rectangular duct	$k \approx 7.33$	ΔP : 6.31	(Ahmad et al. 2017)
<i>Turbulent flow</i>					
Multi-walled CNTs/Water	0.05–1	Double tube heat exchanger	k : 45 h : 83.29 Nu : 40.67	μ : 48 ΔP : 37	(Esfe et al. 2014)
Al ₂ O ₃ /(60:40 EG- water mixture)	1–10	Circular tube	h ($Re=7240$): 81.74	ΔP ($Re=6700$): 370	(Vajjha, Das, and Kulkarni 2010)
CuO/Water	0.015–0.236	Circular tube	h : 42	ΔP : 36	(Fotukian and Esfahany 2010)
TiO ₂ /(40:60 EG- water mixture)	0.0004–0.02	Double pipe heat exchanger with and without helical coil inserts	h (Without helical coil inserts): 10.73 h (With helical coil inserts): 17.71	f (Without helical coil inserts): 8.73 f (With helical coil inserts): 16.58	(Reddy and Rao 2014)
Al ₂ O ₃ /Water	0.02–6	Circular pipe	Nu : 60	μ : 180 $\Delta P \approx 2400$	(Kumar and Ganesan 2012)
Al ₂ O ₃ /Water	1–5.1	Circular pipe	$Nu \approx 85.19$	$\Delta P \approx 4200$	(Esfandiary, Habibzadeh, and Sayehvand 2016)
<i>Both laminar and turbulent flow</i>					
Al ₂ O ₃ /Water	3	Circular tube	k : 11 h (laminar): 15 h (turbulent): 20	μ : 11	(D. Kim et al. 2009)
TiO ₂ /Water	0.24–1.18	Vertical pipe	<u>For 1.1% TiO₂/Water:</u> h (Re :1500): 12 h (Re :5900): >40	μ : 10.5	(He et al. 2007)

EG- Ethylene glycol; TNT- Titanate nanotubes; AC- Amorphous Carbonic; ^AThe nanofluid concentration given is in volume percent unless it is mentioned otherwise.

2.2 Polymer

The viscosity augmentation encountered in the nanofluid systems, especially at a higher concentration is undesirable. The attractiveness and feasibility of nanofluids for heat transfer applications can diminish if the viscosity increment is larger than the HTE. Therefore, it is essential and necessary to improve the thermal-hydraulic efficiency of nanofluids, particularly at high volume fraction. Polymer additives might be beneficial in solving this inherent problem of nanofluids (Tiong, Kumar, and Saptoro 2015).

2.2.1 Experiments on laminar heat transfer and flow characteristics of polymer solutions in non-circular ducts

For fully developed laminar non-circular flow, the addition of polymer additives to a base fluid is believed to enhance the heat transfer performance without increasing the flow resistance. Oliver (1969) who studied the laminar heat transfer in flattened tubes observed a 40% HTE for PAA and PEO aqueous solutions. Moreover, Oliver and Karim (1971) noticed that the flattened tubes gave higher heat transfer coefficient compared to circular tubes. The improved heat transfer was believed to be caused partly by the increment in the wall shear rate, and partly by the effect of secondary flow. It was pointed out that through the increment in the wall shear rate, the heat transfer coefficient of PAA solution could be increased by over 90%. In contrast, by considering solely the effect of secondary flow, the heat transfer coefficient could be enhanced by 45%. The secondary flow effect became negligible at low aspect ratio (height/width) of 0.18 while it reached its maximum when the aspect ratio was at its highest of 0.67.

The secondary flow is a weaker flow superimposed on a primary fluid flow, which is induced from the normal stress difference (Figure 2.6). The normal stress difference is owing to the elastic property of polymer solutions. (The magnitude of the normal stress for an incompressible material is the same in all directions, thus the normal stress difference is zero. For a polymeric liquid, the normal stress difference is owing to the deviation of polymer molecules from their stable and symmetrical shape. The two normal stress differences are the first and second normal stress differences (Dealy and Wang 2013).) The presence of secondary flow in the non-circular ducts for the laminar

regime was proven experimentally, theoretically and numerically by several researchers (Green and Rivlin; Wheeler and Wissler 1966; Townsend, Walters, and Waterhouse 1976; Gervang and Larsen 1991).

Mena et al. (1978) compared the laminar heat transfer behaviour of a viscoelastic solution in various pipes with different cross-sections under the constant wall temperature boundary condition. They discovered that for a rectangular pipe, the polymer additives could augment the heat transfer coefficient by 50% when compared to that of a circular pipe (Figure 2.7). The development of secondary flow promoted this HTE. A triangular duct showed less heat transfer increment over the rectangular pipe. It was also shown that the secondary flow had little impact on the flow rate for all the non-circular ducts considered. Therefore, no effect on the fluid friction was reported.

Hartnett and Kostic (1985) scrutinized the heat transfer characteristic of PAA additives in water for a 2:1 rectangular channel. The Nusselt number was noted to be higher than that of pure water. Hartnett and Kostic (1985) agreed with Mena et al. (1978) that the HTE was due to the secondary flow. In addition, the measured friction factor agreed well with the prediction of Kozicki's power law non-Newtonian model ($fRe^*=16$). The elasticity of PAA did not have an appreciable influence on its flow resistance. According to Kostic (1994), the secondary flow was in the transverse direction of the flow, thus did not have a major effect on the friction factor. Therefore, there was no friction factor increment.

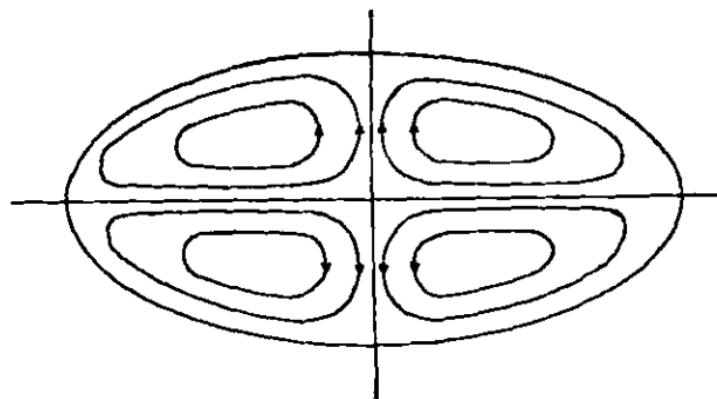


Figure 2.6: Secondary flow pattern of a viscoelastic solution in a non-circular duct (Semjonow 1967).

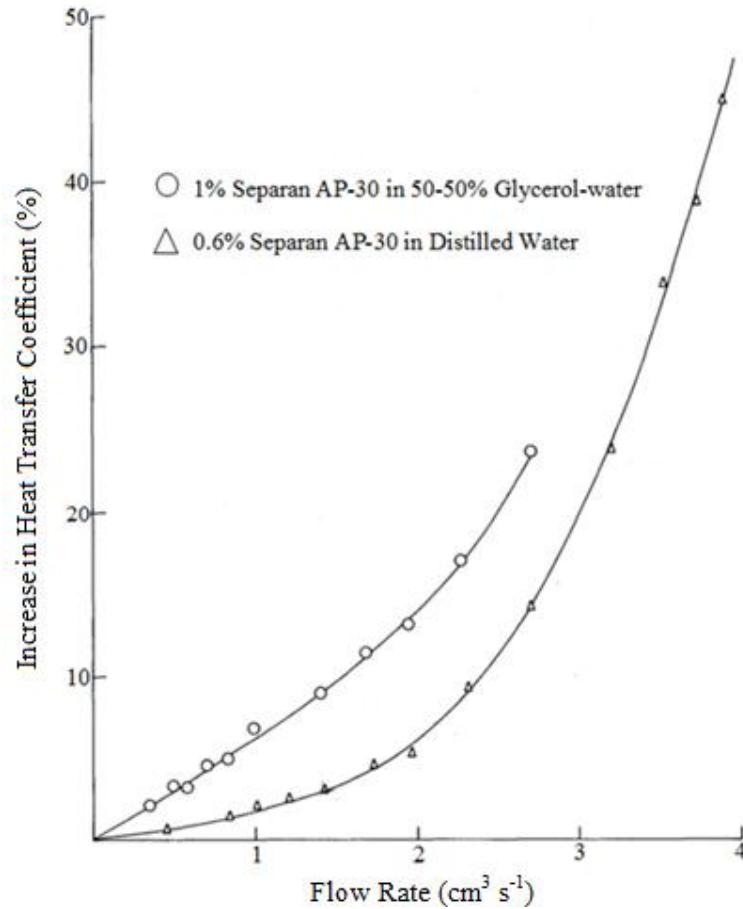


Figure 2.7: Heat transfer coefficient increment of a rectangular duct when compared to a circular pipe (Mena et al. 1978).

Besides, Xie and Hartnett (1992) conducted experiments in a 2:1 rectangular duct using Carbopol 934 and PAA (Separan AP-273). Under top-wall-heated thermal boundary condition, the local Nusselt number of both polymer solutions was measured to be two to three times higher than that of water. Furthermore, they also mentioned that polymer with higher elasticity was able to produce higher HTE.

Rao (1988, 1989) inspected the heat transfer behaviour of PAA and Natrosol solutions in a 5:1 rectangular duct. The Nusselt number of PAA aqueous solution was 25% higher than that of water. For Natrosol solution which had weaker elasticity, its Nusselt number was not distinctly different from the value of water. When compared to the 2:1 rectangular duct employed by Hartnett and Kostic (1985), Rao (1988, 1989)'s experimental data showed that there was only a slight increase in the heat transfer

relative to that of water. This variation could be due to the application of different thermal boundary conditions. Besides, the heat transfer performance in the 2:1 rectangular duct was better than in the 5:1 rectangular duct. It was suggested that weaker secondary flow was generated in the 5:1 rectangular duct, and thus a smaller HTE. The strength of secondary flow was more significant for ducts with higher aspect ratio and it diminished with decreasing aspect ratio. On the other hand, the laminar Fanning friction factor attained by Rao (1988, 1989) acceded with the values predicted from $fRe^*=16$ correlation for all the concentration tested.

Moreover, Hartnett and Kostic (1989) also demonstrated that for a square duct with top wall heated boundary condition, the laminar heat transfer of aqueous PAA and Carbopol solutions could be augmented up to 200–300% as compared to that of Newtonian fluid (water). The HTE was ascribed to the same secondary flow which improved the heat transfer of the rectangular duct. Similar to the case of rectangular duct, the secondary flow did not affect the flow resistance of the square duct.

2.2.2 Experiments on laminar heat transfer and flow characteristics of polymer solutions in circular ducts

Compared to the laminar non-circular flow, less attention is paid to investigate the effect of polymer additives on laminar circular flow. In 1982, Cho and Harnett (1982) measured the pressure loss and heat transfer of a polymer solution in a circular tube. They concluded that the elasticity of polymer played no vital role on the friction factor and heat transfer of the fully developed laminar circular flow. Their experimental results of pressure loss conformed well to the values predicted using the non-Newtonian power law model. Hartnett (1992) claimed that for a steady state laminar flow through a circular pipe, the polymeric solutions behaved like purely viscous fluids, as there was no mechanism showing their elastic nature. The elasticity of polymer additives was manifested merely during unsteady flow, such as pulsating flow and entrance region flow for the circular pipe.

2.2.3 Numerical studies on laminar heat transfer and flow characteristics of polymer solutions

Numerical studies on the laminar heat transfer and flow performance of polymeric solutions had also been carried out following many experiments done in this field. Shin and Cho (1993) hypothesized that the laminar HTE in a 2:1 rectangular duct was a result of temperature effect on the rheological behaviour of PAA solution. They deduced that the viscosity of PAA solution was very sensitive to temperature, particularly at low shear rate ($\dot{\gamma} \leq 0.001 \text{ s}^{-1}$). However, this dependency on temperature was negligible at high shear rate ($\dot{\gamma} \geq 10 \text{ s}^{-1}$). They also introduced a shear rate and temperature-dependent Carreau model to estimate the viscosity of the solution. Shin and Cho (1994) then investigated the effects of temperature-dependent and shear-thinning viscosity of PAA on the laminar heat transfer characteristic in a 2:1 rectangular duct. The influence of secondary flow on the heat transfer was excluded from their study. Their research was subjected to constant axial heat flux and constant peripheral wall temperature boundary condition. A parabolic velocity profile and no slip condition were defined for their simulation which was solved via finite volume method. The Nusselt number was improved by around 70–300% when compared to that of the constant viscosity. Shin and Cho (1994) asserted that this enhancement was attributed to the increased near-wall velocity gradient as the combined effects of temperature-dependent and shear-thinning viscosity.

Shin and Cho (1993, 1994) did not regard polymer solutions as viscoelastic fluids. In contrast, some researchers related the heat transfer augmentation of polymeric solutions to the viscoelastic property, which they represented using different constitutive equations such as White-Metzner, Criminale-Ericksen-Filbey (CEF), Reiner-Rivlin, Phan-Thien-Tanner (PTT), Oldroyd, Giesekus, and Finitely Extensible Nonlinear Elastic- Peterlin (FENE-P).

Naccache and Mendes (1996) examined the laminar heat transfer performance of a polymer solution in a rectangular duct. The viscoelastic property of the polymer solution was described using the CEF model, while the Carreau-Yasuda model was

adopted to express the viscosity of the solution. The boundary conditions employed were no slip condition at walls, symmetrically heated top and bottom walls, and adiabatic vertical side walls. They discovered that the heat transfer was enhanced, but the friction factor was basically unaffected by the secondary flow. The Nusselt number of this non-Newtonian solution was three times larger than the relative Newtonian fluid. The Nusselt number increase was 6–275%, 38–230% and 33–130% for the duct aspect ratio of 1, 0.5 and 0.25, respectively. In contrast to the results obtained by Shin and Cho (1994), Naccache and Mendes (1996) deduced that the effect of shear-thinning viscosity on the heat transfer was negligible in comparison to the impact of secondary flow.

Furthermore, Naccache and Mendes (1996), Townsend, Walters, and Waterhouse (1976), Payvar (1997), Gervang (1989), Gervang and Larsen (1991), Syrjala (1998) and Norouzi, Kayhani, and Nobari (2009) also applied the CEF rheological constitutive equation in modelling the viscoelasticity of polymeric solution. Payvar (1997) affirmed the suitability of the CEF equation for the estimation of laminar heat transfer of the viscoelastic PAA solution. Gervang and Larsen (1991) analyzed the flow of 2% viscarin polymer solution in a rectangular duct and compared the pressure drop calculated from both the power law and CEF models. They disclosed that the effect of secondary flow on the pressure drop was small at low flow rates ($v \leq 3$ m/s) but significant one was detected for high flow rate. According to the results from the CEF model, the secondary flow contributed to 6 and 20% pressure drop increment relative to that of the power law fluid at the velocity of 5 and 10 m/s, respectively. Nevertheless, this was only partly verified through their pressure drop measurement due to the limitation in their pump capacity.

The numerical prediction of Syrjala (1998) demonstrated that the magnitude of the secondary flow was less than 1% of the axial flow. Despite its magnitude was small, it could lead to an appreciable increase in the heat transfer of fully developed laminar flow, especially when the Prandtl number was high. Since the magnitude of the secondary flow was small, its impact on the friction factor was not significant. These findings were consistent with the numerical outcomes of Naccache and Mendes (1996), and the experimental results mentioned in Section 2.2.1 (Oliver and Karim 1971; Mena et al.

1978; Hartnett and Kostic 1985, 1989; Rao 1989; Xie and Hartnett 1992; Kostic 1994). Moreover, Syrjala (1998) also identified that the strength of the secondary flow was determined virtually by the second normal stress difference. An increase in the second normal stress coefficient augmented the intensity of the secondary flow.

Norouzi, Kayhani, and Nobari (2009) inspected the mixed and forced convection of a viscoelastic fluid in a rectangular duct for a very low Reynolds number range ($Re \leq 30$) by utilizing the CEF model. The type of viscoelastic fluid was not mentioned. From their results on forced convection, they pointed out that the velocity of vortices generated by the secondary flow increased with the increasing second normal stress coefficient as depicted in Figure 2.8. However, this vortex velocity increment had no substantial influence on the mean Nusselt number. The mean Nusselt number was augmented primarily as a result of the increment in the main flow velocity.

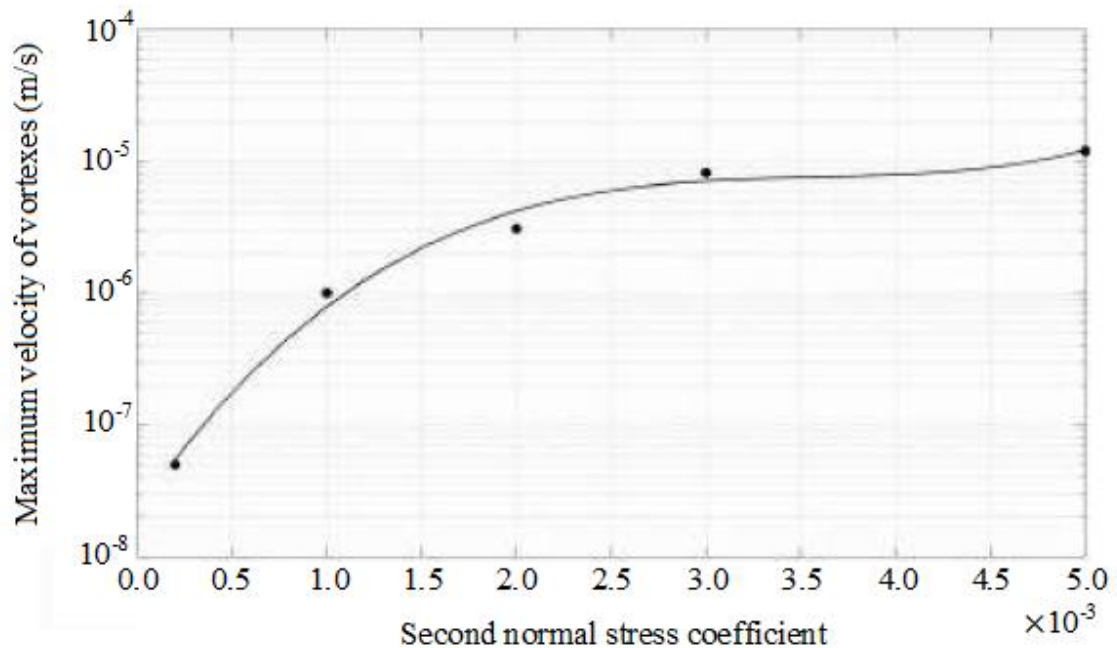


Figure 2.8: Effect of second normal stress coefficient on maximum velocity of vortices (Norouzi, Kayhani, and Nobari 2009).

Using the same viscoelastic model, Bschorer and Brunn (1996) performed a research on a contraction flow of dilute PAA solution. They applied the Carreau model to define the viscosity of the solution and concluded that the flow behaviour of the solution could not be simulated as exclusively shear-thinning fluid without elasticity. In addition, they also tested the same solution with the White-Metzner and Oldroyd relationships. Besides, the Oldroyd model was adopted to compute the viscoelasticity of blood flow (Bodnar, Sequeira, and Prosi 2011; Khambhampati 2013). Khambhampati (2013) observed that the generalized Oldroyd-B model could predict the wall shear stress of blood more accurately when compared to that of the Newtonian model, especially when there was a permanent flow reversal in the bloodstream.

Gao (1993) as well as Gao and Hartnett (1993, 1996) had selected the Reiner-Rivlin model to simulate the flow of aqueous polymeric solution in square and rectangular channels. They attained the same insights as the other authors who considered the CEF constitutive equation (Townsend, Walters, and Waterhouse 1976; Gervang 1989; Gervang and Larsen 1991; Naccache and Mendes 1996; Payvar 1997; Syrjala 1998; Norouzi, Kayhani, and Nobari 2009). The insignificant influence of the secondary flow on the fluid flow rate was indicated through Figure 2.9. The primary velocity of the Reiner-Rivlin polymeric fluid was similar to that predicted from the power law model. Furthermore, Gao and Hartnett (1993, 1996) remarked that the HTE increased with increasing strength of the secondary flow. The strength was more significant for ducts with higher aspect ratio. This statement was also supported by Peres et al. (2009).

Peres et al. (2009) looked into the flow and heat transfer behaviour of 1000 ppm PAA solution. They compared their numerical results with the experimental data of Hartnett and Kostic (1985). They characterized the viscoelasticity of the solution using the PTT constitutive equation, and attributed the Nusselt number augmentation to the rheologically induced secondary flow and the shear-thinning viscosity. Xue, Thien, and Tanner (1995) who employed the same PTT model revealed that the presence of secondary flow was not dependent merely on the fluid elasticity but also on the primary flow rate.

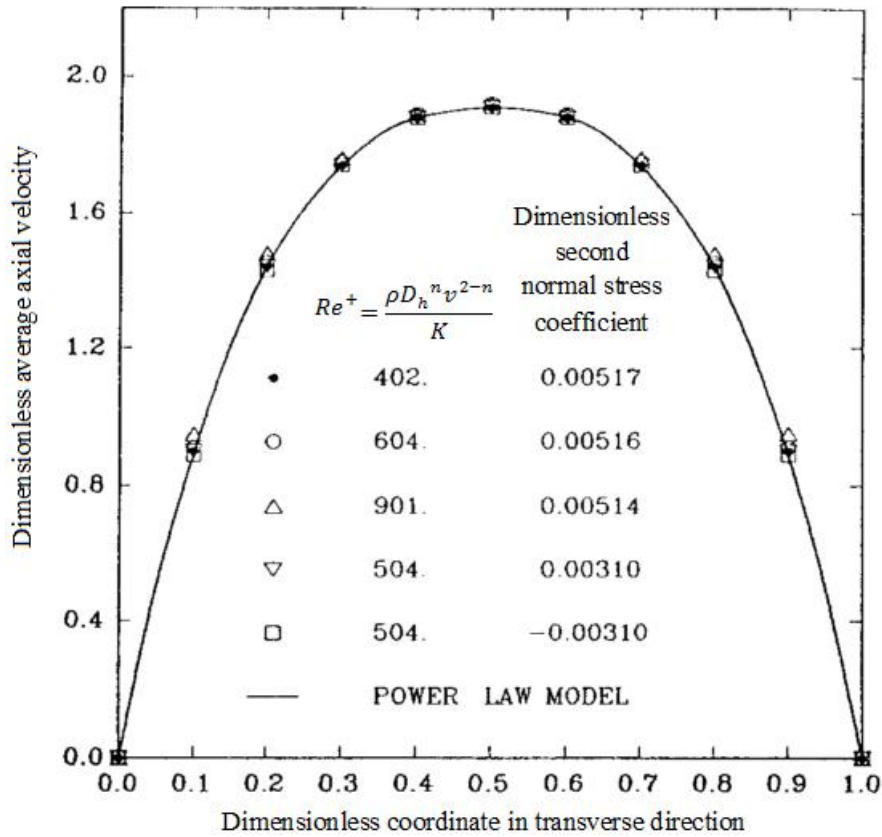


Figure 2.9: Dimensionless axial velocity in a cross-section of a square duct (Gao and Hartnett 1993).

Yue, Dooley, and Feng (2008) used the Giesekus model for a polymer solution in pipe of non-circular cross-section. They confirmed that the primary cause of the secondary flow was the non-zero second normal stress difference. In their numerical study, the relationship between the second normal stress difference and the direction of secondary flow was clarified. Additionally, Purnode and Crochet (1998) measured the rheological properties of 0.5% PAA solution and ascertained that the constitutive equation of FENE-P could also signify its viscoelastic property. The FENE-P model was mostly used to define the viscoelastic behaviour of polymer solutions in the turbulent regime (Dimitropoulos, Sureshkumar, and Beris 1998; Ptasiniski et al. 2003). Summary of the numerical studies of polymeric flow in the non-circular ducts is presented in Table 2.2.

Table 2.2: Summary of numerical studies on the flow of polymeric solution in non-circular ducts.

Type of fluid	Model used	Finding	Reference
1000 ppm PAA solution	Temperature-dependent Carreau model	-HTE by 70–300% was caused by the combined effect of temperature-dependent and shear-thinning viscosity.	(Shin and Cho 1993,1994)
50 ppm PAA solution	Carreau model	-The flow behaviour of PAA solution cannot be described accurately without considering the fluid elasticity.	(Bschorer and Brunn 1996)
1000 ppm PAA solution	CEF with Carreau-Yasuda model	-The Nusselt number was enhanced by 6–275%, 38–230% and 33–130% for the duct aspect ratio of 1, 0.5 and 0.25, respectively. -Effect of the shear-thinning viscosity on HTE was insignificant compared to that of the secondary flow.	(Naccache and Mendes 1996)
1000 ppm PAA solution	CEF model	-Prediction of laminar heat transfer of viscoelastic fluid in non-circular ducts could be done by using the CEF equation.	(Payvar 1997)
20000 ppm viscarin in water	CEF model	-Effect of the secondary flow on pressure drop was inconsiderable at low flow rates but it was the opposite for high flow rate.	(Gervang and Larsen 1991)
Viscoelastic fluid	CEF model	-Effect of secondary flow on the pressure drop was insignificant. -When the second normal stress coefficient increased, the intensity of the secondary flow increased.	(Syrjala 1998)
Viscoelastic fluid	CEF model	-When the second normal stress coefficient increased, the velocity of vortex increased. -The Nusselt number enhancement was caused mainly by the increased main flow velocity.	(Norouzi, Kayhani, and Nobari 2009)
Blood	Oldroyd-B model	-The wall shear stress of blood could be modelled precisely by the Oldroyd-B model compared to that of Newtonian model.	(Khambhampati 2013)
Polymeric solution	Reiner-Rivlin model	-Secondary flow had negligible effect on the fluid flow rate. -The HTE increased with the increase of the intensity of secondary flow. -The intensity of the secondary flow was higher for the ducts with higher aspect ratio.	(Gao 1993; Gao and Hartnett 1993, 1996)
1000 ppm PAA solution	PTT model	-The Nusselt number increment was due to both the secondary flow and shear-thinning behaviour of the solution.	(Peres et al. 2009)
Viscoelastic fluid	PTT model	-Both the elastic property of fluid and main flow rate contributed to the existence of secondary flow.	(Xue, Thien, and Tanner 1995)
Polymeric solution	Giesekus model	-The main cause of the secondary flow is the second normal stress difference.	(Yue, Dooley, and Feng 2008)
5000 ppm PAA solution	FENE-P model	-The FENE-P model could describe the rheological behaviour of the PAA solution.	(Purnode and Crochet 1998)

2.2.4 Studies on turbulent heat transfer and flow characteristics of polymer solutions in circular ducts

Most research on polymer additives were conducted in the turbulent regime. Polymer solutions behave differently in the turbulent regime relative to that of the laminar regime. For turbulent flow, polymer solutions do not enhance the heat transfer performance, but they reduce the drag of the fluid at the expense of heat transfer deterioration. Toms (1949) was the first to identify polymers as effective drag reducing additives. He observed that the addition of polymethyl methacrylate into monochlorobenzene could reduce the turbulent skin friction drag by 80%. McComb and Rabie (1982) discovered that 10–100 ppm PAA and PEO solutions could decrease the pressure loss up to 60–70%. Moreover, N. Kim et al. (2009) measured the drag reduction (DR) in polymer added turbulent flow to study the application of polymer additives in a nuclear district heating system. A DR of greater than 20% was obtained for all the polymer concentrations tested. For example, 20 ppm PEO solution could acquire the maximum DR of 50%.

According to Abubakar et al. (2014), polymer additives could suppress the turbulent burst formation in the buffer layer, which in turn restrained the development and distribution of turbulent eddies, as shown in Figure 2.10. Their assertion was supported by Gupta, Metzner, and Hartnett (1967). Moreover, Dimitropoulos, Sureshkumar, and Beris (1998), Lumley (1969) and Bonn et al. (2005) postulated that polymer-induced DR occurred due to the increased extensional viscosity during the stretching of randomly coiled polymers under fluctuating shear rate. Extensional viscosity, also known as elongational viscosity, is a term used for viscosity when the extensional stress is applied (Fleming 1999). Higher extensional viscosity dampened the turbulent energy in the buffer layer, resulting in lower turbulent energy dissipation and friction. Therefore, this DR increased with the increasing elongational viscosity.

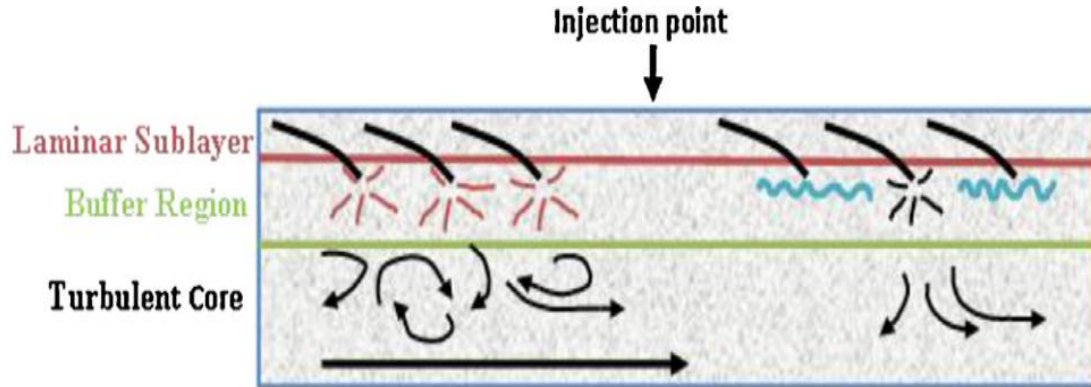


Figure 2.10: Schematic of pipeline turbulent flow regions (Abubakar et al. 2014).

Toonder et al. (1997) and Gillissen (2008) drew a conclusion that the reason leading to DR was the viscous polymer stresses introduced by the extended polymers. They also claimed that the elasticity of polymer played a minor role in the DR mechanism. In addition, Toonder et al. (1997) suggested that the onset of DR was determined by the elasticity of polymer before the polymer became extended. After the extension, the viscous effect caused the DR, thus polymer elasticity had an adverse effect on the DR. Nevertheless, Kwack, Hartnett, and Cho (1982) and Kwack and Hartnett (1983) disagreed and proposed that the DR was originated from the elasticity of polymer solutions. Furthermore, it was also deduced that the DR was related to either the interactions of polymer additives with the near-wall turbulence (McComb and Rabie 1982) or the thickened near-wall viscous layers (Kostic 1994).

Some the aforementioned researchers (Toms 1949; McComb and Rabie 1982; N. Kim et al. 2009) did not investigate the heat transfer performance of polymer solutions in the turbulent regime. Kwack, Hartnett, and Cho (1982) presented that 5 ppm PAA solution reduced the friction and heat transfer up to around 30% and 46%, respectively. Kwack and Hartnett (1983) carried out turbulent heat transfer studies of polymer solution in a circular pipe under constant heat flux boundary condition. It was noticed that at higher concentration where there was substantial DR, the dimensionless heat transfer coefficient decreased drastically. Gupta, Metzner, and Hartnett (1967) measured the heat transfer coefficient of 0.05% and 0.45% PAA in water. Their results showed that both 0.05% and 0.45% PAA minimized drag up to 44% and 36%, respectively, at a flow

rate of 200 pound per minute. The DR was observed to coexist with the reduction in the heat transfer rate. The maximum heat transfer rate reduction of 0.05% and 0.45% PAA were found to be 62% and 90%, respectively.

Besides, Poreh and Paz (1968), Hartnett and Kwack (1986), and Debrule and Sabersky (1974) also stated that the HTR of polymer solutions was larger than the DR for turbulent regime. For HTR, it was plausible that the polymer additives thickened the near-wall elastic buffer layers, thus increasing the thermal resistance between the wall and bulk fluid, resulting in a lower heat transfer rate (Sellin, Hoyt, and Scrivener 1982; Singh 2002, 2011).

Poreh and Paz (1968) reported for a flow of dilute polymeric solution (10–1000 ppm) in a circular duct that the Nusselt number reduction was more significant than the friction factor decrement, especially at higher Reynolds number. Debrule and Sabersky (1974) completed a series of experiments by using PEO in water to predict the heat transfer and friction coefficients for smooth and rough circular tubes. For the rough circular tube, extensive reduction in the friction and heat transfer coefficients were by a factor of 6 and 10, respectively. On the other hand, the friction coefficient of the smooth tube was reduced by a factor of 3, and the heat transfer coefficient by a factor of 5. Their results also indicated that the performance of PEO decreased with increasing Reynolds number and temperature, as PEO was more susceptible to structure degradation.

Toh and Ghajar (1988) conducted a research using two different types of PAA solutions in the thermal entrance region of a turbulent pipe flow. Separan AP-273 was more effective than Separan AP-30, owing to its higher molecular weight and elasticity. For example, at the Reynolds number of 15000, the rate of HTR of 200 ppm Separan AP-273 and Separan AP-30 were 85% and 57%, respectively. Additionally, their results demonstrated that the Nusselt number decreased with the increasing polymer concentration until a certain asymptotic limit. Further increment beyond the limit had no influence on the heat transfer performance.

Recently, Mohsenipour and Pal (2013) explored the synergistic effect of mixed polymer and cationic surfactant system for a turbulent pipe flow. Surfactant is a type of solution

having similar flow characteristic as the polymer solution in the turbulent regime. The DR achieved by the mixed system was 58% and 35% higher compared to that of the pure surfactant and pure polymer, respectively. This synergistic effect was more considerable at low polymer but high surfactant concentration. However, no heat transfer study was performed by Mohsenipour and Pal (2013).

2.2.5 Studies on turbulent heat transfer and flow characteristics of polymer solutions in non-circular ducts

Investigations on the friction factor and heat transfer behaviour of turbulent non-circular polymeric flow are comparatively scarce (Hartnett 1992). Kostic and Hartnett (1985) scrutinized the heat transfer and friction factor of the aqueous PAA solution in a 2:1 rectangular duct. Similar to the turbulent circular flow, the addition of PAA into water could greatly reduce the drag and heat transfer in the rectangular duct. They made a similar remark as Toh and Ghajar (1988) that there was an asymptotic limit for the HTR. The same was encountered for the friction factor. The maximum DR and HTR asymptotes were reached at the PAA concentrations of 100 and 1000 ppm, respectively. Moreover, they affirmed that the friction factor and heat transfer coefficient of PAA solution in the turbulent non-circular flow could be estimated using the available correlations for the turbulent circular flow.

Furthermore, Escudier and Smith (2001) analyzed the DR of 0.1% Carboxymethylcellulose mixed with 0.1% Xanthan gum (CMC/XG), and 0.125% PAA solution in a square duct. The PAA, which was more elastic compared to the CMC/XG, produced higher DR of 77%, while the CMC/XG achieved only a DR of 65% in the turbulent flow.

2.3 Addition of additives to nanofluid

The addition of polymer additives into nanofluid might be able to improve the thermal-hydraulic efficiency of nanofluid. Polymer in nanofluid will probably still maintain its capability to induce the secondary flow for HTE, and the nanofluid continues to have its heat transfer improvement ability. On the other hand, it might have an adverse effect.

The presence of nanoparticles may possibly offset the development and strength of the secondary flow generated by the polymer, while polymer additives may change the flow rheology thus altering the heat transfer behaviour of nanofluid. These are all yet to be tested. To date, only a few researchers have investigated the effect of surfactant on nanofluid for turbulent pipe flow (Liu and Liao 2010; Yang et al. 2012; Drzazga et al. 2013; Li et al. 2013; Yang et al. 2013). Studies examining the influence of polymer additives on nanofluid are limited.

Drzazga et al. (2013) experimentally investigated the influence of nonionic surfactants in CuO nanofluid on the DR in a circular pipe. The nonionic surfactants used were Rokacet O7 and Rokanol K7. The Reynolds number covered was between 8000 to 50000. They did not conduct any heat transfer studies. Their results showed that the nonionic surfactants in nanofluid still reduced drag, while the nanoparticles had a negligible impact on the DR. Better DR performance was noticed at higher surfactant concentration, but the viscosity of the solutions also increased with the increase of surfactant concentration. This considerable viscosity increment might hinder the DR phenomenon. Therefore, trade-off between the DR performance and viscosity increment was essential to obtain the optimal surfactant concentration for the best hydraulic performance.

Liu and Liao (2010) studied the turbulent forced convective heat transfer of a drag reducing fluid with the addition of nanoparticles. They used CNTs and water doped with Cetyltrimethyl Ammonium Chloride (CTAC) surfactant solution in a circular tube with the diameter of 25.6 mm. Their results showed that the DR ability of CTAC solution was maintained, but weakened by the presence of CNTs. It was plausible that some of the CTAC molecules got attached to the CNTs, which in turn reduced the availability of the molecules to form rod-shaped micelles for DR. Furthermore, the heat transfer performance of the CTAC solution was significantly improved by the addition of CNTs. The heat transfer performance of drag reducing CTAC-nanofluid system was found to be dependent on the fluid temperature, nanoparticles and surfactant concentration.

There were also experimental works on the thermal conductivity and shear viscosity of Viscoelastic-Fluid-Based Nanofluid (VFBN), which was the dispersion of Cu nanoparticles in the viscoelastic CTAC/Sodium salicylate (NaSaI) solution (Yang et al. 2012; Li et al. 2013). It was noted that the nanoparticles in the VFBN increased the thermal conductivity of the fluid. In addition, the VFBN exhibited a non-Newtonian shear-thinning behaviour, which was comparable to the rheological behaviour of the base fluid itself. Hence, it was postulated that the VFBN also had the turbulence drag reducing ability.

Yang et al. (2013) performed some experiments on the heat transfer and pressure drop of viscoelastic-fluid-based Cu nanofluid. The Viscoelastic-Based-Fluid (VBF) employed was CTAC/NaSaI with the mass concentration of 600 and 1200 ppm. The nanoparticle loading considered were 0.25, 0.5 and 1.0 vol%. It was observed that the VFBN showed improved heat transfer characteristic compared to that of the VBF (Figure 2.11). This enhancement was attributed to the enhanced thermal conductivity, and it increased with the increasing Cu nanoparticles volume fraction. Furthermore, when the temperature was increased, the heat transfer coefficient of the VFBN increased; while there was not much influence of temperature on the pressure drop. The VBF did not lose its DR ability when nanoparticles were added to it. However, the drag reducing effect was weakened, as presented in Figure 2.12. The authors concluded that the VFBN showed both the features of VBF and nanofluid. The synergetic effect of viscoelasticity and nanofluid characteristics was dependent on the rheological and physical properties of the base fluid, as well as the flow condition (velocity).

Gierczycki et al. (2015) investigated the DR of CuO nanoparticles in CTAC/NaSaI solution for turbulent pipe flow. They agreed with Liu and Liao (2010) that the effect of DR became smaller when the CuO nanoparticles were added to the aqueous solution of CTAC/NaSaI mixture. They did not perform any heat transfer studies on the solution. On the other hand, Akindoyo, Abdulbari, and Yousif (2015) conducted experiments in a rotating disk apparatus using nanofluid of XG polymer and hexadecyl trimethyl ammonium chloride (HTAC) surfactant. Their results indicated that the DR and

mechanical stability for the nanofluid of XG and HTAC were better than that of the XG and HTAC mixture without nanoparticles.

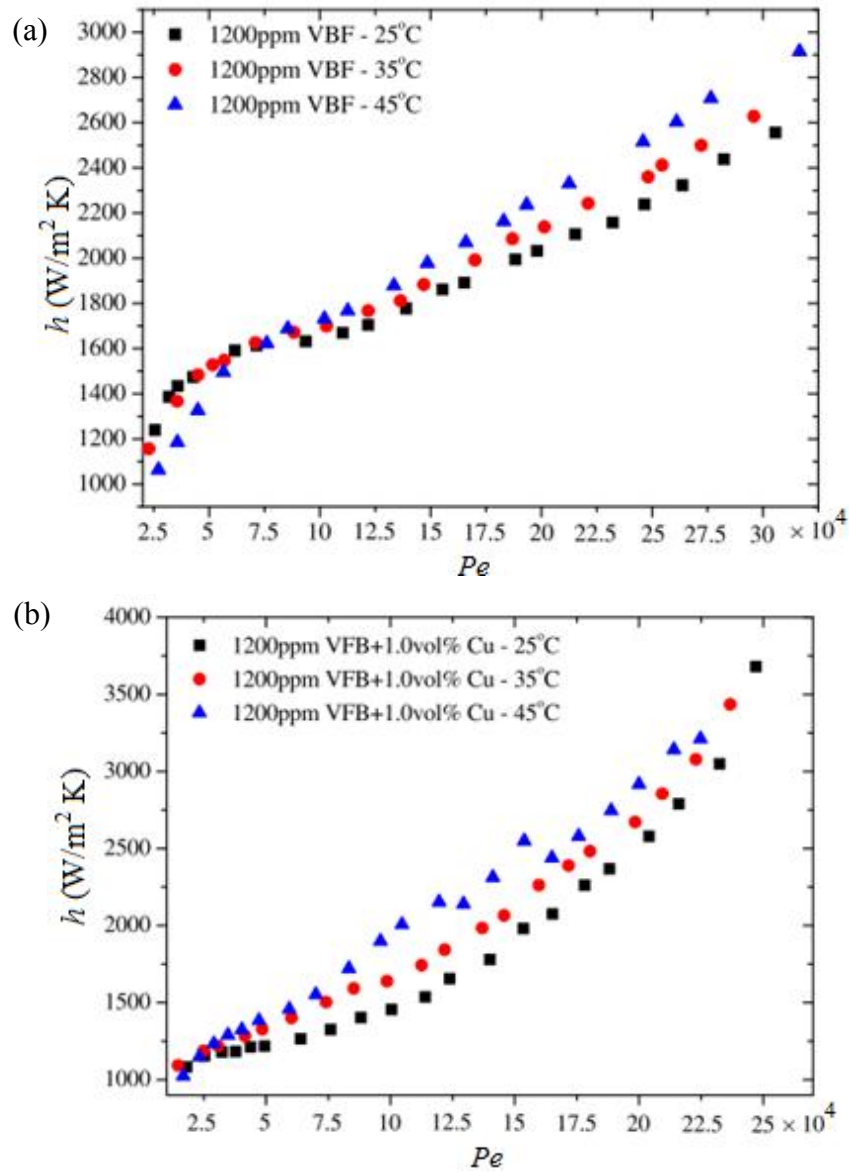


Figure 2.11: Influence of temperature on the convective heat transfer coefficient for 1200 ppm (a) VBF and (b) VBFN (Yang et al. 2013).

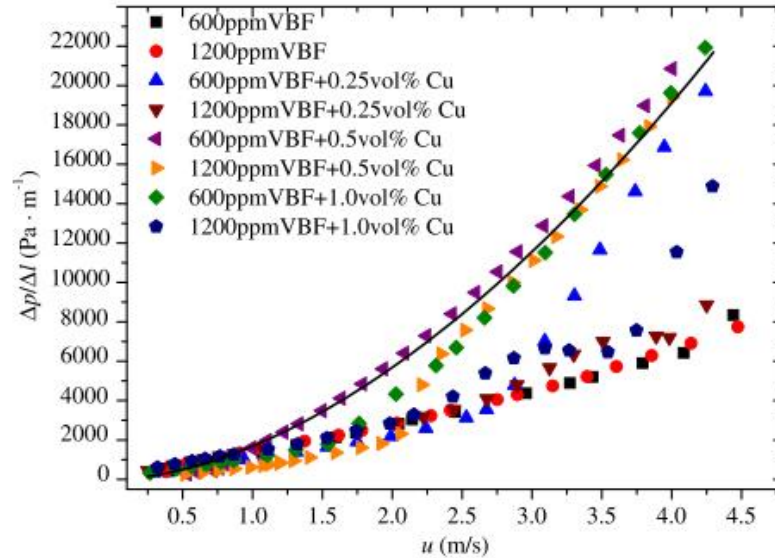


Figure 2.12: Variation of pressure drop per unit length as a function of velocity at different VBF and VFBN concentration (Yang et al. 2013).

Kostic (2013) suggested to develop a new hybrid fluid, which was called poly-nanofluid. His proposed study focused more on the turbulent regime. He hypothesized that the nanoparticles might yield heat transfer augmentation, while the polymer might enhance the flow properties, such as a reduced flow friction and pressure drop. The long-chain polymer was believed to have active chemical and physical interactions with the nanoparticles, thus leading to many more unprecedented applications in the future. Therefore, more research on the poly-nanofluid is necessary. Recently, a thermal conductivity measuring apparatus for this poly-nanofluid was developed (Walleck 2009; Kostic 2013).

Additionally, studies of nanofluid in polymer solution had been carried out in the area of enhanced oil recovery. Fiveland (2015) investigated the hydraulic and hole cleaning performances of nano-silica in XG polymer treated mud system. His results showed that with 0.02 wt% nano-silica in the polymer treated mud system, the filtrate could be reduced by 16.67% and the cutting transport efficiency was improved. Besides, Sharma, Iglauer, and Sangwai (2016) also examined the silica nanofluid in an oilfield polyacrylamide for enhanced oil recovery. They discovered that the silica nanofluid in the oilfield polyacrylamide could remarkably increase the oil recoveries.

2.4 Summary and research gaps

Conventional heat transfer fluids have poor heat transfer performance owing to their low thermal conductivity. Nanofluids can serve as an attractive alternative to the conventional heat transfer fluids because they are reported to improve the heat transfer rate of the fluids. The thermal conductivity and heat transfer coefficient of nanofluids are larger compared to that of the base fluids. This heat transfer augmentation increases with the increasing nanoparticle loading. At the same time, the viscosity of nanofluids also gets higher when the concentration is higher. Some research even demonstrates that the increase in viscosity can be significantly higher in comparison to the HTE. The viscosity increment induces a high pressure drop across the nanofluid systems. The pressure drop accession is undesirable as it diminishes the benefit of nanofluids for heat transfer application. As a result, it is crucial to enhance the thermal-hydraulic efficiency of the nanofluids.

Most studies for nanofluids focus on their heat transfer and flow performance. Although works have been done to inspect the thermal-hydraulic performance index for nanofluids, less attention is paid to improve it. First knowledge gap that this research can fill is to find a way to boost the thermal-hydraulic efficiency of nanofluids. In this present study, it is recommended to add polymer additives into nanofluid to increase the thermal-hydraulic efficiency. Polymers are found to behave differently in different flow regimes and geometries. For laminar flow, polymer additives do not alter the heat transfer performance and fluid friction in the circular pipes when compared to that of the purely viscous fluid. On the other hand, they enhance the heat transfer performance without changing the friction of the fluid in the non-circular ducts. Besides, they reduce friction in the turbulent regime for circular and non-circular channels. However, this reduction in fluid friction is always accompanied by a virtually strong amount of heat transfer performance deterioration.

The research of the suspension of polymer additives in nanofluids is limited. The investigations are mostly done on the heat transfer and flow behaviour of surfactant-based nanofluid, but not on the polymer-based nanofluid (or poly-nanofluid). The

research conducted for poly-nanofluid is particularly on the development of thermal-conductivity measurement device. Besides, the effect of nanofluid in polymer solution is studied for the enhanced oil recovery, but not on the heat transfer and flow behaviour in a pipe flow. This is the second knowledge gap and this research aims to study the influence of polymer additives on the rheological characteristic, heat transfer and flow behaviour of nanofluid.

Furthermore, studies on surfactant-based nanofluids are experimental studies. No CFD modelling has been carried out for poly-nanofluids in the circular and non-circular ducts for the laminar regime. This is the third research gap this present work can contribute some knowledge to, numerically. It is also important to highlight that the experiments done for the surfactant-based nanofluid are merely on the turbulent circular flow. The fourth knowledge gap is the lack of information on the behaviour of poly-nanofluid in the laminar circular and non-circular flow. This study can provide some insight into the laminar forced convective heat transfer of poly-nanofluid in the circular and non-circular ducts.

2.5 Identified problem statement and research questions of the study

This present study addresses the problem of low thermal-hydraulic efficiency of nanofluid in the circular and non-circular ducts. This low efficiency of nanofluid is due to the high pressure drop incurred, especially when the nanofluid concentration is high. The central research question is: Can polymer additives improve the thermal-hydraulic efficiency of nanofluid? Some related sub-questions can be further derived:

1. Will the addition of polymer additives affect the rheology of nanofluid?
2. What is the influence of polymer additives on the heat transfer and flow behaviour of nanofluid?
3. Are the heat transfer and flow characteristics of poly-nanofluid in the circular and non-circular ducts the same?
4. What is the optimum concentration of poly-nanofluid for the best thermal-hydraulic efficiency?

2.6 Aim and objectives of the study

The main aim of this study is to understand the rheological behaviour, heat transfer and flow performance of the poly-nanofluid as well as to evaluate their thermal-hydraulic efficiency in the circular and non-circular ducts for the laminar regime ($250 \leq Re \leq 2000$). In particular, the objectives of this research are:

1. To study the effect of PAA additives on the rheological characteristics of Al_2O_3 nanofluid.
2. To investigate the influence of polymer on the heat transfer performance and pressure drop of Al_2O_3 -water nanofluid in laminar circular pipe flow.
3. To predict the laminar heat transfer performance and pressure drop of poly-nanofluid in non-circular ducts.
4. To find an optimum concentration of poly-nanofluid for the best thermal-hydraulic efficiency.
5. To propose Nusselt number and friction factor correlations for poly-nanofluid in the pipe flow.

CHAPTER 3: RESEARCH METHODOLOGY

The research methodology is briefly presented in Figure 3.1. This study consists of rheology studies, heat transfer and flow studies. The rheology studies were carried out to investigate the rheological behaviour of PAA solution and poly-nanofluid. The viscosity of PAA solution and poly-nanofluid obtained from the rheology measurement served as inputs for the simulations. For the heat transfer and flow studies, both experiments and simulations were involved. The numerical results were validated against the results from experiments and existing literature. The experiments done were for validation purpose and results from the heat transfer and flow studies were mostly numerical. The methodologies of rheology measurements, heat transfer experimental studies and simulation works are given in Sections 3.1, 3.2 and 3.4, respectively.

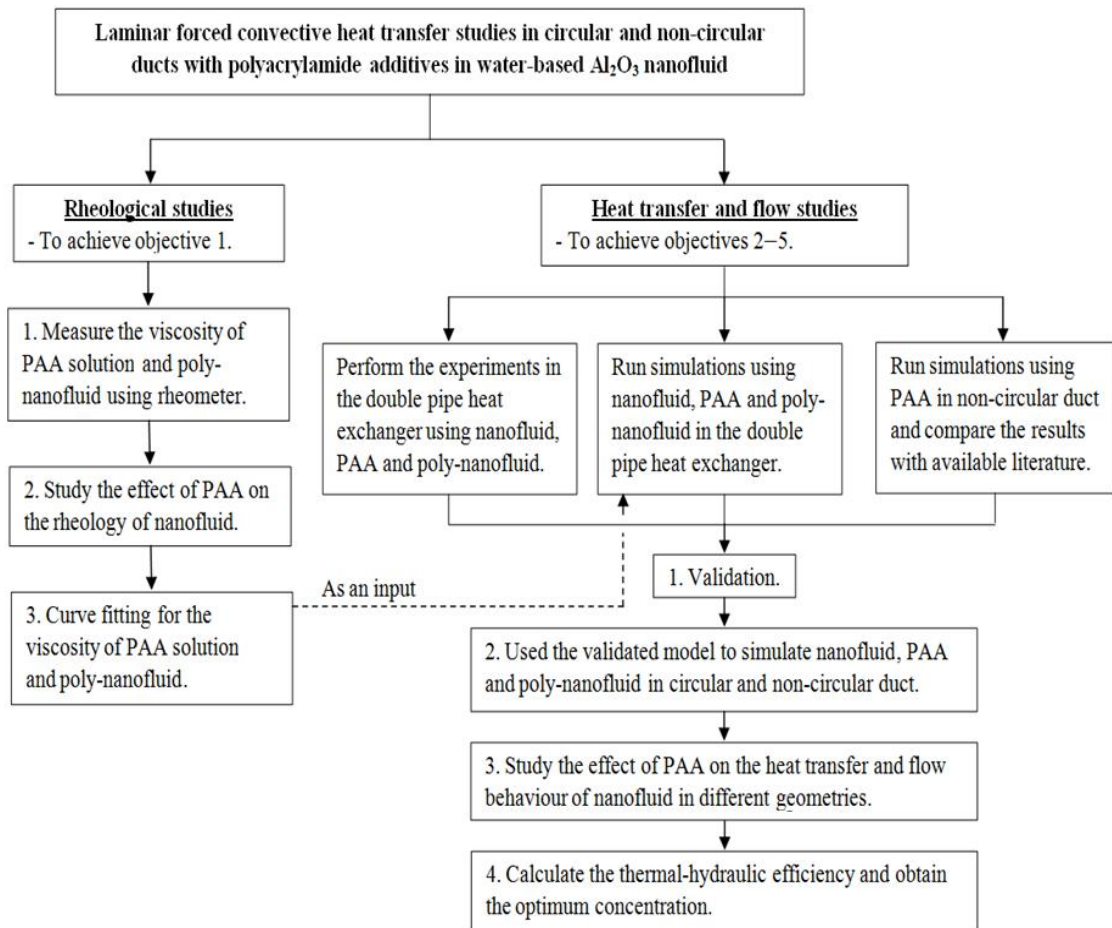


Figure 3.1: Flow chart showing the research methodology of this study.

3.1 Rheology measurement

3.1.1 Experimental setup

Rheometer AR-1500ex (TA Instruments) shown in Figure 3.2 was used for the rheology measurement. It is an advanced controlled stress and strain rate rheometer. This geometry is suitable for homogeneous samples or samples containing particles. The 60 mm cone can be utilized for samples with low viscosity. This geometry can also provide a uniform shear rate throughout the sample. Besides, the rheometer is equipped with a Peltier plate which controls and measures the temperature from a range of -40°C to 200°C to an accuracy of $\pm 0.1^{\circ}\text{C}$. The Peltier system supplies any amount of heating and cooling to the plate by controlling the magnitude of the electric current. The typical heating rate can be up to $50^{\circ}\text{C}/\text{min}$ (*Ar 500/1000 Rheometers Hardware Manual 2000*). The cone-and-plate geometry with 60 mm cone diameter, 2° cone angle and $60\ \mu\text{m}$ gap was employed for the present analysis.

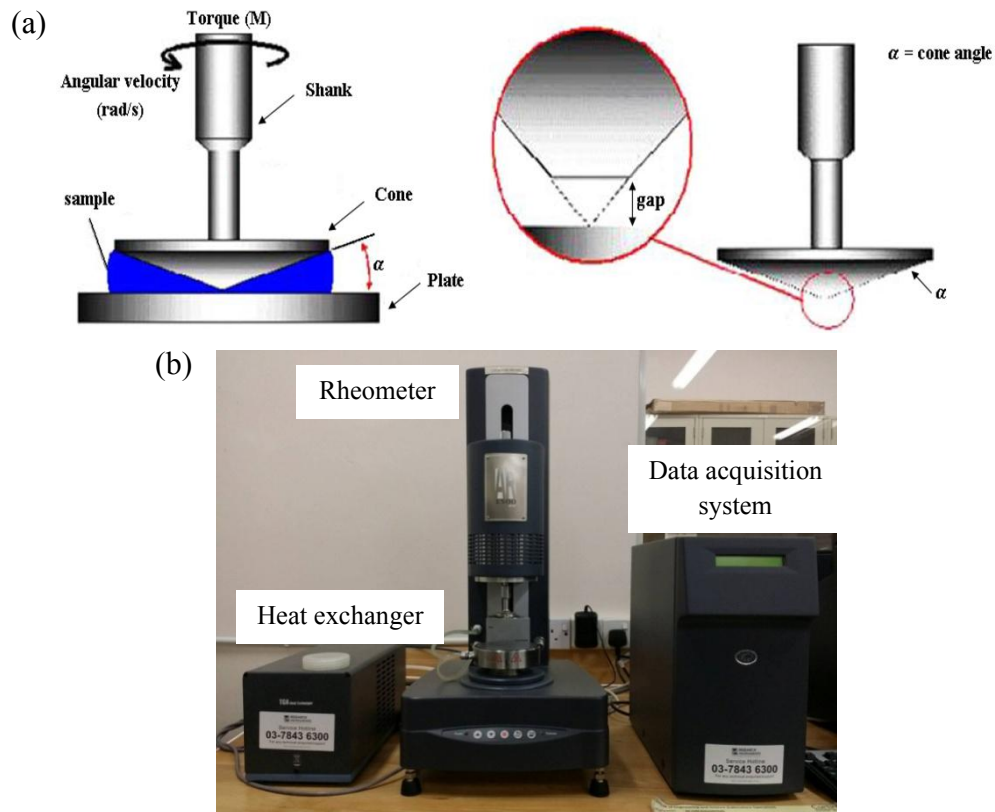


Figure 3.2: (a) Cone-and-plate geometry (Zhang, Wang, and Chen 2009) and (b) rheometer AR-1500ex.

3.1.2 Preparation of test fluids

The concentrations of the PAA solution and poly-nanofluid used for the rheology measurement are recorded in Table 3.1. The Al₂O₃ nanofluid and PAA used in this present research were 20 wt% Al₂O₃ nanoparticles (47 nm) in water, and non-ionic water-soluble polyacrylamide, respectively, produced by Sigma-Aldrich Company.

A desired amount of the PAA additives for a given concentration was weighed using an electronic balance. 10 mL of distilled water which was prepared using a measuring cylinder was poured into a beaker. The PAA additives were shifted gently onto the water surface. Then, the water and PAA additives were stirred with an electromagnetic stirrer in order to dissolve the polymer additives. The low stirring speed of 100 rpm was chosen to minimise the polymer degradation (Xie and Hartnett 1992). To dissolve the PAA additives which were stuck to the wall of the beaker, another 10 mL distilled water was added into the beaker. The PAA solution was ready for the rheological measurement after one day of stirring as no more agglomeration of the PAA additives was observed.

Conversely, to prepare the poly-nanofluid, a required amount of 20 wt% Al₂O₃ nanofluid was first diluted with distilled water to the concentration needed for rheology measurement. The well-dissolved PAA solution was added into the nanofluid according to the required concentration. The final volume of the PAA and poly-nanofluid prepared was 20 mL.

Table 3.1: Solutions used for rheology measurement.

No.	Solution	No.	Solution
1	10 ppm PAA	11	50 ppm PAA in 1.00 vol% nanofluid
2	50 ppm PAA	12	50 ppm PAA in 4.00 vol% nanofluid
3	200 ppm PAA	13	200 ppm PAA in 0.13 vol% nanofluid
4	1000 ppm PAA	14	200 ppm PAA in 0.51 vol% nanofluid
5	10 ppm PAA in 0.13 vol% nanofluid	15	200 ppm PAA in 1.00 vol% nanofluid
6	10 ppm PAA in 0.51 vol% nanofluid	16	200 ppm PAA in 4.00 vol% nanofluid
7	10 ppm PAA in 1.00 vol% nanofluid	17	1000 ppm PAA in 0.13 vol% nanofluid
8	10 ppm PAA in 4.00 vol% nanofluid	18	1000 ppm PAA in 0.51 vol% nanofluid
9	50 ppm PAA in 0.13 vol% nanofluid	19	1000 ppm PAA in 1.00 vol% nanofluid
10	50 ppm PAA in 0.51 vol% nanofluid	20	1000 ppm PAA in 4.00 vol% nanofluid

3.1.3 Experimental procedures

The rheometer was first calibrated with water. Figure 3.3 shows the shear stress of water as a function of shear rate at 298.15 K. From the plot, it can be observed that the shear stress of water is linearly proportional to the shear rate. The shear stress versus shear rate plot is a straight line with the R-squared value close to one. The viscosity of water depicted in Figure 3.4 is constant with increasing shear rate. After the calibration, the rheology measurement was carried out for PAA solution and poly-nanofluid.

Sample loading is an important aspect in the rheological analysis. The test fluids were loaded with a pipette between the cone and plate discs and were ensured not to contain any air bubbles. The cone was then driven closer to the plate surface by an oscillatory force, leaving only $60\ \mu\text{m}$ as a gap between two surfaces. The gap was ensured to be filled properly before running the tests. Solvent trap was used to cover the test fluids during the measurement.

The rheological behaviour of the test fluids was studied through the continuous flow step, where the shear was continually ramped and the data samples were taken at defined intervals (Figure 3.5). The investigations were performed at constant temperatures in the range of 298.15 to 323.15 K and at shearing rate of 0 to $1000\ \text{s}^{-1}$. Each experiment was repeated three times and the average viscosity values were taken as the final values.

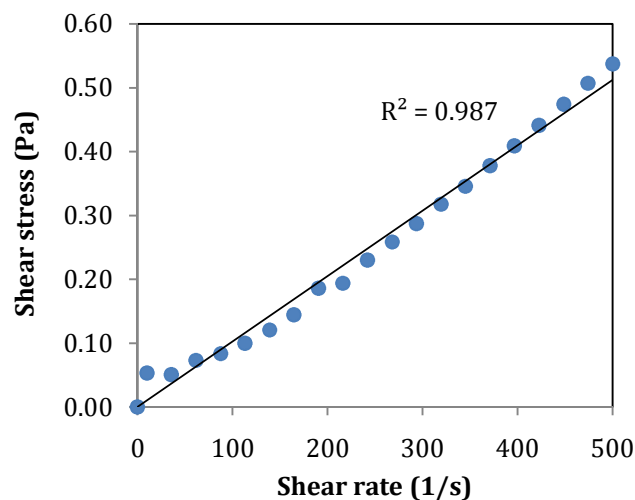


Figure 3.3: Shear stress versus shear rate plot for water at 298.15 K.

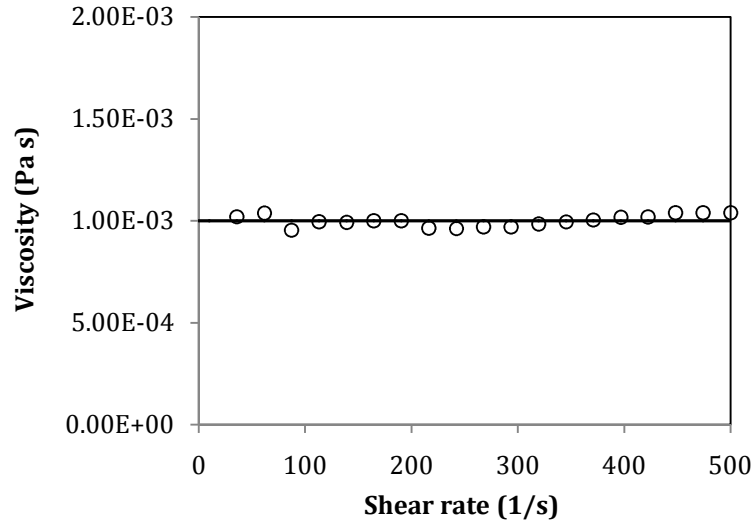


Figure 3.4: Viscosity versus shear rate plot for water at 298.15 K.

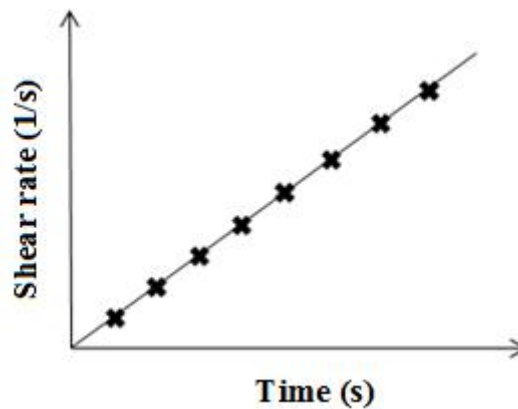


Figure 3.5: Continuous flow step applied for the rheology measurement.

3.2 Heat transfer experimental studies

3.2.1 Experimental setup

The equipment used for heat transfer experiment was the SOLTEQ Heat Exchanger Training Apparatus (model of HE 158-A) as shown in Figure 3.6. It comes with four different types of heat exchangers and two stainless steel tanks. The four different heat exchangers are shell and tube, concentric (double pipe), jacketed vessel with coil and stirrer, and plate heat exchangers. The double pipe heat exchanger is illustrated in Figure 3.7. One of the sump tanks is for the hot solution which is equipped with 11.5 kW immersion-type heater. The heater automatically cuts off when the set temperature

is reached. Each tank has a centrifugal pump with the capacity of 10 L/min. Electronic level switches are installed in the tanks to protect the pumps from dry-run. Electricity supply to the pumps and heater will be cut off when there is a low-level alert in any of the tank. The flow rate measurement is taken using rotameters. K-type thermocouples are mounted at the flow inlet and outlet for temperature measurement. The readings of temperature and flow rate can be obtained from the control panel.

In the present research, only the double pipe heat exchanger was considered. The hot test fluids (nanofluid, PAA solution and poly-nanofluid) flowed in the tube side of the heat exchanger while water flowed in the annuli. The specifications of the double pipe heat exchanger, cold and hot circuits are given in Table 3.2 and Table 3.3, respectively.



Figure 3.6: Schematic of the heat exchanger apparatus.

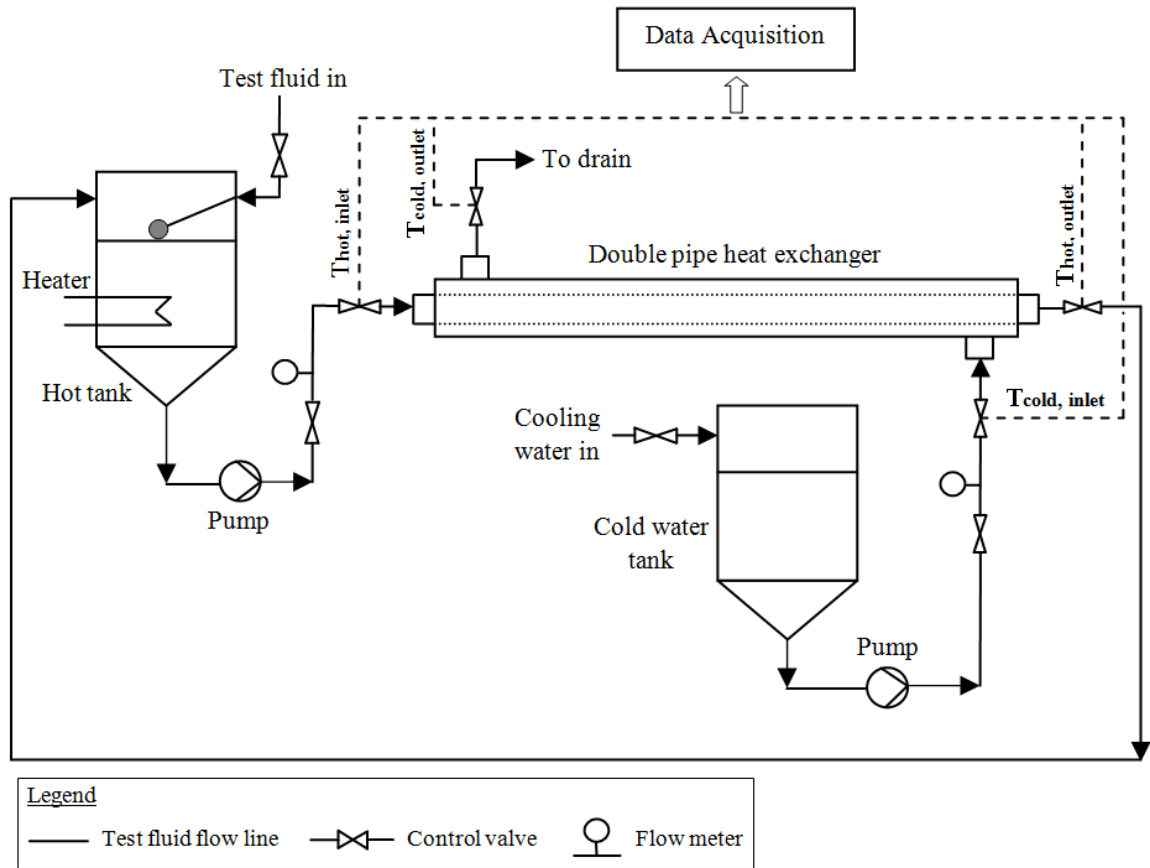


Figure 3.7: Schematic diagram of the double pipe heat exchanger.

Table 3.2: Specifications of the double pipe heat exchanger.

Double pipe heat exchanger	Dimension
Tube inner diameter, d_i (m)	17.12×10^{-3}
Tube outer diameter, d_o (m)	21.34×10^{-3}
Annulus inner diameter, D_i (m)	33.40×10^{-3}
Annulus outer diameter, D_o (m)	42.72×10^{-3}
Length, l (m)	1.50
Number of tube pass	1

Table 3.3: Specifications of the hot and cold circuits.

Cold circuit	
Tank	: 50 L, stainless steel
Level control	: Float type control valve
Circulation pump	: Centrifugal type, 10 L/min, dry-run protected by level switch
Hot circuit	
Tank	: 50 L, stainless steel
Circulation pump	: Centrifugal type, 10 L/min, dry-run protected by level switch
Heating system	: 11.5 kW immersion-type heater protected by temperature controller and level switch

3.2.2 Preparation of test fluids

The concentration of Al_2O_3 nanofluid employed in the heat transfer experimental studies was 0.10 vol%; while for PAA additives, 1000 ppm was used. The two concentrations of poly-nanofluid examined were 10 and 1000 ppm PAA in 0.10 vol% Al_2O_3 nanofluid.

The total volume of solution required for the heat transfer experiments was 32 L. PAA additives were weighed and dissolved in a 5 L beaker accordingly. The solution was stirred at the speed of 100 rpm to ensure complete dissolution of the polymer additives. The prepared solution was then poured into the tank of the heat exchanger and the volume was topped up to 32 L. On the other hand, the Al_2O_3 nanofluid was diluted from 20 wt% to 0.10 vol% (or 0.40 wt%). The nanofluid was also prepared in a 5 L beaker and then topped up to 32 L in the hot solution tank. The nanofluid prepared was stable as there was no precipitation observed. For the poly-nanofluid, 2.5 L nanofluid and polymer solution were prepared separately in two 5 L beakers. They were later mixed in a 5 L beaker to obtain a homogeneous solution before they were poured into the hot solution tank. After that, 27 L of water was added into the hot tank to achieve the total final volume of 32 L.

3.2.3 Experimental procedures

The heat transfer experiments were carried out in counter-current mode with tap water as the cold fluid. The temperature assessed for the test fluids were 313.15, 318.15 and 323.15 K. After the hot tank was filled with 32 L test fluid, the valve of the water inlet to the cold tank was turned on. All valves were checked to be in counter-current condition. The valve position was switched to the double pipe heat exchanger. The heater was turned on to heat up the test fluid in the hot tank to the desired temperature. After the temperature of the test fluid reached the set value, the pumps for the hot and cold circuits were switched on. The cold water flow rate was fixed at 5 L/min while the flow rate of the hot test fluid was adjusted according to the Reynolds number ranges tested. The system was ran for 10 minutes to allow it to reach its steady state. Then, the temperatures of the cold water and hot solution were recorded. With the same cold water flow rate, the heat transfer studies were continued for different flow rates of the

hot test fluid. The investigation was repeated three times for a particular hot and cold flow rates to obtain the average temperature values.

3.3 Uncertainty Analysis

Some background and theory about the uncertainty analysis are given in Appendix A. The total uncertainty, $U_{\bar{r}}$, in an averaged result, \bar{r} , is estimated using the root-sum-square of the bias, $B_{\bar{r}}$, and precision limits, $P_{\bar{r}}$, as shown in Equation 3.1 (Stern et al. 1999). The bias and precision limits are approximated using Equations 3.2 and 3.5, respectively.

$$U_{\bar{r}}^2 = B_{\bar{r}}^2 + P_{\bar{r}}^2 \quad (3.1)$$

$$B_{\bar{r}}^2 = \sum_{i=1}^J \theta_i^2 B_i^2 + 2 \sum_{i=1}^{J-1} \sum_{k=i+1}^J \theta_i \theta_k B_{ik} \quad (3.2)$$

$$\theta_i = \frac{\partial r}{\partial X_i} \quad (3.3)$$

$$B_{ik} = \sum_{j=1}^L (B_i)_j (B_k)_j \quad (3.4)$$

$$P_{\bar{r}} = \frac{t_c S_{\bar{r}}}{\sqrt{M}} \quad (3.5)$$

$$S_{\bar{r}} = \left[\sum_{k=1}^M \frac{(r_k - \bar{r})^2}{M - 1} \right]^{1/2} \quad (3.6)$$

where X_i and X_k are the individual variables, B_i and B_k are the bias limits in X_i and X_k , respectively; B_{ik} is the correlated bias limit in X_i and X_k , θ_i and θ_k are the sensitivity coefficients of X_i and X_k , respectively; r is the desired result calculated using the measured variables, $S_{\bar{r}}$ is the standard deviation of the averaged result, t_c is the coverage factor, M is the number of measurements taken for a variable at the same fixed test condition. In addition, J is the number of variables, and L is the number of correlated bias error sources. The number of measurements taken, M , was 3 because every set of experiment was repeated for three times. A t_c of 2 was used for $M < 10$ (Stern et al. 1999).

In this research, the uncertainty estimation was made at the 95% confidence level. The measurement uncertainty of the viscosity obtained from the rheometer was approximately 0.30 to 6.00%. The precision limit contributed mostly to the total measurement uncertainty of the viscosity. This was due to the deviation in the volume of the solutions loaded for the rheological testing. The volume of the solutions loaded onto the plate of the rheometer could not be exactly the same due to human error. The bias limit of the viscosity was determined based on the last significant digit of the reading that rheometer could give, which was ± 0.000001 Pa s. Its effect on the total uncertainty of the viscosity measured was negligible.

For the heat transfer experiments, the final desired results were the overall heat transfer coefficient, U and the Reynolds number, Re or the generalized Reynolds number, Re' . They were not measured directly. Variables like temperature and flow rate were measured and substituted into a set of data reduction equations to get their desired values. According to Equations 3.80, 3.93 and 3.94 (shown in Section 3.5), the uncertainty of U , Re and Re' were calculated as follows:

$$U_{\bar{U}} = \left[\left(\frac{tS_{\bar{U}}}{\sqrt{M}} \right)^2 + \left(\left(\frac{\partial U}{\partial X_Q} \right)^2 B_Q^2 + \left(\frac{\partial U}{\partial X_{A_t}} \right)^2 B_{A_t}^2 + \left(\frac{\partial U}{\partial X_{\Delta T_{LMTD}}} \right)^2 B_{\Delta T_{LMTD}}^2 \right) \right]^{0.5} \quad (3.7)$$

$$U_{\bar{Re}} = \left[\left(\frac{tS_{\bar{Re}}}{\sqrt{M}} \right)^2 + \left(\frac{\partial Re}{\partial X_\rho} \right)^2 B_\rho^2 + \left(\frac{\partial Re}{\partial X_v} \right)^2 B_v^2 + \left(\frac{\partial Re}{\partial X_D} \right)^2 B_D^2 + \left(\frac{\partial Re}{\partial X_\mu} \right)^2 B_\mu^2 \right]^{0.5} \quad (3.8)$$

$$U_{\bar{Re}'} = \left[\left(\frac{tS_{\bar{Re}'}}{\sqrt{M}} \right)^2 + \left(\frac{\partial Re'}{\partial X_\rho} \right)^2 B_\rho^2 + \left(\frac{\partial Re'}{\partial X_v} \right)^2 B_v^2 + \left(\frac{\partial Re'}{\partial X_D} \right)^2 B_D^2 + \left(\frac{\partial Re'}{\partial X_n} \right)^2 B_n^2 + \left(\frac{\partial Re'}{\partial X_K} \right)^2 B_K^2 \right]^{0.5} \quad (3.9)$$

where B_Q , B_{A_t} , $B_{\Delta T_{LMTD}}$, B_ρ , B_v , B_D , B_μ , B_n and B_K are the bias limits for heat transfer rate, total heat transfer area, logarithmic mean temperature difference, density, velocity, diameter, viscosity, power law exponent and consistency index, respectively. The values of these variables are given in Appendix A (Table A.1 to Table A.3). The bias limits of the logarithmic mean temperature difference and diameter are provided in Table 3.4. The other bias limits listed in Equations 3.7 to 3.9 were predicted using Equation 3.2. From Equation 3.7, the uncertainty of U was estimated to be about 3.36 to 5.98%. More than 60% of the uncertainty of U came from the bias errors. The minor contribution to the bias limits of U is from the logarithmic mean temperature difference, which was less than 0.10% of the total bias limits. Hence, its effect was negligible. The possible sources of the bias errors in U were the calibration, data reduction, and data acquisition errors (Batill 1994; Stern et al. 1999).

Using the similar approach, the uncertainties of Re and Re' were found to be 0.13 to 5.63%, and 0.06 to 3.47%, respectively. The precision errors were mainly responsible for over 90% of the uncertainties in Re and Re' . This was attributed to the difficulties in duplicating the same flow rate in the three repeated sets of experiments due to fluctuations in the readings of the flow rate. The results obtained from the uncertainty analysis are summarised in Table 3.5.

Table 3.4: The bias limits for different individual variables.

Bias limit	Magnitude	Estimation
$B_{\Delta T_{LMTD}}$	0.01 K	Last significant digit
B_D	0.000005 m	Half of the smallest division

Table 3.5: The results of uncertainty analysis.

Parameters	Total uncertainty (%)
Viscosity, $\eta(\dot{\gamma})$	0.30–6.00
Overall heat transfer coefficient, U	3.36–5.98
Reynolds number, Re	0.13–5.63
Generalized Reynolds number, Re'	0.06–3.47

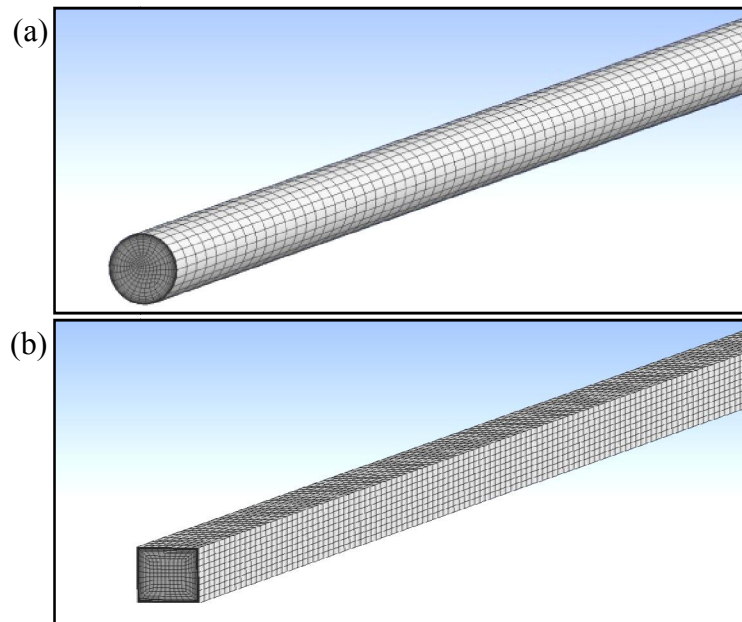
3.4 Simulation works

3.4.1 Geometry creation

The simulation works were carried out using ANSYS FLUENT software Version 15.0. The double pipe heat exchanger was simulated according to its actual dimensions given in Table 3.2. Besides the double pipe heat exchanger, the geometries considered in this present study were a circular pipe, a 2:1 rectangular duct, a 4:1 rectangular duct and a square duct. These circular and non-circular ducts had the same hydraulic diameter. The dimensions of all these ducts are presented in Table 3.6. The computation grids for all these geometries are illustrated in Figure 3.8.

Table 3.6: Dimensions of the simulated circular and non-circular ducts.

Geometries	Height, H (m)	Width, W (m)	Length, l (m)	Hydraulic diameter, D_h (m)
Circular pipe	-	-	6.40	1.20×10^{-2}
2:1 rectangular duct	9.00×10^{-3}	1.80×10^{-2}	6.40	1.20×10^{-2}
4:1 rectangular duct	7.50×10^{-3}	3.00×10^{-2}	6.40	1.20×10^{-2}
Square duct	1.20×10^{-2}	1.20×10^{-2}	6.40	1.20×10^{-2}



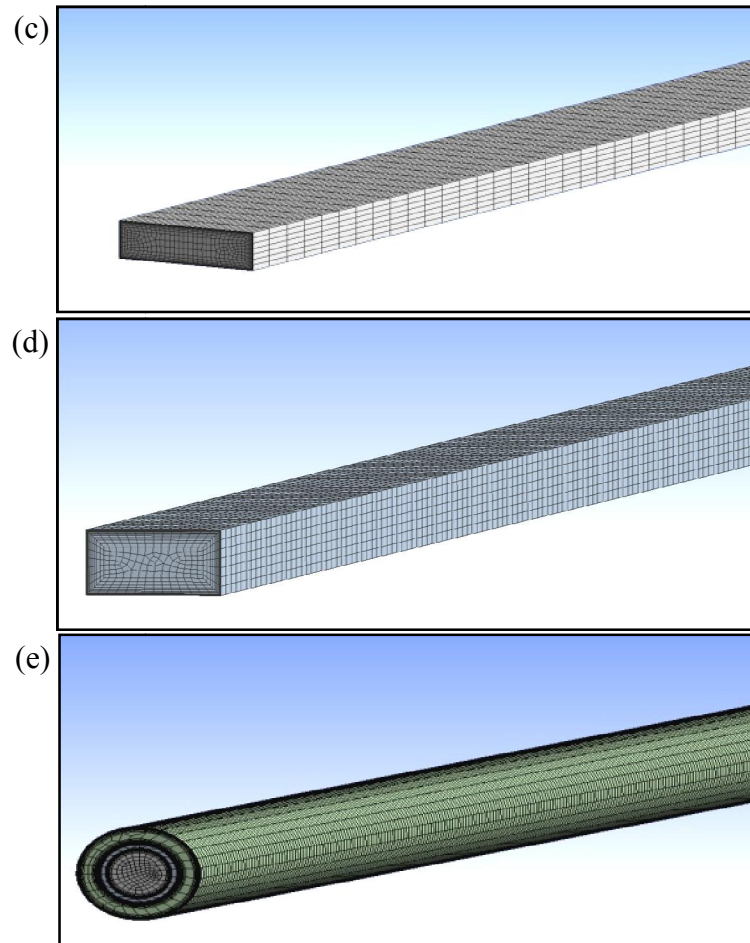


Figure 3.8: Computation grids for (a) circular, (b) square, (c) 4:1 rectangular, (d) 2:1 rectangular ducts, and (e) double pipe heat exchanger.

3.4.2 Meshing

For the meshing of circular and non-circular ducts, the proximity and curvature were selected for the use of advanced size function. The relevance centre was set to the fine option. High smoothing was on to improve the element quality. Slow transition was chosen to ensure a smooth transition from element to element. Inflation was utilized to resolve the near-wall boundary layers. The first layer thickness was used to determine the height of the first inflation layer. In addition, the sweep method was applied for the local sizing control with all quadrilaterals for the free face mesh type.

As for the meshing of the double pipe heat exchanger, the advanced size function of curvature was defined with the relevance center, smoothing and transition adjusted to

coarse, medium and slow, respectively. The near-wall boundary layer was improved through specifying the first layer thickness of the near-wall mesh under the inflation option. The number of mesh element for all the geometries was changed by varying the number of maximum layers and cells across the gap that they had.

3.4.3 Governing equations

In the numerical studies, the flow was assumed to be steady and incompressible. Furthermore, viscous dissipation of the thermal energy and natural convection were negligible. In addition, the duct was assumed to be smooth. The flow incorporated in this present research was laminar ($250 \leq Re \leq 2000$).

Generally, the simulations on nanofluid can be carried out using single-phase or two-phase models. The single-phase model considers the mixture of base fluid and nanoparticles to be a single homogeneous fluid. The nanoparticles are assumed to be well dispersed within the base fluid. Thus, they have the same temperature and velocity field. The single-phase approach is used for many investigations due to its simplicity (Heris et al. 2015; Zhao et al. 2016; Ahmad et al. 2017).

The Eulerian-Eulerian model can be utilized to model the flow of solid-liquid mixtures which have a high solid volume fraction. In the case of nanofluid, even if the nanoparticles are present in small volume fraction, the amount of nanoparticles in the computational domain is still considered to be extremely massive due to their small size (Akbari, Galanis, and Behzadmehr 2011). The popular Eulerian-Eulerian approaches are the volume of fluid (VOF), mixture and Eulerian models. In the two-phase modelling, the behaviour and properties of the nanoparticles and base fluid are considered separately. In this present research, the two-phase modelling was applied solely in the case of nanofluid.

3.4.3.1 Single-phase model

For the incompressible laminar single-phase flow, the governing equations for mass (or continuity), momentum and energy are expressed as follows:

$$\frac{\partial \rho}{\partial t} + \nabla \cdot (\rho \vec{v}) = 0 \quad (3.10)$$

$$\frac{\partial (\rho \vec{v})}{\partial t} + \nabla \cdot (\rho \vec{v} \vec{v}) = -\nabla P + \rho \vec{g} + \nabla \cdot (\bar{\tau}) \quad (3.11)$$

$$\frac{\partial (\rho E)}{\partial t} + \nabla \cdot (\vec{v}(\rho E + P)) = \nabla \cdot (k_{\text{eff}} \nabla T) \quad (3.12)$$

where ρ is the fluid density, t is the time, \vec{v} is the velocity, P is the static pressure, \vec{g} is the gravitational acceleration, $\bar{\tau}$ is the viscous stress tensor, E is the energy, k_{eff} is the effective thermal conductivity and T is the temperature. The terms with time would be reduced to zero for the steady state flow. The viscous stress tensor, $\bar{\tau}$ is given in Equation 3.13, where $\nabla \vec{v}^T$ is the transpose of the velocity gradient tensor. These governing equations were solved to obtain the fluid temperature and pressure drop along the duct. These data were then used to study the heat transfer and flow behaviour of the nanofluid, PAA and poly-nanofluid.

$$\bar{\tau} = \mu [(\nabla \vec{v} + \nabla \vec{v}^T)] \quad (3.13)$$

3.4.3.2 Two-phase mixture model

For the mixture model, different phases are modelled as fluids and they are considered to be interpenetrating continua. The coupling between the phases is assumed to be strong. Relative velocity is utilized to describe the dispersed phase. The continuity, momentum, and energy equations are solved for the mixture, while the volume fraction equation is solved for the secondary phase. The empirical correlations are used to calculate the relative velocity between the phases. The continuity equation of the mixture model is computed using Equation 3.14.

$$\frac{\partial}{\partial t} (\rho_m) + \nabla \cdot (\rho_m \vec{v}_m) = 0 \quad (3.14)$$

$$\vec{v}_m = \frac{\varphi_p \rho_p \vec{v}_p + \varphi_{bf} \rho_{bf} \vec{v}_{bf}}{\rho_m} \quad (3.15)$$

$$\rho_m = \varphi_p \rho_p + \varphi_{bf} \rho_{bf} \quad (3.16)$$

The subscripts m , p and bf refer to the mixture, nanoparticles and base fluid (water), respectively. φ stands for the volume fraction. The momentum equation for the mixture

model is expressed as the summation of individual momentum equations for all the phases.

$$\begin{aligned} \frac{\partial(\rho_m \vec{v}_m)}{\partial t} + \nabla \cdot (\rho_m \vec{v}_m \vec{v}_m) \\ = -\nabla P + \nabla \cdot [\mu_m (\nabla \vec{v}_m + \nabla \vec{v}_m^T)] + \rho_m \vec{g} \\ + \nabla \cdot (\varphi_{bf} \rho_{bf} \vec{v}_{dr,bf} \vec{v}_{dr,bf} + \varphi_p \rho_p \vec{v}_{dr,p} \vec{v}_{dr,p}) \end{aligned} \quad (3.17)$$

$$\mu_m = \varphi_p \mu_p + \varphi_{bf} \mu_{bf} \quad (3.18)$$

where μ_m is the viscosity of the mixture which equals to the viscosity of the base fluid (Goktepe, Atalik, and Erturk 2014). $\vec{v}_{dr,bf}$ and $\vec{v}_{dr,p}$ are the drift velocity of the base fluid and the nanoparticles, respectively. $\vec{v}_{dr,bf}$ and $\vec{v}_{dr,p}$ are described as:

$$\vec{v}_{dr,bf} = \vec{v}_{bf} - \vec{v}_m \quad (3.19)$$

$$\vec{v}_{dr,p} = \vec{v}_p - \vec{v}_m \quad (3.20)$$

The energy equation for the mixture is represented in Equation 3.21 as follows:

$$\begin{aligned} \frac{\partial}{\partial t} (\varphi_p \rho_p E_p + \varphi_{bf} \rho_{bf} E_{bf}) + \nabla \\ \cdot [(\varphi_p \vec{v}_p (\rho_p E_p + P)) + (\varphi_{bf} \vec{v}_{bf} (\rho_{bf} E_{bf} + P))] \\ = \nabla \cdot (k_{eff} \nabla T) \end{aligned} \quad (3.21)$$

$$E = h_e - \frac{P}{\rho} + \frac{v^2}{2} \quad (3.22)$$

$$k_{eff} = (\varphi_p (k_p + k_t)) + (\varphi_{bf} (k_{bf} + k_t)) \quad (3.23)$$

where h_e is the sensible enthalpy, and k_t is the turbulent thermal conductivity which is defined according to the turbulent model employed. The volume fraction equation for secondary phase p takes the following form:

$$\frac{\partial}{\partial t} (\varphi_p \rho_p) + \nabla \cdot (\varphi_p \rho_p \vec{v}_m) = -\nabla \cdot (\varphi_p \rho_p \vec{v}_{dr,p}) \quad (3.24)$$

The slip velocity, $\vec{v}_{p,bf}$ is the velocity of the secondary phase relative to that of the primary phase.

$$\vec{v}_{p,bf} = \vec{v}_p - \vec{v}_{bf} \quad (3.25)$$

The relationship between the drift velocity and the slip velocity is shown in Equation 3.26 below:

$$\vec{v}_{dr,p} = \vec{v}_{p,bf} - \left(\frac{\varphi_p \rho_p}{\rho_m} \vec{v}_{bf,p} \right) \quad (3.26)$$

Manninen, Taivassalo, and Kallio (1996)'s method is applied to obtain the slip velocity (Equation 3.27) while the drag formulation, f_{drag} is calculated through Schiller and Naumann (1935)'s correlation (Equation 3.28).

$$\vec{v}_{p,bf} = \frac{\rho_p d_p^2}{18 \mu_{bf} f_{drag}} \left(\frac{\rho_p - \rho_m}{\rho_p} \right) (\vec{g} - (\vec{v}_m \cdot \nabla) \vec{v}_m) \quad (3.27)$$

$$f_{drag} = \begin{cases} 1 + 0.15 Re^{0.687} & Re \leq 1000 \\ 0.0183 Re & Re > 1000 \end{cases} \quad (3.28)$$

where d_p is the diameter of the nanoparticles.

3.4.3.3 Two-phase Eulerian model

Similar to the mixture model, the Eulerian multiphase model considers the multiple separates as interacting phases. The conservative law of the continuity, momentum and energy are satisfied for each phase individually, but a single pressure field is estimated for all phases. The interaction between the phases is expressed in terms of the lift and drag forces. The sum of the volume fractions for all phases is equal to unity.

The mass, momentum and energy conservative equations for phase q are given in Equations 3.29, 3.30 and 3.31, respectively.

$$\frac{\partial}{\partial t} (\varphi_q \rho_q) + \nabla \cdot (\varphi_q \rho_q \vec{v}_q) = 0 \quad (3.29)$$

$$\begin{aligned} \frac{\partial (\varphi_q \rho_q \vec{v}_q)}{\partial t} + \nabla \cdot (\varphi_q \rho_q \vec{v}_q \vec{v}_q) \\ = -\varphi_q \nabla P + \nabla \cdot \bar{\tau}_q + \varphi_q \rho_q \vec{g} + \sum_{p=1}^n \vec{R}_{pq} + \vec{F}_{lift,q} \end{aligned} \quad (3.30)$$

$$\begin{aligned} \frac{\partial}{\partial t}(\varphi_q \rho_q h_q) + \nabla \cdot (\varphi_q \rho_q \vec{v}_q h_q) \\ = \varphi_q \frac{\partial(P_q)}{\partial t} - \bar{\tau}_q : \nabla \vec{v}_q - \nabla \cdot \bar{q}_q + \sum_{p=1}^n Q_{pq} \end{aligned} \quad (3.31)$$

where $\sum_{p=1}^n \vec{R}_{pq}$ is the phase interaction force, $\vec{F}_{lift,q}$ is the lift force, \bar{q}_q is the heat flux, and Q_{pq} is the intensity of heat exchange between the primary phase, q, and the secondary phase, p.

The phase interaction force, $\sum_{p=1}^n \vec{R}_{pq}$ is expressed as follows:

$$\sum_{p=1}^n \vec{R}_{pq} = \sum_{p=1}^n K_{pq} (\vec{v}_p - \vec{v}_q) \quad (3.32)$$

where K_{pq} is the interphase momentum exchange coefficient.

$$K_{pq} = \frac{\rho_p f}{6\tau_p} d_p A_i \quad (3.33)$$

$$\tau_p = \frac{\rho_p d_p^2}{18\mu_q} \quad (3.34)$$

$$A_i = \frac{6\varphi_p(1 - \varphi_p)}{d_p} \quad (3.35)$$

f is the drag friction, τ_p is the particulate relaxation time, d_p is the diameter of the nanoparticles, and A_i is the interfacial area concentration. The interfacial area concentration is the interfacial area between two phases per unit volume. Symmetric model as shown in Equation 3.35 ensures that when the volume fraction of phase p, φ_p approaches unity, the interfacial area concentration approaches zero. The drag friction is defined using Schiller and Naumann (1935)'s method (Equation 3.36).

$$f = \frac{C_D Re}{24} \quad (3.36)$$

$$C_D = \begin{cases} 24(1 + 0.15Re^{0.687})/Re & Re \leq 1000 \\ 0.44 & Re > 1000 \end{cases} \quad (3.37)$$

$$Re = \frac{\rho_q |\vec{v}_p - \vec{v}_q| d_p}{\mu_q} \quad (3.38)$$

where C_D is the drag coefficient and Re is the relative Reynolds number. The lift force acting on a particulate, $\vec{F}_{lift,q}$, is caused by the presence of velocity gradient in the primary phase flow and it can be determined from the Drew and Lahey (1993)'s equation as follows:

$$\vec{F}_{lift,q} = -0.5\rho_q\varphi_p(\vec{v}_q - \vec{v}_p) \times (\nabla \times \vec{v}_q) \quad (3.39)$$

The stress-strain tensor for phase q, $\bar{\tau}_q$ is demonstrated as:

$$\bar{\tau}_q = \varphi_q\mu_q \left[(\nabla\vec{v}_q + \nabla\vec{v}_q^T) \right] \quad (3.40)$$

The energy transfer between the phases, Q_{pq} is a function of temperature difference between the phases and the interfacial area.

$$Q_{pq} = h_{pq}A_i(T_p - T_q) \quad (3.41)$$

where h_{pq} is the volumetric heat transfer coefficient between phases p and q. It is related to the Nu_p (Nusselt number of phase p) and the k_q (thermal conductivity of phase q) through Equation 3.42. The correlation of Ranz and Marshall (1952) is used to compute the Nu_p .

$$h_{pq} = \frac{k_q Nu_p}{d_p} \quad (3.42)$$

$$Nu_p = 2.0 + 0.6Re_p^{1/2}Pr_q^{1/3} \quad (3.43)$$

where Re_p is the relative Reynolds number based on the relative velocity, $|\vec{v}_p - \vec{v}_q|$, and the diameter of phase p. The Prandtl number of phase q, Pr_q , can be predicted as:

$$Pr_q = \frac{c_{p,q}\mu_q}{k_q} \quad (3.44)$$

3.4.3.4 Two-phase VOF model

The VOF model solves a single set of momentum equation for two or more immiscible fluids and the resulting velocity is shared among the phases. Besides, the volume fraction of each phase is tracked throughout the studied domain. The momentum equation is related to the volume fraction of all phases through the density and viscosity. Similarly, a shared temperature is calculated and shared among the phases from a single energy equation. One limitation of this type of approximation is that the accuracy of the computed velocities (or temperatures) near the interface is low when there is a large velocity difference (or temperature difference) between the phases. In contrast, the mass conservation equation is different for each phase.

The momentum and energy equations for the VOF model are identical to those of the single-phase model, which are indicated in Equations 3.11 and 3.12, respectively. The mass conservative equation is described as:

$$\frac{\partial \rho}{\partial t} + \nabla \cdot (\varphi_q \rho_q \vec{v}_q) = 0 \quad (3.45)$$

The volume fraction equation is not solved for the primary phase, but it will be estimated based on the constraint that the summation of all the volume fractions is equal to unity (Equation 3.46).

$$\sum_{q=1}^n \varphi_q = 1 \quad (3.46)$$

All the physical properties are estimated using the weighted average values between the phases depending on their volume fraction throughout each control volume as shown in Equation 3.47.

$$N = \sum_{q=1}^n \varphi_q N_q \quad (3.47)$$

where N represents the physical property.

3.4.3.5 Viscoelastic property

PAA solution behaves viscoelastically in the non-circular ducts (Gupta, Metzner, and Hartnett 1967; Oliver and Karim 1971; Mena et al. 1978; Hartnett and Kostic 1985). The CEF, Reiner-Rivlin, PTT and FENE-P models can represent the mechanical fluid behaviour of the PAA solution in the non-circular ducts. The CEF and Reiner-Rivlin models are simpler compared to the PTT and FENE-P models as their number of dependent variables are only limited to the pressure and velocity components. Nonetheless, the PTT constitutive relation can be applied for a wide class of flows which is not true for the CEF and Reiner-Rivlin equations. Besides its simplicity, the CEF model was chosen because it can model the viscoelastic property of PAA solution accurately (Payvar 1997; Norouzi, Kayhani, and Nobari 2009).

The stress tensor, $\bar{\tau}$ in Equation 3.11 was decomposed into two terms (Naccache and Mendes 1996); namely, a Newtonian-like term, $\eta(\dot{\gamma})\underline{\dot{\gamma}}$ and a polymeric term, $\bar{\tau}^P$. The latter was resolved using the second and third terms of the CEF constitutive equation as denoted in Equation 3.52.

$$\bar{\tau} = \eta(\dot{\gamma})\underline{\dot{\gamma}} + \bar{\tau}^P \quad (3.48)$$

$$\underline{\dot{\gamma}} = \nabla v + (\nabla v)^T \quad (3.49)$$

$$\dot{\gamma} = \sqrt{(1/2) \text{tr } \dot{\gamma}^2} \quad (3.50)$$

$$\dot{\gamma} = \left[2 \left(\frac{\partial u}{\partial x} \right)^2 + 2 \left(\frac{\partial v}{\partial y} \right)^2 + 2 \left(\frac{\partial w}{\partial z} \right)^2 + \left(\frac{\partial u}{\partial y} + \frac{\partial v}{\partial x} \right)^2 + \left(\frac{\partial u}{\partial z} + \frac{\partial w}{\partial x} \right)^2 + \left(\frac{\partial v}{\partial z} + \frac{\partial w}{\partial y} \right)^2 \right]^{1/2} \quad (3.51)$$

$$\bar{\tau} = \eta(\dot{\gamma})\underline{\dot{\gamma}} - \frac{1}{2}\psi_1(\dot{\gamma})\frac{\Delta}{\dot{\gamma}_2} + \psi_2(\dot{\gamma})\underline{\dot{\gamma}}^2 \quad (3.52)$$

$$\frac{\Delta}{\dot{\gamma}_2} = \frac{d\dot{\gamma}}{dt} - \left[(\nabla v)^T \cdot \underline{\dot{\gamma}} + \underline{\dot{\gamma}} \cdot (\nabla v) \right] \quad (3.53)$$

$$\frac{N_1}{|\tau|} = 14(1-n)(1+6n)^{-1} \quad (3.54)$$

$$n = \frac{d \log \tau}{d \log \dot{\gamma}} \quad (3.55)$$

$$K = 10^{(\log \tau - n \log \dot{\gamma})} \quad (3.56)$$

$$N_1 = \bar{\tau}_{11} - \bar{\tau}_{22} = \psi_1 \dot{\gamma}^2 \quad (3.57)$$

$$N_2 = \bar{\tau}_{22} - \bar{\tau}_{33} = \psi_2 \dot{\gamma}^2 \quad (3.58)$$

$\underline{\dot{\gamma}}$ is the rate-of-deformation tensor, $\eta(\dot{\gamma})$ is the viscosity function, ∇v is the velocity gradient, $(\nabla v)^T$ is the transpose of the velocity gradient, and $\underline{\dot{\gamma}_2}$ is the second rate-of-deformation tensor. The scalar rate-of-deformation tensor, $\dot{\gamma}$ is given in Equations 3.50 and 3.51. Besides, n is the power law exponent (or slope of the flow curve), K is the consistency index, N_1 is the first normal stress difference, N_2 is the second normal stress difference, ψ_1 is the first normal stress coefficient, and ψ_2 is the second normal stress coefficient. The first normal stress difference of the polymeric solution, N_1 is dependent on the shear stress. It can be determined from the general equation of the flow curve as expressed in Equation 3.54 (Steller 2016). According to Bird, Armstrong, and Hassager (1987), the second normal stress coefficient for the PAA solution is in the range of $-0.20\psi_1 < \psi_2 < -0.01\psi_1$. In this present study, the value of the second normal stress coefficient was such that $\psi_2 = -0.10\psi_1$ (Gervang and Larsen 1991; Bschorer and Brunn 1996; Syrjala 1998).

The components of the second and third terms of the CEF equation appear as expressions in the source term in the general transport equation. Under the steady state condition, the second term is demonstrated by (Gervang 1989):

$$\begin{aligned} \frac{1}{2} \psi_1 \Delta_{\dot{\gamma}_{ij}} = \frac{1}{2} \psi_1 \left\{ v(k) \left[\frac{\partial^2 v(i)}{\partial x_k \partial x_j} + \frac{\partial^2 v(j)}{\partial x_k \partial x_i} \right] + 2 \frac{\partial v(k)}{\partial x_j} \frac{\partial v(k)}{\partial x_i} \right. \\ \left. + \frac{\partial v(k)}{\partial x_i} \frac{\partial v(j)}{\partial x_k} + \frac{\partial v(k)}{\partial x_j} \frac{\partial v(i)}{\partial x_k} \right\} \end{aligned} \quad (3.59)$$

where $i, j,$ and k can be 1, 2, or 3. The $x_1, x_2,$ and x_3 denote the $x, y,$ and z direction, respectively. For the velocity part, the $v(1), v(2),$ and $v(3)$ refer to the velocity values in $x, y,$ and z direction, respectively. The triangle superscript represents the upper-convected derivative. The third term of the CEF equation is given by (Gervang 1989):

$$\psi_2\{\dot{\gamma}_{ik}\dot{\gamma}_{kj}\} = \psi_2\left\{\frac{\partial v(k)}{\partial x_j}\frac{\partial v(i)}{\partial x_k} + \frac{\partial v(i)}{\partial x_k}\frac{\partial v(j)}{\partial x_k} + \frac{\partial v(k)}{\partial x_j}\frac{\partial v(k)}{\partial x_i} + \frac{\partial v(k)}{\partial x_i}\frac{\partial v(j)}{\partial x_k}\right\} \quad (3.60)$$

The complete form of the components of the extra stress tensor is outlined in Appendix B. Three assumptions were made to establish the expression of the terms in the extra stress tensor. Firstly, the secondary flow velocity components and their derivatives were notably smaller in comparison to the axial velocity and its derivatives. This assumption was based on a statement highlighted by several researchers (Xue, Thien, and Tanner 1995; Payvar 1997) that the secondary flows were weak until the point where they found it hard to measure directly. Secondly, the derivatives of the velocity components in the axial direction were neglected as the hydrodynamic entrance length was expected to be short. Lastly, the viscoelastic property of polymer solution was determined substantially by the second normal stress difference regardless of the magnitude of the first normal stress difference. Hence, the effect of the first normal stress difference was insignificant. The stress tensor was simplified to Equations 3.61 to 3.65, as subjected to the three assumptions made in this analysis. These equations were written and inserted for the simulations as user-defined functions (UDFs). The UDFs is shown in Appendix C.

$$\bar{\tau}_{11} = 2\eta\frac{\partial u}{\partial x} + \psi_2\left(\frac{\partial w}{\partial x}\frac{\partial w}{\partial x}\right) \quad (3.61)$$

$$\bar{\tau}_{12} = \bar{\tau}_{21} = \eta\left(\frac{\partial u}{\partial y} + \frac{\partial v}{\partial x}\right) + \psi_2\left(\frac{\partial w}{\partial x}\frac{\partial w}{\partial y}\right) \quad (3.62)$$

$$\bar{\tau}_{13} = \bar{\tau}_{31} = \eta\left(\frac{\partial w}{\partial x}\right) \quad (3.63)$$

$$\bar{\tau}_{22} = 2\eta\frac{\partial v}{\partial y} + \psi_2\left(\frac{\partial w}{\partial y}\frac{\partial w}{\partial y}\right) \quad (3.64)$$

$$\bar{\tau}_{23} = \bar{\tau}_{32} = \eta\left(\frac{\partial w}{\partial y}\right) \quad (3.65)$$

3.4.4 Thermo-physical properties

The thermo-physical properties are important in order to model or predict the behaviour of the test fluids (nanofluid, PAA solution and poly-nanofluid) accurately. The thermo-

physical properties include the density (ρ), viscosity (μ), thermal conductivity (k), and heat capacity (C_p). Both temperature-independent and temperature-dependent properties for water and nanofluid were considered in this present study. For PAA solution and poly-nanofluid, only the temperature-dependent properties were employed.

3.4.4.1 Water

Water was the base fluid. The temperature-independent thermo-physical properties of the base fluid are presented in Table 3.7 (Bianco et al. 2009). In the case of temperature-dependent properties, their values were obtained from Perry Handbook (Green and Perry 2008), the Handbook of Chemistry and Physics (Haynes 2015), and the book of Introduction to Heat Transfer by Incropera and Dewitt (1996). These temperature-dependent properties are tabulated in Table 3.8 for the temperature range of 293.15 – 353.15 K. In the simulation using temperature-dependent approach, the thermo-physical properties of water, \emptyset were defined as polynomial function of temperature, as given in Equation 3.66. The coefficients in Equation 3.66, were obtained by curve fitting method. The resulting curve fitting equations were shown in Figure 3.9. In each case, y is the property and x is the temperature in Kelvin.

$$\emptyset(T) = A_1 + A_2T + A_3T^2 + \dots \quad (3.66)$$

Table 3.7: Temperature-independent thermo-physical properties of water used.

Thermo-physical properties	
ρ_{bf} (kg/m ³)	998.2
$C_{p_{bf}}$ (J/kg K)	4182
k_{bf} (W/m K)	0.597
μ_{bf} (Pa s)	9.93×10^{-4}

Table 3.8: Temperature-dependent properties of water.

Temperature (K)	ρ (kg/m ³)	C_p (J/kg K)	k (W/m K)	$\mu \times 10^4$ (Pa s)
293.15	998.2	4181.8	0.598	10.00
303.15	995.6	4178.4	0.615	7.97
313.15	992.2	4178.5	0.631	6.53
323.15	988.0	4180.6	0.644	5.47
333.15	983.2	4184.3	0.654	4.66
343.15	977.8	4189.5	0.663	4.04
353.15	971.8	4196.3	0.670	3.54

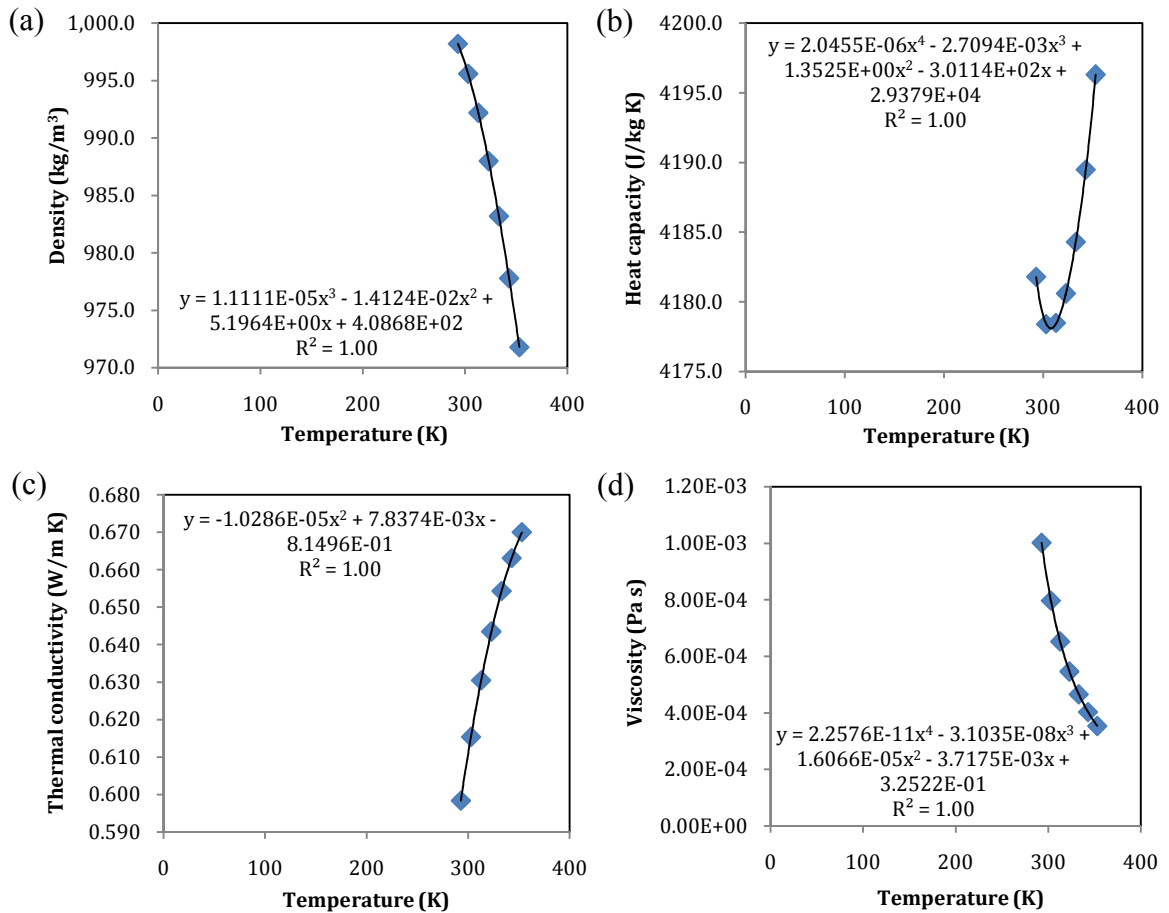


Figure 3.9: (a) Density, (b) heat capacity, (c) thermal conductivity, and (d) viscosity of water with the fitted trendline for each case.

3.4.4.2 Al_2O_3 nanofluid

The nanoparticles considered in this study were 47 nm Al_2O_3 nanoparticles. The nanoparticle loadings utilized for the simulation were 0.01, 0.09, 0.13, 0.25, 0.51, 1.00 and 4.00 vol%. The conversion between weight and volume fraction of nanofluid can be completed through Equation 3.67 (Pak and Cho 1998; Rea et al. 2009; Teng et al. 2011; Ghanbarpour, Haghigi, and Khodabandeh 2014).

For the single-phase modelling, the temperature-independent values of nanofluid density and heat capacity were approximated based on Equations 3.68 and 3.69, respectively (Bianco et al. 2009; Kumar and Ganesan 2012). Besides, the thermal conductivity and viscosity of the nanofluid were estimated using the empirical formulas shown in

Equations 3.70 and 3.71 (Pak and Cho 1998; Kumar and Ganesan 2012; Yang, Li and Nakayama 2013).

$$\varphi = \frac{w_w \rho_{bf}}{\rho_p(1 - w_w) + w_w \rho_{bf}} \quad (3.67)$$

$$\rho_{nf} = \varphi \rho_p + (1 - \varphi) \rho_{bf} \quad (3.68)$$

$$C_{p_{nf}} = \varphi C_{p_p} + (1 - \varphi) C_{p_{bf}} \quad (3.69)$$

$$k_{nf} = k_{bf}(1 + 7.47\varphi) \quad (3.70)$$

$$\mu_{nf} = \mu_{bf}(1 + 39.11\varphi + 533.9\varphi^2) \quad (3.71)$$

where w_w is the weight fraction and the subscript nf refers to the nanofluid. The properties of Al_2O_3 nanoparticles utilized in the calculations are tabulated in Table 3.9 (Sundar and Sharma 2010; Kumar and Ganesan 2012; Sonawane, Khedkar, and Wasewar 2013). The predicted temperature-independent properties of nanofluid using Equations 3.68 to 3.71 are presented in Table 3.10.

Table 3.9: Thermo-physical properties of the nanoparticles used in this study.

Thermo-physical properties		
ρ_p	(kg/m ³)	3970
C_{p_p}	(J/kg K)	880
k_p	(W/m K)	36
μ_p	(Pa s)	-

Table 3.10: Temperature-independent thermo-physical properties of nanofluid.

Nanofluid volume percent (vol%)	Nanofluid weight percent (wt%)	ρ (kg/m ³)	C_p (J/kg K)	k (W/m K)	$\mu \times 10^4$ (Pa s)
0.01	0.05	998.6	4181.6	0.598	9.98
0.09	0.35	1000.8	4179.1	0.601	10.28
0.10	0.40	1001.2	4178.7	0.601	10.33
0.13	0.50	1002.0	4177.8	0.603	10.43
0.25	1.00	1005.7	4173.6	0.608	10.95
0.51	2.00	1013.4	4165.1	0.620	12.05
1.00	4.00	1029.0	4147.8	0.643	14.53
4.00	16.60	1117.1	4049.9	0.775	33.95

The effect of temperature on the thermal conductivity and viscosity of nanofluid was computed using Equations 3.72 (Rea et al. 2009; Azari, Kalbasi, and Rahimi 2014) and 3.73 (Meybodi et al. 2016), respectively. Although Equations 3.68 and 3.69 are not a function of temperature, the temperature-dependent density and heat capacity of nanofluid were estimated by using the temperature-dependent density and heat capacity of the base fluid. The density and heat capacity of the nanoparticles were considered to be temperature-independent. Since the nanoparticle concentration studied was small, the variation of their density and heat capacity with temperature was considered to be negligible when compared to the variation of the same properties of water with temperature. In addition, the density and heat capacity of solid particles do not really vary with temperature.

$$k(\varphi, T) = k_{bf}(T)(1 + 4.5503\varphi) \quad (3.72)$$

$$\mu_{nf} = \mu_{bf} \times \frac{E_1 + E_2 \exp\left(\frac{\varphi}{s}\right) + E_3 \left(\exp\left(\frac{\varphi}{s}\right)\right)^2 + E_4 \left(\exp\left(\frac{\varphi}{s}\right)\right)^3}{E_5 + E_6 \frac{\ln(s)}{T} + E_7 \frac{(\ln(s))^2}{T}} \quad (3.73)$$

where for Equation 3.73, s represents the nanoparticle size in nm, temperature is in Kelvin, φ is in %, and the coefficients (Meybodi et al. 2016) are given in Table 3.11.

Similar to water, the polynomial function of temperature was chosen to model the temperature-dependent properties of nanofluid. The polynomial equations for the properties would be different for different nanofluid concentration. These polynomial functions were used for the single-phase modelling of nanofluid under the temperature-dependent approach. On the other hand, only the thermo-physical properties of nanoparticles listed in Table 3.9 were required for the two-phase modelling.

Table 3.11: Coefficients for Equation 3.73.

E_1	:	1.30×10^2
E_2	:	-3.44×10^2
E_3	:	2.90×10^2
E_4	:	-7.90×10^1
E_5	:	9.12×10^{-1}
E_6	:	3.23×10^1
E_7	:	-1.17×10^1

3.4.4.3 PAA solution

The concentrations of the PAA solution investigated were 10, 50, 200 and 1000 ppm. The thermo-physical properties of PAA solution except viscosity were taken to be the same as the values of water. The influence of PAA additives on the density, thermal-conductivity and heat capacity of water was negligible as PAA concentration considered was small (Hartnett and Kostic 1985).

The viscosity of PAA solution was estimated using non-Newtonian Carreau model as shown in equation below:

$$\frac{\eta(\dot{\gamma}) - \eta_{\infty}}{\eta_o - \eta_{\infty}} = \frac{1}{[1 + (\lambda\dot{\gamma})^2]^{(n')/2}} \quad (3.74)$$

where η_{∞} is the infinite-rate viscosity, η_o is the zero-rate viscosity, λ is the characteristic time, and n' is the rate index. The parameters of the Carreau model were obtained from the rheology studies. As mentioned, PAA solution behaves to be viscoelastic in the non-circular ducts (Gupta, Metzner, and Hartnett 1967; Oliver and Karim 1971; Mena et al. 1978; Hartnett and Kostic 1985). The viscoelastic property was modelled using the CEF equation described in Section 3.4.3.5. In contrast, PAA solution behaves like a purely viscous fluid in the circular duct (including the double pipe heat exchanger) (Cho and Harnett 1982; Hartnett 1992; Kostic 1994). Therefore, the CEF equation was not used for the modelling of PAA solution in the circular duct. The Carreau model was enough to describe their purely viscous behaviour.

3.4.4.4 Poly-nanofluid

The concentrations of poly-nanofluid considered were 10, 50, 200 and 1000 ppm PAA in 0.13, 0.51, 1.00 and 4.00 vol% Al₂O₃ nanofluid, respectively. The same thermo-physical properties of nanofluid were applied for the poly-nanofluid except for the viscosity. It was believed that the influence of PAA additives on the density, heat capacity and thermal conductivity of nanofluid could be neglected since their concentration in nanofluid was small (Liu and Liao 2010).

The results from the rheology measurement indicate that the addition of PAA additives changes the rheology behaviour of nanofluid. Poly-nanofluid has similar rheology behaviour as PAA solution (the details are discussed in Chapter 4). Therefore, the viscosity of poly-nanofluid was modelled in a similar way as that of PAA solution. Besides, poly-nanofluid was predicted to be viscoelastic in the non-circular ducts and this viscoelastic property was also computed in the same way as that of PAA solution.

3.4.5 Boundary conditions

The boundary condition set for the circular and non-circular ducts was similar. Uniform velocity profile and temperature of 293.15 K prevailed at the duct inlet. The direction of the flow was normal to the boundary. In the case of temperature-dependent properties, the density and viscosity values for the Reynolds number calculation were taken with reference to the inlet temperature. The outflow boundary condition was adopted for duct outlet. No slip boundary condition was imposed along the periphery of the duct. Moreover, heat transfer under both circumferential and axial constant heat flux (also known as H2) boundary condition was prescribed in this present study. The constant heat flux of 1000 W/m^2 was applied at the wall boundary. For the rectangular and square ducts, all the four walls were heated for the H2 boundary condition.

As for the double pipe heat exchanger, the test fluid (nanofluid, PAA solution or poly-nanofluid) flowed in the tube side while water flowed in the annuli. The flow in the annulus was fixed to be 5 L/min. The test fluid and water entered the domain boundary from different directions (counter-current flow) with uniform velocity profile. The flow was also normal to the boundary. The working temperatures of the solution in the tube side were 313.15, 318.15 and 323.15 K. Water served as the cooling fluid, entering the annuli at room temperature. The pressure outlet boundary condition was applied at the outlet boundary as this was recommended by ANSYS for heat transfer modelling in two separate fluid regions. No slip boundary condition was enforced at the tube and annulus walls. The outer annulus wall was insulated.

For the two-phase modelling using the mixture and Eulerian models, the inlet velocities of the nanoparticles and base fluid were defined to be the same (Goktepe, Atalik, and

Erturk 2014). In contrast, only the velocity of the mixture of nanoparticles and the base fluid was required for the VOF model. In addition, the volume fraction of the nanoparticles was specified as input for the two-phase simulations.

3.4.6 Numerical solution strategy

The CFD solver ANSYS FLUENT 15.0 was employed to solve the governing equations along with the inlet and boundary conditions iteratively. FLUENT works based on a finite volume approach. The finite volume method consists of three main stages. The first one is the domain discretization into finite set of control volumes (mesh). The second stage is the discretization of governing equations on each control volume to yield algebraic equations for the discrete dependent variables. Lastly, the discretized equations are linearized and solved numerically (*Ansys Fluent 15.0 User's Guide* 2013).

Double precision solver was activated to balance the rate of heat transfer in the computational domain. Pressure-based solver was selected for the simulation instead of density-based solver because this study only considered incompressible flow. The density-based solver is generally used to model the compressible flow. The two formulations under the pressure-based solver are the coupled and segregated algorithms (shown in Appendix D Figure D.1).

The details of solution strategy for the simulations are listed in Appendix E (Table E.1 to Table E.5). The segregated algorithm was selected for all the simulations except for the two-phase nanofluid modelling because the memory requirement for the coupled algorithm was 1.5–2 times greater than the segregated solver (*Ansys Fluent 15.0 User's Guide* 2013). Nonetheless, the coupled algorithm was more preferable in the two-phase nanofluid analysis as this algorithm improved the stability and convergence speed of the multiphase modelling considerably compared to the segregated algorithm.

The Semi Implicit Method for Pressure Linked Equations (SIMPLE) algorithm was adopted to resolve the pressure velocity coupling in single phase simulation. For the mixture and VOF models, the coupled scheme was implemented, while it was the phase coupled SIMPLE scheme used for the Eulerian model. Moreover, the least square cell

based gradient was applied as the gradient spatial discretization scheme for all the simulation. It is suitable for any type of mesh and less expensive to compute over the node-based method (*Ansys Fluent 15.0 User's Guide* 2013).

The pressure interpolation schemes available in the pressure-based solver are Standard, Second order, Linear, Pressure Staggering Option (PRESTO), and Body-force-weighted schemes. The pressure term of the single-phase modelling was approximated by the second order scheme. It has improved accuracy over the Standard and Linear schemes. As for the Body-force-weighted scheme, it is accurate for the situation with huge body forces. Besides, PRESTO is more useful for the mixture or VOF multiphase models as well as for the flow with high swirl numbers, natural convection or high-speed rotating flow (*Ansys Fluent 15.0 Theory Guide* 2013). Therefore, PRESTO was used for the multiphase nanofluid modelling.

The available discretization schemes include the first order, second order, Quadratic Upwind Interpolation for Convective Kinetics (QUICK), third-order Monotonic Upstream-Centred Scheme for Conservation Laws (MUSCL) and power law. The second order upwind scheme was adopted for all the discretization of the momentum and energy terms. The second order upwind is more accurate than the first order upwind scheme. The power law scheme yields similar accuracy as the first order scheme (*Ansys Fluent 15.0 Theory Guide* 2013). In this present study, the second order upwind scheme was sufficient because the QUICK and third-order MUSCL could not contribute to the substantial improvement in the accuracy. The QUICK and third-order MUSCL could give better accuracy for the rotating or swirling flow, which was not the case for this study. Furthermore, for the multiphase modelling, the first order scheme was used for the discretization of the volume fraction term.

The under-relaxation factors utilized to control the update of the computed variables at each iteration were set at their default values. These default values are given in Appendix E (Table E.6 to Table E.13). However, the courant number under the mixture and VOF models was reduced from its default value of 200 to 4, so that the stability of the solution could be increased and the fluctuation in the residual values reduced (*Ansys Fluent 15.0 Theory Guide* 2013). The convergence criterion was based on the residual

values set for each governing equation and calculated variable. The residual values were set as 10^{-6} for all the variables. The solution was considered as converged when the sum of normalized residuals of all the equations and variables were lower than the set residual value. Moreover, the mass imbalance was monitored as another convergence indicator. The net mass imbalance should be less than 1% of the inlet mass flux through the computational domain.

3.4.7 Grid independence study

Grid independence study was performed to obtain the optimum mesh size without compromising the accuracy of the simulation results. The number of mesh element was varied to study its effect on the Nusselt number and friction factor.

The Nusselt number and friction factor of water reach a constant value beyond a certain number of mesh elements. Beyond this, the increment in mesh element does not further improve the Nusselt number and friction factor, but it only increases the computation time. The percentage variations of the Nusselt number and friction factor from the chosen grid for all the geometries are calculated. From Figure 3.10, it can be deduced that for the circular pipe, the percentage variations of the Nusselt number and friction factor from the chosen grid gradually decrease as the number of mesh element approaches the mesh size of the chosen grid. The Nusselt number and friction factor variations for mesh size greater than the chosen grid are within $\pm 0.50\%$, which is very small. Therefore, it can be concluded that the meshes have reached their grid independence. Similar remarks are made for the other geometries and their percentage variations of the Nusselt number and friction factor from the chosen grid were displayed in Appendix F (Figure F.1 to Figure F.4).

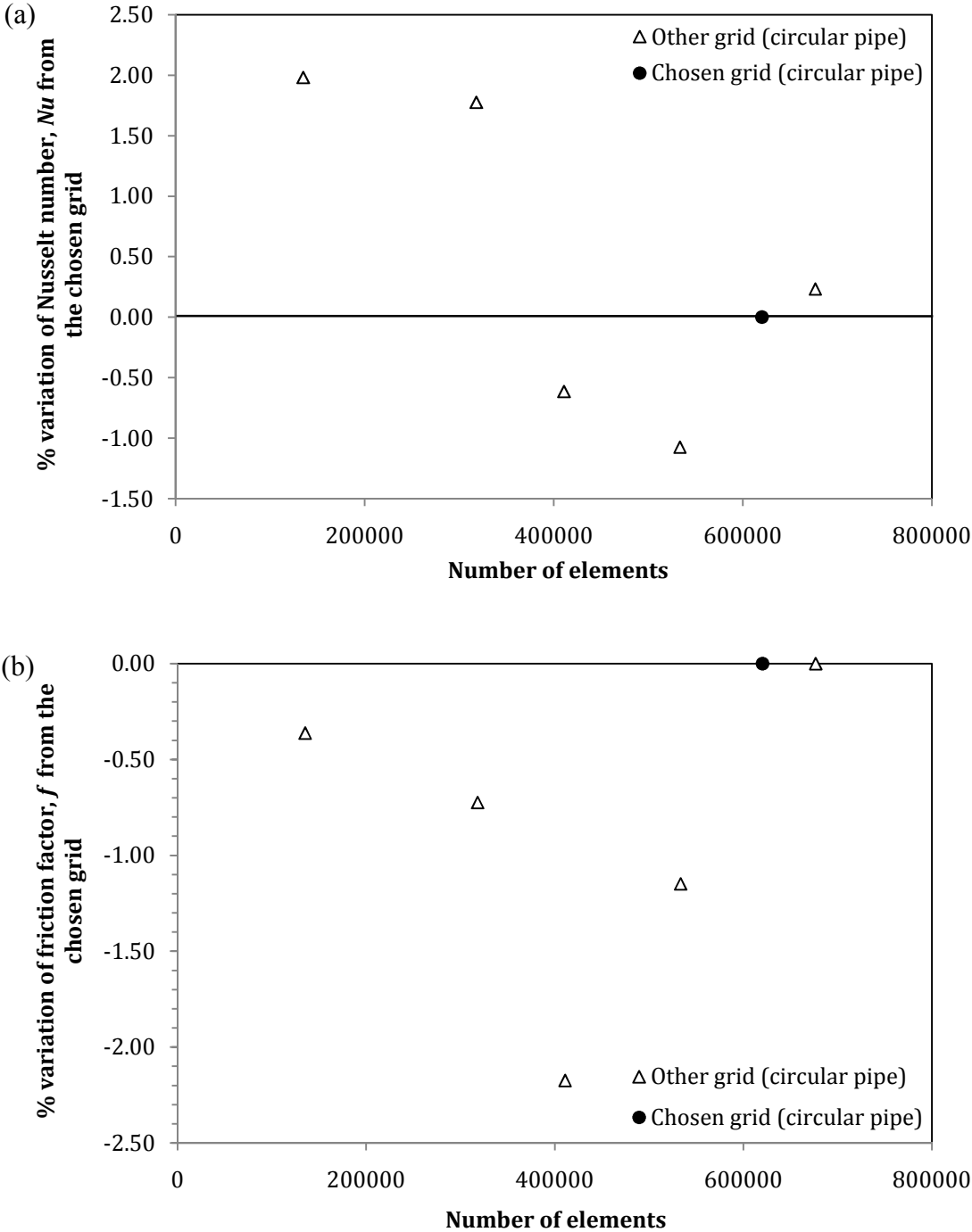


Figure 3.10: Variations of (a) Nusselt number and (b) friction factor of the grids from the chosen grid (%) for circular pipe.

Mesh quality also plays a crucial role in determining the accuracy and stability of the simulation. Skewness and orthogonal quality are part of the main quality measures for a mesh. Skewness is a measure of how close a face or cell is to the shape of an equilateral or quad cell of the same volume. A skewness value close to 1 means the cell is highly degenerated while a value of 0 indicates an equilateral cell. Highly skewed cells can lead to high inaccuracy in the simulation results. Orthogonal quality is calculated using the face normal vectors (\vec{A}), the vectors from the cell centroid to the centroid of the adjacent faces (\vec{f}), and the vectors from the cell centroid to the centroid of the adjacent cells (\vec{c}) as displayed in Figure 3.11. The range of orthogonal quality is from 0 to 1, where the best cells will have a value close to 1.

The mesh quality in terms of average skewness and orthogonal quality for the grid independent meshes are presented in Table 3.12. For all the geometries, the cell quality is good as the average skewness is between 0 to 0.3, while the average orthogonal quality is close to 1.

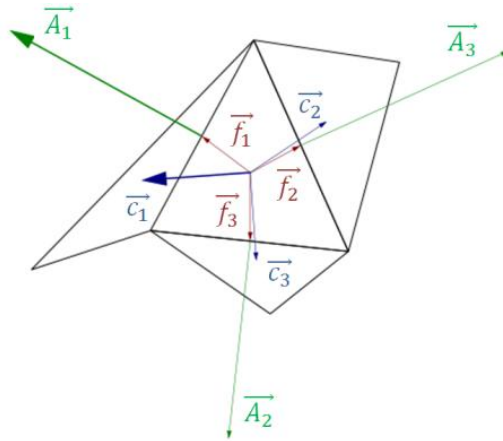


Figure 3.11: Vectors used to compute the orthogonal quality
(Ansys Fluent 15.0 User's Guide 2013).

Table 3.12: Mesh quality of different geometries.

Geometry	Average skewness	Average orthogonal quality
Circular pipe	0.1107	0.9831
Square duct	0.2651	0.8847
4:1 rectangular duct	0.2377	0.9049
2:1 rectangular duct	0.2734	0.8871
Double pipe heat exchanger	0.1095	0.9623

3.5 Data reduction

The average heat transfer coefficient, h_{av} and Nusselt number, Nu_{av} were calculated to examine the heat transfer characteristic of the test fluids. The average heat transfer coefficient is defined as:

$$h_{av} = \frac{q''}{T_w - T_b} \quad (3.75)$$

$$T_b = \frac{T_o + T_i}{2} \quad (3.76)$$

where q'' is the heat flux, T_w is the wall temperature, T_b is the bulk temperature, T_o is the outlet temperature, and T_i is the inlet temperature. The average Nusselt number is calculated using Equation 3.77.

$$Nu_{av} = \frac{h_{av} \cdot D_h}{k} \quad (3.77)$$

$$D_h = \frac{4A_c}{p} \quad (3.78)$$

where D_h is the hydraulic diameter, A_c is the cross-sectional area and p is the wetted perimeter of the cross-section. For the double pipe heat exchanger, the heat transfer rate, Q and the overall heat transfer coefficient, U are also computed.

$$Q = mC_p(T_o - T_i) \quad (3.79)$$

$$Q = UA_t\Delta T_{LMTD} \quad (3.80)$$

$$A_t = \pi d_o l \quad (3.81)$$

$$\Delta T_{LMTD} = \frac{[(T_{h,i} - T_{c,o}) - (T_{h,o} - T_{c,i})]}{\ln[(T_{h,i} - T_{c,o}) / (T_{h,o} - T_{c,i})]} \quad (3.82)$$

$$U = \frac{1}{\frac{1}{h_s} + \frac{1}{h_{od}} + \frac{d_o}{d_i h_{id}} + \frac{d_o}{d_i h_i} + \frac{d_o \ln(d_o/d_i)}{2k_w}} \quad (3.83)$$

where m is the mass flow rate, A_t is the total heat transfer area, l is the channel length, ΔT_{LMTD} is the logarithmic mean temperature difference, $T_{h,i}$ is the hot inlet temperature, $T_{h,o}$ is the hot outlet temperature, $T_{c,i}$ is the cold inlet temperature, and $T_{c,o}$ is the cold outlet temperature. Besides, h_s is the outside fluid film coefficient, h_i is the inside fluid

film coefficient, h_{od} is the outside dirt coefficient, h_{id} is the inside dirt coefficient, k_w is the thermal conductivity of the material for tube wall, d_o is the tube outer diameter, and d_i is the tube inner diameter. The enhancement in the average heat transfer coefficient, average Nusselt number and average overall heat transfer coefficient for the test fluids are given in Equations 3.84, 3.85 and 3.86, respectively.

$$h \text{ enhancement} = \left(\frac{(h_{av})_{tf} - (h_{av})_{bf}}{(h_{av})_{bf}} \right) \times 100\% \quad (3.84)$$

$$Nu \text{ enhancement} = \left(\frac{(Nu_{av})_{tf} - (Nu_{av})_{bf}}{(Nu_{av})_{bf}} \right) \times 100\% \quad (3.85)$$

$$U \text{ enhancement} = \left(\frac{U_{tf} - U_{bf}}{U_{bf}} \right) \times 100\% \quad (3.86)$$

where the subscript tf refers to the test fluid.

The Darcy friction factor, f can be estimated using Equations 3.87 and 3.88.

$$f = \frac{2\Delta P D_h}{\rho v^2 l} \quad (3.87)$$

$$f = \frac{8\tau_w}{\rho v^2} \quad (3.88)$$

$$\Delta P = P_{in} - P_{out} \quad (3.89)$$

where ΔP is the pressure drop and τ_w is the wall shear stress. The pressure drop and wall shear stress increment can be predicted using Equations 3.90 and 3.91, respectively. In addition, the thermal-hydraulic efficiency, η is estimated using Equation 3.92 (Mashaie, Hosseinalipour, and Bahiraei 2012; Mashaie, Hosseinalipour, and Muslmani 2014; Heris et al. 2015).

$$\Delta P \text{ increment} = \left(\frac{(\Delta P)_{tf} - (\Delta P)_{bf}}{(\Delta P)_{bf}} \right) \times 100\% \quad (3.90)$$

$$\tau_w \text{ increment} = \left(\frac{(\tau_w)_{tf} - (\tau_w)_{bf}}{(\tau_w)_{bf}} \right) \times 100\% \quad (3.91)$$

$$\eta = \frac{(h_{av})_{tf}/(h_{av})_{bf}}{((\Delta P)_{tf}/(\Delta P)_{bf})^{1/3}} \quad (3.92)$$

The Reynolds number, Re is demonstrated in the equation below:

$$Re = \frac{\rho v D_h}{\mu} \tag{3.93}$$

For non-Newtonian fluids like PAA solution and poly-nanofluid, the generalized Reynolds number is estimated using Equations 3.94 and 3.95 (Hartnett and Kostic 1985) for the circular and non-circular ducts, respectively.

$$Re' = \rho v^{2-n} D_h^n / \left[8^{n-1} K \left(\frac{3n+1}{4n} \right)^n \right] \tag{3.94}$$

$$Re^* = \rho v^{2-n} D_h^n / \left[8^{n-1} K \left(\frac{a+bn}{n} \right)^n \right] \tag{3.95}$$

where n and K are calculated using Equations 3.55 and 3.56, respectively. The constants a and b are dependent on the type of geometry as shown in Table 3.13 (Hartnett and Kostic 1985). In Chapters 4 to 8, the Reynolds number mentioned for PAA solution and poly-nanofluid refers to the generalized Reynolds number.

In the present numerical study, velocity is taken as the mass-weighted average value while the wall temperature, wall shear stress and shear rate is estimated as the area-weighted average value (Tokit, Yusoff, and Mohammed 2013).

Table 3.13: Value of constants in Equation 3.95.

Aspect ratio	0.25	0.50	1.0
a	0.3212	0.2440	0.2121
b	0.8182	0.7276	0.6766

CHAPTER 4: RHEOLOGICAL STUDY

4.1 Introduction

The rheological studies are performed to achieve the first objective of this research, which is to understand the effect of PAA additives on the rheological behaviour of Al_2O_3 nanofluid. This chapter discusses about the rheology of PAA solution and poly-nanofluid. Furthermore, the results of curve fitting for PAA solution and poly-nanofluid are also presented.

4.2 Rheology of PAA solution

Figure 4.1 illustrates the viscosity versus shear rate curve for 10, 200 and 1000 ppm PAA solution at 298.15 K. It can be clearly seen that the PAA solution shows a non-Newtonian shear-thinning behaviour. As the shear rate increases, the viscosity of the solution decreases. The shear-thinning behaviour of the PAA solution is perceived by other researchers as well (Xie and Hartnett 1992; Shin and Cho 1993, 1998). Moreover, it can also be observed that the viscosity of the solution increases with the increasing concentration.

According to Figure 4.2, the viscosity of 1000 ppm PAA solution decreases at a higher temperature. This is attributed to the decreased shear stress as the temperature increases (Yang 2001). Besides, when the temperature is raised, the energy level of molecules in the PAA solution increases, leading to an increment in the distance between the molecules. As a result, the intermolecular force decreases and this reduces the viscosity of the solution (Barnes, Hutton, and Walters 1989).

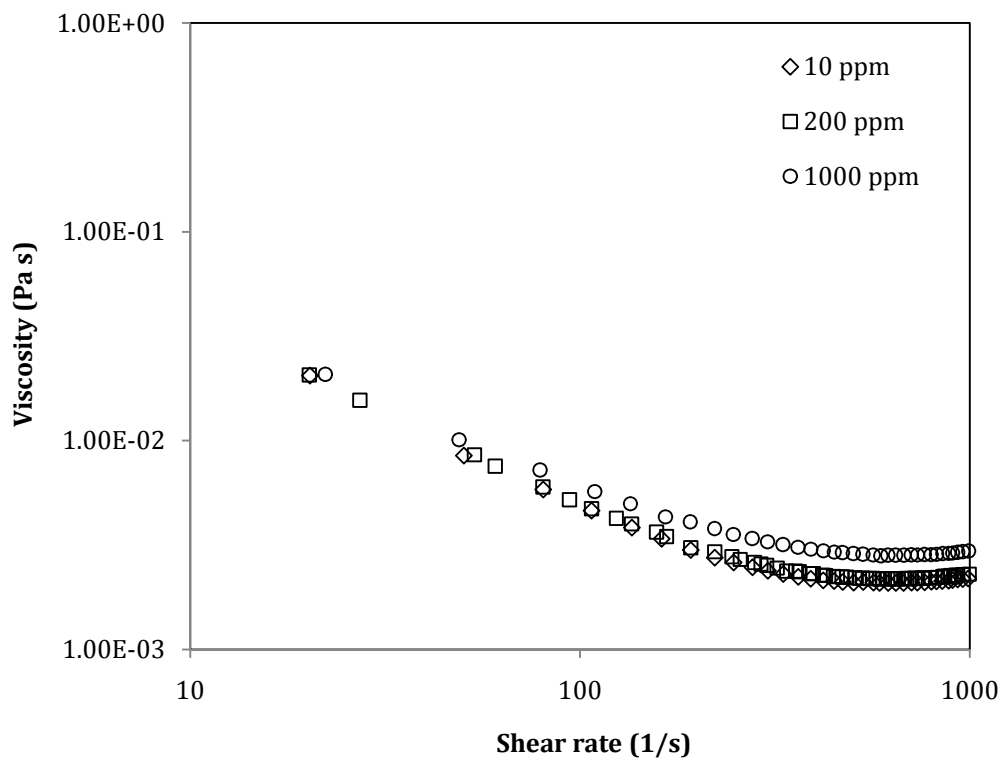


Figure 4.1: Viscosity of PAA solution at 298.15 K.

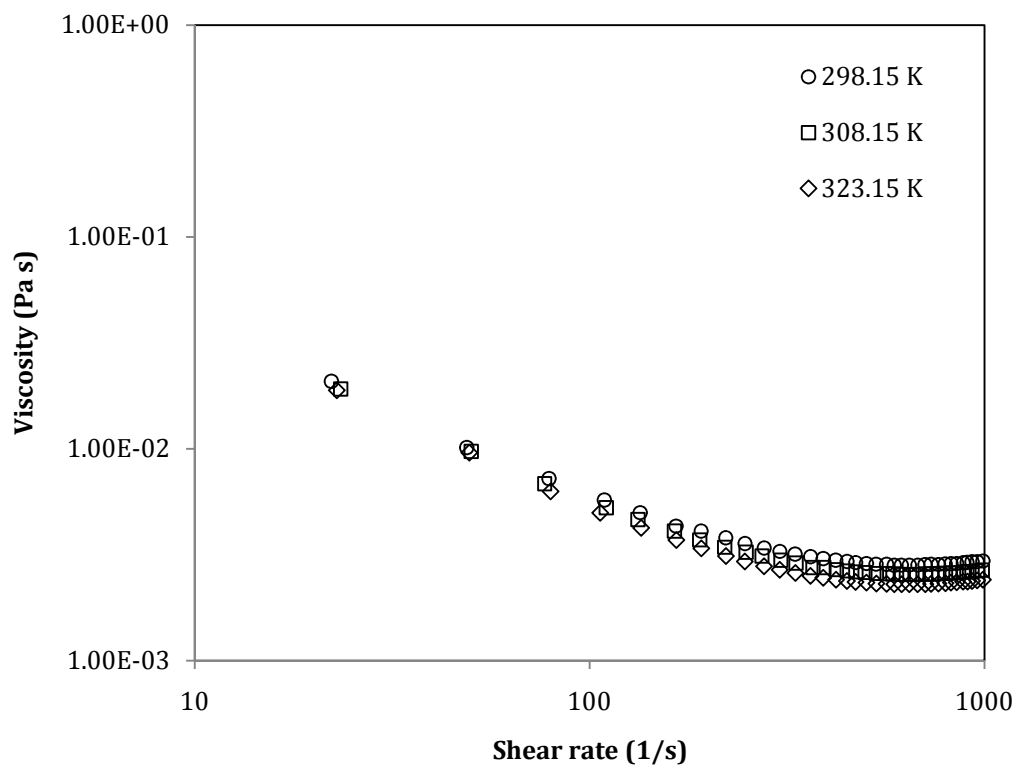


Figure 4.2: Viscosity of 1000 ppm PAA solution.

4.3 Rheology of poly-nanofluid

The rheological behaviour of the nanofluid changes when the PAA additive is dissolved in it. Instead of being Newtonian like the nanofluid (Chandrasekar, Suresh, and Bose 2010; Sundar et al. 2013), the poly-nanofluid manifests a non-Newtonian shear-thinning characteristic like the pure polymer solution (Figure 4.3). When the concentration of the PAA additives or/and Al_2O_3 nanofluid in the poly-nanofluid increase, the viscosity increases. Increasing the nanoparticle loading in the poly-nanofluid with higher PAA concentration results in more significant viscosity increment when compared to that of poly-nanofluid with low PAA concentration. For example, the average viscosity of 10 ppm PAA in 4% nanofluid is solely 3.4% higher than that of 10 ppm PAA in 0.13% nanofluid. Nonetheless, the average viscosity of 1000 ppm PAA in 4% Al_2O_3 nanofluid is approximately 83% larger than that of 1000 ppm PAA in 0.13% nanofluid. In addition, it can be seen from Figure 4.4 that the viscosity of the poly-nanofluid is higher than that of the pure PAA solution, especially for the poly-nanofluid with high nanoparticle loading.

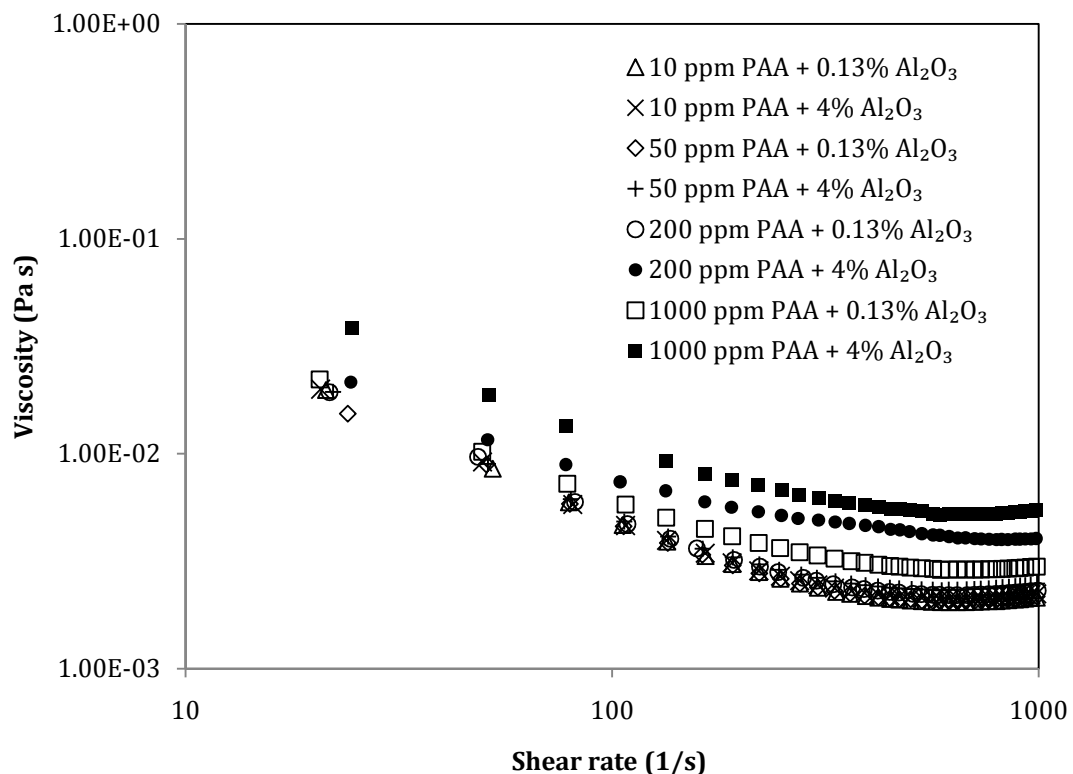


Figure 4.3: Viscosity of poly-nanofluid at 298.15 K.

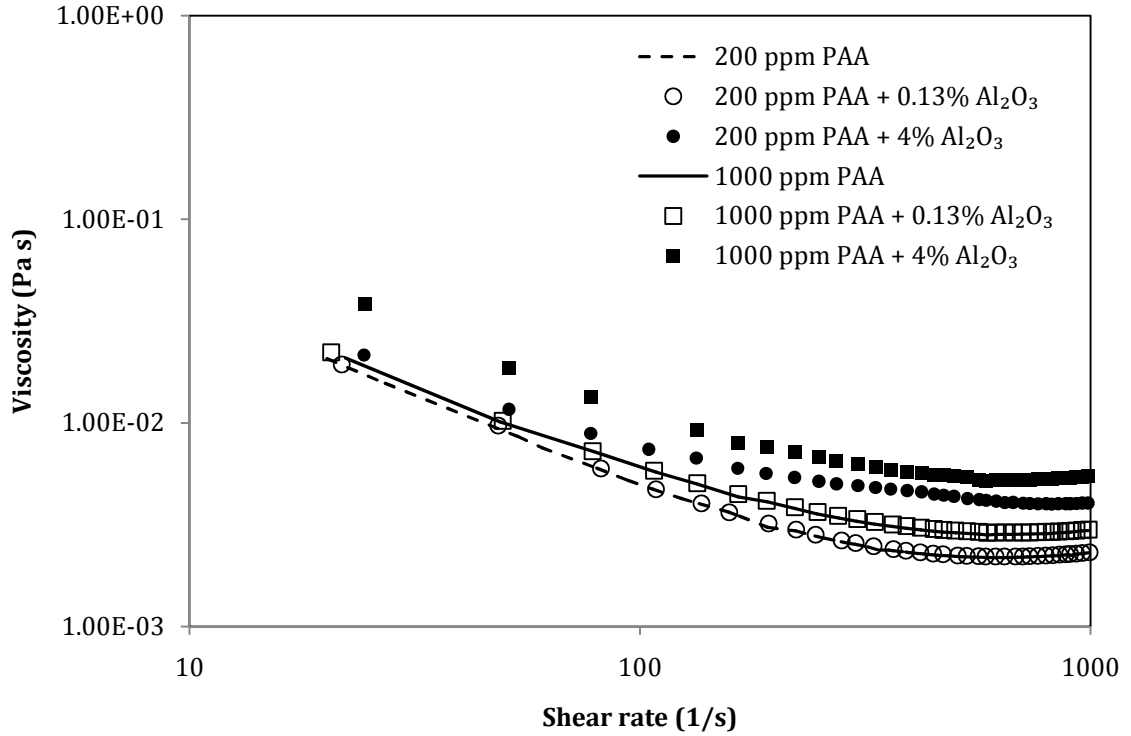


Figure 4.4: Comparison of the viscosity of PAA solution and poly-nanofluid at 298.15 K.

It is clear from Figure 4.4 that the rheological behaviour of PAA does not change when it is added into the nanofluid. Therefore, it is appropriate to model the rheology of the poly-nanofluid in the same manner as PAA solution for the numerical studies.

4.4 Curve fitting for PAA solution and poly-nanofluid

The viscosity of the aqueous PAA solution and poly-nanofluid are well-fitted with the Carreau model for all the concentration and temperature ranges considered, as shown in Figure 4.5. The parameters in the Carreau model (Equation 3.74) such as the infinite-rate viscosity (η_∞), zero-rate viscosity (η_o), characteristic time (λ) and rate index (n') were obtained from the rheometer. Their values vary with temperature. Therefore, each of these parameters was curve fitted as a function of temperature and they can be expressed as follows:

$$\eta_\infty = A_1 + A_2 \left(\frac{1}{T}\right) + A_3 \left(\frac{1}{T}\right)^2 + A_4 \left(\frac{1}{T}\right)^3 \quad (4.1)$$

$$\eta_o = B_1 \exp^{[B_2(1/T)]} \quad (4.2)$$

$$\lambda = C_1 + C_2 \left(\frac{1}{T}\right) + C_3 \left(\frac{1}{T}\right)^2 + C_4 \left(\frac{1}{T}\right)^3 \quad (4.3)$$

$$n' = D_1 + D_2 \left(\frac{1}{T}\right) + D_3 \left(\frac{1}{T}\right)^2 + D_4 \left(\frac{1}{T}\right)^3 \quad (4.4)$$

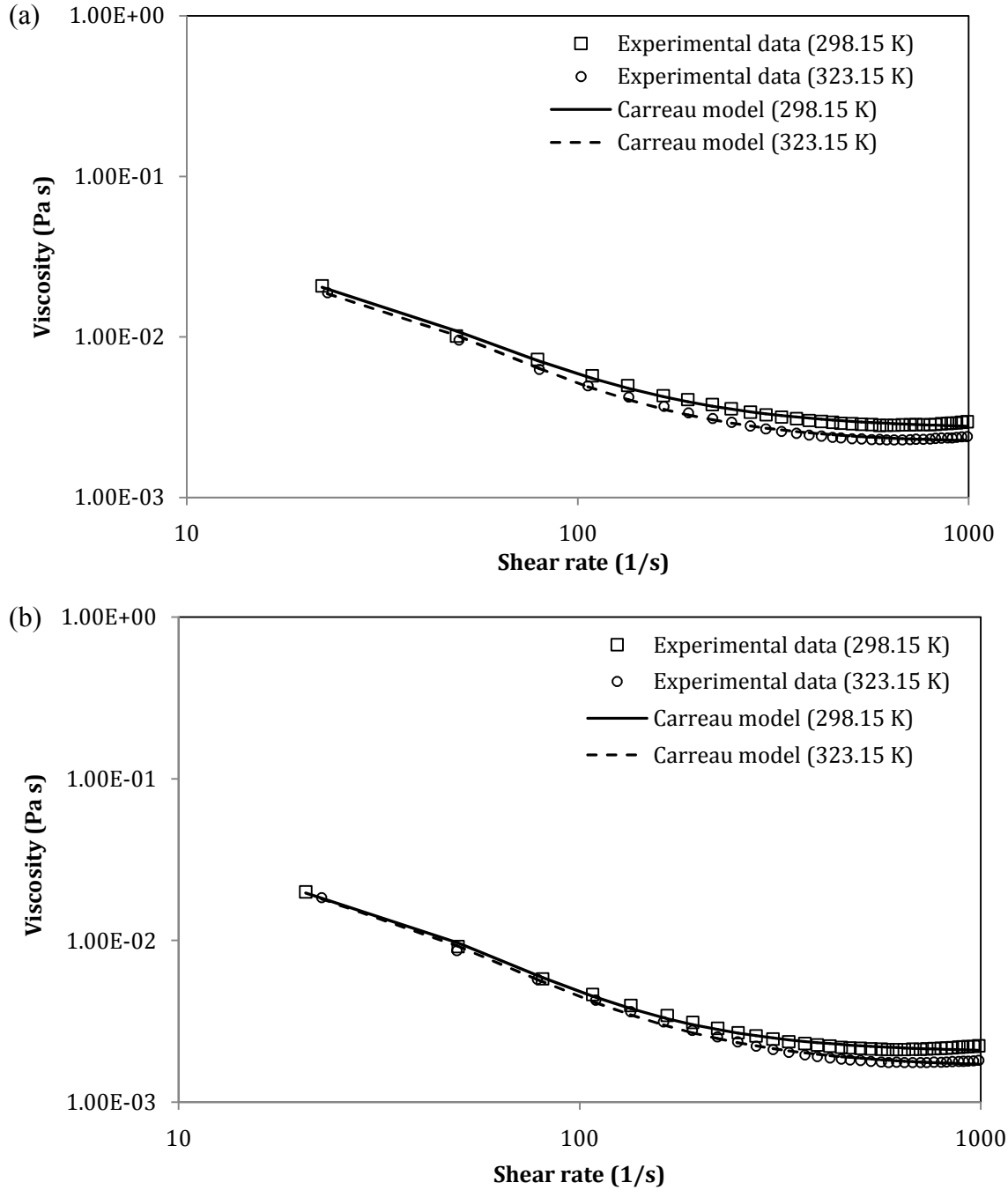


Figure 4.5: Comparison of the viscosity obtained from the experiments with that of the Carreau model for (a) 1000 ppm PAA and (b) 10 ppm PAA in 4% Al₂O₃ nanofluid.

The values of the constants in Equations 4.1 to 4.4 for different solutions are given in Appendix G (Table G.1 to Table G.4). Equations 4.1 to 4.4 are valid for $0/s \leq \dot{\gamma} \leq 1000/s$ and $298.15 \text{ K} \leq T \leq 323.15 \text{ K}$. The experimental viscosity value is plotted against the predicted value from Equations 4.1 to 4.4 in Figure 4.6 for two types of solutions. From this figure, the fit and the estimation of the parameters are accurate enough with the errors less than $\pm 10\%$. This good agreement suggests that Equations 4.1 to 4.4 can reasonably approximate the viscosity of the PAA solution and poly-nanofluid.

Moreover, the shear stress of the PAA solution and poly-nanofluid can be written in terms of the shear rate as:

$$\tau = a + b(\log \dot{\gamma}) + c(\log \dot{\gamma})^2 + d(\log \dot{\gamma})^3 \quad (4.5)$$

$$a = a_o + a_1T + a_2T^2 \quad (4.6)$$

$$b = b_o + b_1T + b_2T^2 \quad (4.7)$$

$$c = c_o + c_1T + c_2T^2 \quad (4.8)$$

$$d = d_o + d_1T + d_2T^2 \quad (4.9)$$

Equations 4.5 to 4.9 are also valid for $0/s \leq \dot{\gamma} \leq 1000/s$ and $298.15 \text{ K} \leq T \leq 323.15 \text{ K}$. The constants for a , b , c and d were obtained by using curve fitting method. These constants are given in Appendix G Table G.5, Table G.6, Table G.7 and Table G.8, respectively. Equation 4.5 is used to calculate the power law exponent, n in Equation 3.55. In addition, the first normal stress coefficient, ψ_1 is estimated from Equations 3.54 and 3.57. It can be represented as a function of shear rate as seen below:

$$\psi_1 = e(\dot{\gamma}^f) \quad (4.10)$$

The constants for Equation 4.10 were also obtained through curve fitting method and they are tabulated in Appendix G (Table G.9). Equation 4.10 is valid for $0/s \leq \dot{\gamma} \leq 600/s$. Although the viscosity of the PAA solution and poly-nanofluid are functions of shear rate and temperature, the first normal stress coefficient for both of the solutions is merely the decreasing function of shear rate. This is because there is no significant change in the first normal stress coefficient when the temperature changes, as depicted in Figure 4.7.

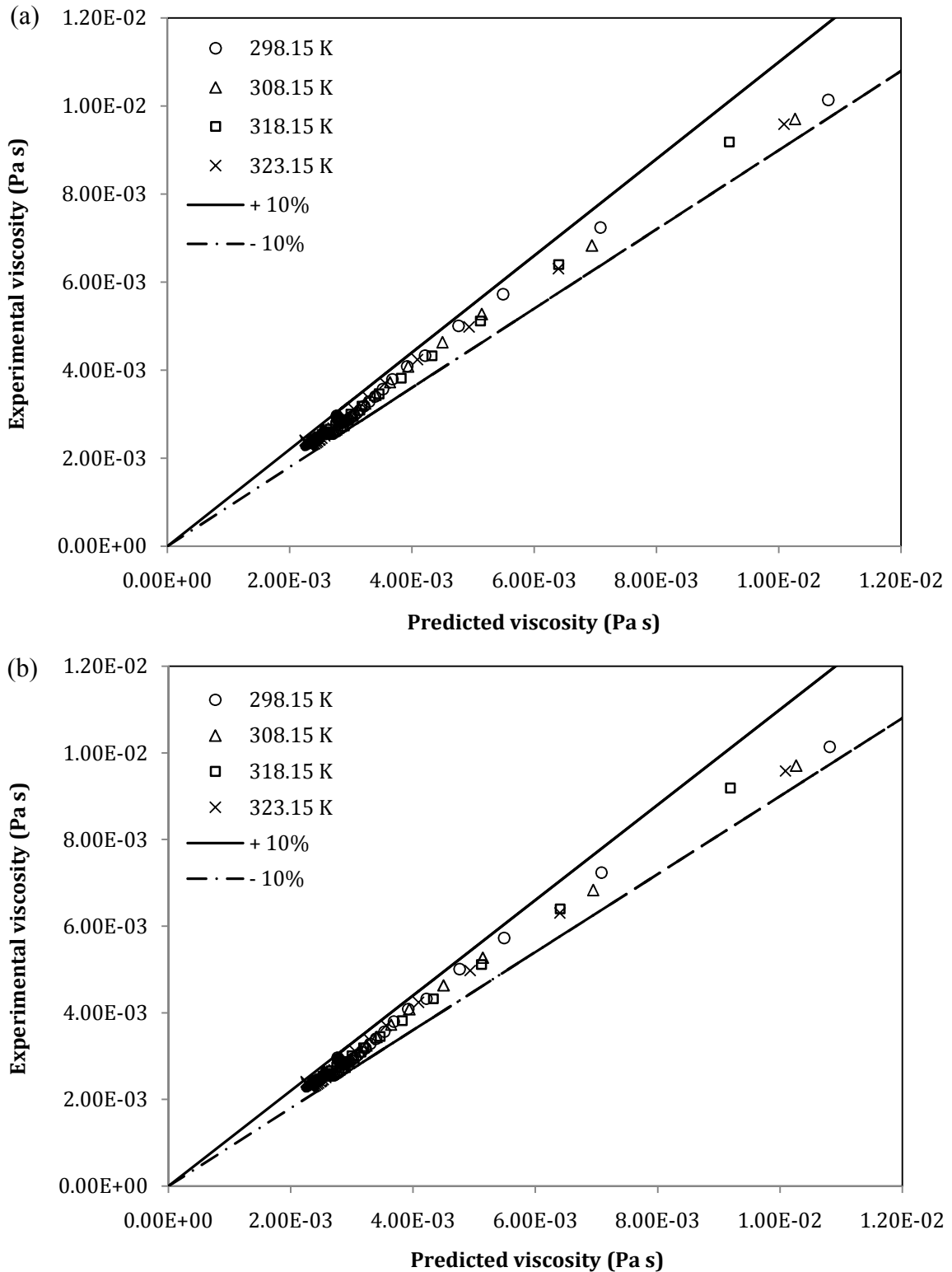


Figure 4.6: Comparison between experimental viscosity and predicted viscosity from Carreau model using Equations 4.1 to 4.4 for (a) 1000 ppm PAA and (b) 10 ppm PAA in 4% nanofluid.

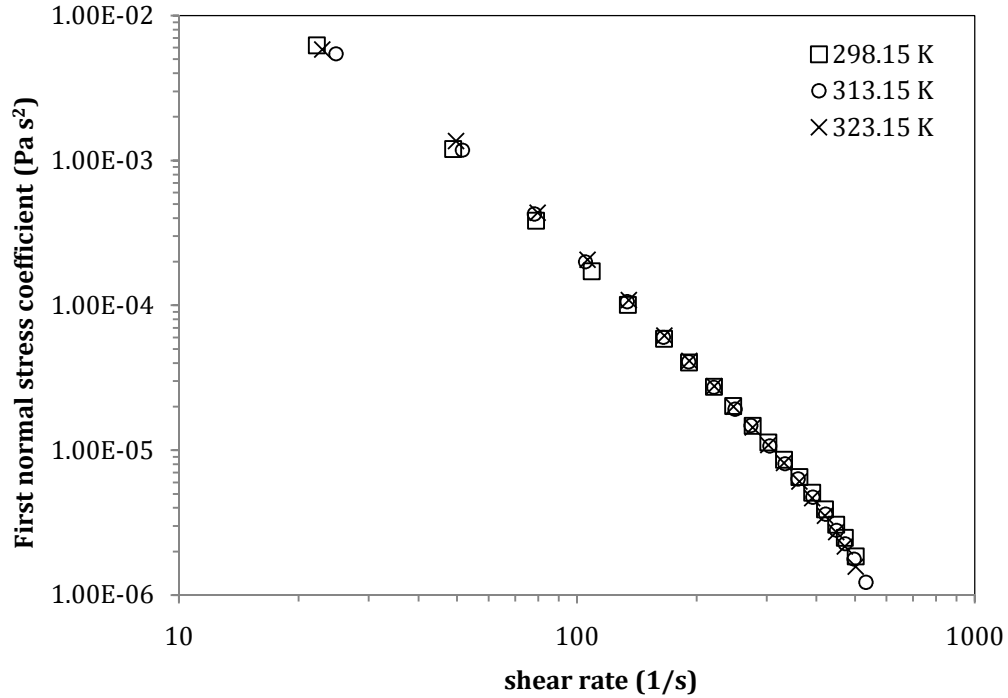


Figure 4.7: First normal stress coefficient of 1000 ppm PAA solution.

The estimated first normal stress coefficient is applied for the simulations of PAA solution and poly-nanofluid under the heat transfer and flow studies.

4.5 Summary

From the rheological investigation, the following findings are observed:

1. PAA solution is found to be non-Newtonian shear-thinning.
2. When PAA is added into the nanofluid, the rheology of nanofluid changes from Newtonian to non-Newtonian shear-thinning.
 - The rheology of poly-nanofluid resembles the behaviour of pure PAA solution.
 - Increment in the nanoparticle loading or/and PAA concentration in the poly-nanofluid increase the viscosity of the solution to be higher than that of the pure PAA solution.
3. The viscosity of the PAA solution and poly-nanofluid which are functions of shear rate and temperature are well described using the Carreau model.
4. The first normal stress coefficients for both of the solutions is found to be a decreasing function of shear rate.

CHAPTER 5: HEAT TRANSFER PERFORMANCE OF NANOFLUID, POLYMER AND POLY-NANOFLUID

5.1 Introduction

The heat transfer performance of nanofluid, PAA solution and poly-nanofluid is evaluated using the overall heat transfer coefficient for the double pipe heat exchanger, as well as the heat transfer coefficient and Nusselt number for the circular and non-circular ducts. This chapter starts with the validation of numerical heat transfer results of the solutions against the results from experiments or existing literature. Following that is the examination of the heat transfer performance of nanofluid in different geometries using both single and two-phase (mixture, Eulerian and VOF) approaches. The heat transfer results between these two approaches are discussed and compared in this chapter. Besides, the heat transfer behaviour of PAA solution and poly-nanofluid in different ducts are also presented. The heat transfer results for poly-nanofluid are only obtained using the single-phase modelling. Moreover, the effect of PAA additives on the heat transfer characteristic of nanofluid is assessed. Correlations are proposed to predict the Nusselt number of poly-nanofluid in the circular and non-circular ducts.

5.2 Result validation

5.2.1 Water

Before initiating the heat transfer experiments using nanofluid, polymer and poly-nanofluid, the accuracy and reliability of the experimental result was examined using water as the working fluid. The experimental overall heat transfer coefficient, U was calculated through Equation 3.80 using the temperatures measured in the experiment. It was then compared with the analytical value predicted from Equation 3.83. The numerical heat transfer result of water in the double pipe heat exchanger was also validated against the experimental result and analytical value. The comparison is shown in Figure 5.1, with error bars of 10% presented for the experimental data.

A close agreement between the experimental results and the analytical values of water at different hot inlet temperatures is noticed from Figure 5.1. For all the hot inlet temperatures studied, the deviation of the experimental results from the analytical values is less than 10%. It is also observed that the numerical heat transfer results compare well with the experimental and analytical values. The deviations are all within 10%.

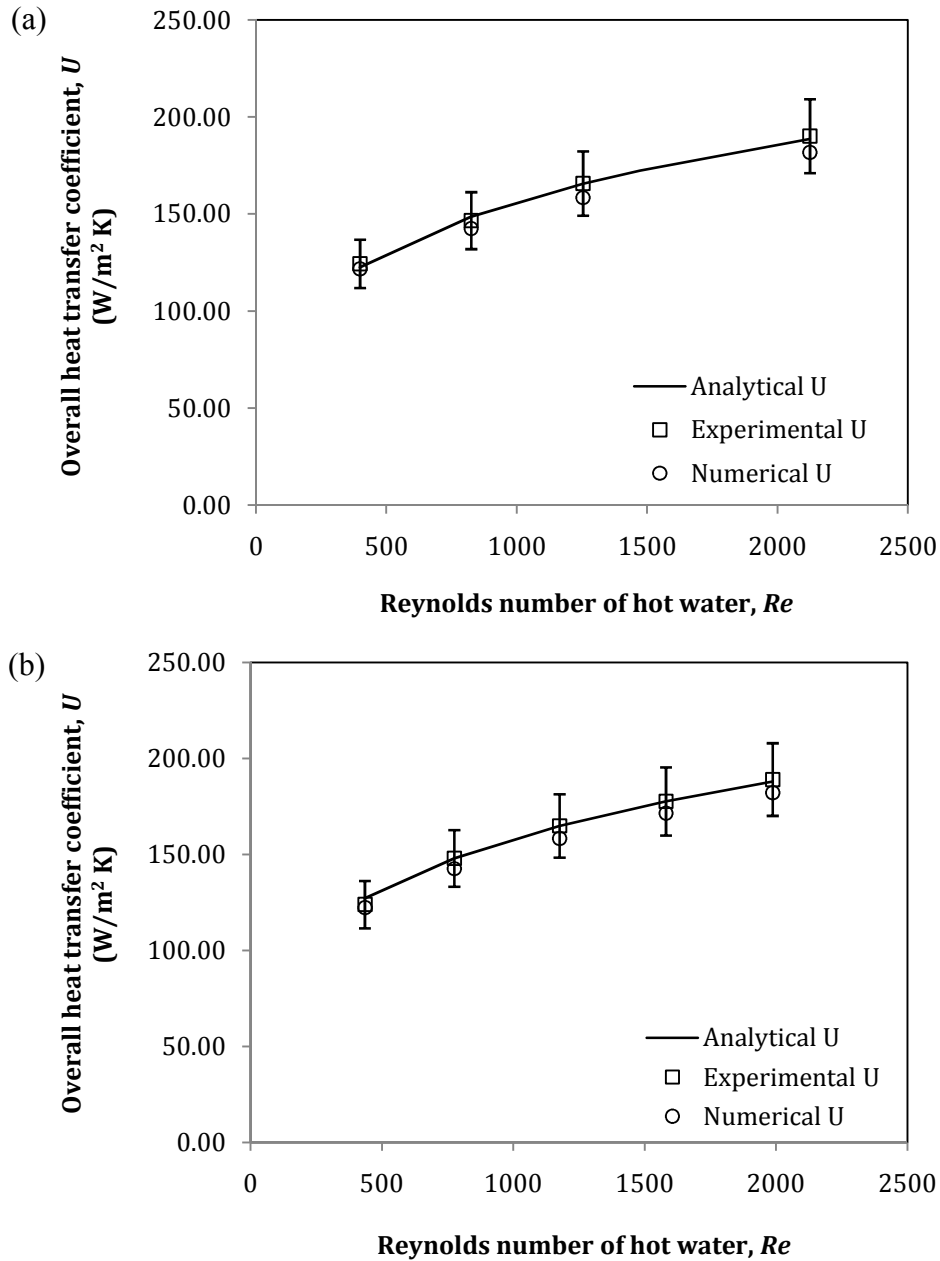


Figure 5.1: Overall heat transfer coefficient of water in double pipe heat exchanger at hot inlet temperatures of (a) 313.15 K and (b) 323.15 K.

On the other hand, the laminar Nusselt number of water in the circular and non-circular ducts was compared with the theoretical Nusselt number (Shah and London 1971) for the H2 boundary condition. It can be noted from Table 5.1 that the numerical Nusselt number of water for different geometries is in good agreement with the theoretical value in both the cases of temperature-independent and temperature-dependent properties. The Nusselt number deviations are within 3% for all the ducts studied. Therefore, the numerical model is accurate to be used.

Table 5.1: Comparison of numerical Nu_{H2} of water with the theoretical value ($Re=250$).

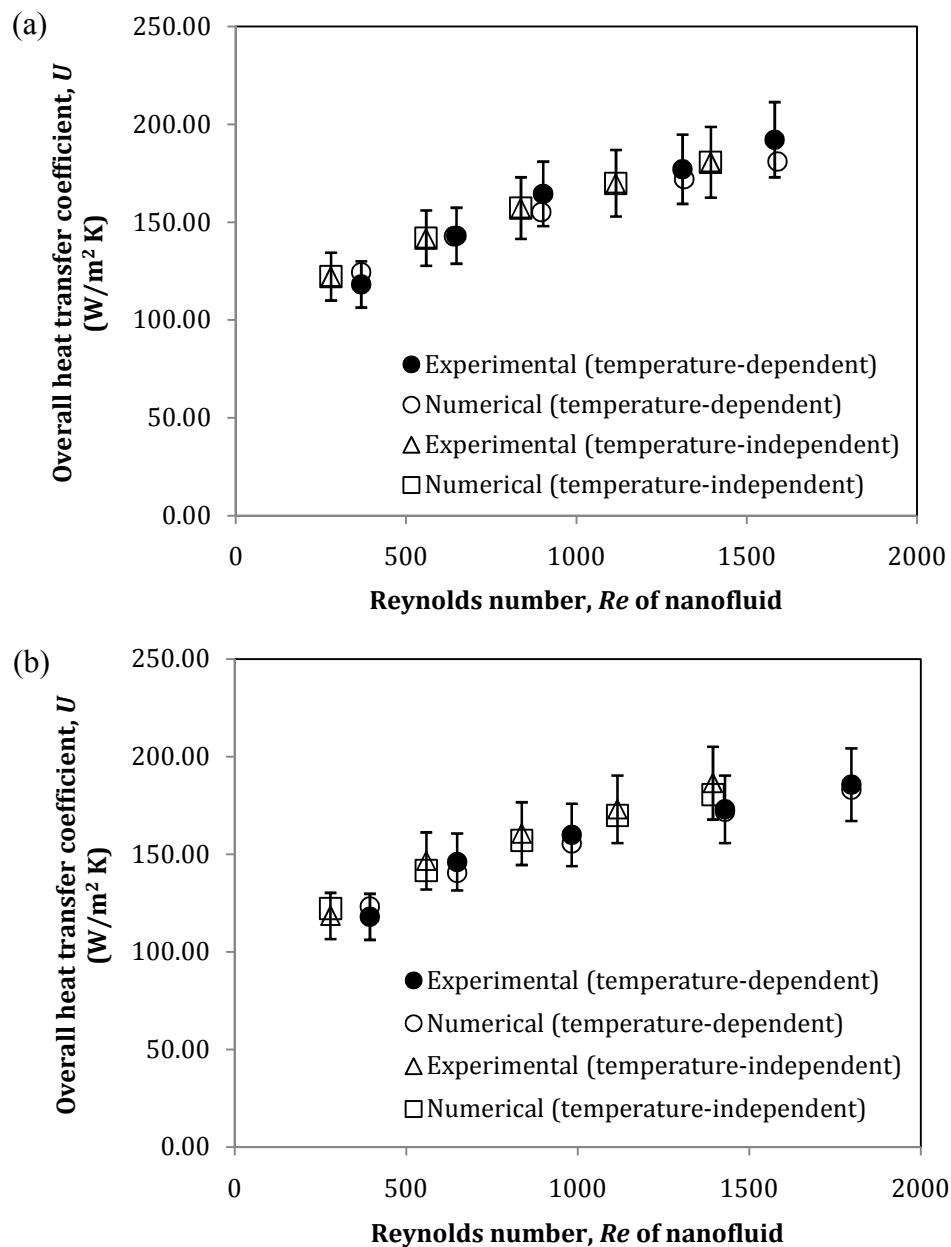
Geometries	Nu_{H2}		
	Current numerical work	Theoretical value	% deviation
<i>Temperature-independent properties</i>			
Circular pipe	4.450	4.360	2.07
2:1 rectangular duct	3.031	3.020	0.38
4:1 rectangular duct	2.988	2.940	1.63
Square duct	3.112	3.091	0.69
<i>Temperature-dependent properties</i>			
Circular pipe	4.419	4.360	1.36
2:1 rectangular duct	3.010	3.020	0.42
4:1 rectangular duct	2.960	2.940	0.67
Square duct	3.090	3.091	0.03

5.2.2 Al_2O_3 nanofluid

In order to ensure the validity and accuracy of the present model and numerical method for the forced convective heat transfer of Al_2O_3 nanofluid, the numerical results were compared with the experimental data obtained using the double pipe heat exchanger. The comparison was carried out for 0.10% Al_2O_3 nanofluid at three different working temperatures. The overall heat transfer coefficient from both single-phase temperature-independent and temperature-dependent approaches were compared. Vertical error bars of 10% are presented in Figure 5.2 for the experimental overall heat transfer coefficient calculated using both the temperature-dependent and temperature-independent properties.

For the temperature-dependent approach, the numerical overall heat transfer coefficient agrees with the experimental value within $\pm 10\%$. Similar trend is observed for the

temperature-independent approach, except at the hot inlet temperature of 323.15 K and Reynolds number of 1400, the deviation between the experimental and numerical overall heat transfer coefficient is approximately 11.80%. Besides, the comparison also shows that the Reynolds number is under-estimated in the case of temperature-independent approach compared to that of the temperature-dependent approach. This is because the viscosity is supposed to be lower at higher temperature, but for the case of temperature-independent approach, the viscosity is constant though higher. With this higher fluid viscosity, the Reynolds number estimated is lower.



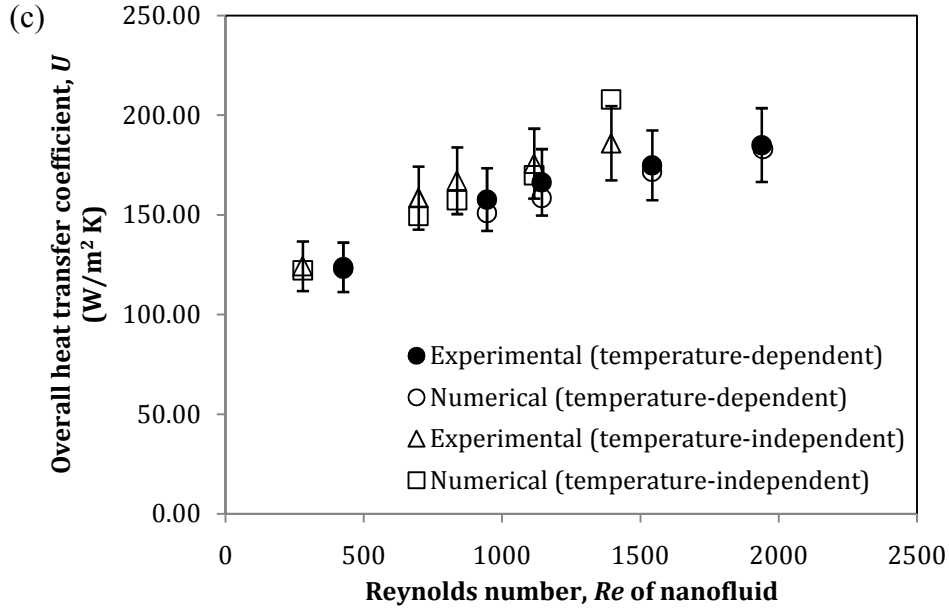


Figure 5.2: Overall heat transfer coefficient of 0.10% nanofluid at hot inlet temperatures of (a) 313.15 K, (b) 318.15 K and (c) 323.15 K.

5.2.3 PAA solution

The numerical results of PAA solution were made credible by comparing them with the experimental results obtained using the double pipe heat exchanger. The comparison was made for the overall heat transfer coefficient of 1000 ppm PAA solution at three different inlet temperatures of 313.15 K, 318.15 K and 323.15 K (Figure 5.3). Error bars of 10% are given for the experimental results. It can be seen from Figure 5.3 that the numerical overall heat transfer coefficient is in good agreement with the experimental data. The deviation between the experimental and numerical values is approximately 0.13–7.27%. Since the current numerical setting which treats the PAA solution as a purely viscous fluid is able to predict the heat transfer of 1000 ppm PAA solution in the double pipe heat exchanger precisely, the same numerical method is applied to the circular pipe.

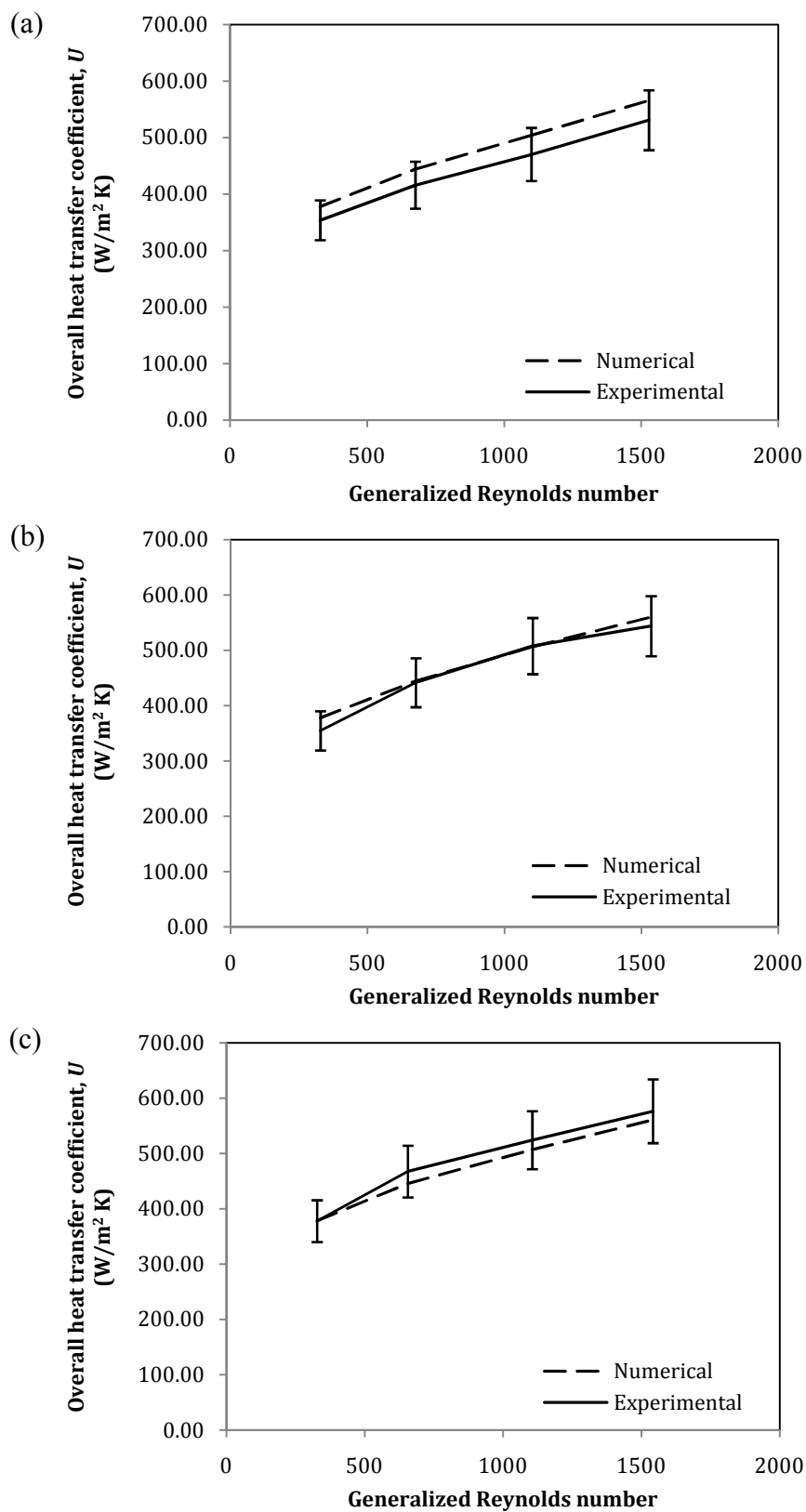


Figure 5.3: Comparison between the experimental and numerical overall heat transfer coefficient of 1000 ppm PAA solution at (a) 313.15 K, (b) 318.15 K and (c) 323.15 K.

In addition, to demonstrate the accuracy and validity of the numerical model and procedure for the PAA solution in the non-circular ducts, comparison with the experimental data of Hartnett and Kostic (1985) for 2:1 rectangular duct had been done. The thermal boundary condition was made similar to their experimental condition, with the top wall heated and the other walls adiabatic. The dimension of the 2:1 rectangular duct considered in this present study was exactly the same as that of Hartnett and Kostic (1985).

The viscosity data of 1000 ppm PAA solution employed by Hartnett and Kostic (1985) was utilized in the simulation used for comparison. The method assuming the PAA solution as a purely viscous fluid failed to predict the observed heat transfer augmentation of Hartnett and Kostic (1985) in the 2:1 rectangular duct. Therefore, a more complex model than the purely viscous non-Newtonian flow was necessary. The CEF equation was used to simulate the PAA solution in the non-circular ducts. However, the limitation of Hartnett and Kostic (1985)'s work was that they only showed the data of shear viscosity of 1000 ppm PAA solution. The information on the rheological data and fluid elastic properties were lacking, so the first normal stress difference of their solution was calculated using Equation 3.54. The comparison of their experimental data with the present numerical results modelled using the CEF equation is shown in Figure 5.4.

An excellent agreement is observed with the deviation below 5.00%. The soundness of the estimation method for the first normal stress difference, the assumptions made for the extra stress tensor (described in Chapter 3 Section 3.4.3.5) and the numerical procedure of PAA modelling in the 2:1 rectangular duct were authenticated through this comparison. Hence, the method utilized for PAA modelling in the 2:1 rectangular duct was employed for the 4:1 rectangular and square ducts.

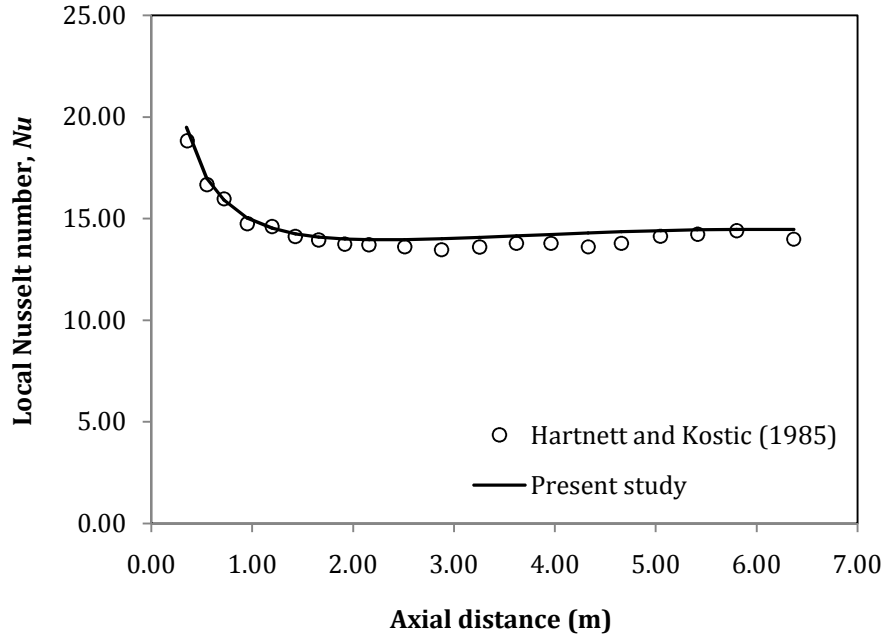


Figure 5.4: Comparison between the numerical local Nusselt number with the experimental values of Hartnett and Kostic (1985) for 1000 ppm PAA solution in the 2:1 rectangular duct ($Re^*=1368$).

5.2.4 Poly-nanofluid

The numerical results of poly-nanofluid were validated against the experimental results to check the reliability of the numerical setup. The comparison between the experimental and numerical results of 10 and 1000 ppm PAA in 0.10% Al_2O_3 nanofluid in the double pipe heat exchanger are depicted in Figure 5.5 and Figure 5.6, respectively. The maximum discrepancy between the experimental and numerical results is approximately 5.00 and 5.95% for 10 and 1000 ppm PAA in 0.10 vol% Al_2O_3 nanofluid, respectively. This confirms the reliability of the numerical procedure for the poly-nanofluid in the circular flow. Since the poly-nanofluid has similar rheological behaviour as the PAA solution, the numerical methods applied to PAA solution in the non-circular ducts are valid to be used for poly-nanofluid in the same geometries.

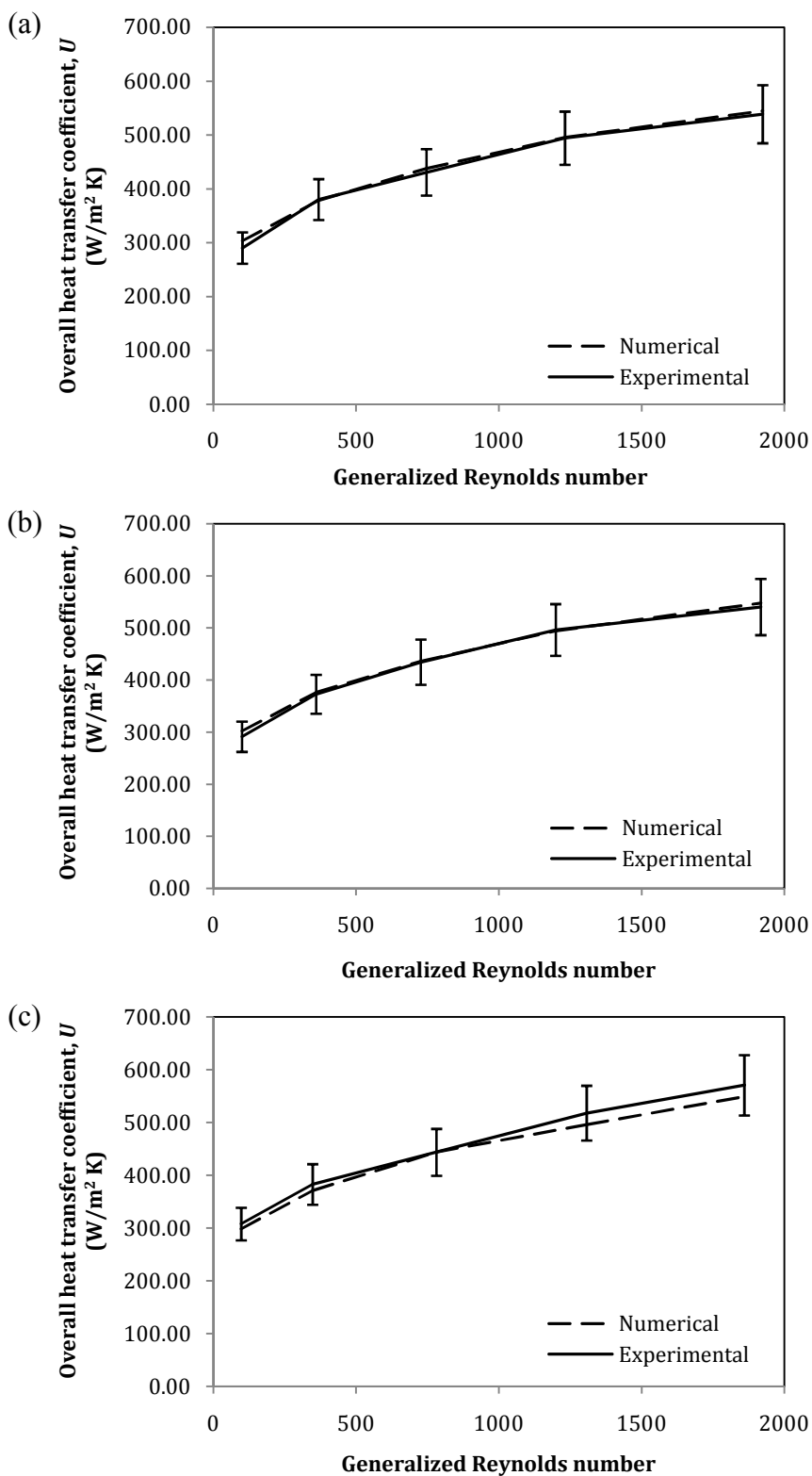


Figure 5.5: Comparison between the experimental and numerical overall heat transfer coefficient of 10 ppm PAA in 0.10% nanofluid at hot inlet temperatures of (a) 313.15 K, (b) 318.15 K and (c) 323.15 K.

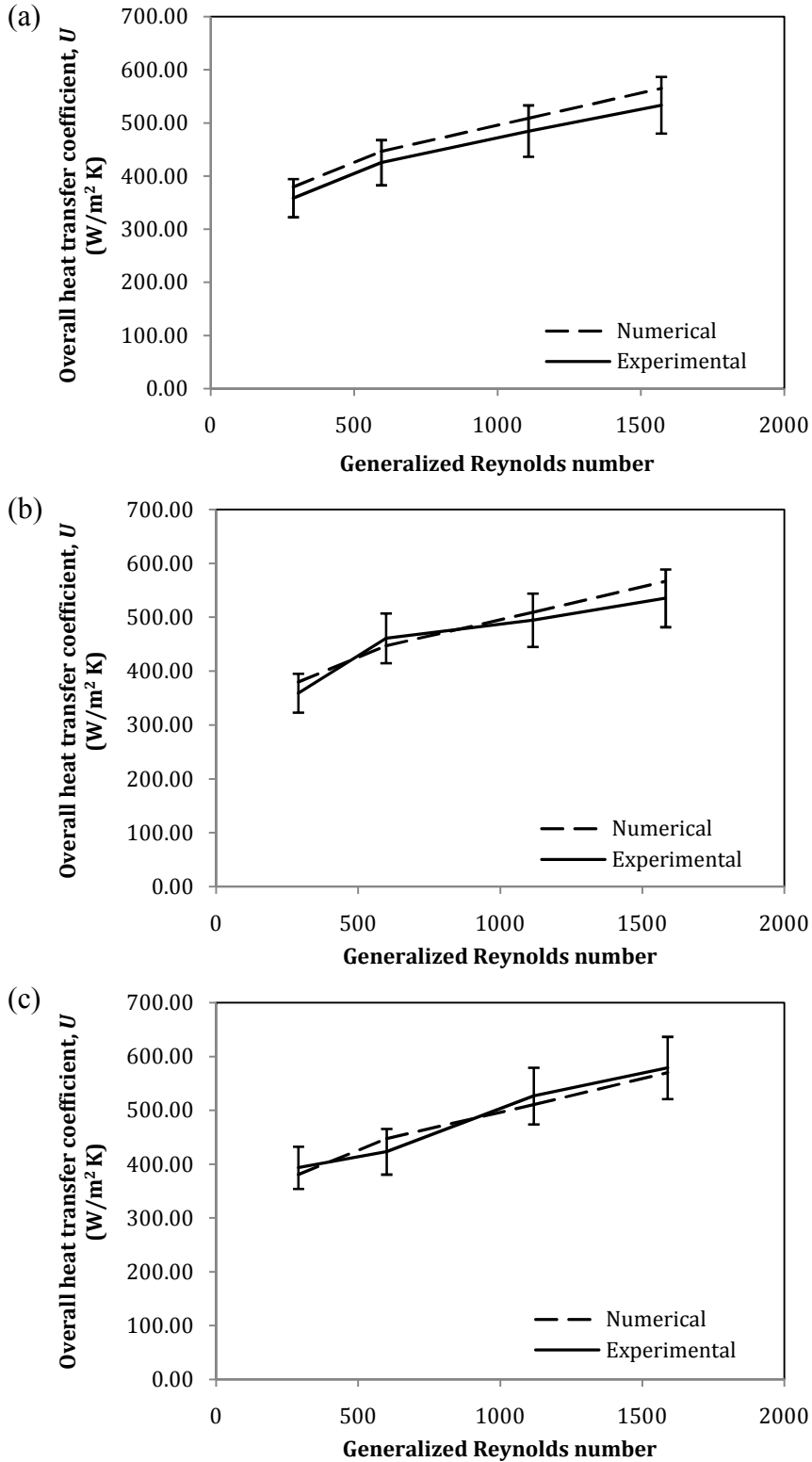


Figure 5.6: Comparison between the experimental and numerical overall heat transfer coefficient of 1000 ppm PAA in 0.10% nanofluid at hot inlet temperatures of (a) 313.15 K, (b) 318.15 K and (c) 323.15 K

5.3 Heat transfer characteristic of Al₂O₃ nanofluid

5.3.1 Single-phase modelling in double pipe heat exchanger

Heat transfer takes place from the inner tube with the hot nanofluid to the cooling water flowing in the outer tube of the heat exchanger. Figure 5.7 demonstrates the magnitude of the enhancement in the overall heat transfer coefficient of nanofluid with comparison to pure water at the hot inlet temperature of 323.15 K. It is observed that the enhancement in the overall heat transfer coefficient of nanofluid increases with the increasing concentration. At the Reynolds number of 1300, 0.01% and 4% Al₂O₃ nanofluid enhance the overall heat transfer coefficient by approximately 2% and 21%, respectively.

In this present study, it is determined that the HTE is attributed to the increased thermal conductivity of nanofluid with relative to pure water. The convective heat transfer between the wall and the fluid is more efficient when the thermal conductivity of the fluid is higher (Bianco et al. 2009). The thermal conductivity of nanofluid increases with the increasing of nanoparticle loading, thus higher HTE is experienced when higher nanofluid concentration is used. Furthermore, as the nanoparticle concentration increases, the fluid viscosity to density ratio also increases. Following the increased viscosity to density ratio, the inlet velocity (at the same *Re*) of nanofluid with increased concentration gets higher. With this higher inlet velocity, the heat transfer rate is raised. Hence, the HTE is larger at higher nanoparticle loading.

Other researchers also hypothesized that the nanoparticles which suspended in the base fluid provided a larger surface area for heat transfer to occur, leading to the instant availability for thermal interaction (Rashmi et al. 2013; Sonawane, Khedkar, and Wasewar 2013). They also believed that the mobility of nanoparticles in the base fluid generated micro-convection and accelerated the energy exchange. Besides, some researchers proposed the migration of nanoparticles within the flow field as one of the reasons for HTE (Wen and Ding 2004). However, it remains debatable over the exact mechanism of the HTE.

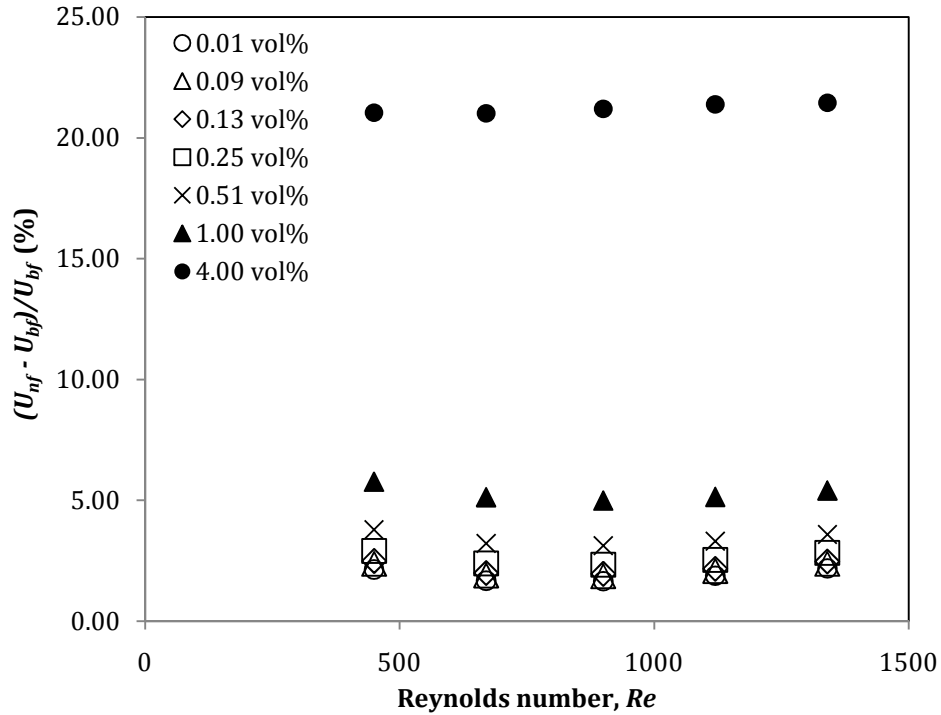


Figure 5.7: Enhancement in overall heat transfer coefficient of Al_2O_3 nanofluid with comparison to pure water at hot inlet temperature of 323.15 K.

Figure 5.8 shows the heat transfer rate and overall heat transfer coefficient of 4% nanofluid at different hot inlet temperatures. According to Figure 5.8(a), the heat transfer rate of 4% nanofluid increases from 203.71 J/s to 359.34 J/s when the hot inlet temperature is increased from 313.15 K to 323.15 K ($Re=1300$). This increment is attributed to the increase in the thermal conductivity and heat capacity of nanofluid when the temperature increases.

Nevertheless, as depicted in Figure 5.8(b), the effect of temperature on the overall heat transfer coefficient of nanofluid is not as significant as that of the heat transfer rate. Besides, the overall heat transfer coefficient decreases slightly with the increasing temperature. This is because the ratio of heat transfer rate to the logarithmic mean of temperature difference, $Q/\Delta T_{LMTD}$, is higher at a lower temperature. The ΔT_{LMTD} is the driving force for the heat exchange between the fluids in the double pipe heat exchanger. At a higher temperature, there is a higher heat transfer rate, thus higher ΔT_{LMTD} . Although both the heat transfer rate and ΔT_{LMTD} increase with the increasing temperature, the increment in the ΔT_{LMTD} is more than the increment in the heat transfer

rate at 323.15 K. Therefore, the ratio of $Q/\Delta T_{LMTD}$ is lower at 323.15 K, leading to lower overall heat transfer coefficient relative to the case of 313.15 K. A similar trend is also discovered for other nanoparticle concentrations. Their results are depicted in Appendix I Figure I.1.

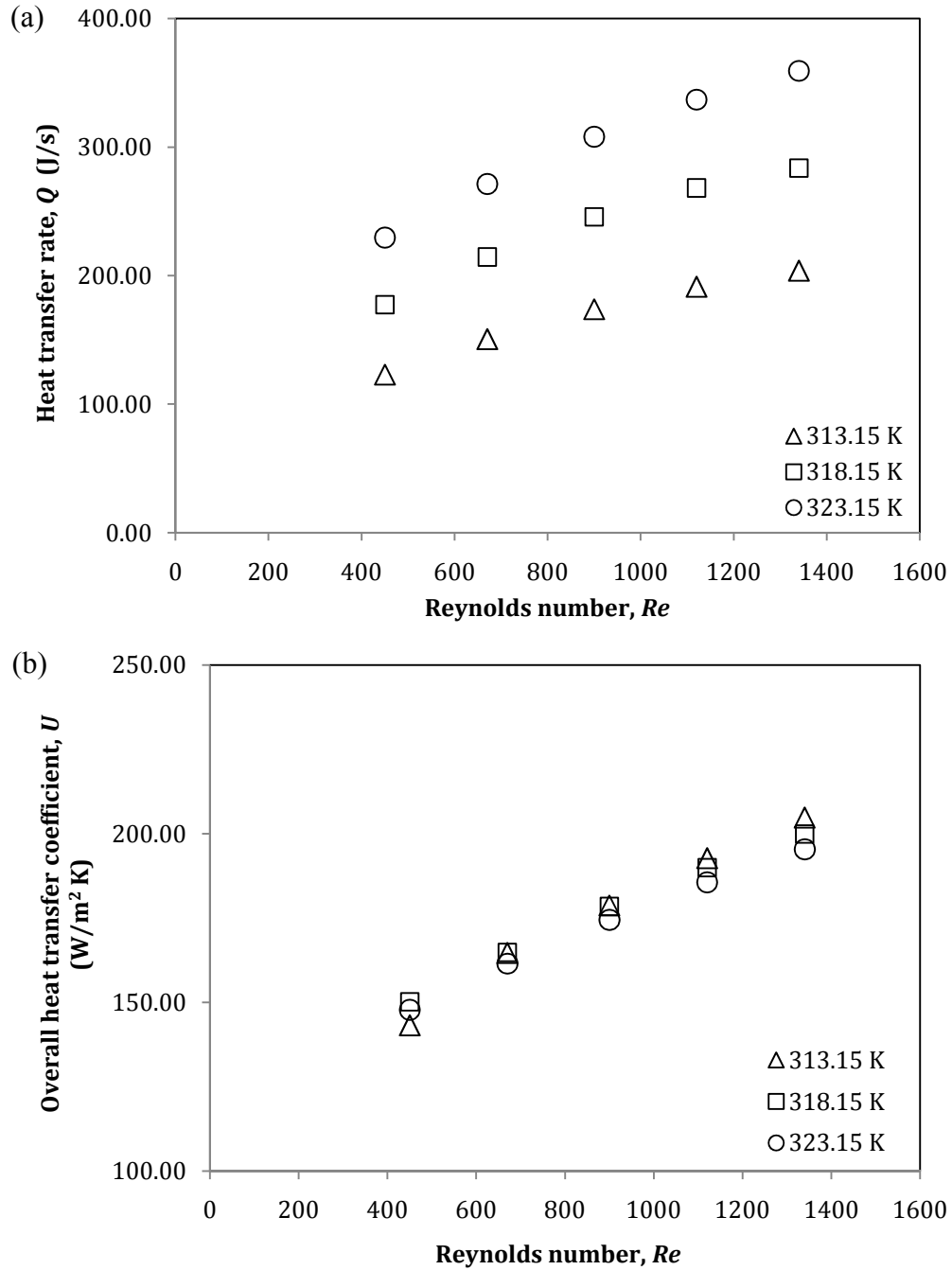
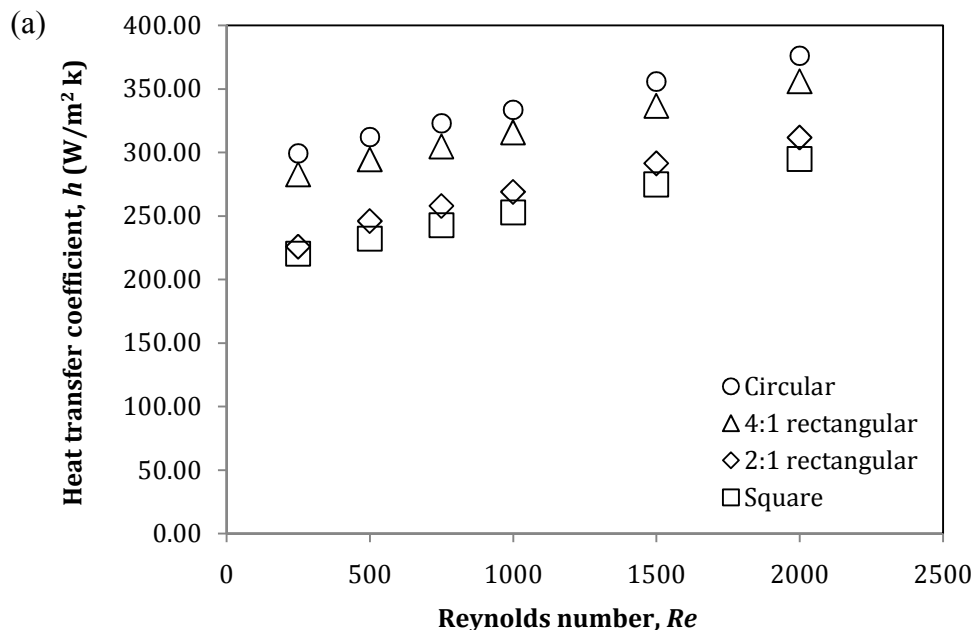


Figure 5.8: (a) Heat transfer rate and (b) overall heat transfer coefficient of 4% Al₂O₃ nanofluid at different hot inlet temperatures.

5.3.2 Single-phase modelling in circular and non-circular ducts

The heat transfer coefficient and Nusselt number of 4% Al_2O_3 nanofluid for the case of temperature-dependent approach is shown in Figure 5.9. It is observed that the heat transfer coefficient and Nusselt number of nanofluid increase with the increasing Reynolds number. Higher nanofluid velocity (or higher Re) induces higher heat transfer rate, thus lower temperature difference between pipe wall and the fluid. According to $h \propto 1/(T_w - T_b)$, the heat transfer coefficient is higher at lower temperature difference between wall and the bulk fluid. Higher heat transfer coefficient improves the Nusselt number. Hence, the heat transfer coefficient and Nusselt number of the nanofluid are higher when the Reynolds number is higher. This assertion is supported by Heris, Nassan, and Noie (2011) that a higher Reynolds number promotes better dispersion and migration of nanoparticles through the fluid flow, leading to a better heat transfer rate.

Figure 5.9 also reveals that for a particular nanofluid concentration, the heat transfer rate obtained in various ducts is different. The heat transfer coefficient and Nusselt number of nanofluid are the highest in the circular pipe, followed by 4:1 rectangular, 2:1 rectangular and square ducts. These trends are attributed to the fact that the heat transfer rate increases with the decreasing of channel aspect ratio (Shah and Sekulic 2003). The area of heat transfer increases when the aspect ratio decreases.



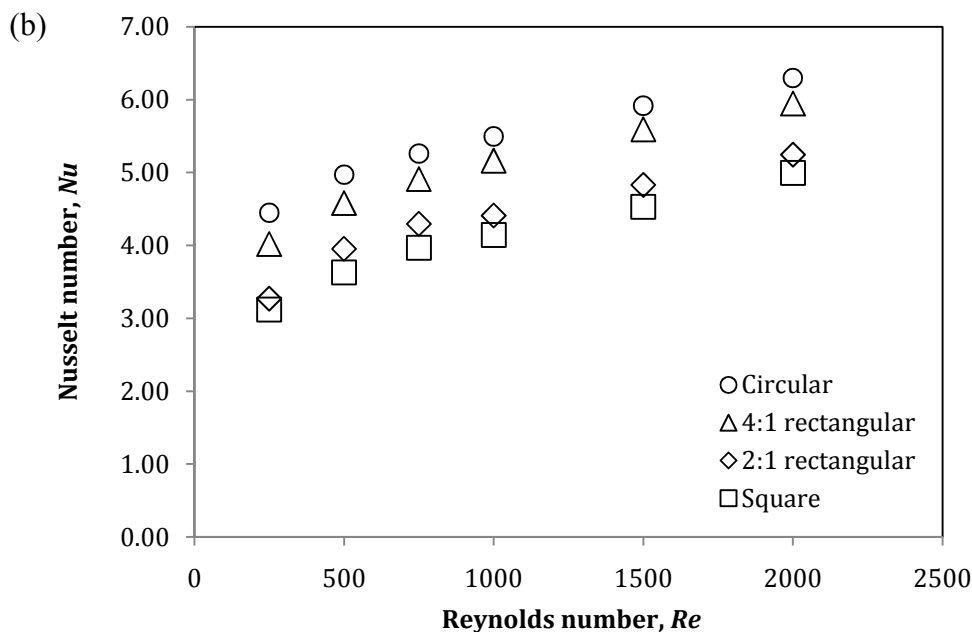


Figure 5.9: (a) Heat transfer coefficient and (b) Nusselt number of 4% Al_2O_3 nanofluid (from temperature-dependent approach).

The h enhancement and Nu enhancement of nanofluid are calculated using Equations 3.84 and 3.85, respectively. Their results are tabulated in Table 5.2 and Table 5.3. The h and Nu enhancement attained for the non-circular ducts are given in Table I.1 to Table I.6 (Appendix I). These results show that the average heat transfer coefficient and Nusselt number of nanofluid are greatly augmented compared to the values of water for all the geometries studied.

Table 5.2: h enhancement (%) of nanofluid in circular pipe.

Reynolds number	Nanoparticles volume concentration (%)						
	0.01	0.09	0.13	0.25	0.51	1.00	4.00
<u>Temperature-independent properties</u>							
250	0.11	0.75	1.07	2.16	4.37	8.64	36.65
750	0.13	0.93	1.33	2.71	5.52	11.06	49.44
1000	0.14	1.01	1.45	2.94	6.02	12.07	53.78
1500	0.16	1.13	1.63	3.30	6.74	13.51	59.47
2000	0.17	1.22	1.75	3.53	7.21	14.42	62.93
<u>Temperature-dependent properties</u>							
250	0.81	1.12	1.25	1.77	2.81	5.50	17.85
750	1.42	1.71	1.84	2.36	3.31	5.73	20.09
1000	1.67	1.95	2.08	2.54	3.51	5.87	20.71
1500	2.28	2.53	2.66	3.09	4.00	6.09	22.12
2000	2.66	2.90	3.03	3.43	4.32	6.37	22.81

Table 5.3: *Nu* enhancement (%) of nanofluid in circular pipe.

Reynolds number	Nanoparticles volume concentration (%)						
	0.01	0.09	0.13	0.25	0.51	1.00	4.00
<i>Temperature-independent properties</i>							
250	0.02	0.09	0.13	0.35	0.57	1.01	5.18
750	0.04	0.27	0.42	0.83	1.65	3.29	15.00
1000	0.05	0.36	0.47	1.07	2.06	4.24	18.34
1500	0.07	0.48	0.64	1.39	2.88	5.67	22.82
2000	0.08	0.57	0.77	1.65	3.23	6.41	25.43
<i>Temperature-dependent properties</i>							
250	0.41	0.39	0.39	0.36	0.36	0.36	0.79
750	1.39	1.35	1.31	1.25	1.07	0.96	2.73
1000	2.04	1.96	1.91	1.78	1.57	1.32	3.39
1500	2.54	2.44	2.39	2.23	1.95	1.70	4.27
2000	2.86	2.73	2.69	2.69	2.69	2.69	4.86

When temperature-independent properties are considered, the h and Nu enhancement of nanofluid generally increase with the increasing concentration and Reynolds number. The effect of the Reynolds number on the h and Nu enhancement is more pronounced at a higher nanofluid concentration, especially at 4%. The maximum h and Nu enhancement of nanofluid attained in the circular pipe are 62.93% and 25.43%, respectively. These enhancement are acquired by 4% nanofluid at the Reynolds number of 2000.

In contrast, the maximum h and Nu enhancement achieved in the circular pipe by using the temperature-dependent properties are 22.81% and 4.86%, respectively (also at $Re=2000$ and 4% nanofluid). For temperature-dependent approach, only the h enhancement is proportional to the increasing nanofluid concentration. The Nu enhancement decreases when the nanoparticle loading is increased from 0.01% to 1%. It only increases when the concentration is further increased to 4%. This is because the $(h_{nf} - h_{bf})/h_{bf}$ to $(k_{nf} - k_{bf})/k_{bf}$ ratio for 1% nanofluid is lower than those of the lower concentrations. At the Reynolds number of 2000, this ratio of 0.01%, 1% and 4% nanofluid are 1.027, 1.018 and 1.053, respectively. Since the effect of nanofluid concentration on the h enhancement is insignificant for concentration below 4%, the heat transfer coefficient of 0.01% and 1% nanofluid are similar. The $(k_{nf} - k_{bf})/k_{bf}$ for 1% nanofluid is larger than that of 0.01% nanofluid. As a result, 1% nanofluid which has a similar heat transfer coefficient with 0.01% nanofluid but higher thermal conductivity,

has a lower *Nu enhancement*. In both cases of temperature-independent and temperature-dependent properties, the magnitude of *h enhancement* is larger than that of the *Nu enhancement*.

In addition, as indicated in Table 5.2 and Table 5.3, the magnitude of *h* and *Nu enhancement* obtained from the temperature-dependent approach are not as significant as in the case of temperature-independent approach, even at higher nanofluid concentrations. When the temperature effect is not considered, the thermal-conductivity of nanofluid is always higher, even at lower temperature. Therefore, the heat transfer enhancement achieved in the case of temperature-independent approach is higher than that of the temperature-dependent approach.

Both temperature-independent and temperature-dependent properties have been used by other researchers for nanofluid studies. In comparison to the temperature-independent approach, the temperature-dependent approach is more accurate as the temperature effect is taken into consideration. This is very crucial for the heat transfer processes. Bianco, Manca, and Nardini (2011) and Goktepe, Atalik, and Erturk (2014) also claimed that the temperature-dependent properties yielded better heat transfer prediction. Therefore, in this present study, it is determined that the temperature-dependent approach must be applied for heat transfer study.

Figure 5.10 presents the *Nu enhancement* of Al_2O_3 nanofluid obtained using the temperature-dependent model for different geometries. It shows that although the Nusselt number of Al_2O_3 nanofluid is the highest in the circular pipe, its *Nu enhancement* is the lowest compared to channels with other cross-sections. These results demonstrate that the nanofluid aids in improving the thermal performance in the non-circular ducts more than the circular duct. The sharp corners of the non-circular ducts present some stagnant sections for the conventional heat transfer fluids, leading to ineffective heat transfer in those areas. The flow of nanoparticles near the sharp corners reduces these stagnant sections, thus enhancing the heat transfer rate (Sahin 1998; Heris, Nassan, and Noie 2011; Heris et al. 2013). The Nusselt number of 4% nanofluid obtained in the square duct from the temperature-dependent approach is approximately 5.12% higher than that of water ($Re=2000$).

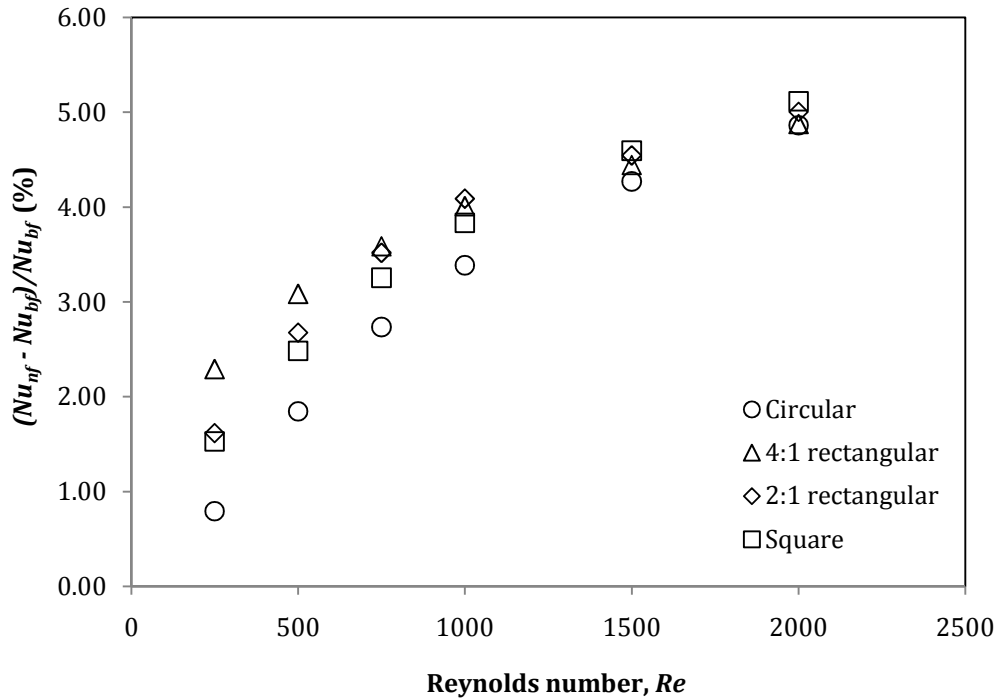


Figure 5.10: Nu enhancement of 4% nanofluid for temperature-dependent approach.

The temperature profile at the outlet of circular and 4:1 rectangular ducts ($Re=2000$) is displayed in Figure 5.11. It is noted that the temperature is distributed symmetrically with a high temperature gradient near the duct wall. The minimum temperature is found to occur at the centre of the duct. It is also discovered that the temperature profile of the nanofluid becomes flatter compared to that of water, especially at a higher concentration. Heris et al. (2012) believed that the increment in the nanofluid concentration intensified the dispersion and movement of the nanoparticles in the base fluid, leading to better mixing between them. This changed the temperature profile of the nanofluid to a flatter one resembling that of the turbulent flow, and hence the heat transfer was better. From Figure 5.11, the temperature profile in the 4:1 rectangular duct is flatter compared to that of the circular pipe, and this explains the reason of higher HTE of nanofluid in the non-circular ducts.

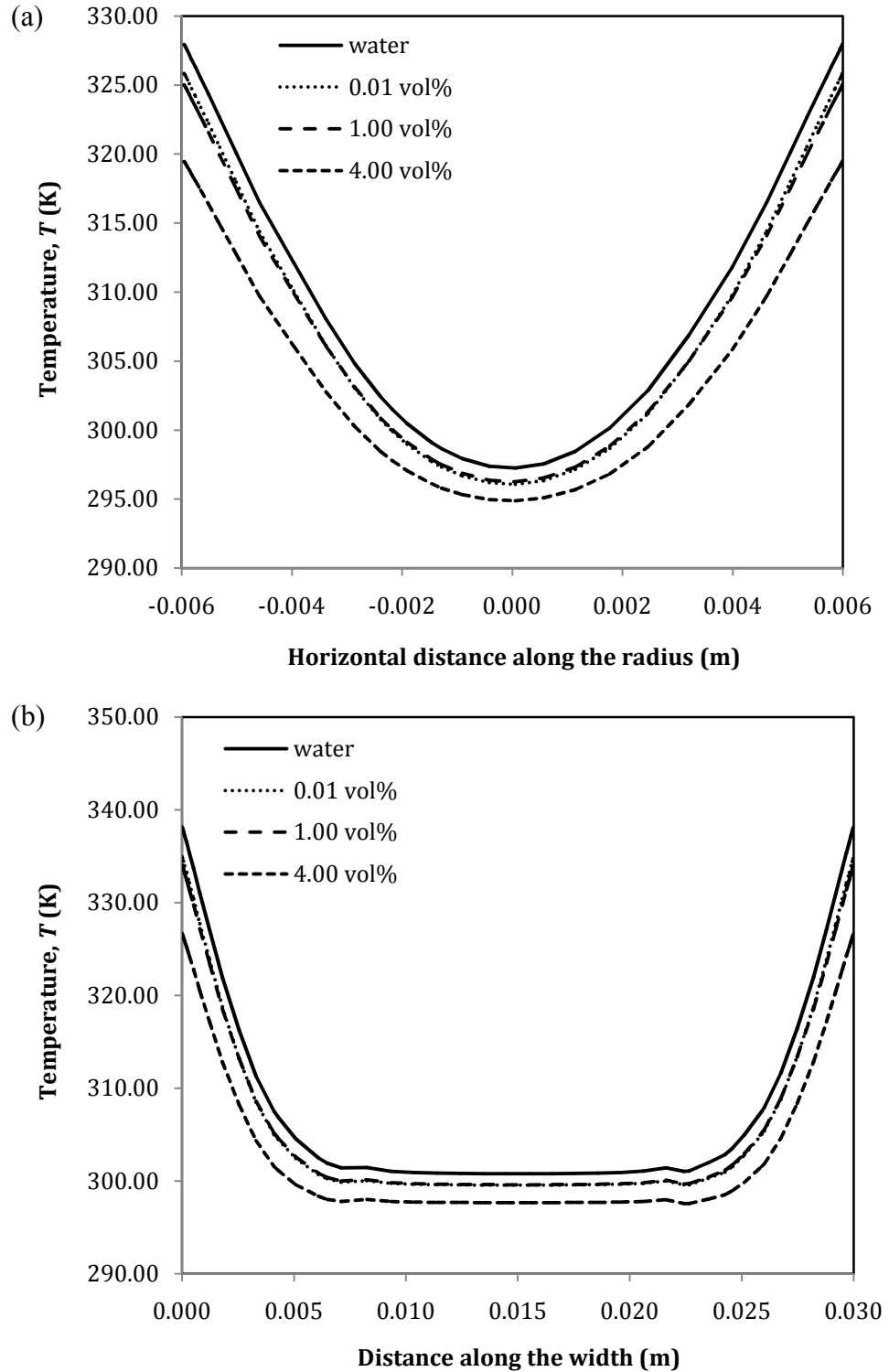


Figure 5.11: Temperature profile at the outlet of (a) circular and (b) 4:1 rectangular ducts (for temperature-dependent properties and $Re=2000$).

Comparison of the present results with the numerical results of Bianco et al. (2009) and Maiga et al. (2005) is depicted in Figure 5.12. The Nusselt number is calculated for the pipe axial distance to diameter ratio, x/D_h of 100 to enable the comparison with their average Nusselt number. This is because the dimension of their circular pipe is different from the one considered in this present study. Their circular pipe is 1 m with the diameter of 0.01 m. The maximum deviation is approximately 11%, 22% and 29%, for the cases of 1% (temperature-independent properties), 1% (temperature-dependent properties) and 4% (temperature-dependent properties), respectively. This might be due to the different correlations used to estimate the thermo-physical properties of nanofluid as the properties play a vital role in the thermal performance. Besides, the nanoparticle size considered is different. Nevertheless, a good agreement with Bianco et al. (2009) is found for 4% nanofluid (temperature-independent properties) with the maximum deviation of 5%.

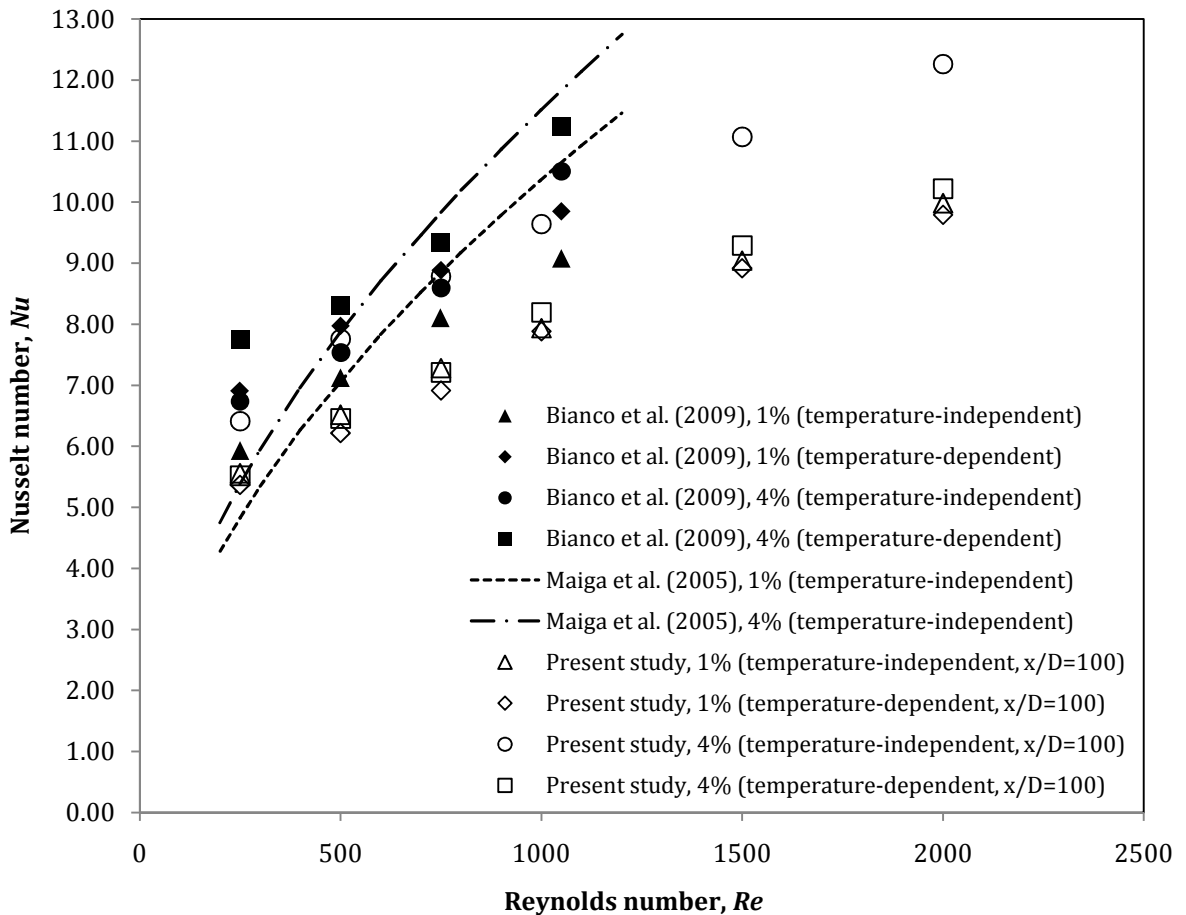


Figure 5.12: Nusselt number of 1% and 4% Al_2O_3 nanofluid.

Another comparison of the local Nusselt number is made with the experimental data of Anoop, Sundararajan, and Das (2009). It can be clearly noted from Figure 5.13 that the local Nusselt number at $x/D_h = 147$ is in close agreement with that of Anoop, Sundararajan, and Das (2009). The maximum error of 5% is estimated for both temperature-independent and temperature-dependent cases. The nanoparticle size studied by Anoop, Sundararajan, and Das (2009) was 45 nm, which was similar to the case of present study. The nanoparticle size used in the present study was 47 nm. Therefore, small deviation in the results is obtained.

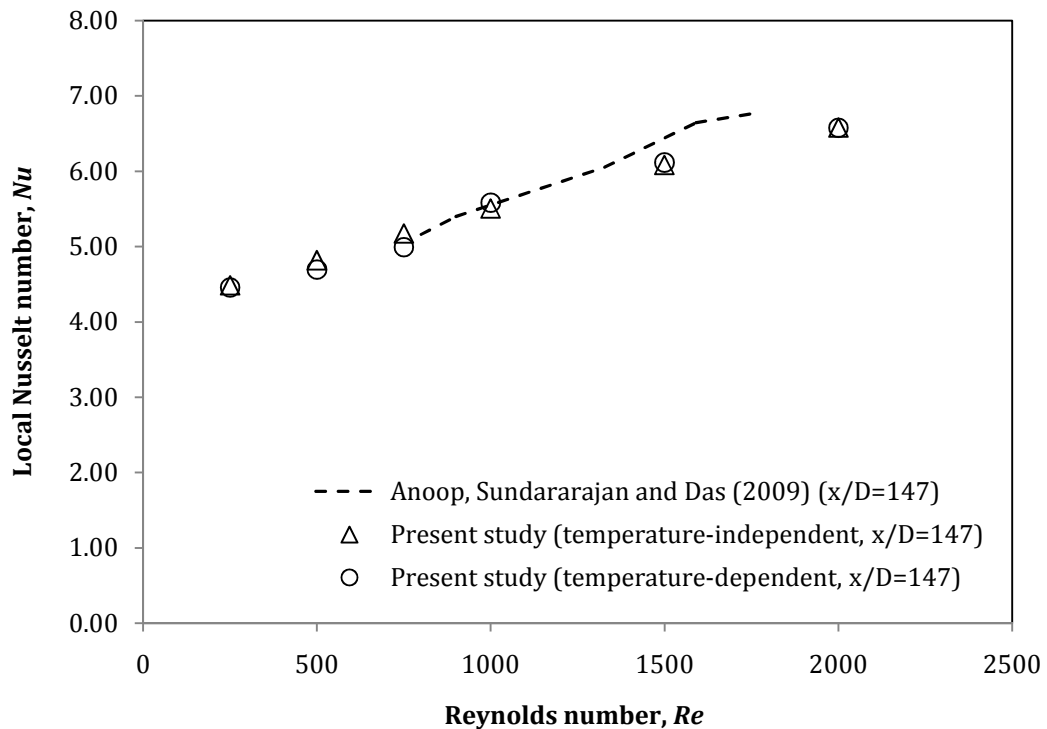


Figure 5.13: Local Nusselt number of 1% Al_2O_3 nanofluid.

5.3.3 Two-phase modelling in different geometries

Besides the single-phase model, the two-phase mixture, Eulerian and VOF models were also used to study the heat transfer performance of nanofluid. The comparison between the heat transfer results obtained from these two-phase models for different geometries is illustrated in Figure 5.14 and Figure 5.15. These three two-phase models are found to predict similar heat transfer at a particular Reynolds number, temperature and concentration. Akbari, Galanis, and Behzadmehr (2011) and Shahmohammadi and

Jafari (2014) also stated that their heat transfer results from the mixture, Eulerian and VOF models were essentially similar.

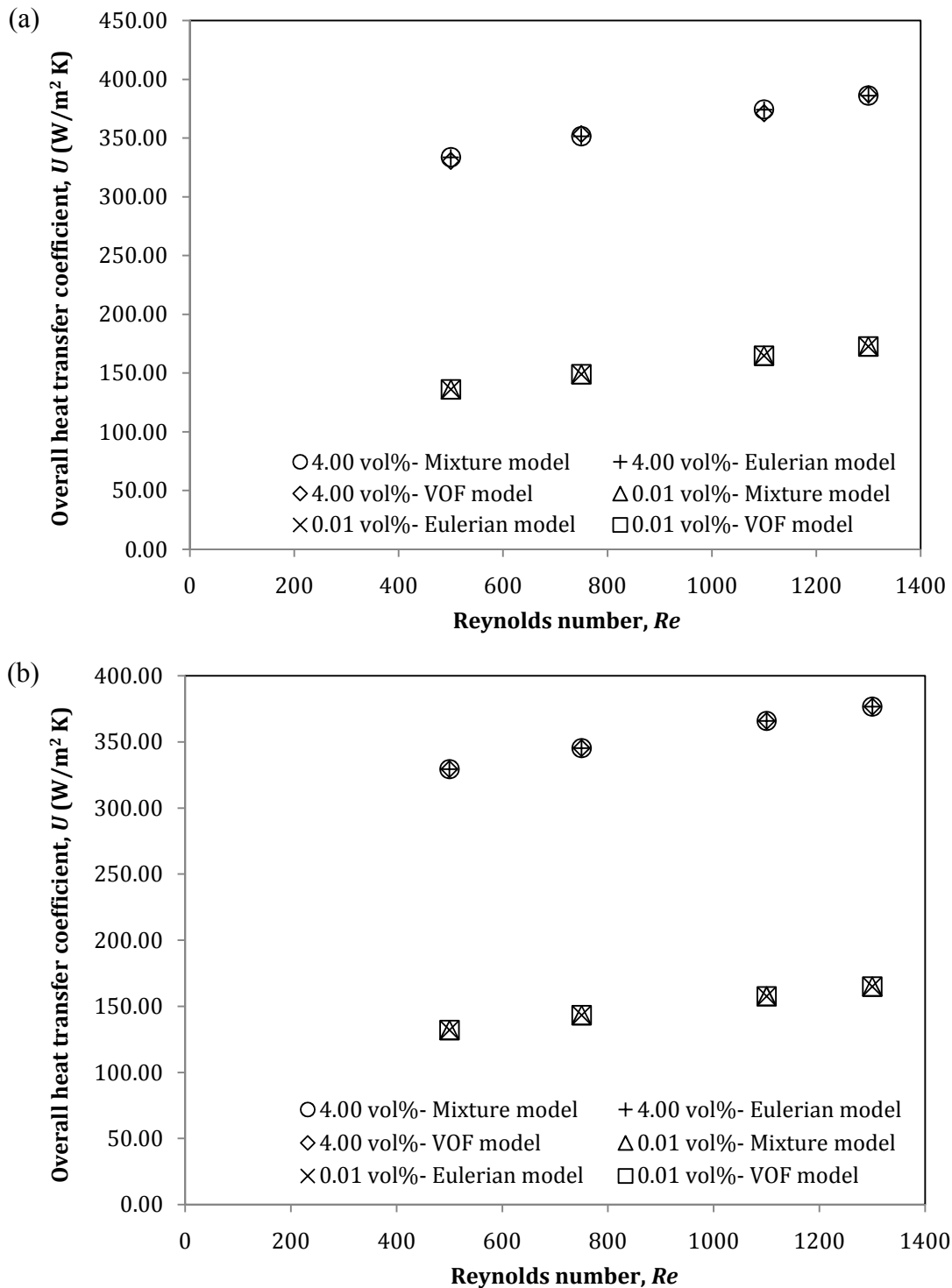


Figure 5.14: Overall heat transfer coefficient of 0.01% and 4% nanofluid obtained using two-phase models at the hot inlet temperatures of (a) 313.15 K and (b) 323.15 K.

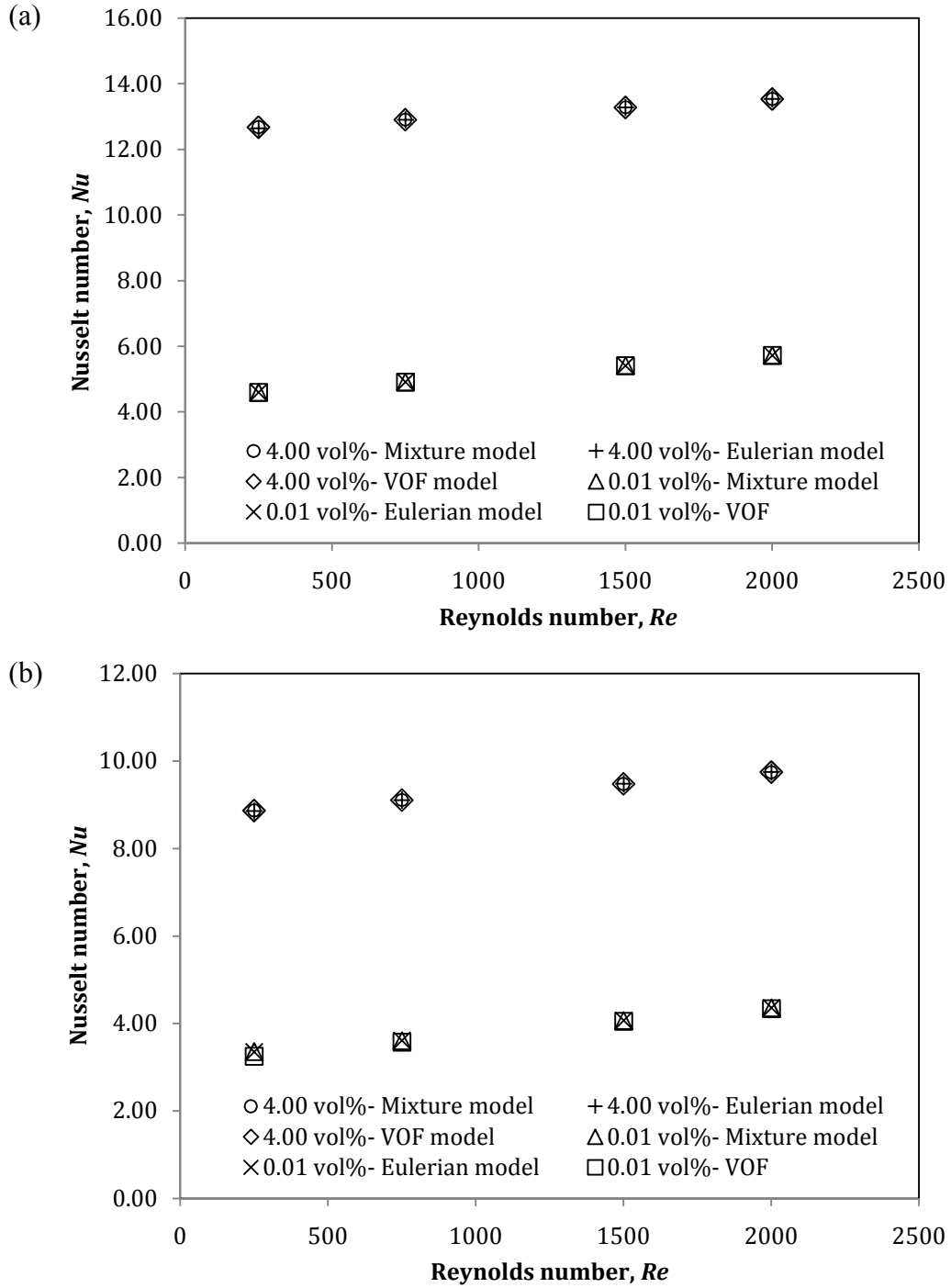


Figure 5.15: Nusselt number of 0.01% and 4% Al₂O₃ nanofluid obtained from two-phase models for (a) circular pipe and (b) square duct.

For the double pipe heat exchanger, the overall heat transfer coefficient of nanofluid decreases when the temperature increases, which is similar to the case of single-phase model (Figure 5.14). Besides, from Figure 5.16, it can be observed that the overall heat

transfer coefficient of 4% nanofluid estimated from the mixture model is approximately 136% relative to that of water ($Re=1300$ and at 323.15 K). On the other hand, the Nusselt number of 4% nanofluid computed from the mixture model for different geometries is displayed in Figure 5.17. This result is comparable to that of the single-phase model as the Nusselt number of nanofluid is also found to be the highest in the circular pipe, followed by the 4:1 rectangular, 2:1 rectangular and square ducts.

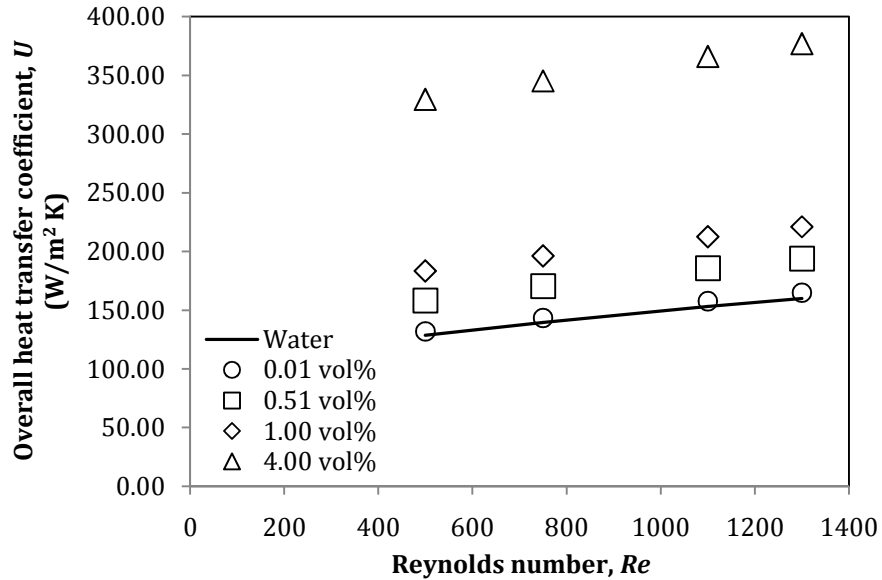


Figure 5.16: Overall heat transfer coefficient of nanofluid obtained using the mixture model at the hot inlet temperature of 323.15 K.

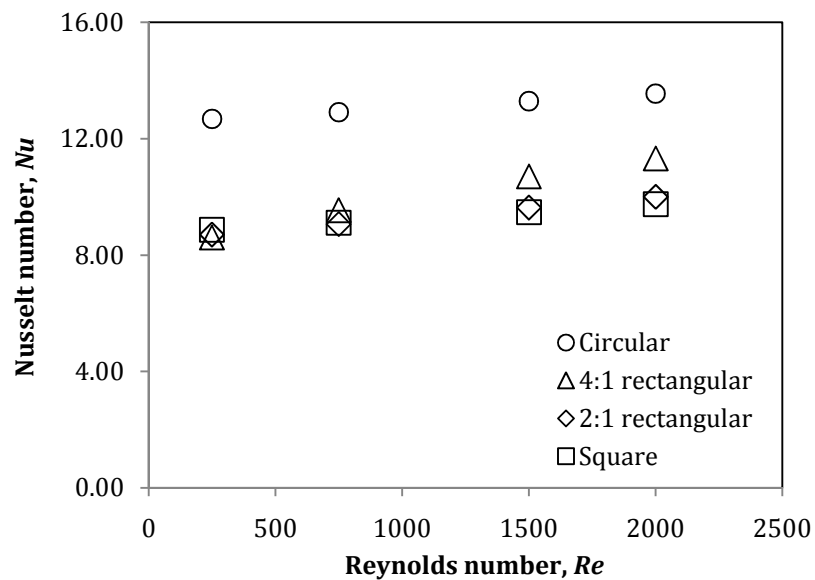


Figure 5.17: Nusselt number of 4% nanofluid obtained from the mixture model.

The comparison of the present results from the mixture model and some literature data is shown in Figure 5.18. As mentioned, the present Nusselt number predicted from the mixture and Eulerian models are similar. Nonetheless, the Nusselt number obtained by Lotfi, Saboohi, and Rashidi (2010) using these two models are different. For x/D_h of 116, the present Nusselt number from the mixture model is close to the value estimated by Lotfi, Saboohi, and Rashidi (2010) from the same model. On the other hand, the results of the present study agree with those of Shahmohammadi and Jafari (2014) and Wen and Ding (2004) at certain Reynolds number only. This deviation might be caused by the difference in the pipe diameter used. The pipe diameter considered by Lotfi, Saboohi, and Rashidi (2010) was 10 mm while it was 4.5 mm for both Shahmohammadi and Jafari (2014) and Wen and Ding (2004). The pipe diameter utilized in this present study was 12 mm, which was closer to that of Lotfi, Saboohi, and Rashidi (2010). The pipe diameter is a crucial parameter in determining the thermal entrance length that affects the development of the thermal boundary condition (Incropera and Dewitt 1996; Dharaiya and Kandlikar 2012). Therefore, different pipe diameters yield different degrees of HTE.

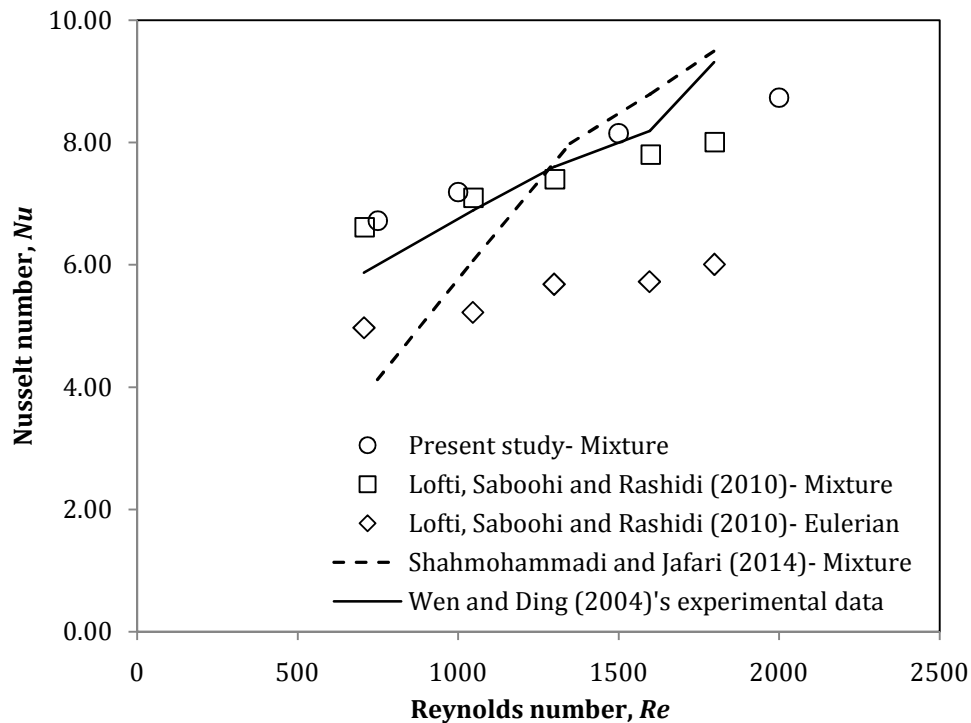


Figure 5.18: Nusselt number of 1% nanofluid at x/D_h of 116.

5.3.4 Comparison of results from single- and two-phase models

The comparison between the heat transfer results obtained from the single-phase temperature-dependent properties and two-phase mixture model for nanofluid in the double pipe heat exchanger is shown in Figure 5.19. For the hot inlet temperature of 313.15 K, it is discovered that the overall heat transfer coefficient of 0.01% nanofluid predicted from the mixture model agrees reasonably with the result from the single-phase model, with the maximum difference of 3.29%. As the nanofluid concentration increases, the deviation between the results from the single and two-phase models increases. For 4% nanofluid, this deviation increases to a maximum of 112.50%. In addition, the HTE of 4% nanofluid estimated from the two-phase mixture model is also higher than that of the single-phase model for different hot inlet temperatures. As mentioned in the previous section, the overall heat transfer coefficient of 4% nanofluid obtained from the single-phase and two-phase mixture models are 21% and 136% higher than the value of water, respectively (at $Re=1300$ and 323.15 K).

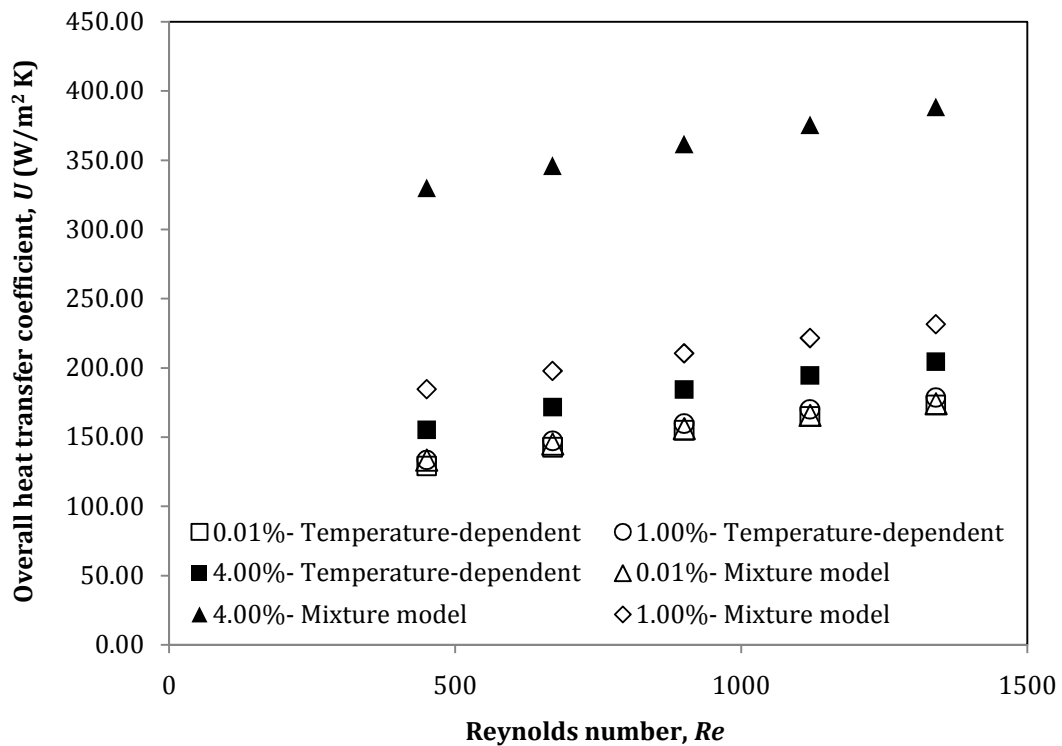


Figure 5.19: Overall heat transfer coefficient of nanofluid from the single and two-phase models at the hot inlet temperature of 313.15 K.

The Nusselt number of nanofluid obtained from different models for the circular pipe is depicted in Figure 5.20. The comparison done for the non-circular ducts is shown in Appendix I (Figure I.2). It is noticed that the Nusselt number of 0.01% nanofluid predicted from the single-phase temperature-independent and temperature-dependent models are close to the value from the mixture model, with the maximum deviation of 8.11%. The maximum difference identified between the single-phase (temperature-dependent) and mixture models is approximately 185.06% when the nanofluid concentration is increased to 4%. This finding of higher heat transfer estimated from the two-phase mixture model, especially when the nanoparticle loading is high, is similar to the case of double pipe heat exchanger. (Akbari, Galanis, and Behzadmehr 2011) also obtained a higher heat transfer from the two-phase model compared to that of the single-phase model at high nanofluid concentration.

The deviation between the heat transfer results from single and two-phase models is due to the difference in the value of thermal-conductivity computed from these models. For the single-phase temperature-dependent model, the thermal-conductivity of nanofluid is estimated using Equation 3.72 while for the two-phase mixture model, the value is predicted from Equation 3.23. For example, the thermal-conductivity of 4% nanofluid in the double pipe heat exchanger is approximately 0.74 and 2.04 W/m K from the estimation of Equations 3.72 and 3.23, respectively (at the hot inlet temperature of 313.15 K). The thermal-conductivity of nanofluid computed from the two-phase Eulerian and VOF model are similar to that of the mixture model under the same boundary condition and nanofluid concentration. Higher thermal-conductivity estimated for the two-phase models results in higher heat transfer compared to the case of single-phase model.

Some researchers indicated that the two-phase models could model the heat transfer of nanofluid more precisely compared to the single-phase model (Fard, Esfahany, and Talaie 2010; Akbari, Galanis, and Behzadmehr 2011; Moraveji and Esmaeili 2012; Shahmohammadi and Jafari 2014). However, Tokit, Yusoff, and Mohammed (2013) and Kumar and Puranik (2016) pointed out that the single-phase model was able to characterize the heat transfer of nanofluid to a reasonably good accuracy. In this present

study, the single-phase model is also found to be adequate in modelling the nanofluid. In addition, the single-phase model is simpler than the two-phase models. Therefore, the single-phase model is chosen for the numerical studies of poly-nanofluid.

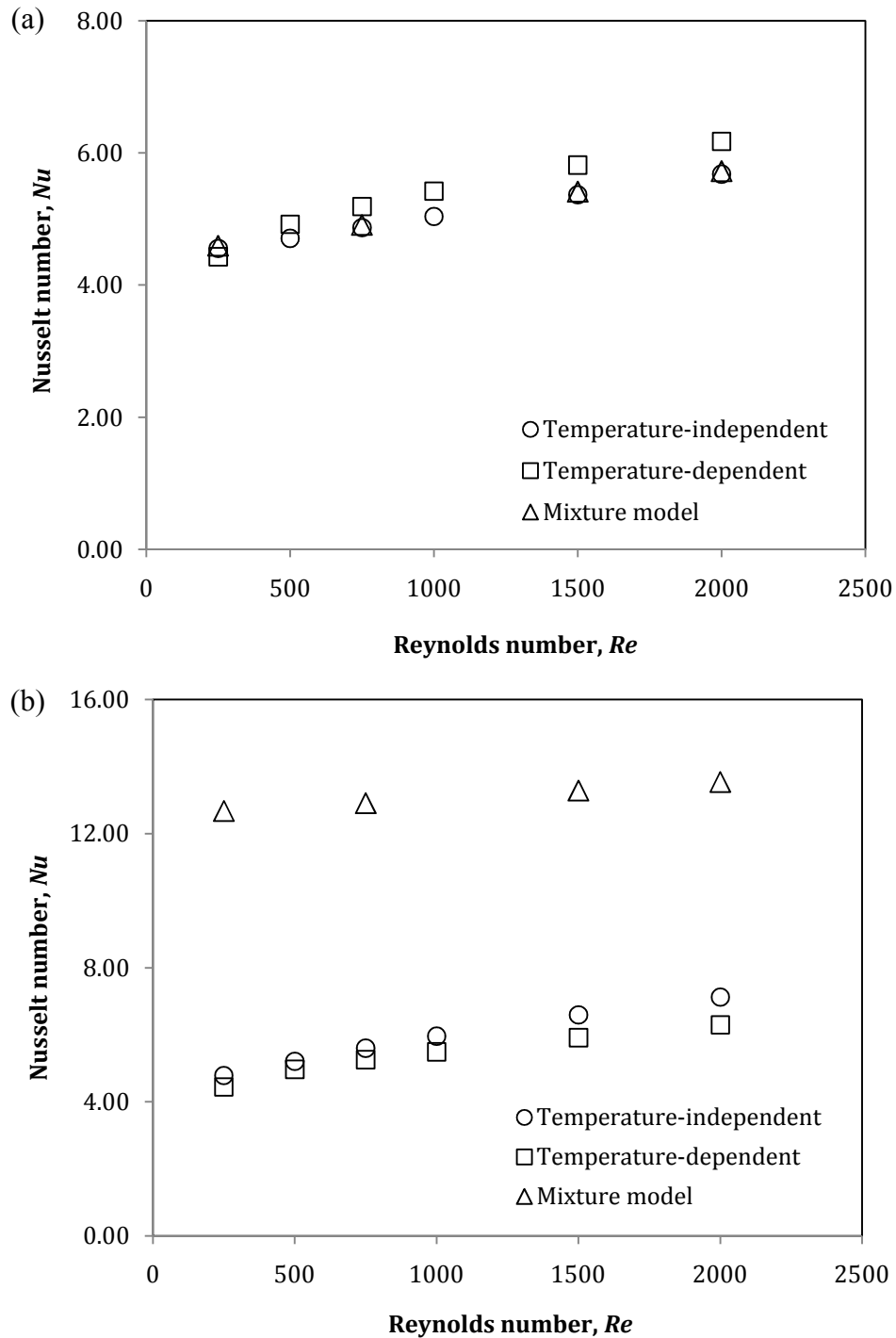


Figure 5.20: Comparison of the Nusselt number obtained from different models for (a) 0.01% and (b) 4% Al_2O_3 nanofluid in circular pipe.

5.4 Heat transfer characteristic of PAA solution

5.4.1 Double pipe heat exchanger

The overall heat transfer coefficient of PAA solution at the hot inlet temperature of 323.15 K is depicted in Figure 5.21. Similar to the case of nanofluid, the overall heat transfer coefficient of the solution increases as the concentration and Reynolds number increase. However, the effect of PAA concentration on the overall heat transfer coefficient is not substantial, particularly at low concentration. The variation between the overall heat transfer coefficient of 200 and 1000 ppm PAA solution is approximately 0.21–6.52%. This difference gets smaller as the concentration reduces. This is attributed to the fact that the thermo-physical properties (except the viscosity) are the same for the PAA solution with different concentrations. The viscosity of 50 and 200 ppm PAA solution merely vary approximately 1.88 and 4.37% on average compared to that of 10 ppm PAA solution, respectively. The difference in the viscosity between 10 and 1000 ppm PAA solution is about 26.13% on average (refer to Chapter 4 Section 4.1). As a result, for PAA solution with lower concentrations, the overall heat transfer coefficient achieved is similar. Besides, it is shown in Figure 5.22 that the influence of PAA inlet temperature on the overall heat transfer coefficient is not significant. This might be because the temperature range considered in this study is not big enough to see its importance.

From Figure 5.23, it is observed that with a low PAA concentration of 10 ppm, the overall heat transfer coefficient is improved to be three times higher relative to water. Since the only difference between the PAA solution and water is on their rheology behaviour, it is postulated that this HTE is owing to the purely viscous shear-thinning characteristics of PAA solution. Furthermore, the viscosity of the PAA solution is higher compared to water, thus, its velocity is higher at a particular Reynolds number. Higher velocity promotes larger heat transfer rate.

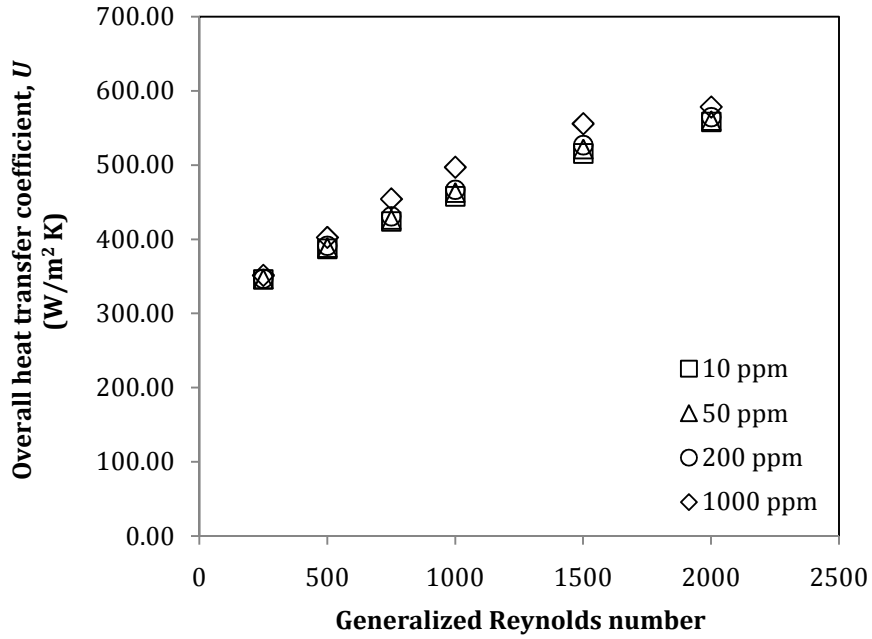


Figure 5.21: Overall heat transfer coefficient of PAA solution in the double pipe heat exchanger at hot inlet temperature of 323.15 K.

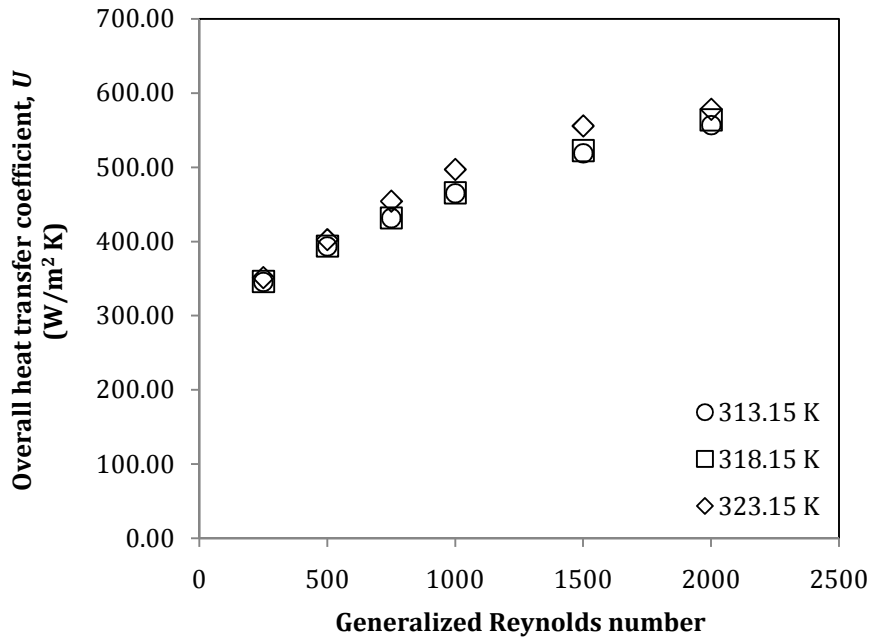


Figure 5.22: Overall heat transfer coefficient of 1000 ppm PAA solution at different hot inlet temperatures.

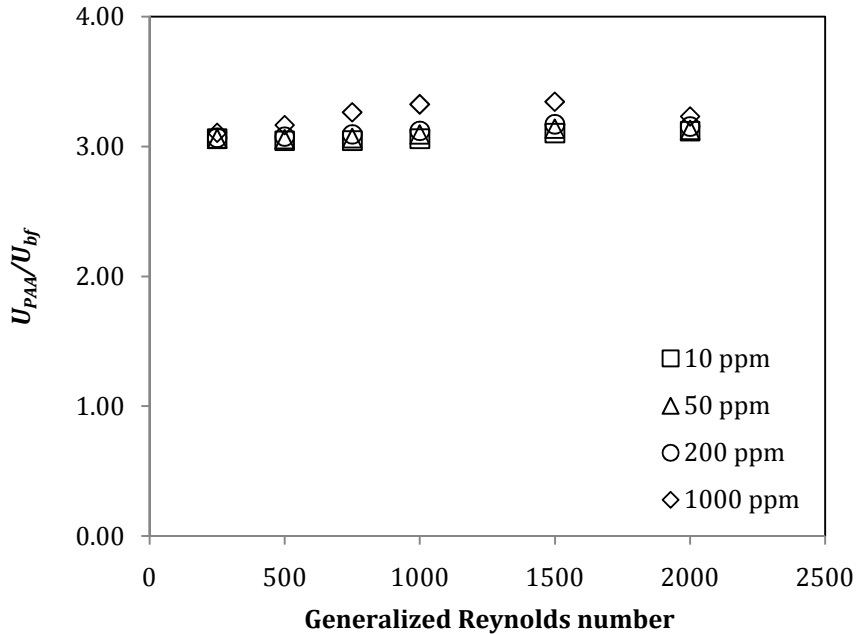


Figure 5.23: Ratio of overall heat transfer coefficient of PAA solution to that of water at hot inlet temperature of 323.15 K.

5.4.2 Circular and non-circular ducts

The Nusselt number of PAA solution in the circular and 4:1 rectangular ducts is shown in Figure 5.24. It is clear from this figure that the effect of PAA concentration on the Nusselt number is more significant in the non-circular duct. This is owing to PAA solution behaving like purely viscous fluid in the circular pipe, while the PAA solution is viscoelastic in the non-circular ducts (Gupta, Metzner, and Hartnett 1967; Oliver and Karim 1971; Mena et al. 1978; Hartnett and Kostic 1985). Due to the viscoelasticity, secondary flow is induced by the second normal stress difference of the solution for HTE. The presence of the secondary flow in the non-circular ducts is illustrated in Figure 5.25. The vortices of the secondary flow bring the hotter near-wall fluid further away from the wall, distribute and circulate the fluid across the duct, thus promoting better heat transfer rate. Figure 5.26 shows that there is no secondary flow induced for PAA solution in the circular pipe. Although PAA solution does enhance the heat transfer in the circular pipe, the HTE is far weaker than that obtained for the non-circular ducts (Figure 5.27).

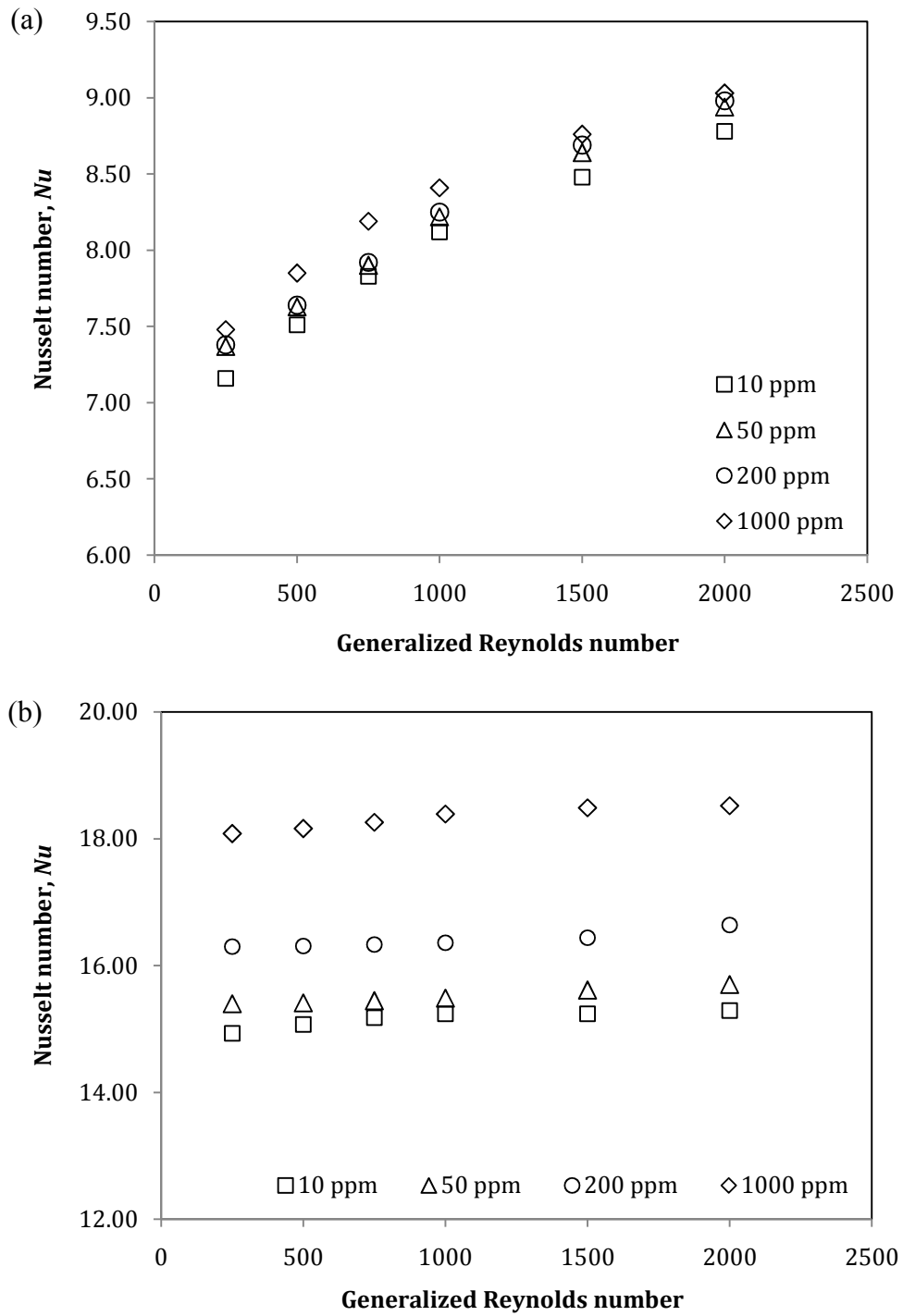
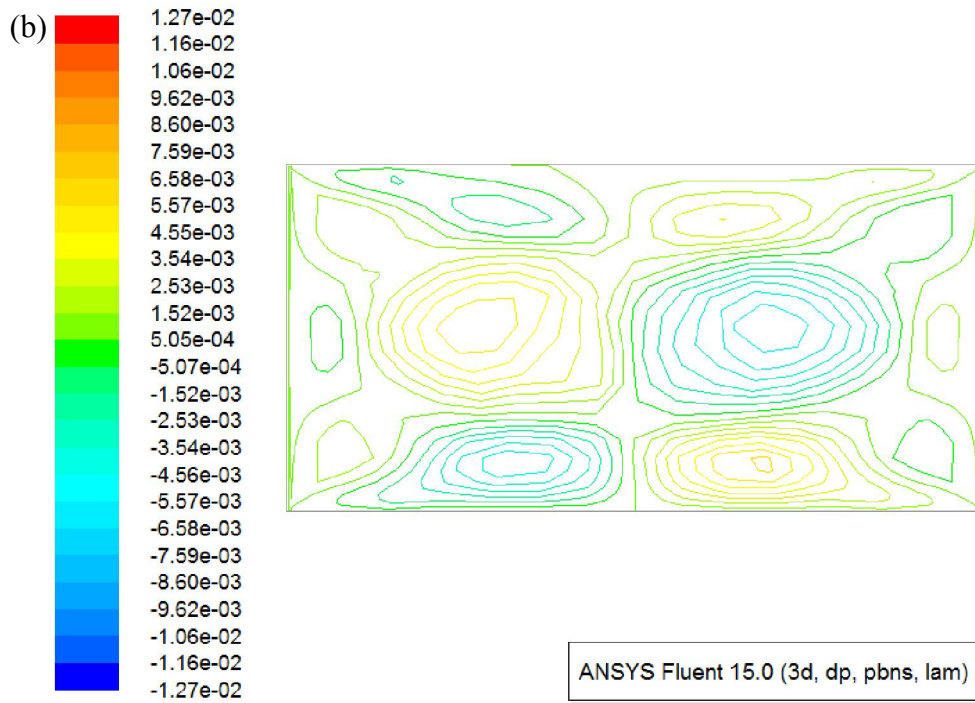
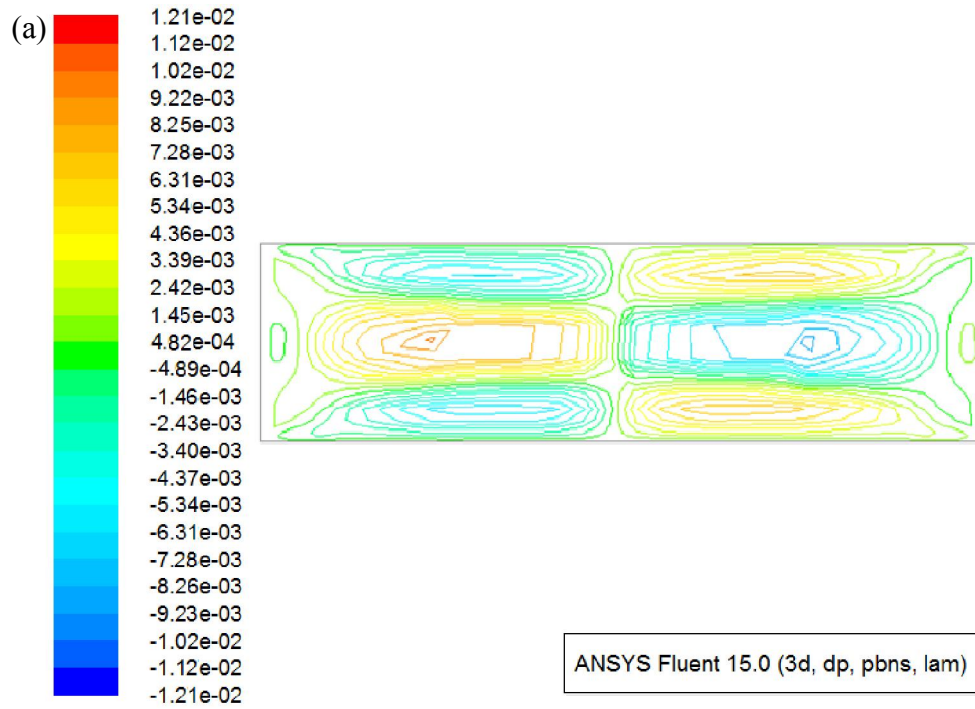


Figure 5.24: Nusselt number of PAA solution in (a) circular and (b) 4:1 rectangular ducts.



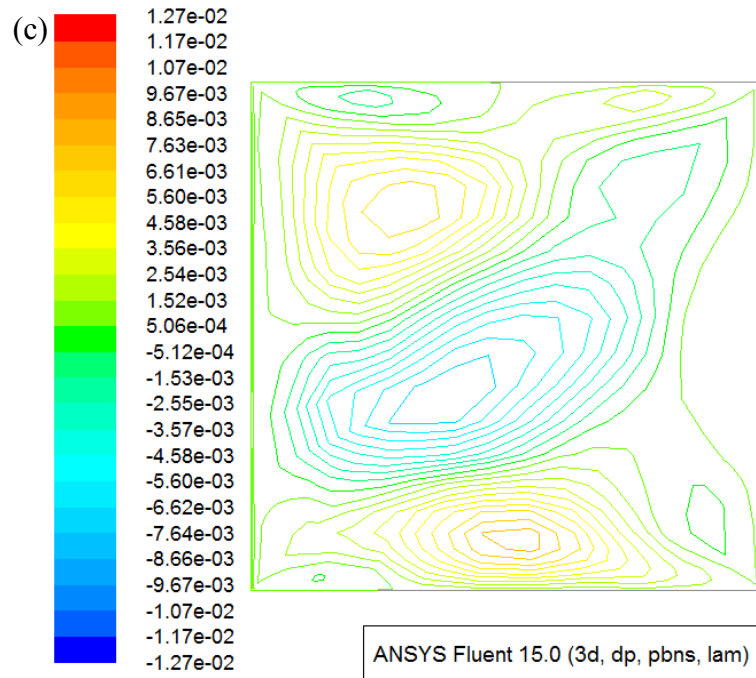


Figure 5.25: Velocity contour (m/s) of secondary flow for 1000 ppm PAA solution at the outlet cross-section of (a) 4:1 rectangular, (b) 2:1 rectangular and (c) square ducts ($Re^*=1000$).

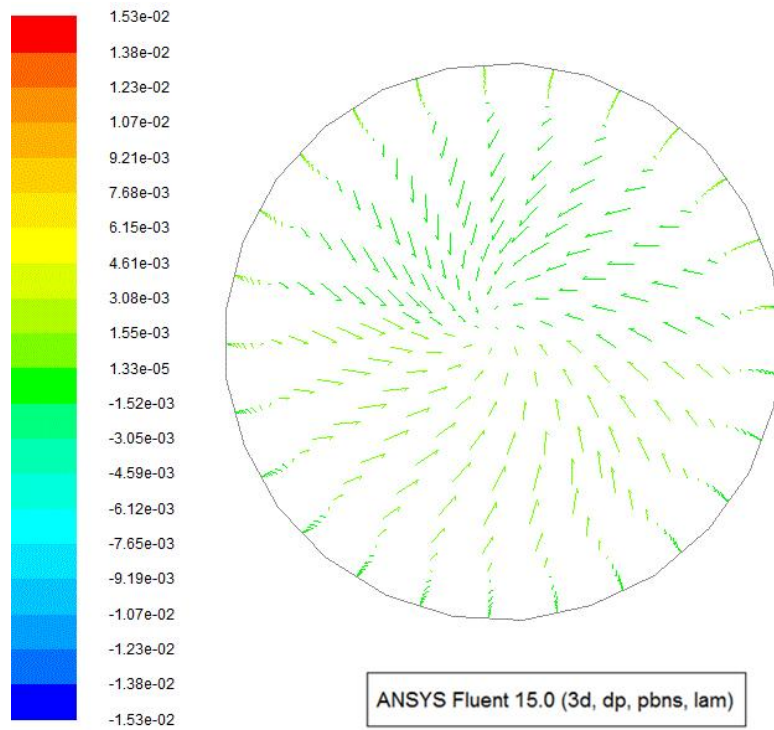


Figure 5.26: Radial velocity vector (m/s) of 1000 ppm PAA solution at the outlet cross-section of circular pipe.

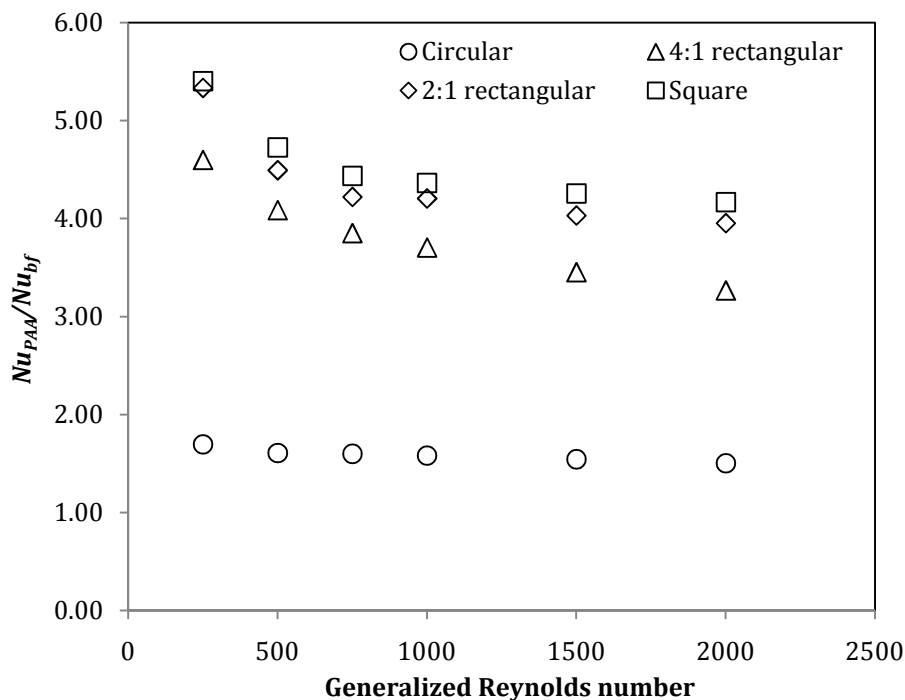


Figure 5.27: Nusselt number ratio of 1000 ppm PAA solution to that of water.

Moreover, it is also observed from Figure 5.27 that the ratio of Nusselt number of PAA solution to that of water, Nu_{PAA}/Nu_{bf} , is the largest in the square duct, followed by the 2:1 rectangular and 4:1 rectangular ducts. The maximum Nu_{PAA}/Nu_{bf} achieved by 1000 ppm PAA solution (at $Re^*=250$) in the square, 2:1 rectangular and 4:1 rectangular ducts are 5.40, 5.33 and 4.60, respectively. For PAA solution, the square duct has the greatest Nusselt number augmentation because the intensity of the secondary flow is stronger in the duct with higher aspect ratio. The higher the intensity, the greater the HTE (Oliver and Karim 1971; Rao 1988, 1989; Gao 1993; Gao and Hartnett 1993, 1996; Naccache and Mendes 1996).

It can also be noted from Figure 5.27 that the Nu_{PAA}/Nu_{bf} decreases with increasing Reynolds number. As the Reynolds number increases, the magnitude of Nusselt number augmentation for PAA solution decreases. This is because the Nusselt number of water is very low compared to that of the PAA solution at the Reynolds number of 250. However, as the Reynolds number increases, the Nusselt number of water also increases, thus leading to smaller difference between the Nusselt number of water and PAA solution.

5.5 Heat transfer characteristic of poly-nanofluid

5.5.1 Double pipe heat exchanger

Figure 5.28 illustrates the overall heat transfer coefficient of 1000 ppm PAA added into nanofluid with different concentrations for the double pipe heat exchanger. It is noticed that the overall heat transfer coefficient of poly-nanofluid increases when the nanoparticle loading increases. It also increases when the PAA with higher concentration is added into the nanofluid (Figure 5.29). Moreover, the overall heat transfer coefficient of poly-nanofluid is found to be larger compared to that of the pure nanofluid and PAA solution. The overall heat transfer coefficient of 1000 ppm PAA in 4% Al_2O_3 nanofluid is approximately 161–210% and 9–18% higher relative to 4% nanofluid and 1000 ppm PAA solution, respectively. This enhancement is attributed to the combined effect of higher thermal conductivity of nanofluid and shear-thinning characteristic of PAA. Since the HTE is greater when compared to that of the pure nanofluid, it is ascertained that the shear-thinning behaviour of PAA has the dominant effect on the HTE over the increased thermal conductivity of nanofluid.

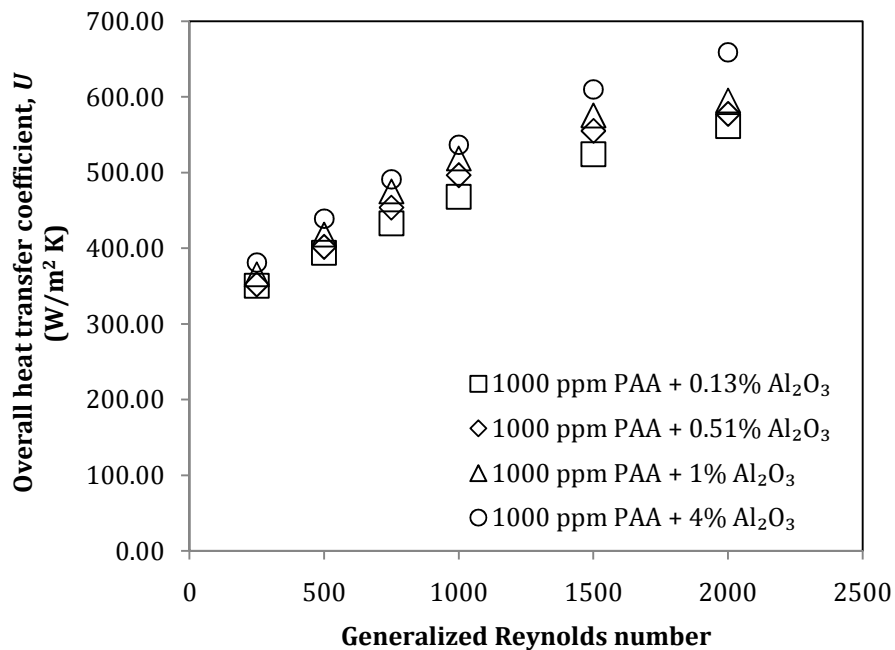


Figure 5.28: Overall heat transfer coefficient of 1000 ppm PAA in nanofluid for double pipe heat exchanger.

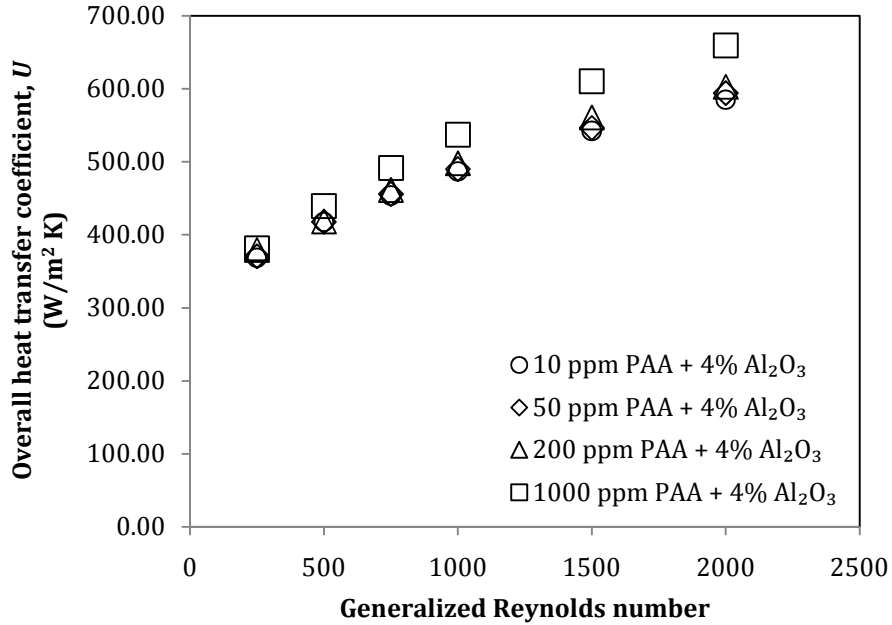


Figure 5.29: Overall heat transfer coefficient of PAA in 4% Al₂O₃ nanofluid for double pipe heat exchanger.

The overall heat transfer coefficient of poly-nanofluid at different hot inlet temperatures is presented in Figure 5.30. According to this figure, the overall heat transfer coefficient is similar for the three temperatures considered. The temperature range studied might not be big enough to examine the importance of temperature effect on the heat transfer.

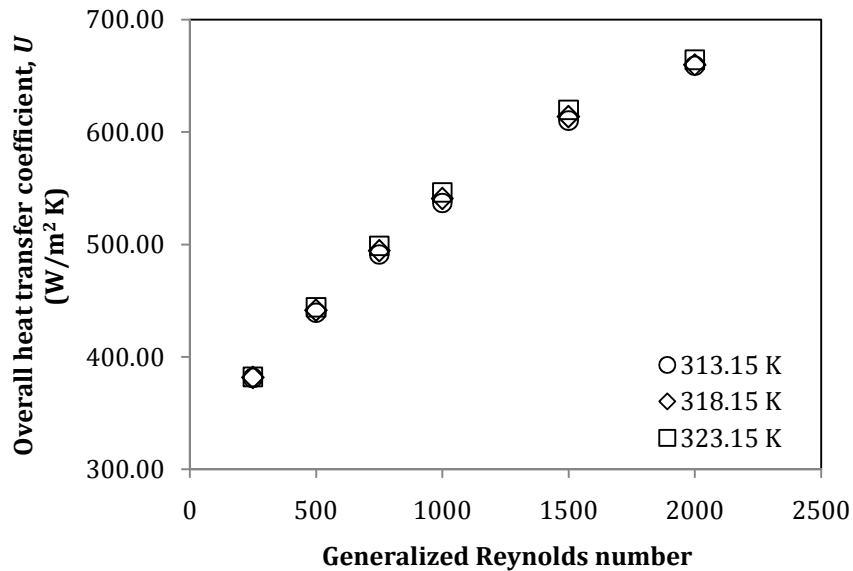


Figure 5.30: Overall heat transfer coefficient of 1000 ppm PAA in 4% Al₂O₃ nanofluid at different hot inlet temperatures.

5.5.2 Circular and non-circular ducts

The heat transfer coefficient of PAA with different concentrations in 4% Al_2O_3 nanofluid for circular and square ducts is presented in Figure 5.31. It is noted that for a fixed nanofluid concentration, increasing the PAA concentration yields a greater heat transfer coefficient for the poly-nanofluid. Besides, the heat transfer coefficient of poly-nanofluid increases significantly when the Reynolds number is higher than 1000, especially for poly-nanofluid with 1000 ppm PAA. Heat transfer coefficient obtained by adding 10 ppm PAA into nanofluid with various concentrations for circular and square ducts is shown in Figure 5.32. The heat transfer coefficient of poly-nanofluid increases with the increasing nanoparticle loading. This is ascribed to the increased thermal conductivity of poly-nanofluid with higher Al_2O_3 nanoparticle loading.

However, as seen from Figure 5.33, for the same case of 10 ppm PAA in nanofluid with different concentrations, the Nusselt number does not increase when the nanoparticle loading increases. Poly-nanofluid containing 10 ppm PAA in 4% nanofluid has the lowest Nusselt number for both circular and square ducts. The reason is that the increment in the heat transfer coefficient to that of the thermal conductivity for 10 ppm PAA in 4% nanofluid is lower when compared to those of the poly-nanofluid with lower nanofluid concentrations.

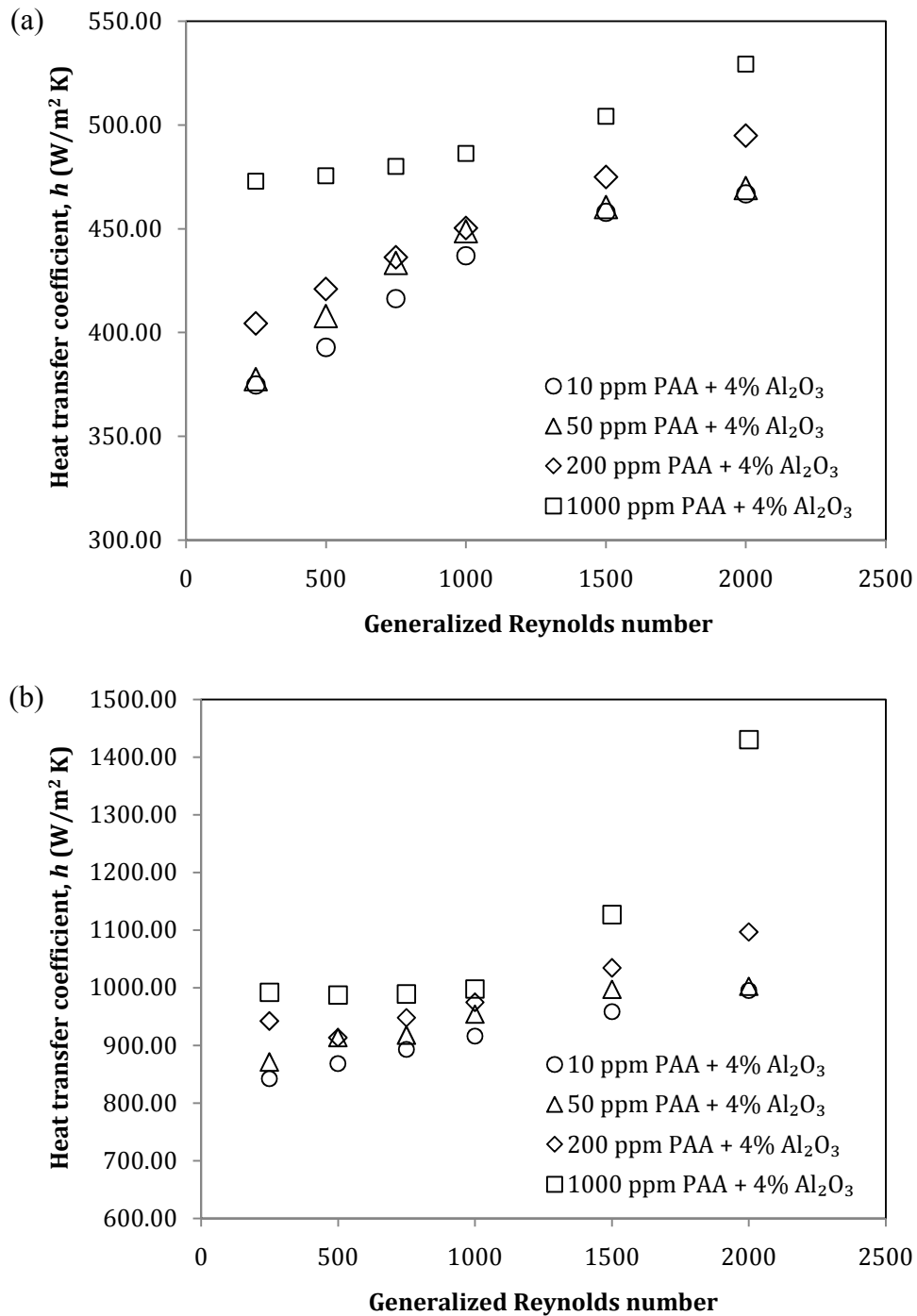


Figure 5.31: Heat transfer coefficient of PAA in 4% Al₂O₃ nanofluid for (a) circular and (b) square ducts.

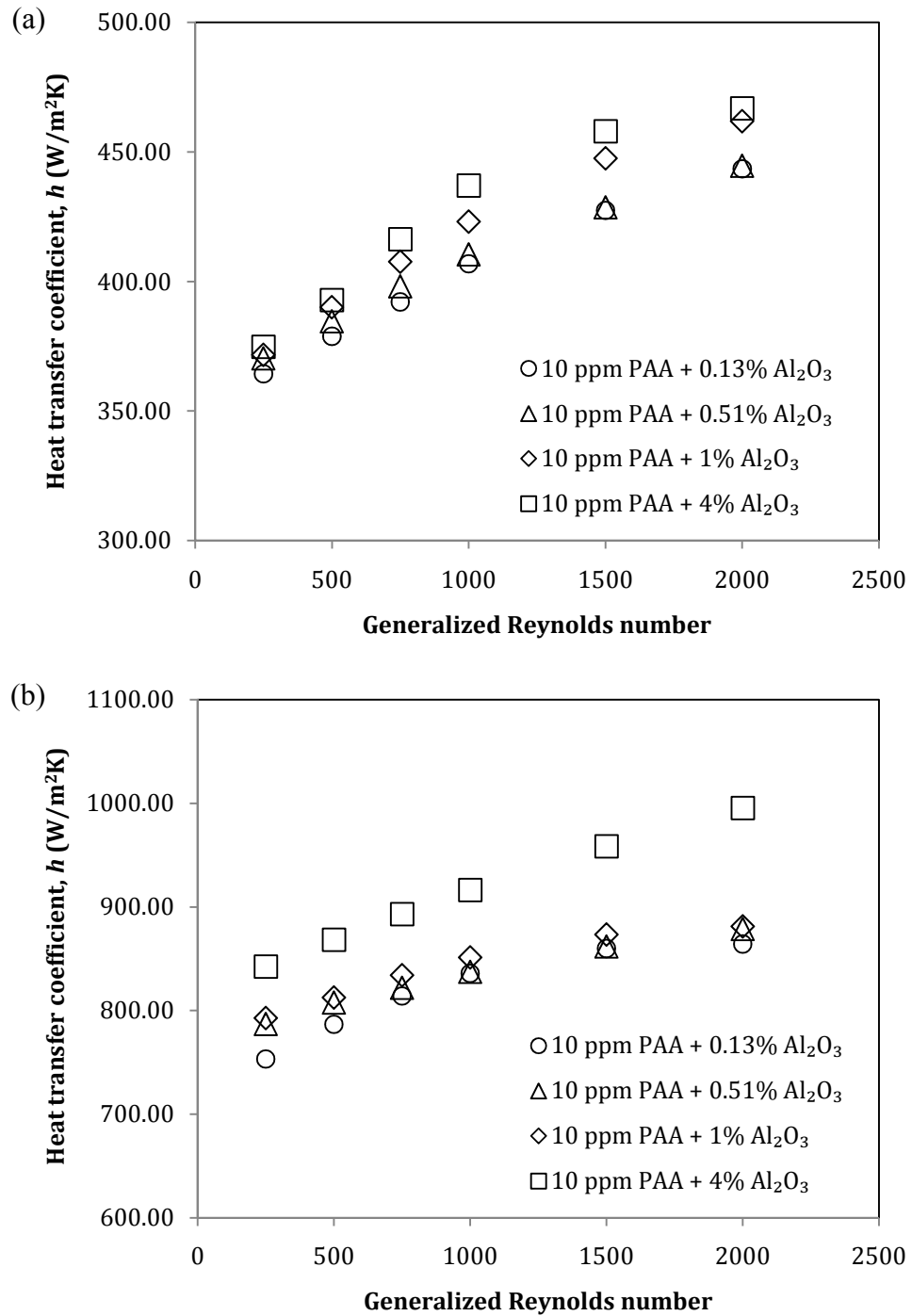


Figure 5.32: Heat transfer coefficient of 10 ppm PAA in nanofluid for (a) circular and (b) square ducts.

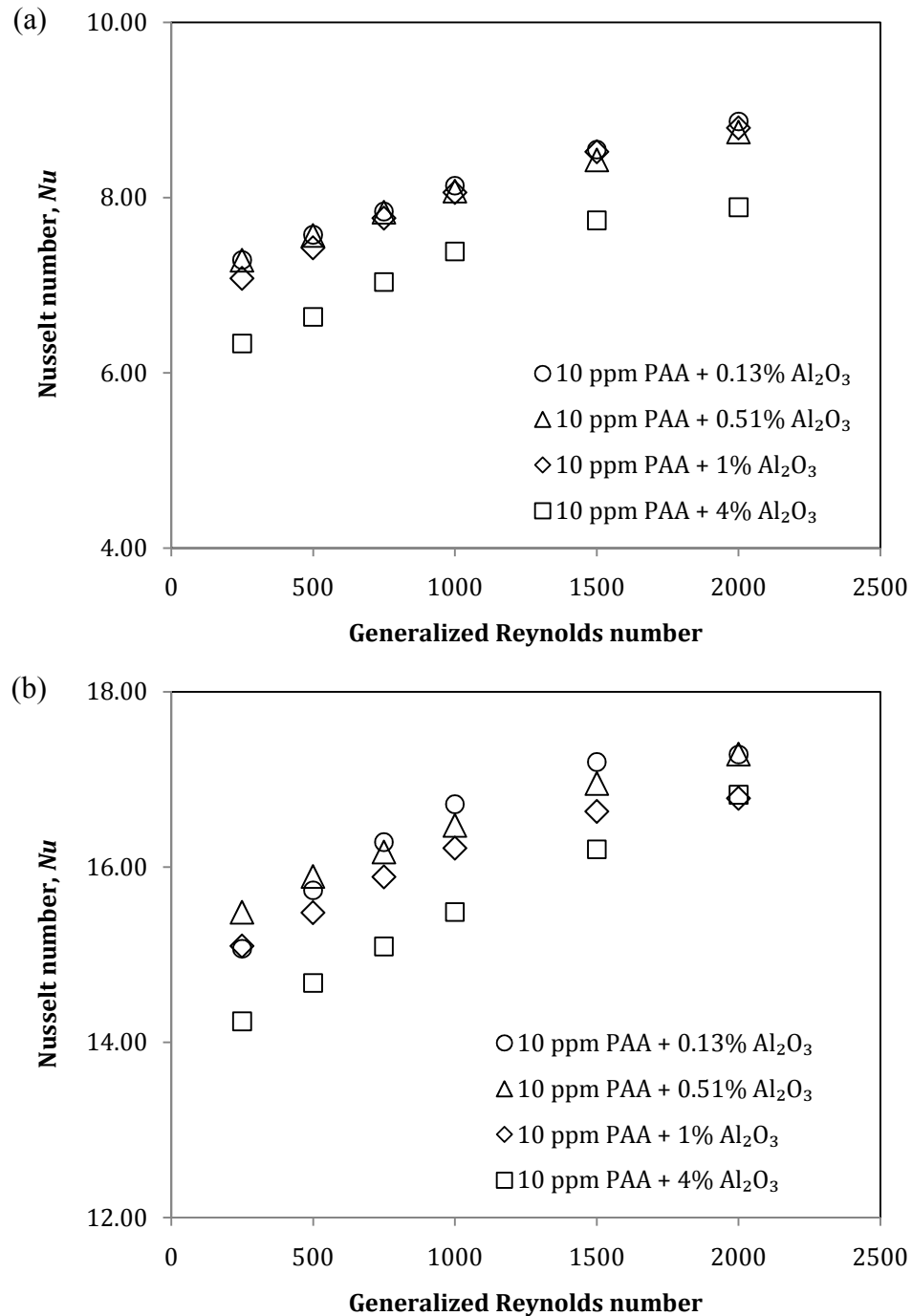


Figure 5.33: Nusselt number of 10 ppm PAA in nanofluid for (a) circular and (b) square ducts.

As discussed in the previous sections, both nanofluid and PAA solution enhance heat transfer in the circular and non-circular ducts for the laminar regime. When PAA additives are added into the nanofluid, this new solution also exhibits the heat transfer

augmentation ability. The PAA additives aids the nanofluid to achieve a much better heat transfer performance. The effect of PAA addition on the heat transfer of nanofluid is shown in Figure 5.34, which reveals that the Nusselt number ratio of poly-nanofluid to nanofluid, $Nu_{poly-nf}/Nu_{nf}$ is the highest in the square duct, followed by the 2:1 rectangular, 4:1 rectangular and circular ducts. This trend is similar to the case of PAA solution.

The heat transfer performance of poly-nanofluid in the circular pipe is not as good as those attained in the non-circular ducts. Similar to the case of double pipe heat exchanger, the poly-nanofluid behaves like purely viscous shear-thinning fluid in the circular pipe. The HTE encountered in the circular pipe is primarily attributed to the shear-thinning behaviour of the solution. The presence of secondary flow is only manifested for poly-nanofluid flowing in the non-circular ducts. The effect of secondary flow on the HTE is far stronger than the effect of shear-thinning behaviour of the solution. Therefore, the HTE in the circular pipe is lower because there is no secondary flow induced in the circular pipe.

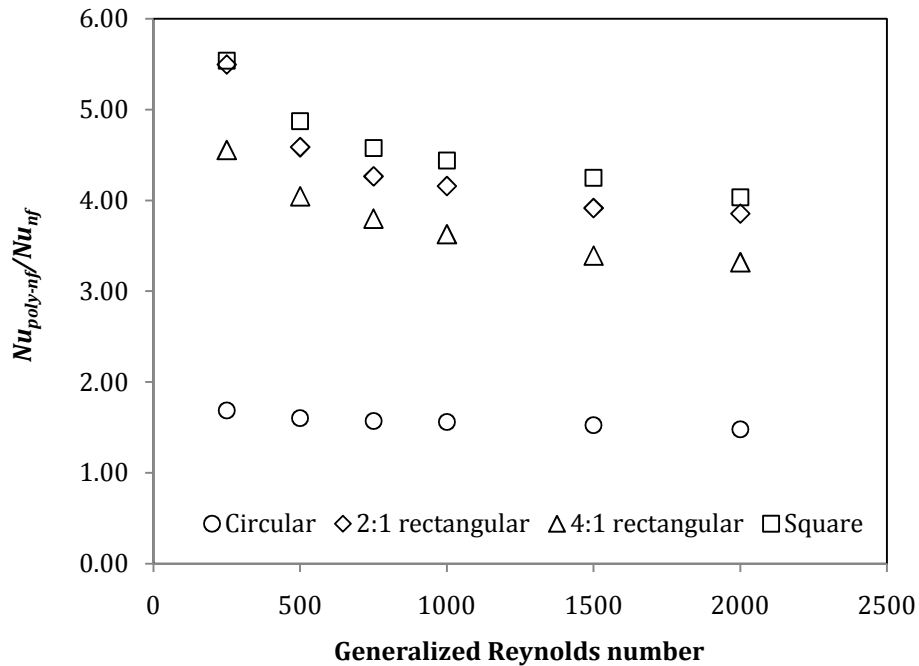


Figure 5.34: Nusselt number ratio of 1000 ppm PAA in 0.13% nanofluid to that of 0.13% nanofluid.

For the non-circular ducts, the secondary flow is the main reason for larger HTE of poly-nanofluid than that of pure nanofluid. Figure 5.35 shows the temperature contour of different solutions in the square duct. From this figure, 4% nanofluid at the centre of the duct is not heated as much as the wall is heated. When PAA additives are added, more heat is transferred from the wall to the centre of the duct. As the nanofluid or/and PAA concentration in poly-nanofluid increase, the ratio of the average temperature obtained at the outlet cross-section to the wall temperature increases. Therefore, it can be asserted that the secondary flow aids to distribute the heat. Thus the fluid at the centre of the duct can achieve a temperature closer to the wall temperature. This brings to a smaller difference between the wall and bulk temperatures, leading to higher heat transfer rate.

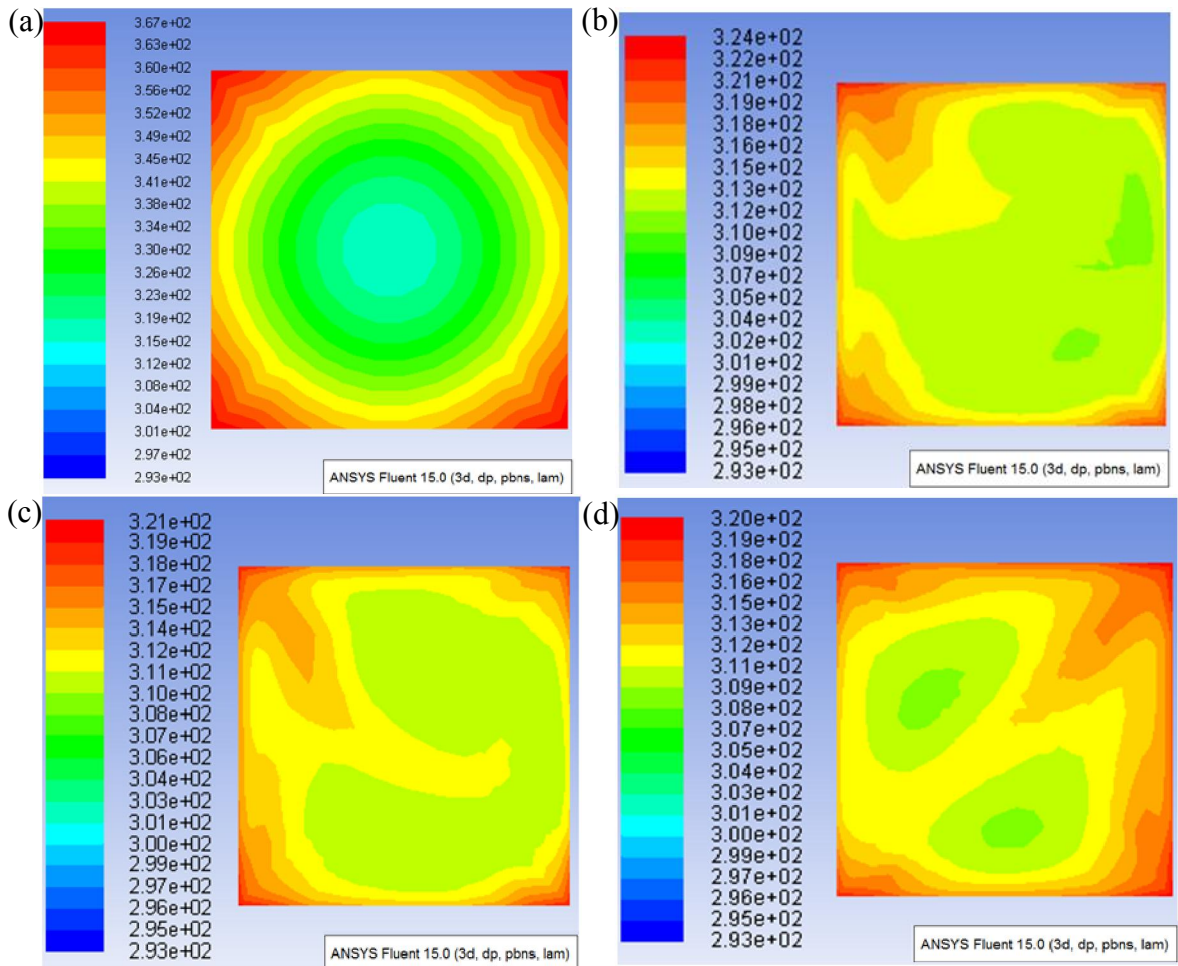
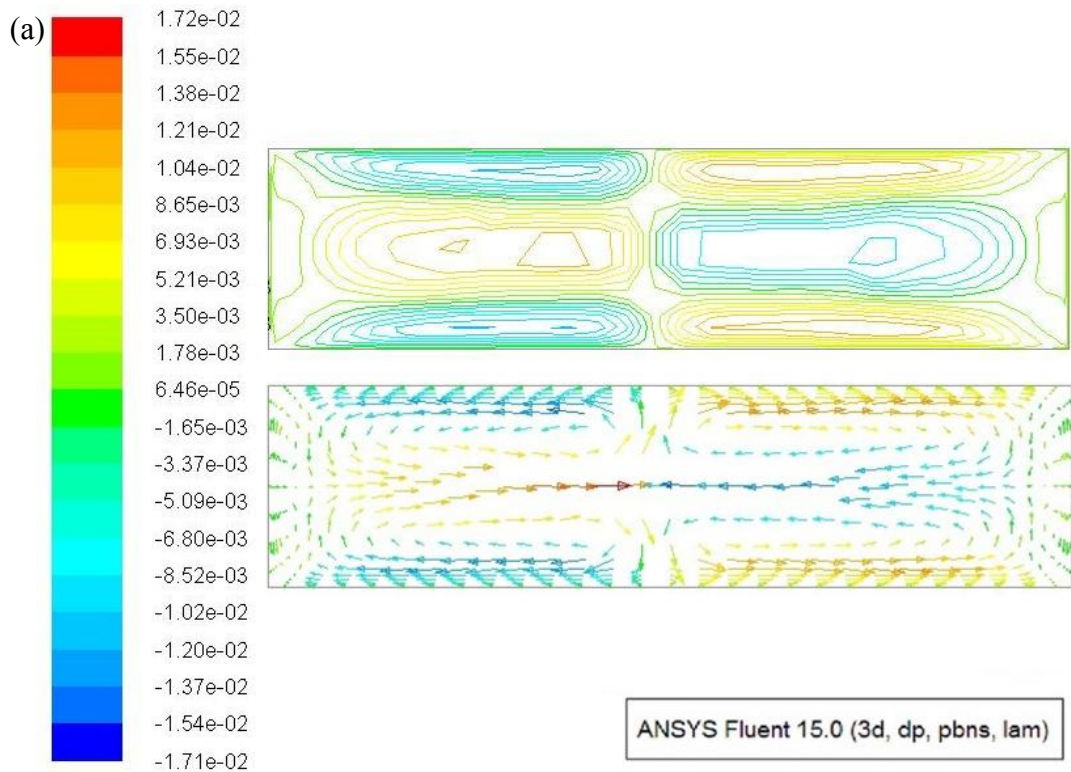


Figure 5.35: Temperature contour (K) of (a) 4% Al_2O_3 nanofluid, (b) 10 ppm PAA in 0.13% nanofluid, (c) 10 ppm PAA in 4% nanofluid and (d) 1000 ppm PAA in 4% nanofluid at the outlet cross-section of the square duct ($Re^*=250$).

The secondary flow induced in the non-circular ducts is shown in terms of velocity contour and vector plot in Figure 5.36. The plot shows that poly-nanofluid is flowing along the wall towards the corner and then leaving the corner to generate vortices. There are two dominant vortices formed in the square duct. The size of these two vortices in the square duct is found to be larger compared to those of the rectangular ducts, where larger size indicates greater strength of secondary flow. Although the number of vortices are more in the rectangular ducts, the strength of the secondary flow is distributed, thus the size of the vortices reduces.

Furthermore, it is also noticed from Figure 5.36 that there are two bigger and two smaller vortices in the 2:1 rectangular duct. The four vortices in the 4:1 rectangular duct have similar size. The two dominant vortices in the 2:1 rectangular duct have larger size compared to any of the four vortices formed in the 4:1 rectangular duct. Besides, more flow circulations are discovered in the 2:1 rectangular duct, hence, the secondary flow in the 2:1 rectangular duct is stronger than that of the 4:1 rectangular duct.



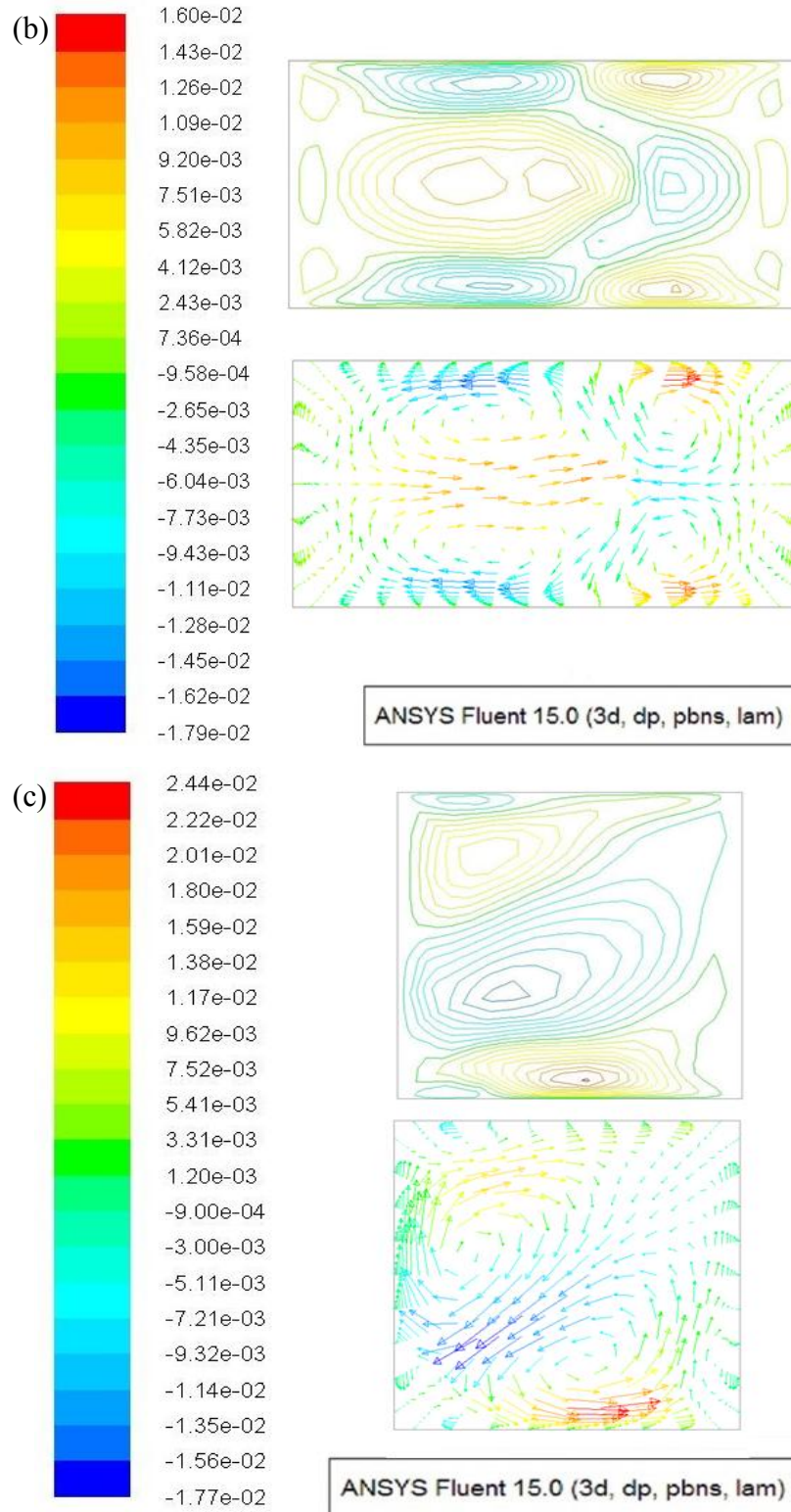
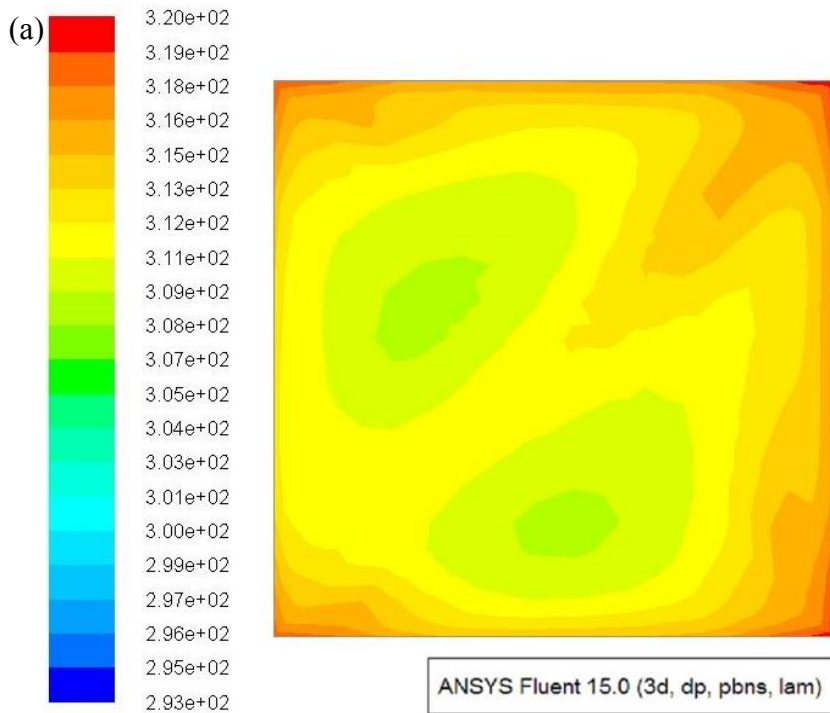


Figure 5.36: Velocity contour and vector (m/s) of secondary flow for 1000 ppm PAA in 4% nanofluid at the outlet cross-section of (a) 4:1 rectangular, (b) 2:1 rectangular and (c) square ducts ($Re^*=250$).

Since the strength of secondary flow is greater in the square duct, better heat transfer enhancement is expected. This better heat transfer enhancement can be seen from the temperature contour of poly-nanofluid as depicted in Figure 5.37. For the square duct, the velocity of secondary flow which is larger near the duct wall brings the near-wall fluid with higher temperature to the center of the duct to mix with fluid of lower temperature. Vortices with larger size in the square duct also help to better distribute the heat, thereby accelerating the energy exchange. From Figure 5.37, the bulk temperature achieved for the square duct is higher compared to the case of 2:1 and 4:1 rectangular ducts. This is because heat is better transferred to the poly-nanofluid flowing in the square duct, hence, the heat transfer enhancement is better in the square duct. Figure 5.36 and Figure 5.37 also explain the reason of the observed trend in Figure 5.34 that the magnitude of Nusselt number enhancement of poly-nanofluid (compared to pure nanofluid) is the highest in the square duct, followed by 2:1 rectangular and 4:1 rectangular ducts.



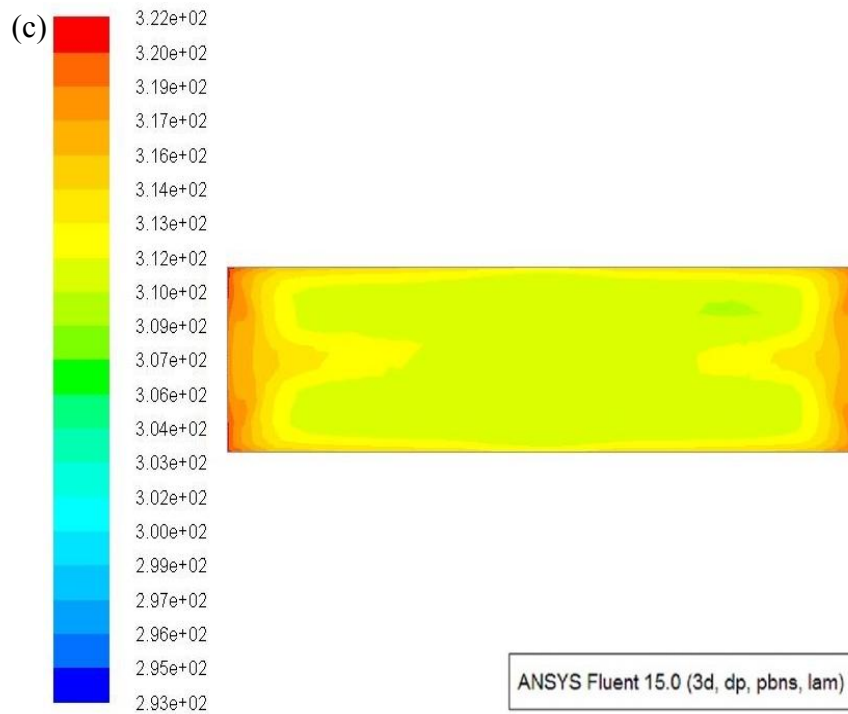
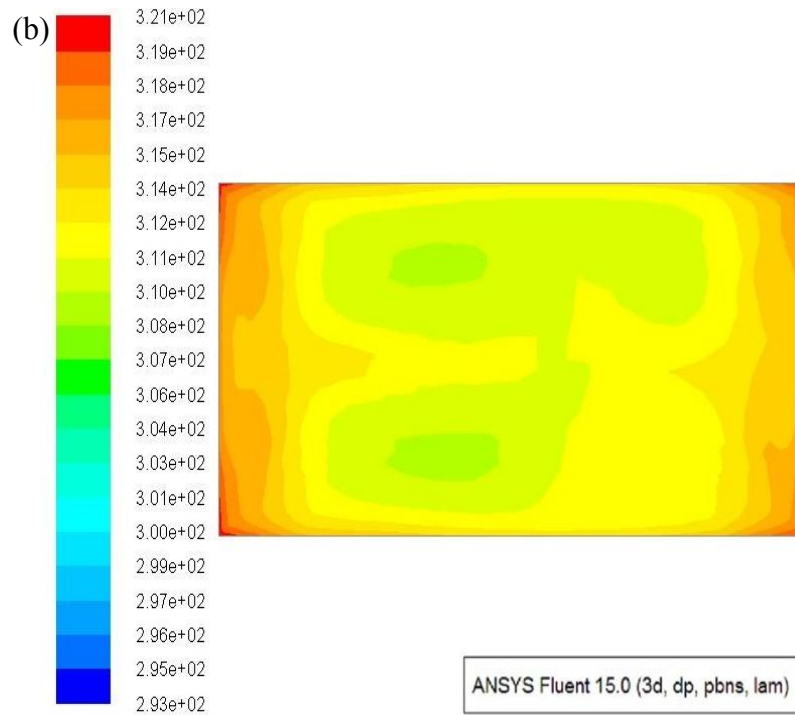


Figure 5.37: Temperature contour (K) of 1000 ppm PAA in 4% nanofluid at the outlet cross-section of (a) square, (b) 2:1 rectangular and (c) 4:1 rectangular ducts ($Re^*=250$).

The $Nu_{poly-nf}/Nu_{nf}$ for the square duct is tabulated in Table 5.4. The $Nu_{poly-nf}/Nu_{nf}$ for circular, 4:1 rectangular and 2:1 rectangular ducts are presented in Appendix I (Figure I.14 to Figure I.15 and Table I.11 to Table I.13). For the maximum enhancement achieved, the Nusselt number of poly-nanofluid is approximately 5.95 times higher compared to the value of pure nanofluid (as highlighted in the table). The maximum $Nu_{poly-nf}/Nu_{nf}$ obtained for the circular, 4:1 rectangular and 2:1 rectangular ducts are 1.80, 4.56, and 5.60, respectively.

On the other hand, the Nusselt number ratio of poly-nanofluid to PAA, $Nu_{poly-nf}/Nu_{PAA}$ for the square duct is tabulated in Table 5.5. This result for the rectangular ducts is given in Appendix I (Table I.14 to Table I.15). For all the ducts, the $Nu_{poly-nf}/Nu_{nf}$ acquired is larger compared to $Nu_{poly-nf}/Nu_{PAA}$. The Nusselt number of poly-nanofluid is not significantly different from that of the PAA solution, but is far higher than that of pure nanofluid. This again helps to confirm that the addition of PAA additives improves the heat transfer of nanofluid.

Table 5.4: $Nu_{poly-nf}/Nu_{nf}$ for square duct.

Concentration of poly-nanofluid		Generalized Reynolds number				
PAA (ppm)	Nanofluid (vol%)	250	500	1000	1500	2000
10	0.13	4.89	4.40	4.09	3.85	3.52
	0.51	5.02	4.45	4.04	3.81	3.52
	1.00	4.90	4.33	3.97	3.74	3.42
	4.00	4.56	4.04	3.74	3.58	3.37
50	0.13	5.16	4.55	4.09	3.82	3.55
	0.51	5.24	4.57	4.09	3.85	3.58
	1.00	5.36	4.67	4.19	3.96	3.72
	4.00	4.72	4.25	3.89	3.72	3.39
200	0.13	5.38	4.69	4.17	3.86	3.56
	0.51	5.31	4.59	4.11	3.89	3.67
	1.00	5.67	4.86	4.26	3.97	3.73
	4.00	5.10	4.25	3.98	3.86	3.71
1000	0.13	5.54	4.87	4.44	4.25	4.04
	0.51	5.95	5.15	4.56	4.27	3.98
	1.00	5.80	5.10	4.59	4.22	3.86
	4.00	5.38	4.60	4.07	4.20	4.84

Table 5.5: $Nu_{poly-nf}/Nu_{PAA}$ for square duct.

Concentration of poly-nanofluid		Generalized Reynolds number				
PAA (ppm)	Nanofluid (vol%)	250	500	1000	1500	2000
10	0.13	1.01	1.01	1.04	1.04	1.03
	0.51	1.03	1.02	1.02	1.02	1.03
	1.00	1.01	1.00	1.01	1.00	1.00
	4.00	0.95	0.94	0.96	0.98	1.01
50	0.13	1.01	1.02	1.01	1.00	1.02
	0.51	1.03	1.02	1.01	1.01	1.03
	1.00	1.05	1.04	1.04	1.04	1.07
	4.00	0.94	0.97	0.98	0.99	0.99
200	0.13	1.02	1.02	1.01	1.00	1.00
	0.51	1.01	1.00	0.99	1.00	1.03
	1.00	1.08	1.06	1.03	1.02	1.05
	4.00	0.98	0.94	0.98	1.01	1.06
1000	0.13	1.03	1.04	1.04	1.03	1.00
	0.51	1.10	1.10	1.07	1.03	0.99
	1.00	1.08	1.09	1.08	1.02	0.96
	4.00	1.01	1.00	0.97	1.03	1.22

5.6 Correlation to predict the Nusselt number of poly-nanofluid in circular and non-circular ducts

Equations 5.1 and 5.2 (Khairul et al. 2017), Equation 5.3 (Moraveji and Esmaeili 2012), and Equation 5.4 (Maiga et al. 2005) are some of the existing Nusselt number correlations for nanofluids. These existing correlations are used to predict the Nusselt number of poly-nanofluid and the result is depicted in Figure 5.38. From Figure 5.38, it is noticed that all these four existing Nusselt number correlations for nanofluids fail to estimate the Nusselt number of poly-nanofluid in the circular pipe.

For Al_2O_3 /water nanofluid in laminar regime:

$$Nu = 0.86(Re)^{0.205}(Pr)^{0.33}(\varphi_{nf})^{0.1} \quad (5.1)$$

For CuO/water nanofluid in laminar regime:

$$Nu = 1.04(Re)^{0.205}(Pr)^{0.33}(\varphi_{nf})^{0.1} \quad (5.2)$$

$$Nu = 0.716(Re)^{0.314}(Pr)^{0.6}(\varphi_{nf})^{0.3} \quad (5.3)$$

-for $1\% \leq \varphi_{nf} \leq 4\%$, $250 \leq Re \leq 1050$

$$Nu = 0.086(Re)^{0.55}(Pr)^{0.5} \quad (5.4)$$

-for constant heat flux, $\varphi_{nf} \leq 10\%$, $Re \leq 1000$

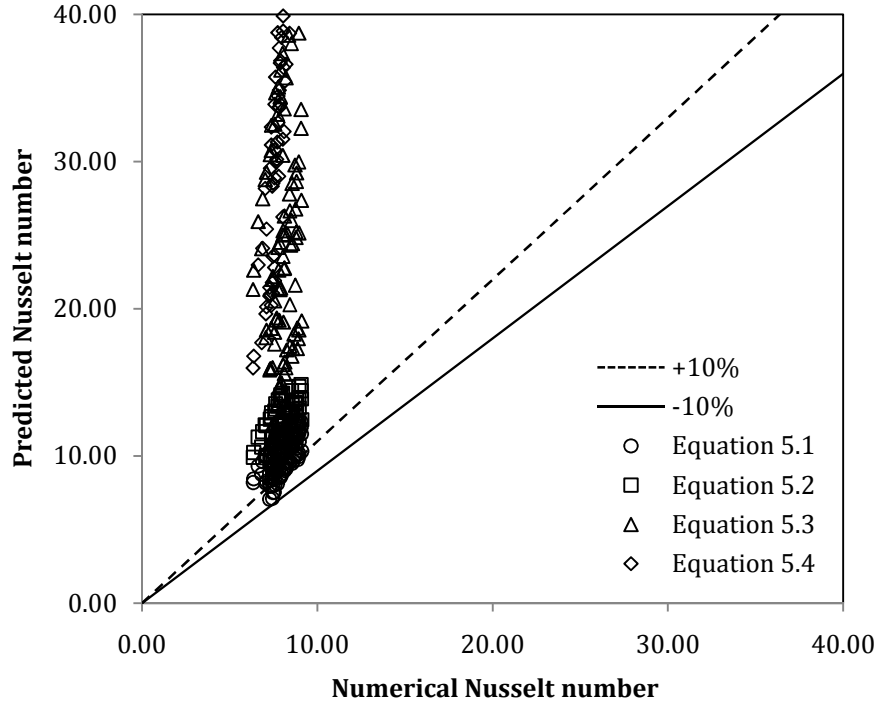


Figure 5.38: Comparison of numerical and predicted Nusselt number of poly-nanofluid (circular pipe) based on Equations 5.1 to 5.4.

Therefore, new correlations are proposed to predict the Nusselt number of poly-nanofluid in different geometries. They are obtained using the multiple regression method. These new correlations are presented in Equations 5.5, 5.6, 5.7 and 5.8 for the circular pipe, square, 2:1 rectangular and 4:1 rectangular ducts, respectively. The proposed correlations are functions of generalized Reynolds number, Prandtl number, nanofluid volume fraction and PAA concentration (in fraction).

$$Nu = 2.011(Re')^{0.1160}(Pr)^{0.1384}(\varphi_{nf})^{0.0002}(\varphi_{PAA})^{0.0056} \quad R^2 = 0.9035 \quad (5.5)$$

$$Nu = 9.198(Re^*)^{0.0626}(Pr)^{0.0821}(\varphi_{nf})^{0.0004}(\varphi_{PAA})^{0.0213} \quad R^2 = 0.8229 \quad (5.6)$$

$$Nu = 11.409(Re^*)^{0.0560}(Pr)^{0.0591}(\varphi_{nf})^{0.0004}(\varphi_{PAA})^{0.0271} \quad R^2 = 0.8088 \quad (5.7)$$

$$Nu = 7.134(Re^*)^{0.0706}(Pr)^{0.1603}(\varphi_{nf})^{0.0223}(\varphi_{PAA})^{0.0242} \quad R^2 = 0.8165 \quad (5.8)$$

Validation of the proposed correlations is made by comparing the present numerical Nusselt number with the prediction from Equations 5.5 to 5.8. These results are shown in Figure 5.39 to Figure 5.42 for the circular pipe, square, 2:1 rectangular and 4:1 rectangular ducts, respectively. There are good agreements between the numerical

Nusselt number and the predicted values from the newly introduced correlations. Maximum deviations of +6.40% and -6.80%, +6.60% and -7.30%, +7.40% and -7.60% as well as +8.40% and -8.00% are observed for the circular, square, 2:1 rectangular and 4:1 rectangular ducts, respectively. These correlations are valid for $0.13\% \leq \varphi_{nf} \leq 4\%$, $10 \text{ ppm} \leq \varphi_{PAA} \leq 1000 \text{ ppm}$, $250 \leq Re^*$ or $Re' \leq 2000$, and $Pr > 50$.

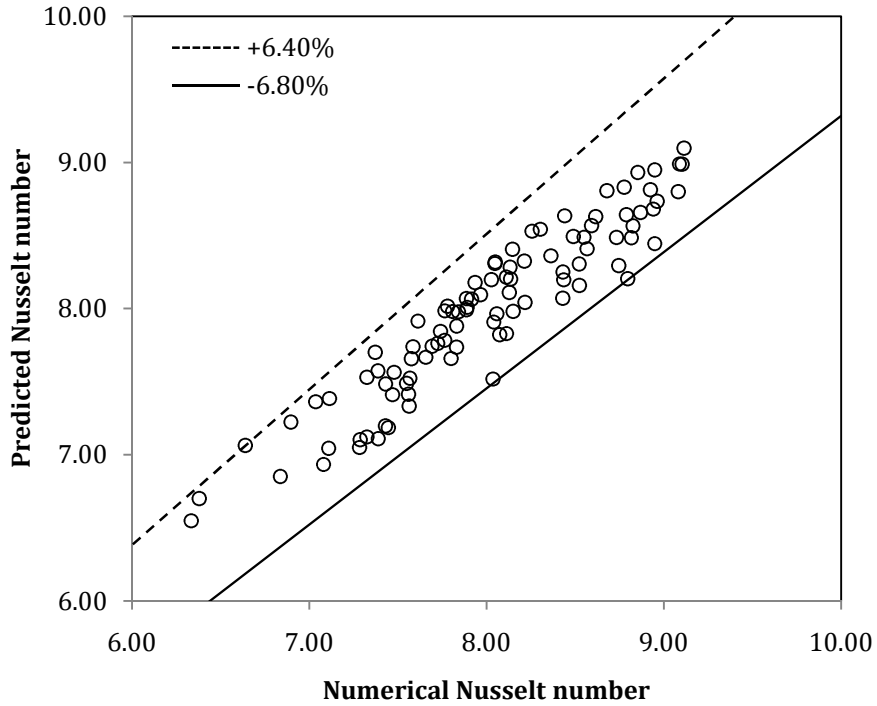


Figure 5.39: Comparison of numerical and predicted Nusselt number of poly-nanofluid in circular pipe based on new correlation (Equation 5.5).

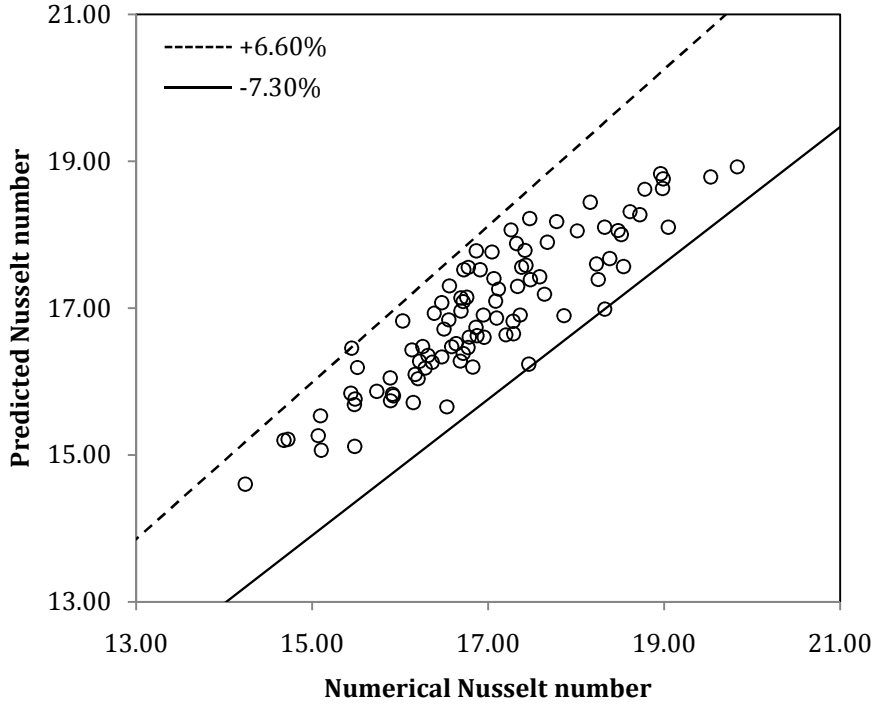


Figure 5.40: Comparison of numerical and predicted Nusselt number of poly-nanofluid in square duct based on new correlation (Equation 5.6).

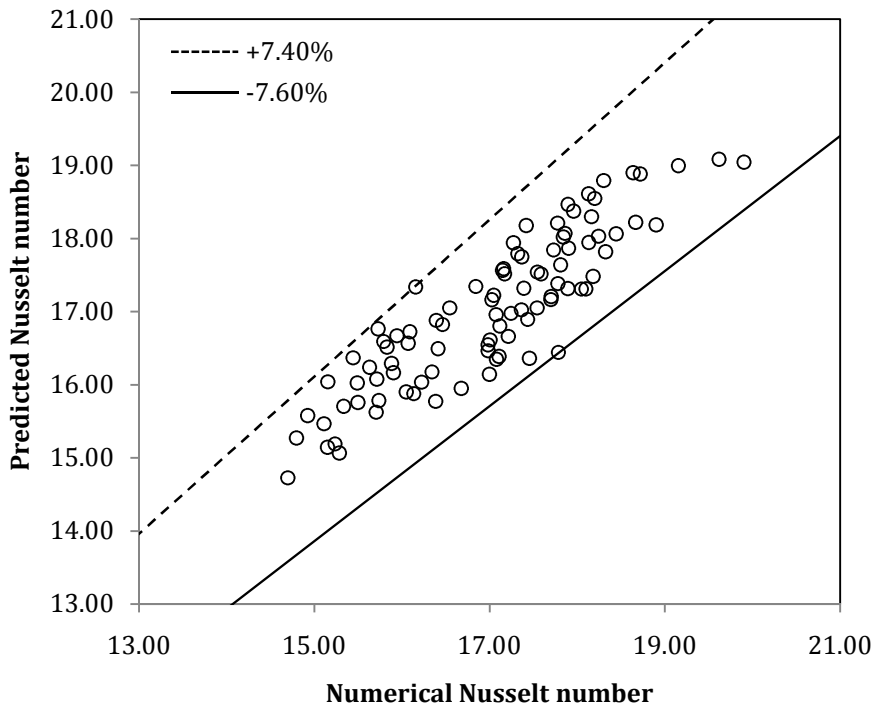


Figure 5.41: Comparison of numerical and predicted Nusselt number of poly-nanofluid in 2:1 rectangular duct based on new correlation (Equation 5.7).

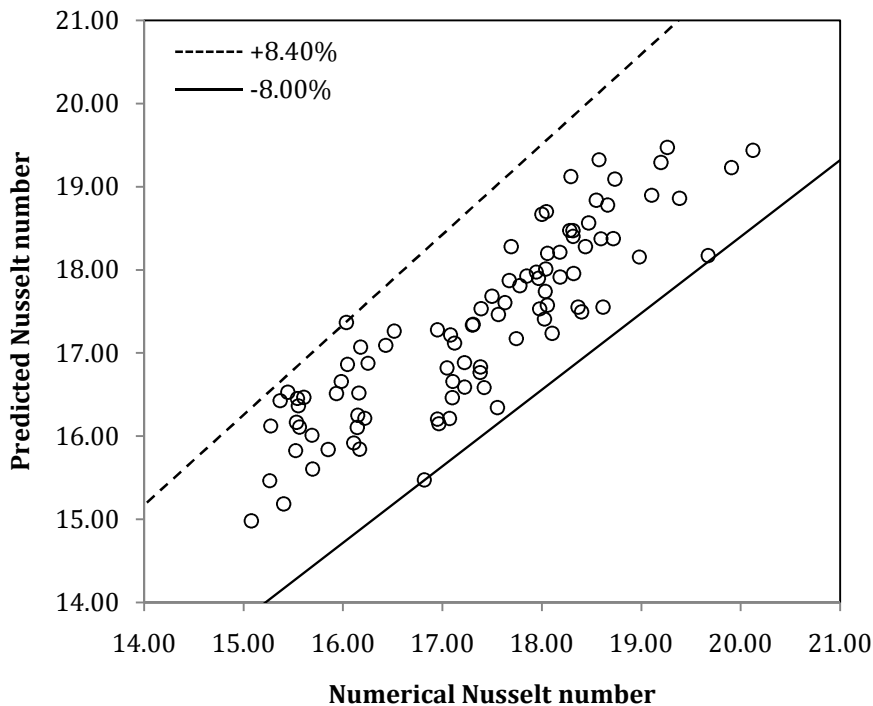


Figure 5.42: Comparison of numerical and predicted Nusselt number of poly-nanofluid in 4:1 rectangular duct based on new correlation (Equation 5.8).

5.7 Summary

The heat transfer studies show that:

1. Al_2O_3 nanofluid improves the heat transfer in the double pipe heat exchanger, circular and non-circular ducts.
 - This HTE is attributed to the increased thermal-conductivity of nanofluid with relative to that of the base fluid.
 - The Nusselt number of nanofluid is found to be the highest in the circular pipe. Nevertheless, when compared to water, the Nusselt number enhancement of nanofluid in the non-circular ducts is higher than the enhancement in the circular pipe.
2. It is ascertained that the temperature effect on the thermo-physical properties must be considered for heat transfer study.

- For all the geometries studied, the heat transfer rate of nanofluid computed from the single-phase temperature-independent properties is greater than that of the temperature-dependent properties.
 - The variation of thermal-conductivity with temperature is not considered when temperature-independent approach is used. Therefore, the thermal-conductivity of nanofluid is always high even at low temperature, hence, resulting in higher heat transfer estimated compared to that of the temperature-dependent approach.
3. The heat transfer results estimated from the two-phase mixture, Eulerian and VOF models are similar at a particular Reynolds number and nanofluid concentration.
 4. The two-phase models predict higher heat transfer of nanofluid compared to that of the single-phase model, especially when the concentration is high.
 - This is because the thermal-conductivity of nanofluid predicted from the two-phase models is higher compared to the value obtained from the single-phase model.
 5. It is concluded that the single-phase model is adequate to predict the heat transfer of nanofluid to a reasonably good accuracy. The single-phase approach is also chosen to model the heat transfer of poly-nanofluid due to its simplicity.
 6. PAA solution also enhances heat transfer.
 - With a low concentration of 10 ppm, the overall heat transfer coefficient of PAA solution in the double pipe heat exchanger is three times higher relative to water.
 - The HTE in the circular pipe (including double pipe heat exchanger) is ascribed to the purely viscous shear-thinning characteristic of the solution.
 - In contrast, the presence of secondary flow is the primary reason for the heat transfer augmentation in the non-circular ducts.
 - The heat transfer of PAA solution in the non-circular ducts is better than in the heat exchanger and circular pipe.
 - The Nusselt number augmentation of PAA solution is the highest in the square duct, with the maximum enhancement of approximately 5.40 times when compared to water.
 - The intensity of the secondary flow is higher in duct with higher aspect ratio.

7. When PAA additives are added into Al_2O_3 nanofluid, the heat transfer of nanofluid is further augmented.
 - The heat transfer rate of poly-nanofluid increases when nanoparticles or PAA concentration increases.
 - The reason of HTE of poly-nanofluid in the circular pipe is ascribed to the increased thermal conductivity and the shear-thinning characteristic of the solution, where the latter has the dominant effect.
 - The presence of secondary flow induces higher heat transfer augmentation of poly-nanofluid in the non-circular ducts than that of the circular pipe.
 - Similar to PAA solution, the heat transfer is enhanced the most in the square duct, with the maximum $Nu_{poly-nf}/Nu_{bf}$ of 5.95.
8. Correlations are proposed for the Nusselt number of poly-nanofluid in the circular and non-circular ducts. They are valid for the Reynolds number, Prandtl number and concentration ranges investigated. The maximum error of these proposed correlations is less than 10%.

CHAPTER 6: FLOW FEATURE OF NANOFLUID, POLYMER AND POLY-NANOFLUID

6.1 Introduction

The flow feature of nanofluid, PAA solution and poly-nanofluid are studied in terms of their pressure drop and friction factor. Chapter 6 consists of three main parts, which are the flow behaviour of nanofluid, PAA solution and poly-nanofluid. This chapter begins with the validation of numerical pressure drop and friction factor of water, nanofluid and PAA solution against the analytical values. This chapter also compares the pressure drop of nanofluid obtained in different geometries using the single and two-phase models. Furthermore, the pressure drop and friction factor of PAA solution and poly-nanofluid in the double pipe heat exchanger, circular and non-circular ducts are also discussed. The influence of PAA additives on the flow behaviour of nanofluid is evaluated. Lastly, a friction factor correlation is proposed to estimate the friction factor of poly-nanofluid in different geometries.

6.2 Result validation

6.2.1 Water

To ensure the reliability of the numerical model, the numerical pressure drop of water in the double pipe heat exchanger was compared with the analytical pressure drop predicted from Equation 3.87 (in Chapter 3). Error bars of 10% are given for the analytical pressure drop value in Figure 6.1. The numerical pressure drop observes a good trend with the analytical value, with the deviation smaller than 10%.

Furthermore, the numerical friction factor of water obtained in the circular and non-circular ducts were validated against the values from the theoretical correlations (Incropera et al. 2011). The results for laminar friction factor of water in the circular and 2:1 rectangular ducts are presented in Figure 6.2. The friction factor obtained for both ducts agree reasonably with the values estimated from the theoretical correlations.

The friction factor results attained for the 4:1 rectangular and square ducts are given in Appendix H (Figure H.1).

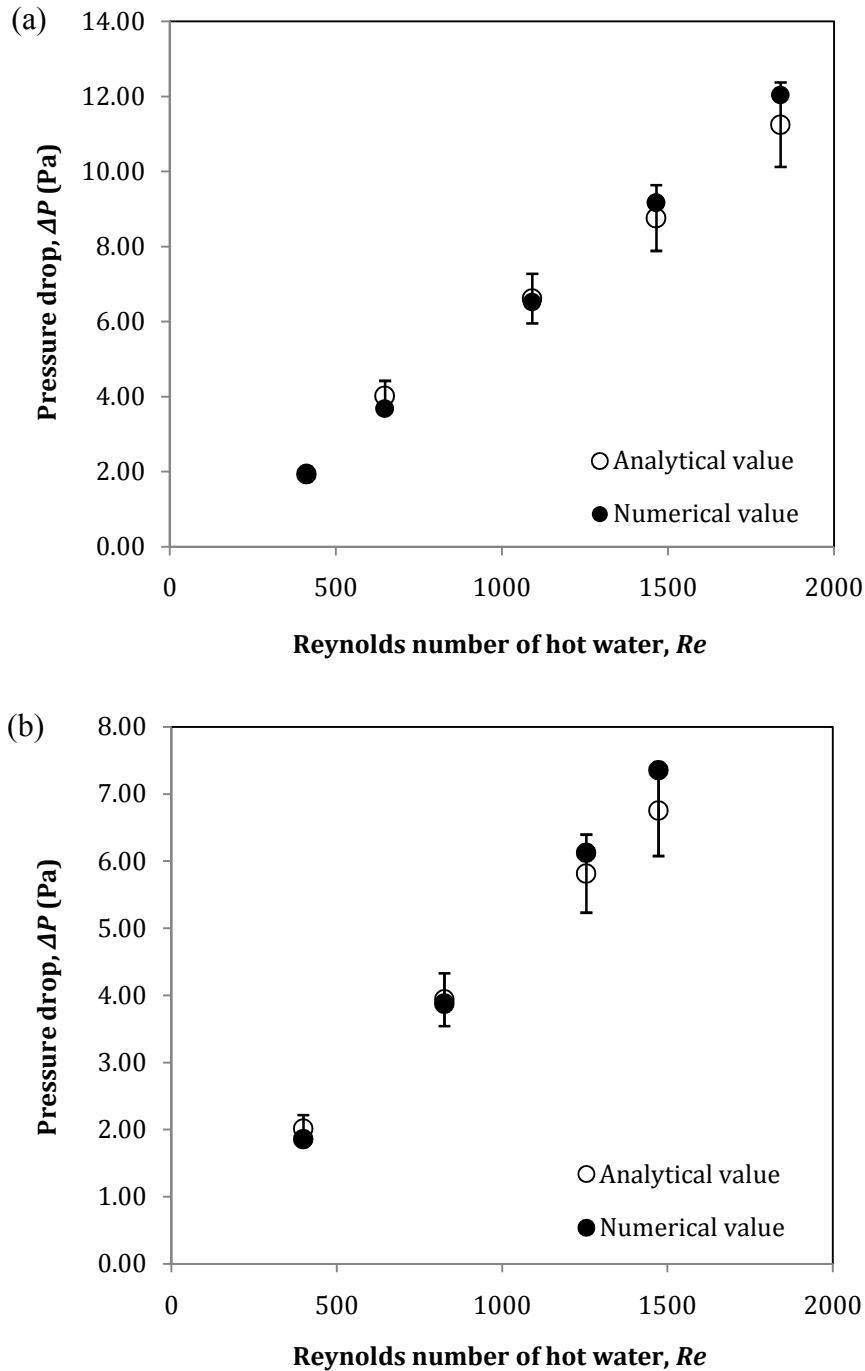


Figure 6.1: Pressure drop of water in the double pipe heat exchanger at hot inlet temperatures of (a) 313.15 K and (b) 323.15 K.

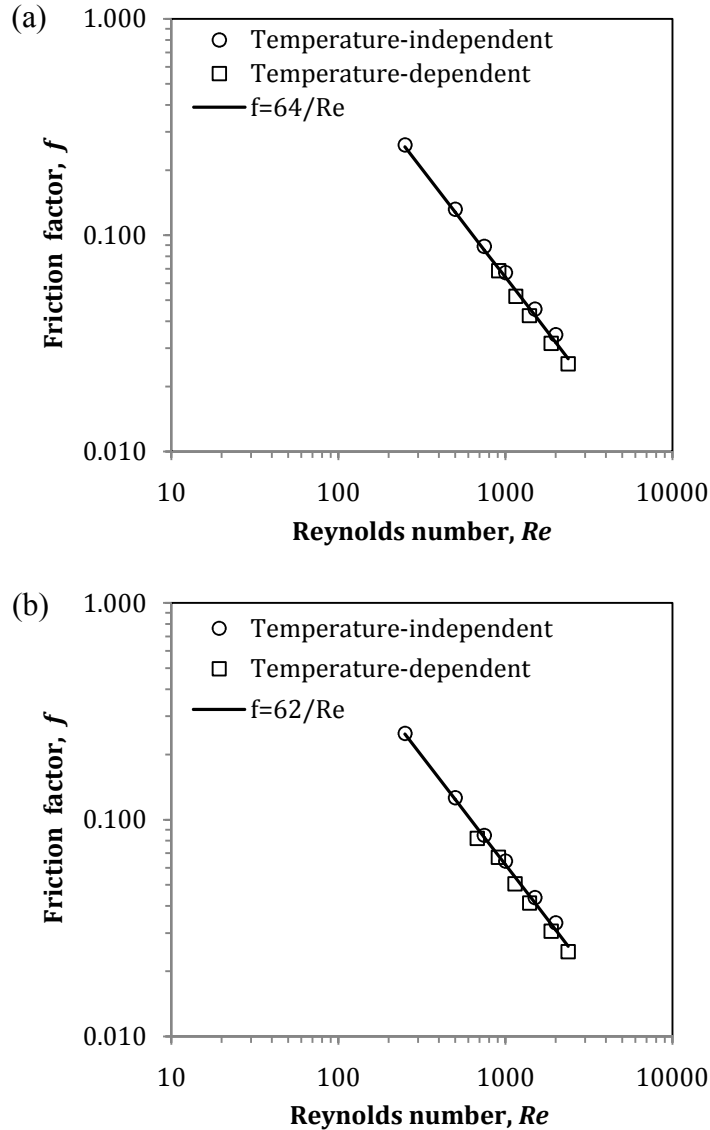
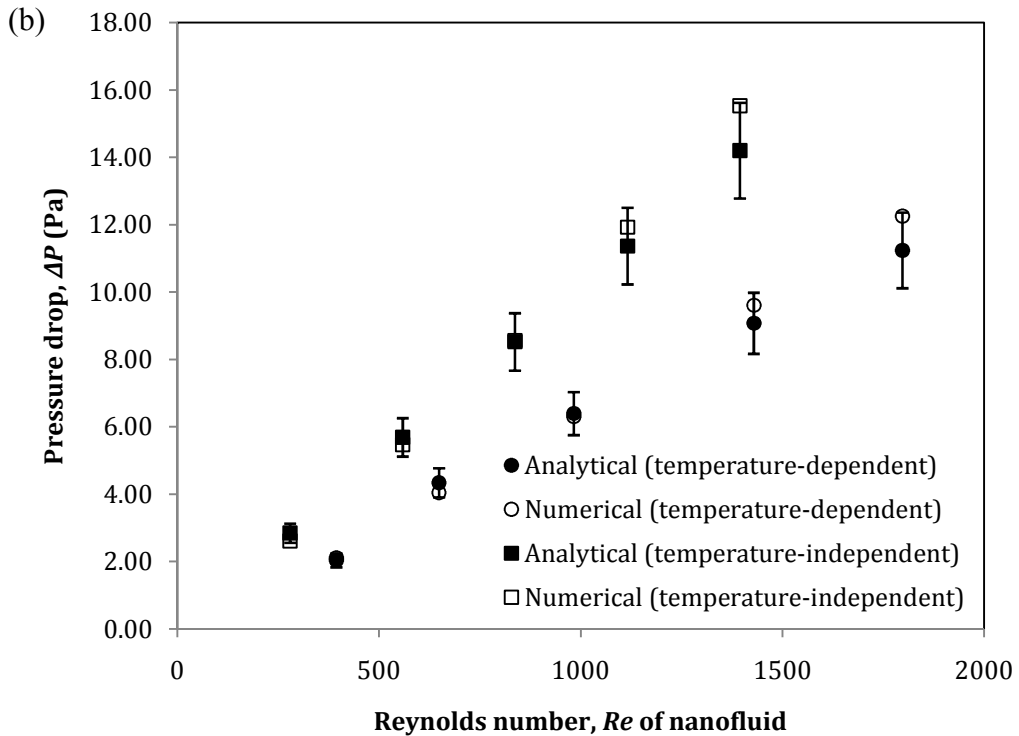
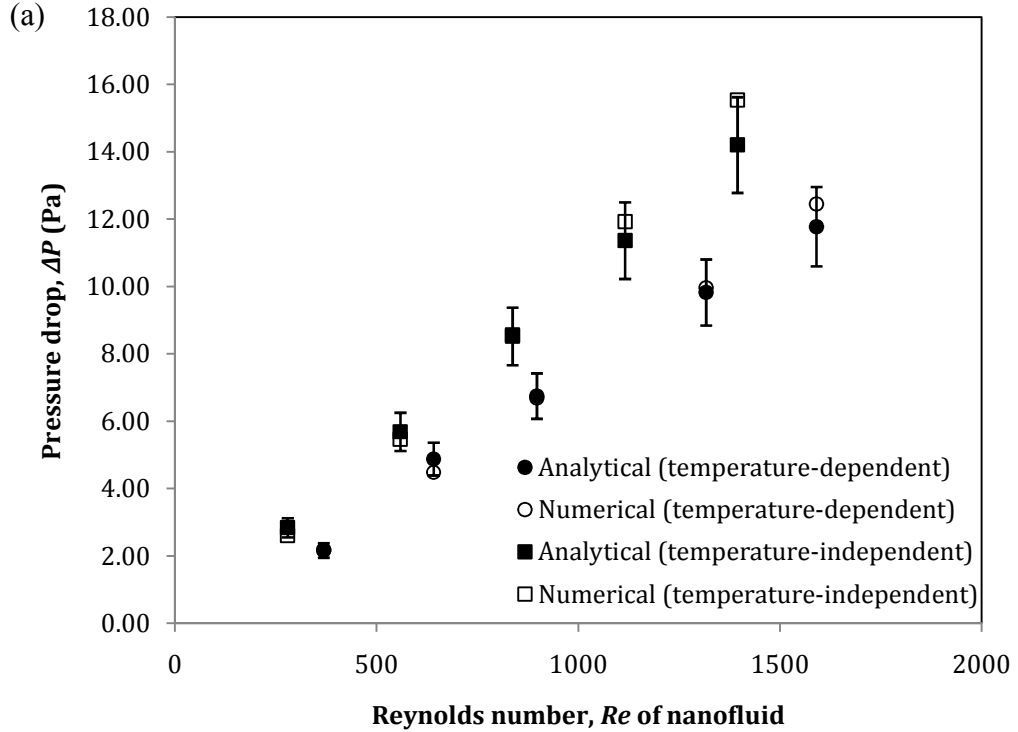


Figure 6.2: Friction factor for water in (a) circular and (b) 2:1 rectangular ducts for temperature-independent and temperature-dependent properties.

6.2.2 Al_2O_3 nanofluid

The numerical pressure drop of nanofluid computed for the double pipe heat exchanger was also compared with the analytical value calculated from Equation 3.87 to ensure the accuracy of the present model and numerical approach. This comparison for 0.10% nanofluid is presented in Figure 6.3. Error bars of 10% are presented for both the pressure drop acquired analytically using the temperature-independent and temperature-dependent properties. This figure shows a remarkable agreement between the numerical

and analytical pressure drop for all the three temperatures studied, in both cases of temperature-dependent and temperature-independent approaches. In both cases, the deviation is within 10%.



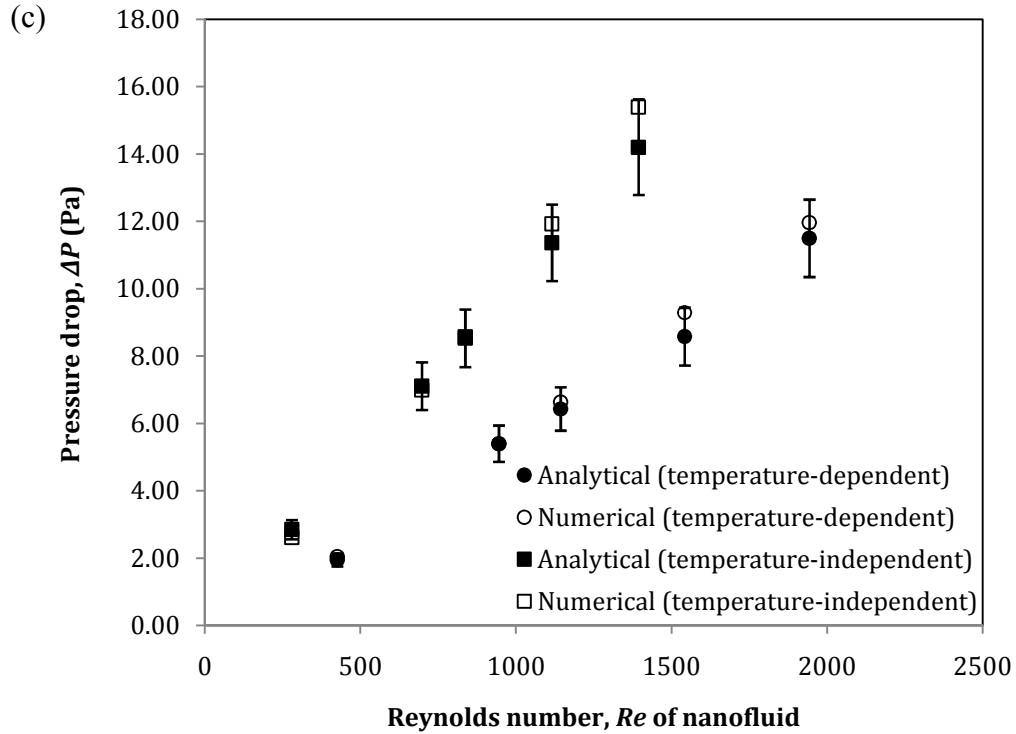


Figure 6.3: Pressure drop of 0.10% nanofluid at hot inlet temperatures of (a) 313.15 K, (b) 318.15 K and (c) 323.15 K.

6.2.3 PAA solution

To ensure the credibility and precision of the friction factor of the PAA solution, the numerical results were compared with data from the correlation available in the literature. The friction factor of 1000 ppm PAA solution was compared with that of the Koziicki's power law non-Newtonian model, $f=16/Re'$ (Hartnett and Kostic 1985). It is noticed from Figure 6.4 that the numerical friction factor is in very good agreement with the value from the correlation. The errors are approximately 0.07–5.47%. Therefore, the soundness of the numerical procedure for the PAA solution in terms of the flow behaviour is confirmed.

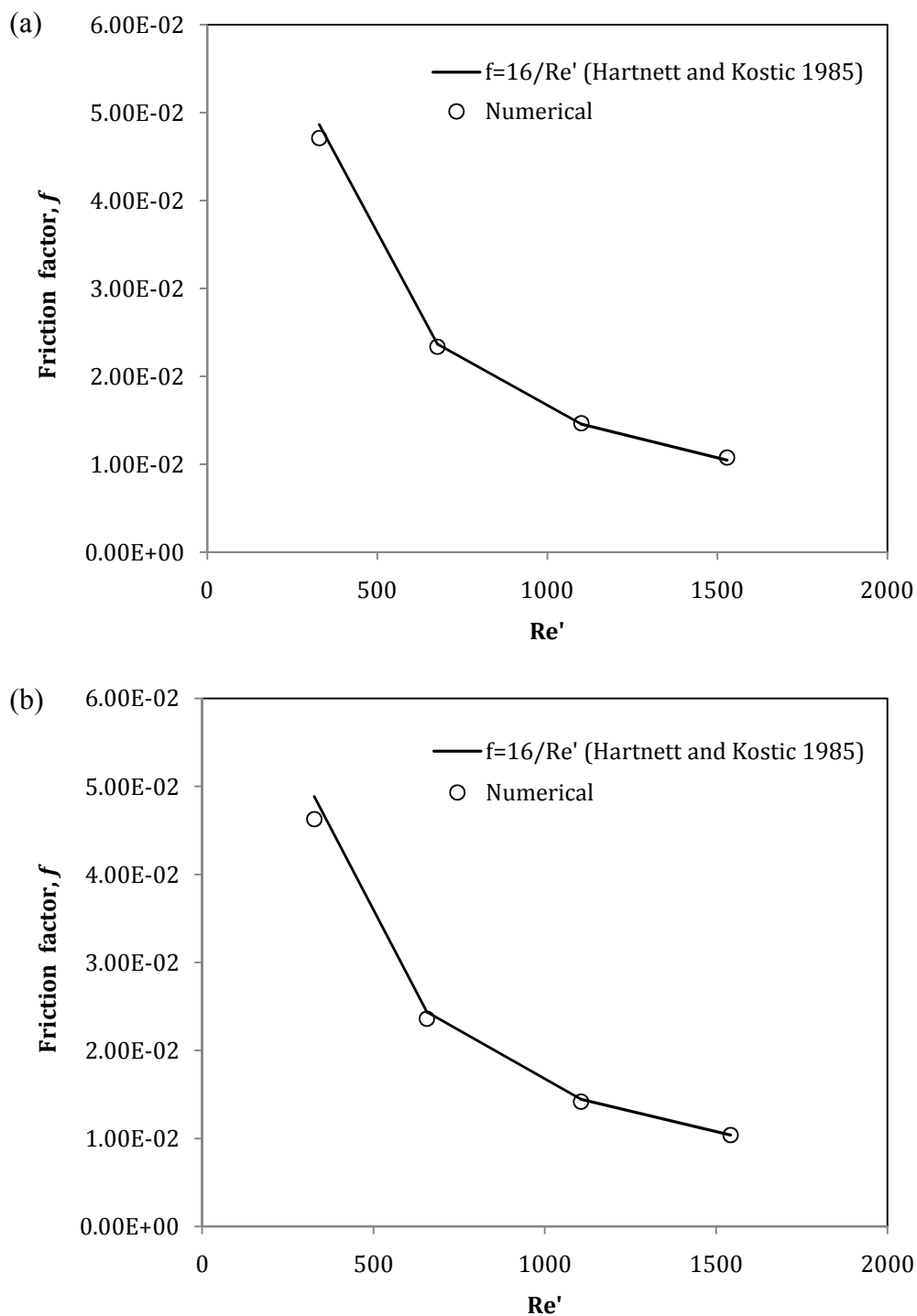


Figure 6.4: Comparison of friction factor for 1000 ppm PAA at the hot inlet temperatures of (a) 313.15 K and (b) 323.15 K.

6.3 Flow feature of Al_2O_3 nanofluid

6.3.1 Pressure drop in double pipe heat exchanger (single-phase modelling)

The pressure drop of nanofluid at the hot inlet temperature of 323.15 K is shown in Figure 6.5. It is obvious that the pressure drop of the nanofluid is far higher than the value of water. The increased pressure drop is due to the increased viscosity of nanofluid relative to that of the base fluid. Besides, the pressure drop of the nanofluid increases when the nanoparticle loading is raised from 0.51% to 1% and 4%. Conversely, the pressure drop for nanofluid concentration lower than 1% is similar. This is because the viscosity of the nanofluid with concentration lower than 1% is similar, but it increases remarkably when the concentration is further increased to 4%. The increase in viscosity causes higher wall shear stress, which is responsible for the higher pressure drop. This is observed in Figure 6.6 which shows the wall shear stress of nanofluid with different concentrations.

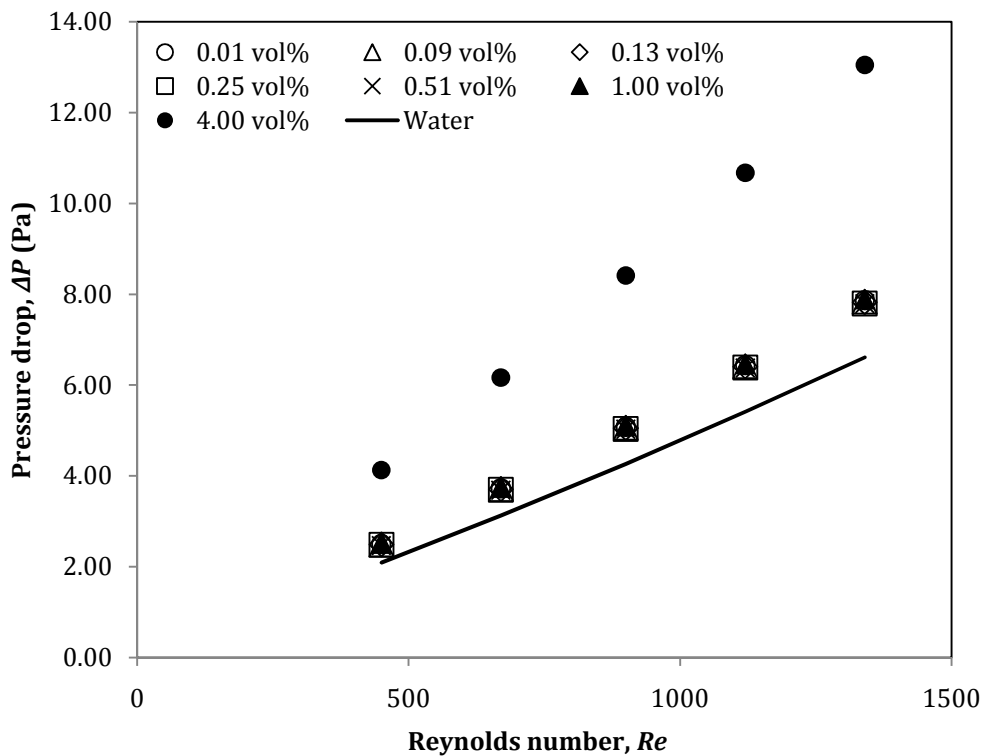


Figure 6.5: Pressure drop of nanofluid at hot inlet temperature of 323.15 K.

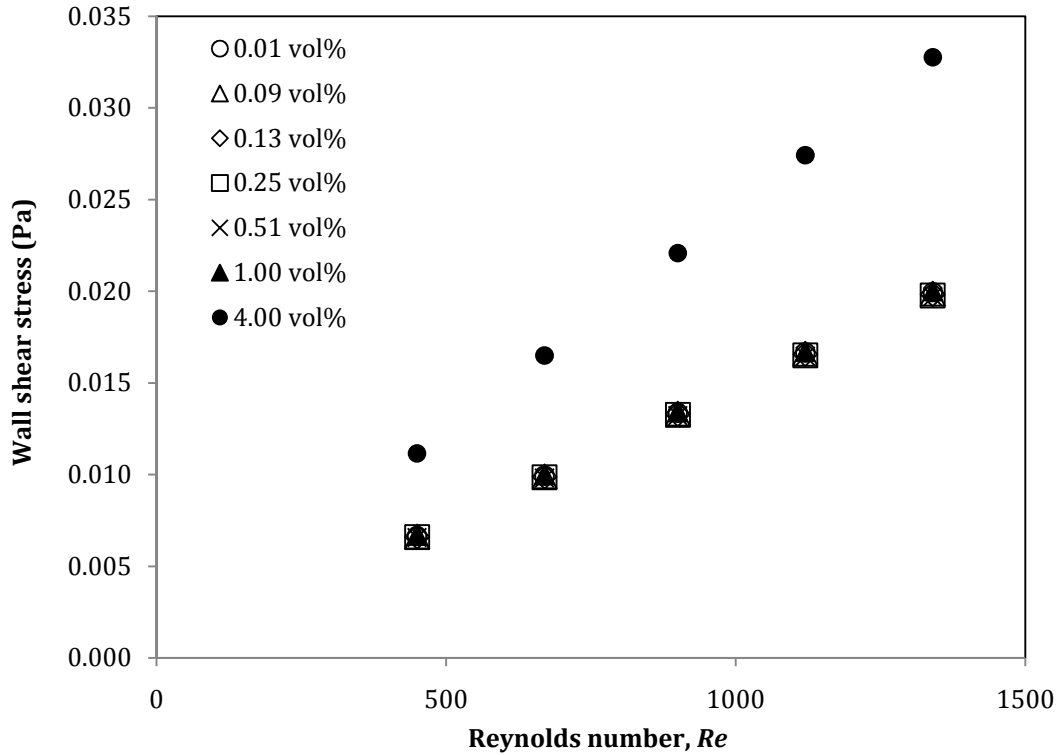


Figure 6.6: Wall shear stress of nanofluid at hot inlet temperature of 323.15 K.

The pressure drop of 4% nanofluid at various temperatures is illustrated in Figure 6.7. The pressure drop of nanofluid decreases with the increasing temperature. When the fluid temperature is raised, the viscosity of nanofluid decreases. Lower nanofluid viscosity means lower wall shear stress. Consequently, the pressure drop of nanofluid also reduces.

As shown in Figure 6.8, the magnitude of ΔP increment decreases slightly with the increasing temperature. The ΔP increment of 4% Al_2O_3 nanofluid at the temperature of 313.15 K, 318.15 K, 323.15 K are 106%, 102 % and 97%, respectively, at the Reynolds number of 1300. The dependence of ΔP increment on the temperature at a particular nanoparticle loading is not significant for the temperature range considered in this present study.

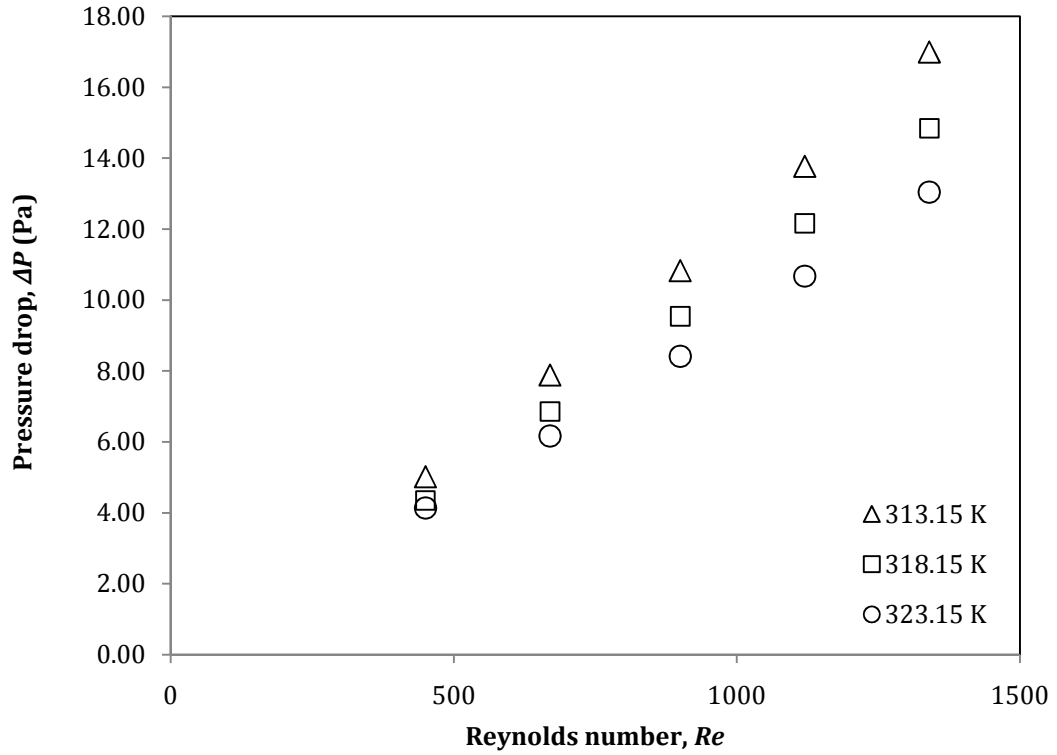


Figure 6.7: Pressure drop of 4% nanofluid at different hot inlet temperatures.

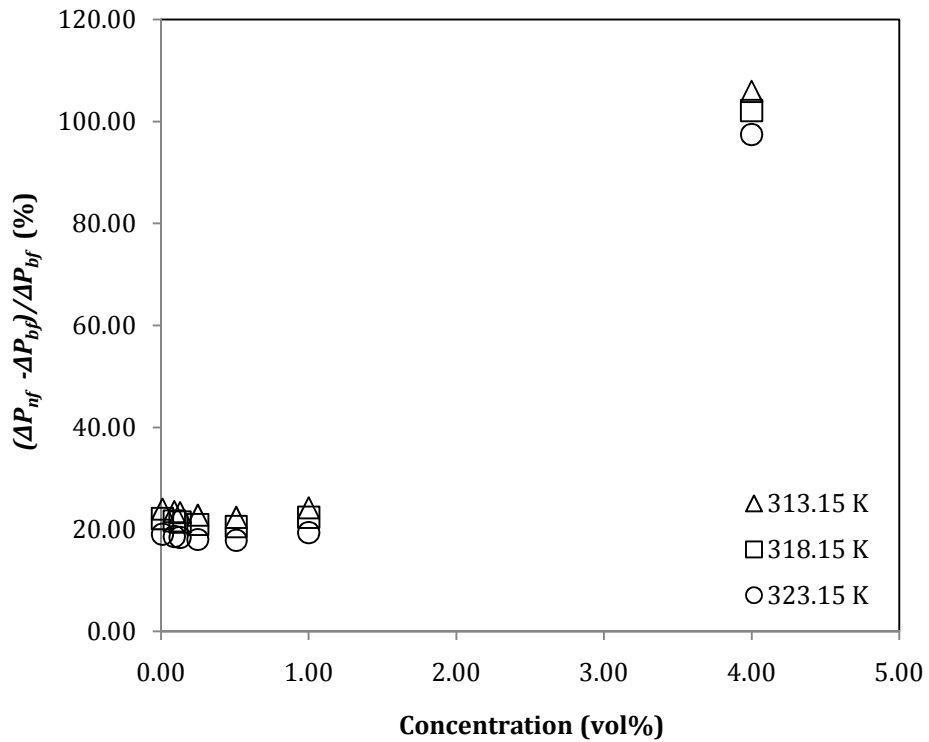
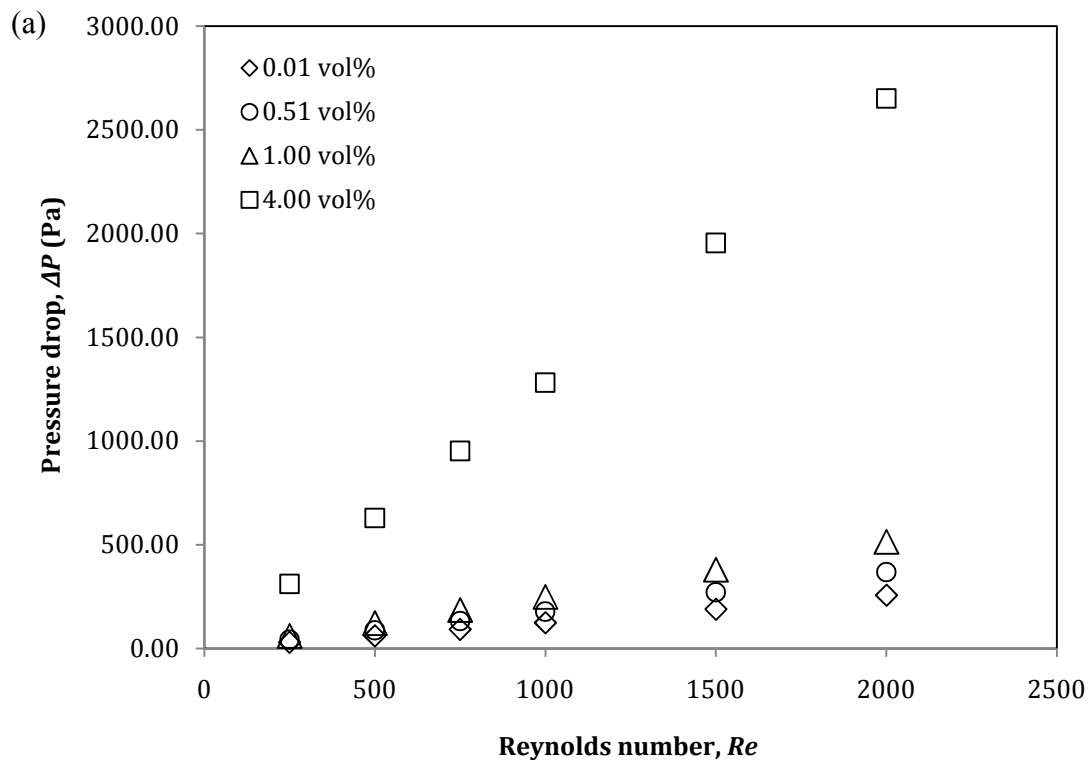


Figure 6.8: Magnitude of ΔP increment at Reynolds number of 1300.

6.3.2 Pressure drop in circular and non-circular ducts (single-phase modelling)

Variation of the pressure drop with the nanoparticle loading in the circular pipe for both temperature-independent and temperature-dependent properties is displayed in Figure 6.9. For the temperature-independent approach, the pressure drop of nanofluid increases with the increasing of Reynolds number and volume fraction. Nonetheless, for the temperature-dependent approach, the pressure drop only increases when the nanofluid concentration is raised from 1% to 4%. For low concentration ($< 1\%$), the pressure drop of the nanofluid reduces slightly when the concentration is increased from 0.01 to 0.51%, but the magnitude is still higher when compared to that of water. The reduction in the pressure drop between 0.01 and 0.51% nanofluid is about 1.45%, which is very small. Besides, the pressure drop estimated from the temperature-dependent approach also increases when the Reynolds number increases. The pressure drop of nanofluid in the non-circular ducts has a similar trend with that of the circular pipe and the result is shown in Figure I.3 to Figure I.5 (Appendix I).



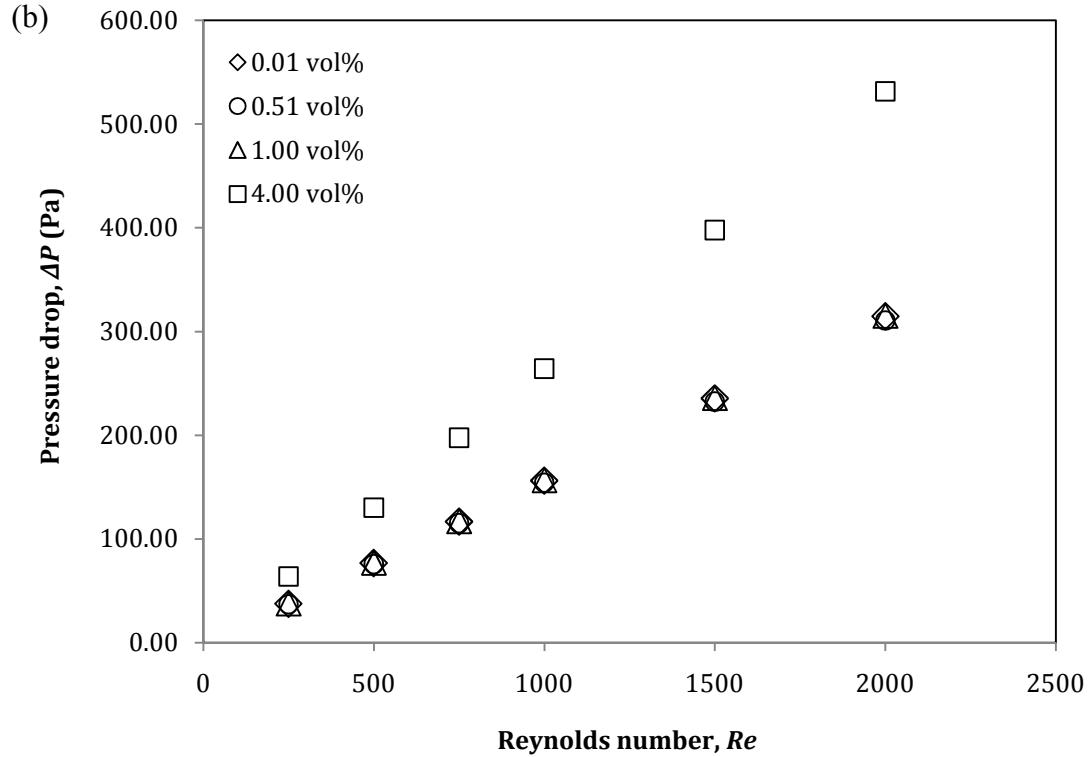


Figure 6.9: Pressure drop variation with nanoparticle concentration in the circular pipe for the cases of (a) temperature-independent and (b) temperature-dependent properties.

The increased pressure drop of nanofluid relative to that of pure water can also be explained using the velocity profile. Figure 6.10 depicts the velocity profile at the duct outlet for different nanofluid concentrations. It is noticed that the peak of the velocity profile increases with the increasing concentration. Higher peak actuates greater near-wall velocity gradient, causing higher wall shear stress. Therefore, higher pressure drop is expected for nanofluid with higher volume fraction. Furthermore, Figure 6.11 shows the effect of Reynolds number on the velocity profile of nanofluid for the circular pipe. The peak of the velocity profile increases when the Reynolds number increases. As a result, the pressure drop is higher when the Reynolds number is higher.

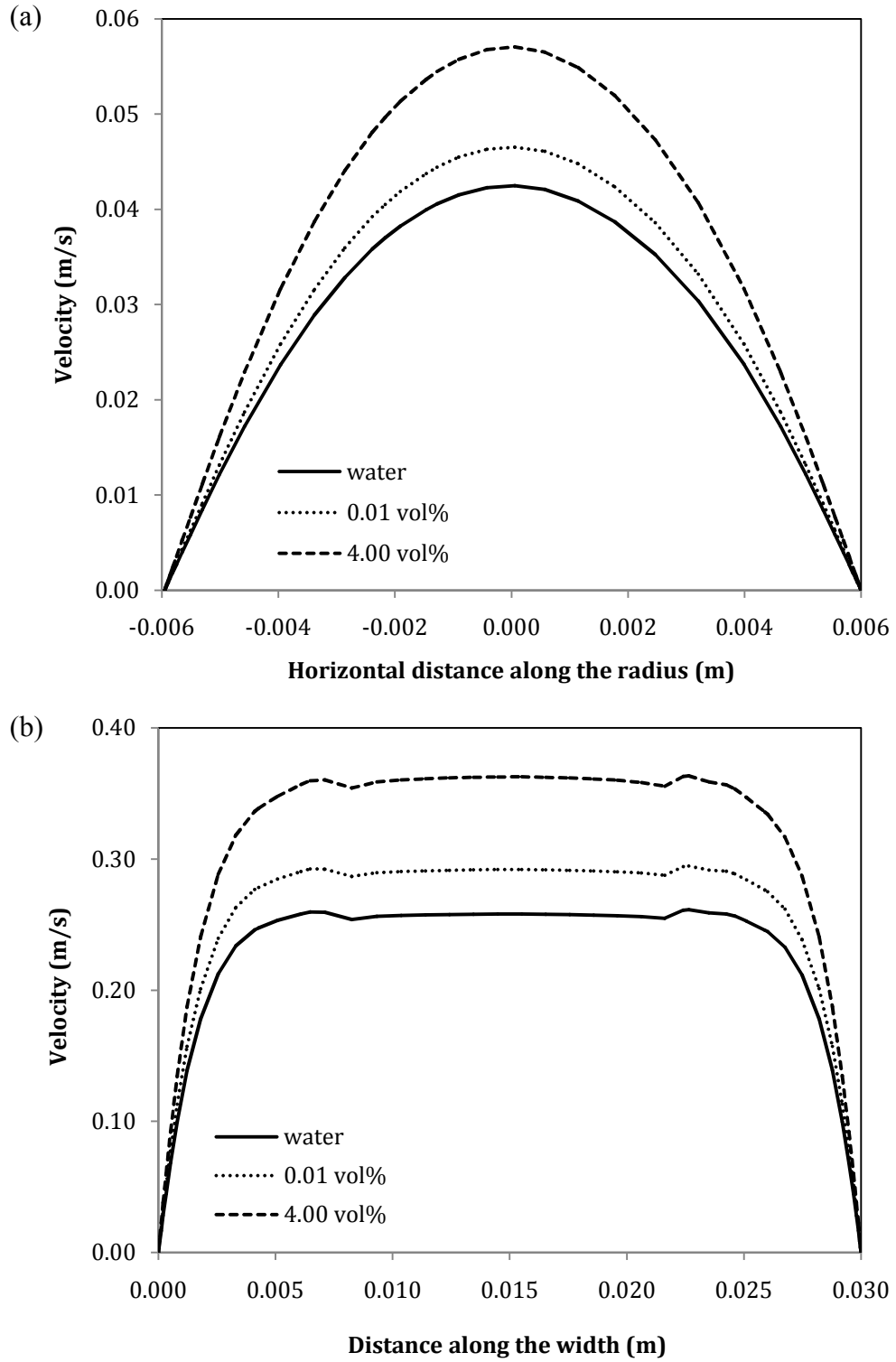


Figure 6.10: Effect of nanofluid concentration on velocity profile at the outlet of (a) circular and (b) 4:1 rectangular ducts (temperature-dependent properties, $Re=2000$).

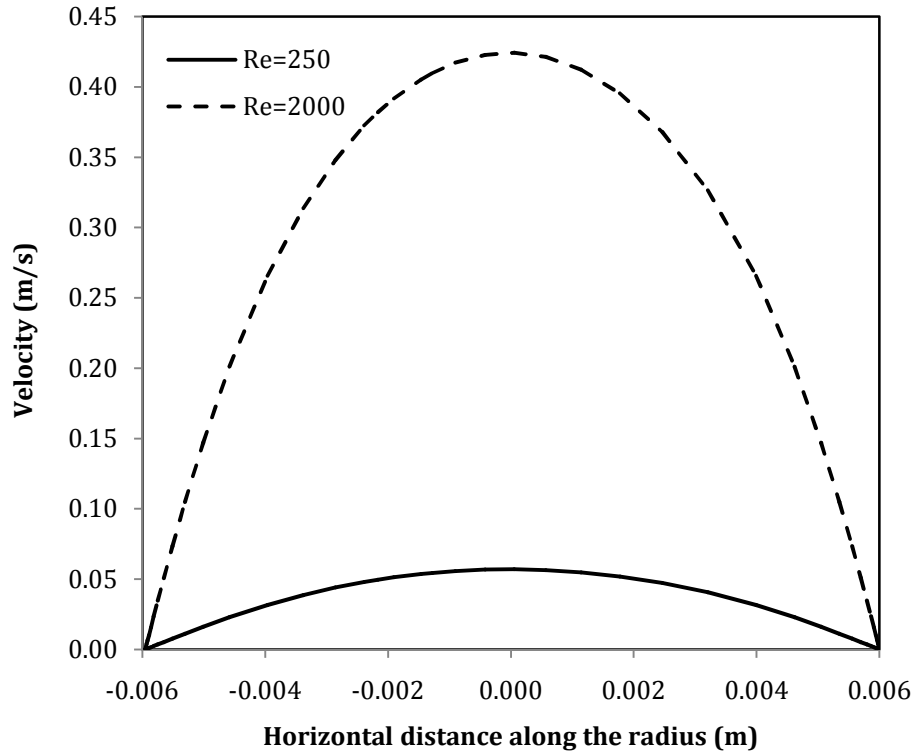


Figure 6.11: Effect of Reynolds number on velocity profile along the horizontal direction of outlet cross-section of circular pipe (temperature-dependent properties).

Table 6.1 and Table 6.2 show the percentage in τ_w and ΔP increment of nanofluid in the circular pipe. The results for other ducts are given in Appendix I (Table I.7 to Table I.10). From Table 6.1 and Table 6.2, it is noticed for temperature-independent and temperature-dependent models that the τ_w increment is similar to the ΔP increment at a particular nanoparticle loading. This indicates that the pressure drop of nanofluid increases linearly with the increased wall shear stress. For both approaches, the type of geometry has negligible influence on the τ_w and ΔP increment. In addition, the effect of Reynolds number on the τ_w and ΔP increment is also negligible.

The maximum ΔP increment occurs at the nanofluid concentration of 4.00%. For the circular pipe, it is approximately 945.69% and 117.75% in the cases of temperature-independent and temperature-dependent approach, respectively. The value of ΔP increment for the former case is higher. The temperature-independent approach predicts higher pressure drop because the variation of viscosity with temperature is not considered. Therefore, the estimated viscosity is higher even when the temperature is

high. The maximum deviation in pressure drop obtained from temperature-dependent and temperature-independent approaches is approximately 400% for the circular pipe. Pressure drop is a function of temperature, so it is important to consider the temperature variation in the computation. Therefore, it is determined from this present study that the temperature-dependent approach is more suitable to be used compared to the temperature-independent approach, especially when heat transfer is involved.

Table 6.1: τ_w increment (%) of Al_2O_3 nanofluid in the circular pipe.

Reynolds number	Nanoparticles volume concentration (%)						
	0.01	0.09	0.13	0.25	0.51	1.00	4.00
<i>Temperature-independent properties</i>							
250	1.08	6.99	10.03	20.81	45.24	103.07	945.69
750	0.96	6.86	9.90	20.67	45.06	102.62	944.44
1000	0.96	6.86	9.90	20.67	45.06	102.63	944.43
1500	0.96	6.86	9.89	20.66	45.06	102.65	944.42
2000	0.96	6.89	9.91	20.66	45.06	102.62	944.42
<i>Temperature-dependent properties</i>							
250	27.91	27.91	27.91	27.17	26.44	28.20	116.85
750	28.76	28.28	28.04	27.56	27.08	28.96	116.20
1000	28.72	28.18	27.88	27.46	26.98	29.02	117.01
1500	28.87	28.28	27.96	27.56	27.12	29.19	116.93
2000	28.98	28.32	27.99	27.61	27.19	29.27	116.89

Table 6.2: ΔP increment (%) of Al_2O_3 nanofluid in the circular pipe.

Reynolds number	Nanoparticles volume concentration (%)						
	0.01	0.09	0.13	0.25	0.51	1.00	4.00
<i>Temperature-independent properties</i>							
250	1.08	6.99	10.03	20.81	45.24	103.07	945.69
750	0.96	6.86	9.90	20.67	45.06	102.62	944.44
1000	0.96	6.86	9.90	20.66	45.06	102.63	944.43
1500	0.96	6.86	9.89	20.66	45.06	102.64	944.42
2000	0.96	6.89	9.91	20.66	45.06	102.62	944.42
<i>Temperature-dependent properties</i>							
250	28.01	27.60	27.57	26.96	26.11	28.22	116.95
750	28.81	28.38	28.16	27.57	27.08	28.97	117.63
1000	28.77	28.34	28.07	27.48	27.04	28.92	117.53
1500	28.92	28.48	28.20	27.61	27.21	29.06	117.67
2000	28.98	28.55	28.26	27.67	27.29	29.12	117.75

Figure 6.12 illustrates the pressure drop of 4% nanofluid in different geometries for the temperature-dependent approach. The 4:1 rectangular duct has the highest pressure drop when compared to the other ducts. The same is observed for the other nanoparticle loadings and in the case of temperature-independent approach (shown in Appendix I Figure I.6 and Figure I.7). The 4:1 rectangular duct has the lowest aspect ratio when compared to the 2:1 rectangular and square ducts. Geometry with lower aspect ratio would experience a higher pressure drop (Shah and Sekulic 2003). As the aspect ratio reduces, the flow cross-sectional area increases, and the flow would encounter larger amount of shear stress (Gingrich, Cho, and Shyy 1992a).

The addition of nanoparticles into water does not alter the friction factor of the base fluid in the laminar regime (detail is given in Section 6.3.5). The friction factor of nanofluid in the circular, square, 2:1 rectangular and 4:1 rectangular ducts still follows the friction factor relationship of water, which is $64/Re$, $57/Re$, $62/Re$ and $73/Re$, respectively. From these friction factor relationships, it is also discovered that the 4:1 rectangular duct has the highest pressure drop among the ducts as its $f \cdot Re$ is the highest.

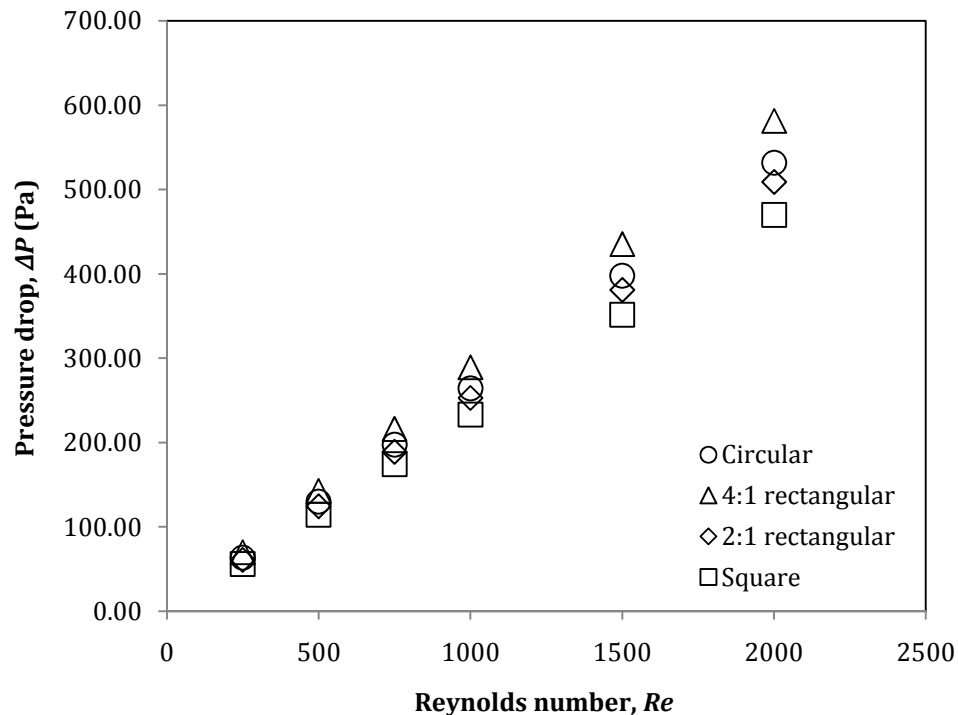
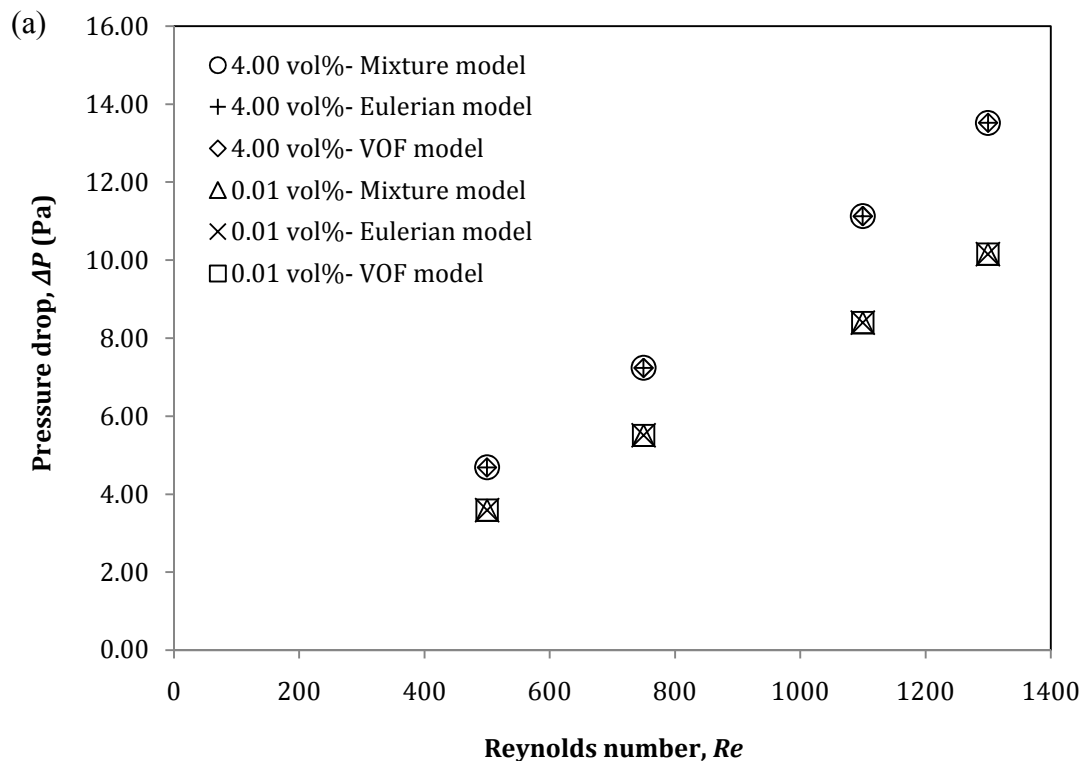


Figure 6.12: Pressure drop of 4% nanofluid for temperature-dependent approach.

6.3.3 Pressure drop in different geometries (two-phase modelling)

For all the geometries studied, the prediction from all the three two-phase models gives essentially similar pressure drop results for nanofluid at a particular Reynolds number and concentration, as displayed in Figure 6.13 and Figure 6.14 for the double pipe heat exchanger and circular pipe, respectively. The pressure drop results obtained from the two-phase models for the non-circular ducts are shown in Appendix I (Figure I.8 to Figure I.11). This finding agrees with that of Akbari, Galanis, and Behzadmehr (2011) as they also obtained similar flow characteristic result for nanofluid at a particular Reynolds number from the two-phase models.

Similar to the case of single-phase model, the pressure drop of nanofluid from the two-phase model also increases when the hot inlet temperature of nanofluid decreases (Figure 6.13). According to Figure 6.15, the two-phase models also predict the pressure drop of nanofluid to be higher than the value of water. At the Reynolds number of 1300, the pressure drop of 4% nanofluid is approximately 69.51% higher than the value of water.



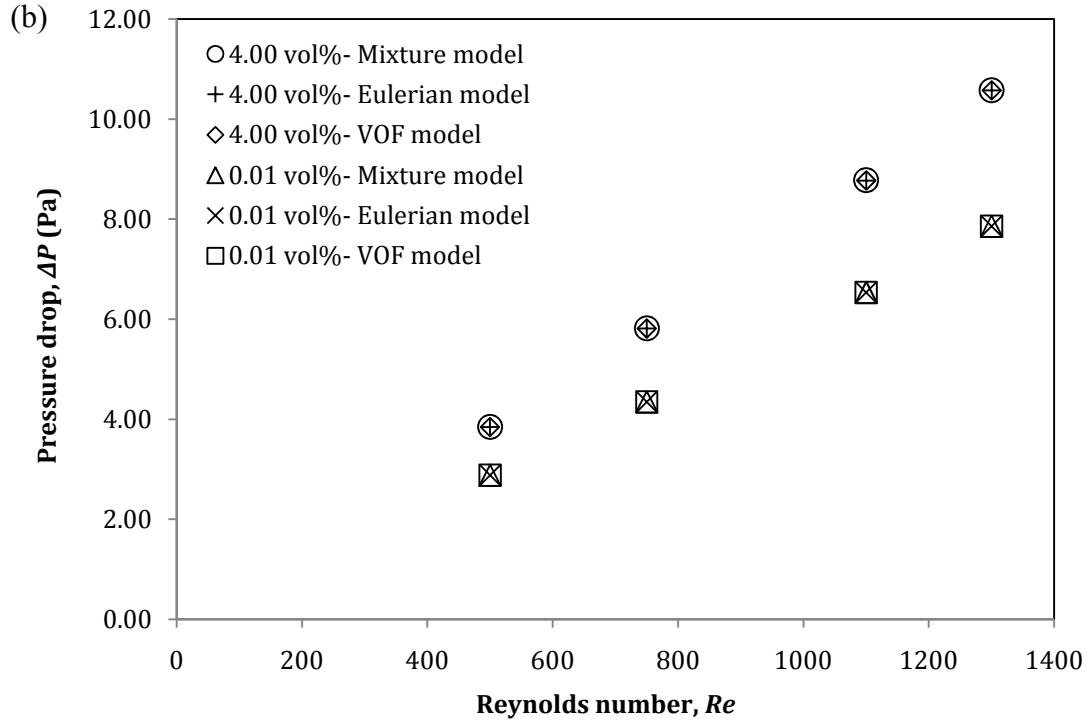


Figure 6.13: Pressure drop of 0.01% and 4% nanofluid obtained using two-phase models at the hot inlet temperatures of (a) 313.15 K and (b) 323.15 K.

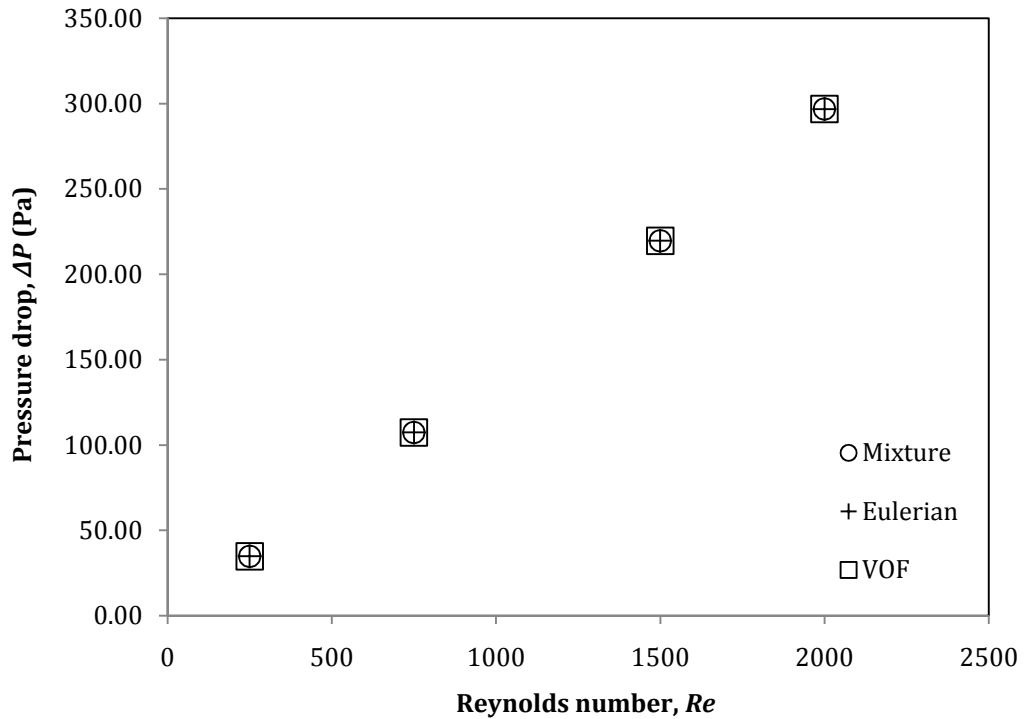


Figure 6.14: Pressure drop of 4% Al_2O_3 nanofluid obtained from two-phase models for circular pipe.

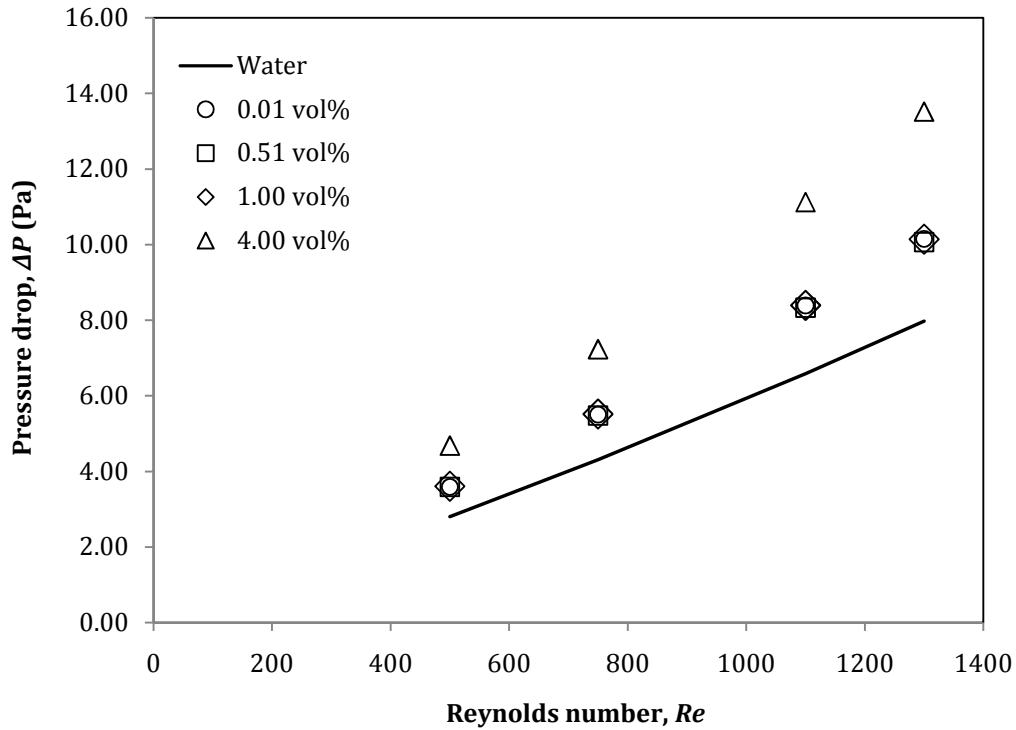


Figure 6.15: Pressure drop of nanofluid obtained in the double pipe heat exchanger using the mixture model at hot inlet temperature of 313.15 K.

6.3.4 Comparison of results from single- and two-phase models

For the double pipe heat exchanger, the pressure drop of 1% nanofluid computed using the single-phase temperature-dependent approach is close to the value predicted from the two-phase model, as depicted in Figure 6.16. When the concentration is increased to 4%, the pressure drop from the mixture model is lower than that of the temperature-dependent model, with the maximum deviation of 19%. Lower pressure drop estimated from the mixture model for 4% Al_2O_3 nanofluid is also encountered in the circular (Figure 6.17) and non-circular ducts (Appendix I Figure I.12). Esfandiary, Habibzadeh, and Sayehvand (2016) also discovered a lower pressure drop from the mixture model when compared to that of the single-phase model.

The mixture model predicts a lower pressure drop because the viscosity of 4% nanofluid calculated using the model is smaller in comparison to that of the temperature-dependent method at the same Reynolds number. For example, in the double pipe heat exchanger,

the viscosity of 4% nanofluid computed from the single- and two-phase models are approximately 1.04×10^{-3} Pa s and 6.98×10^{-4} Pa s, respectively.

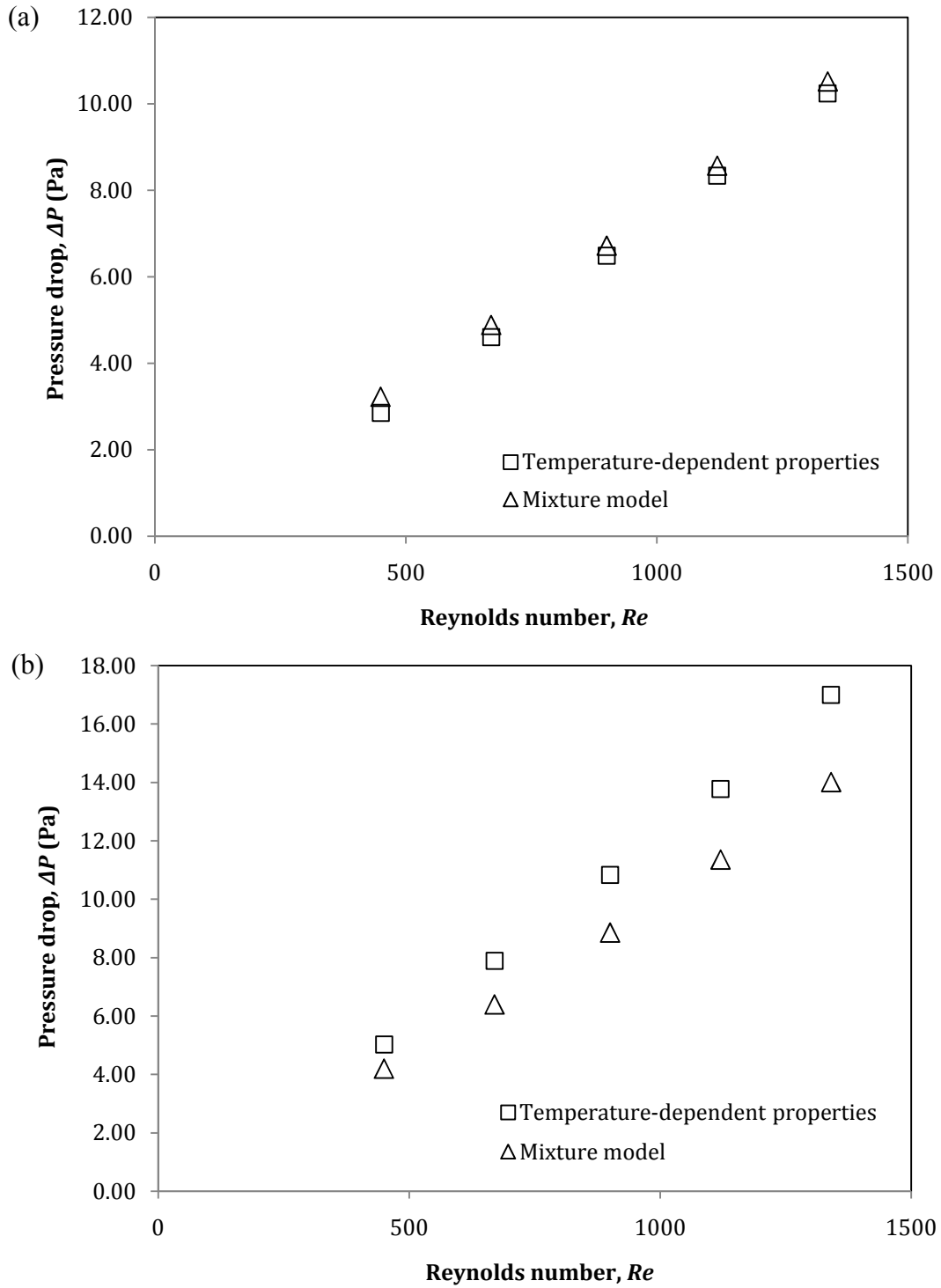


Figure 6.16: Pressure drop obtained from different models for (a) 1% and (b) 4% nanofluid in double pipe heat exchanger at hot inlet temperature of 313.15 K.

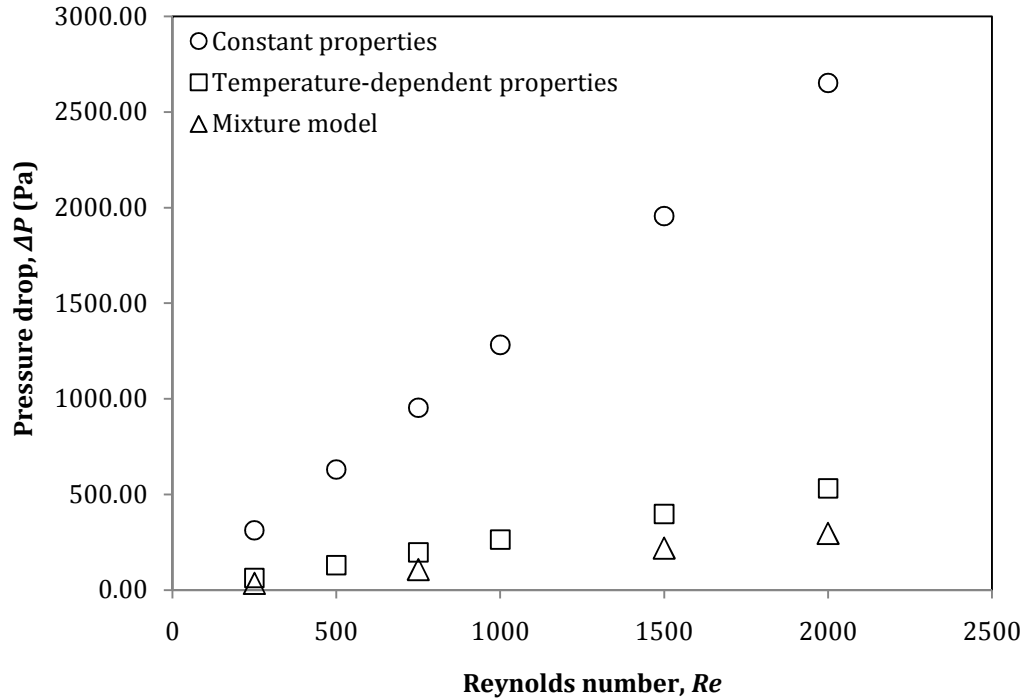


Figure 6.17: Comparison of pressure drop obtained from different models for 4% nanofluid in circular pipe.

In this present study, it is determined that the single-phase model is adequate to model the flow behaviour of nanofluid. As mentioned in Chapter 5 Section 5.3.4, the single-phase model is also recognized by other researchers to be able to predict the behaviour of nanofluid with a reasonably good accuracy (Tokit, Yusoff, and Mohammed 2013; Kumar and Puranik 2016). Therefore, merely the single-phase model is applied for the simulations of poly-nanofluid.

6.3.5 Friction factor for different geometries

As shown in Figure 6.18, the friction factor of nanofluid agrees well with that of water regardless of the nanoparticle loading. This finding is supported by Wang et al. (2013) and Mirmasoumi and Behzadmehr (2008) that the friction coefficient does not vary with the nanofluid concentration in the fully developed region. This implies that the friction factor correlation of water can be extended for the nanofluid. This is true for all the geometries considered. The friction factor of 4% nanofluid in different ducts is depicted in Figure 6.19. The friction factor in the 4:1 rectangular duct is the highest, followed by

the circular, 2:1 rectangular and square channels. As expected, the friction factor of nanofluid decreases when the Reynolds number increases.

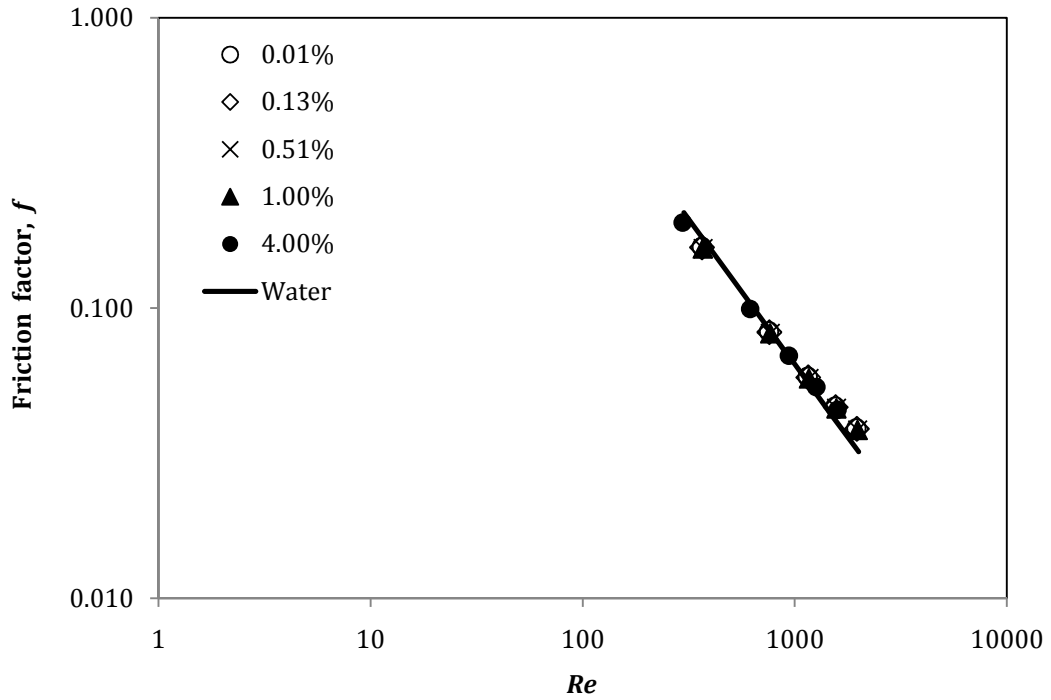


Figure 6.18: Friction factor of nanofluid at hot inlet temperature of 323.15 K.

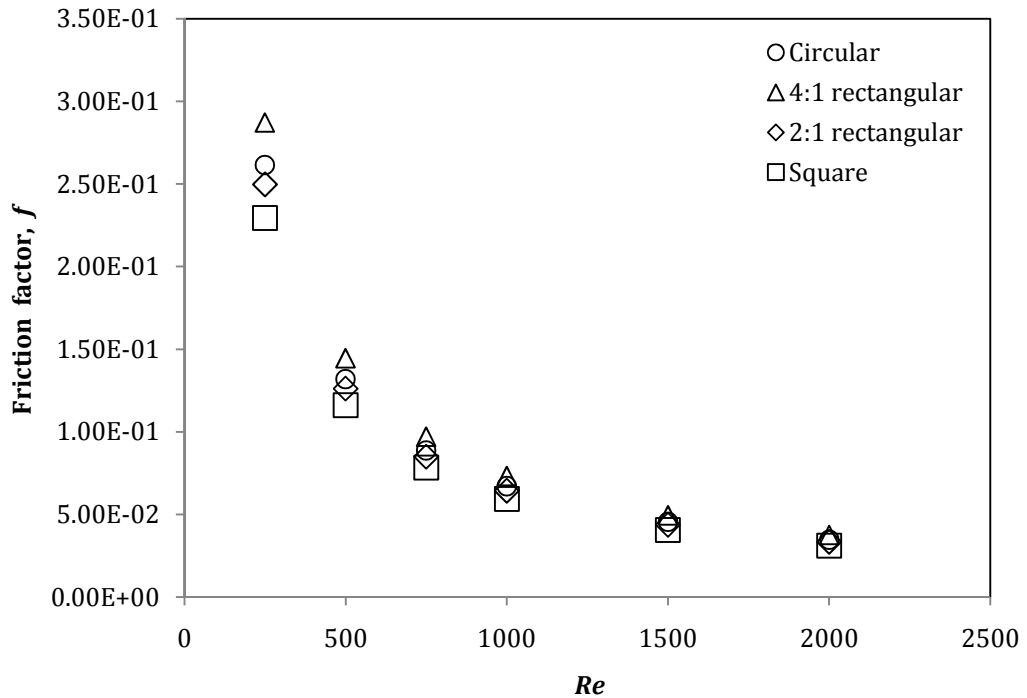


Figure 6.19: Friction factor of 4% nanofluid (temperature-dependent approach).

6.4 Flow feature of PAA solution

6.4.1 Pressure drop in double pipe heat exchanger

Figure 6.20 shows the pressure drop of PAA solution in the double pipe heat exchanger at the hot inlet temperature of 323.15 K. The pressure drop of PAA solution increases with the increasing of Reynolds number. When the Reynolds number increases, the increment in the flow rate leads to a higher pressure loss. From Figure 6.20, it is also observed that the pressure drop of PAA solution increases when the concentration increases. This is the same as that of nanofluid, which the solution becomes more viscous when the concentration is raised. Therefore, larger shear stress is experienced near the duct wall, leading to larger pressure loss to keep the solution flowing.

In addition, as displayed in Figure 6.21, when the inlet temperature of the PAA solution increases, the pressure drop decreases. As mentioned in Chapter 4, the reduction in viscosity occurs when the temperature of the solution increases. Higher temperature increases the motion and vibration of the liquid molecules, and this reduces the resistance of the fluid flow, so the pressure drop is lower.

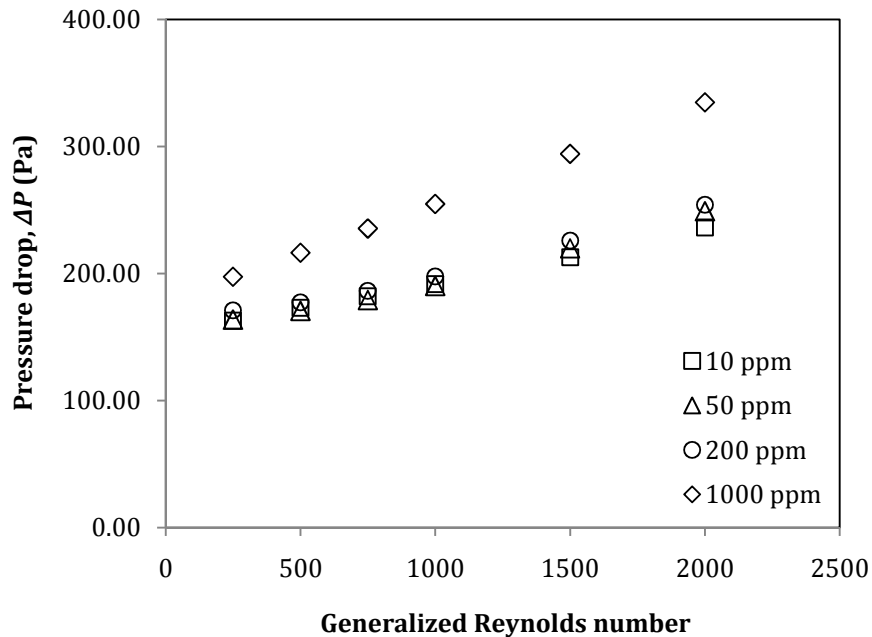


Figure 6.20: Pressure drop of PAA solution in double pipe heat exchanger at hot inlet temperature of 323.15 K.

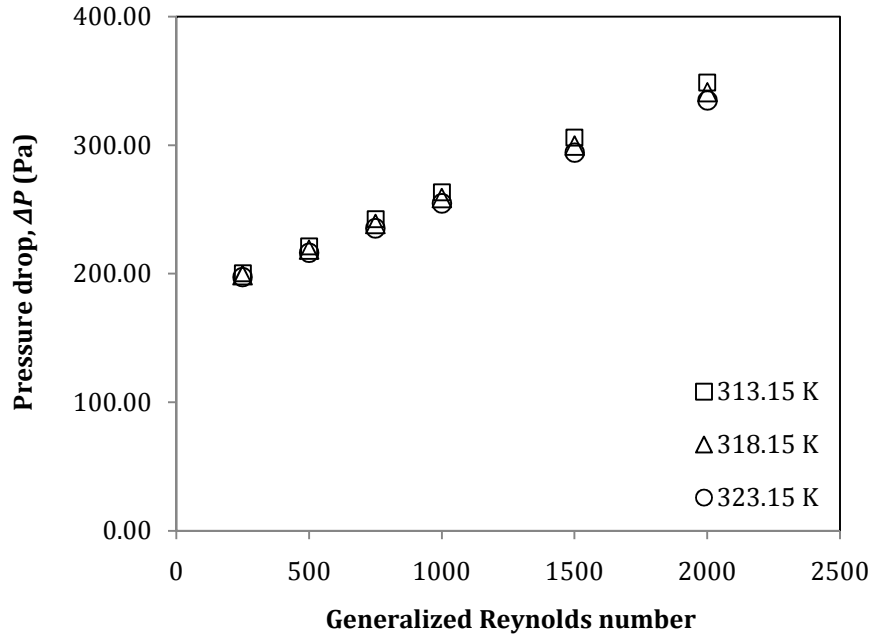


Figure 6.21: Pressure drop of 1000 ppm PAA solution at different hot inlet temperatures.

6.4.2 Pressure drop in circular and non-circular ducts

Figure 6.22 shows the flow behaviour of PAA solution in different ducts. It can be observed from Figure 6.22 that the influence of geometry on the pressure drop of PAA solution becomes more significant at higher Reynolds number. This is because when the fluid velocity increases, the pressure drop increases. Besides, when considering merely the non-circular ducts, the pressure drop is the highest in the 4:1 rectangular duct, followed by the 2:1 rectangular and square ducts. This is the same as that encountered for the nanofluid.

The pressure drop of PAA solution in the circular pipe is slightly lower when compared to those of the non-circular ducts. Since the pressure drop encountered in the circular pipe is not significantly different from that of the non-circular ducts. It can be deduced that the elasticity of the PAA solution does not alter its flow behaviour in the non-circular ducts (Hartnett and Kostic 1985, 1989).

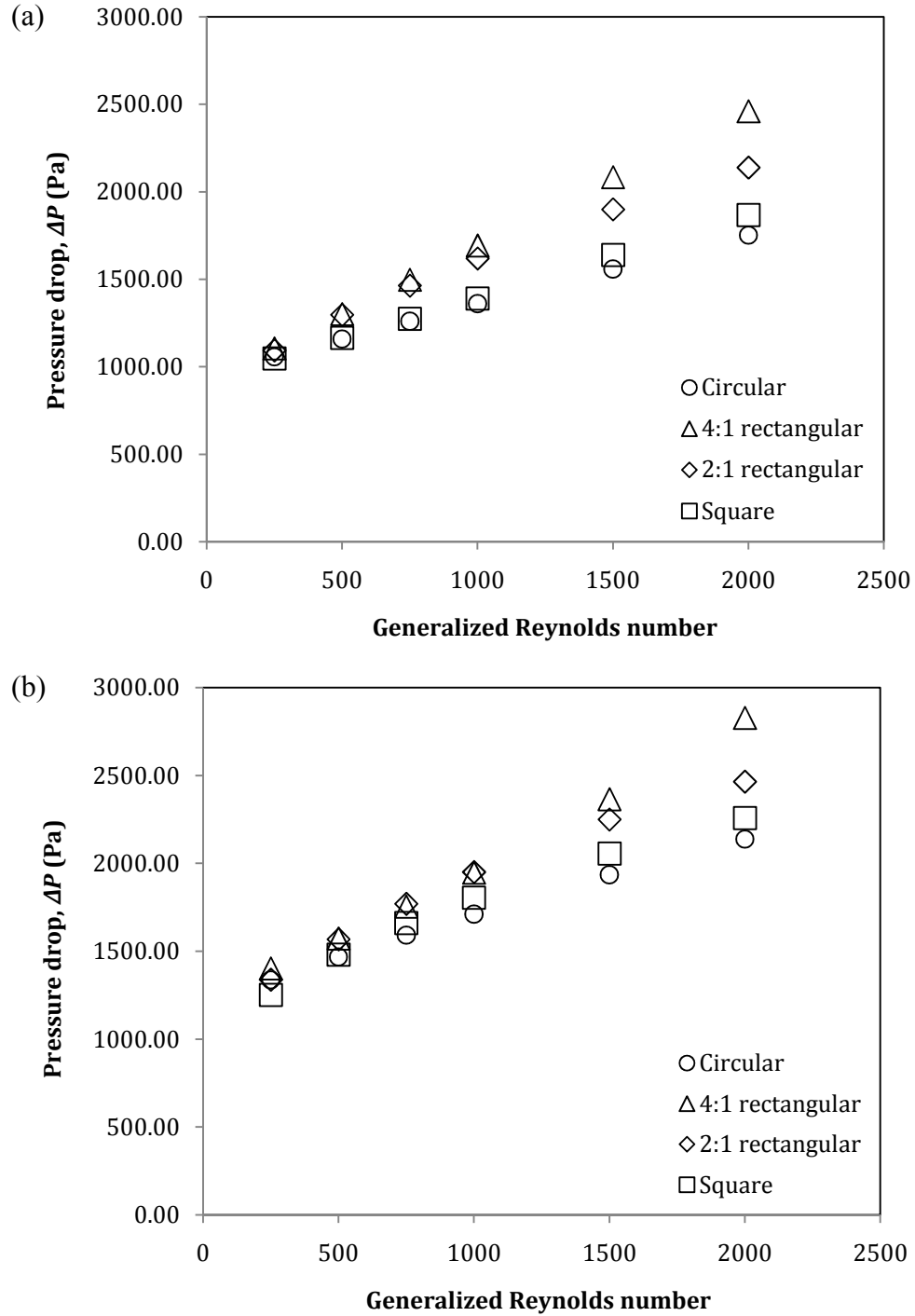


Figure 6.22: Pressure drop of (a) 10 and (b) 1000 ppm PAA solution.

According to Figure 6.23, the pressure drop of 1000 ppm PAA solution is extremely large, which is approximately 43–56 times larger compared to the value of water at the generalized Reynolds number of 250. This large pressure drop increment is due to the high viscosity of PAA solution relative to that of water. At the generalized Reynolds

number of 250, the ratio of bulk viscosity of 1000 ppm PAA solution to the value of water is approximately 60. Furthermore, another reason for the large pressure drop increment is that high velocity is required for the PAA solution to achieve the same Reynolds number as water. For example, to attain the generalized Reynolds number of 250, the velocity of 1000 ppm PAA is about 7 times greater than that of water.

Figure 6.23 and Figure 6.24 also indicate that the pressure drop ratio of PAA solution to water, $\Delta P_{PAA}/\Delta P_{bf}$ is the largest at the Reynolds number of 250 and it decreases with the increasing Reynolds number. Besides, the effect of PAA concentration on the pressure drop ratio is more considerable when the Reynolds number is small (Figure 6.24). This is due to the low pressure drop of base fluid encountered at the Reynolds number of 250. When the Reynolds number increases, the pressure drop of the base fluid increases remarkably, hence, the pressure drop difference between the PAA solution and the base fluid reduces. According to Figure 6.23, $\Delta P_{PAA}/\Delta P_{bf}$ is similar for all the geometries considered, particularly when the Reynolds number is greater than 250. Therefore, it can be deduced that the influence of geometry on the $\Delta P_{PAA}/\Delta P_{bf}$ is not substantial as the Reynolds number increases.

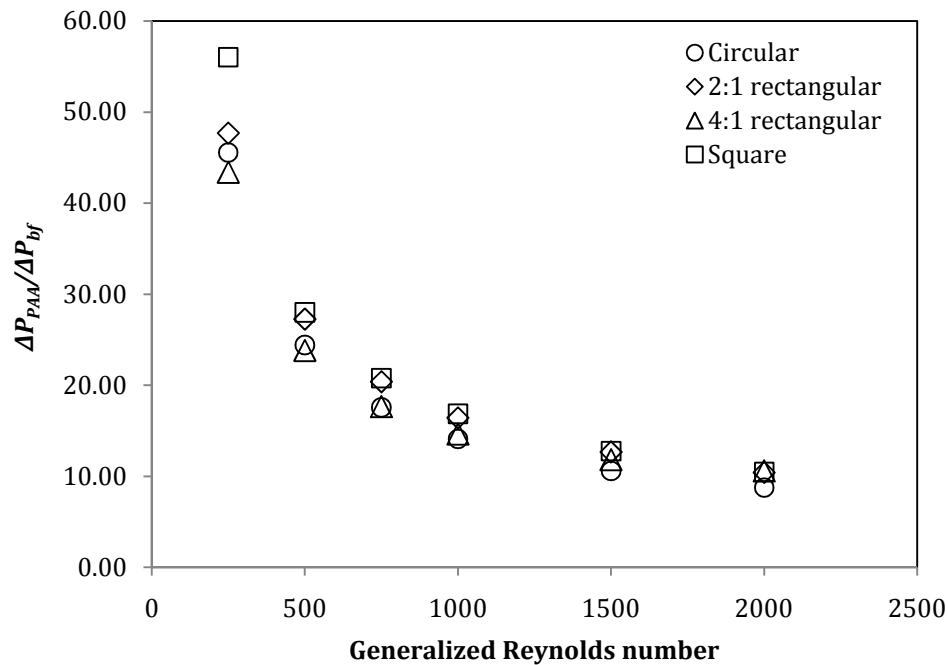


Figure 6.23: Pressure drop ratio of 1000 ppm PAA solution to that of water.

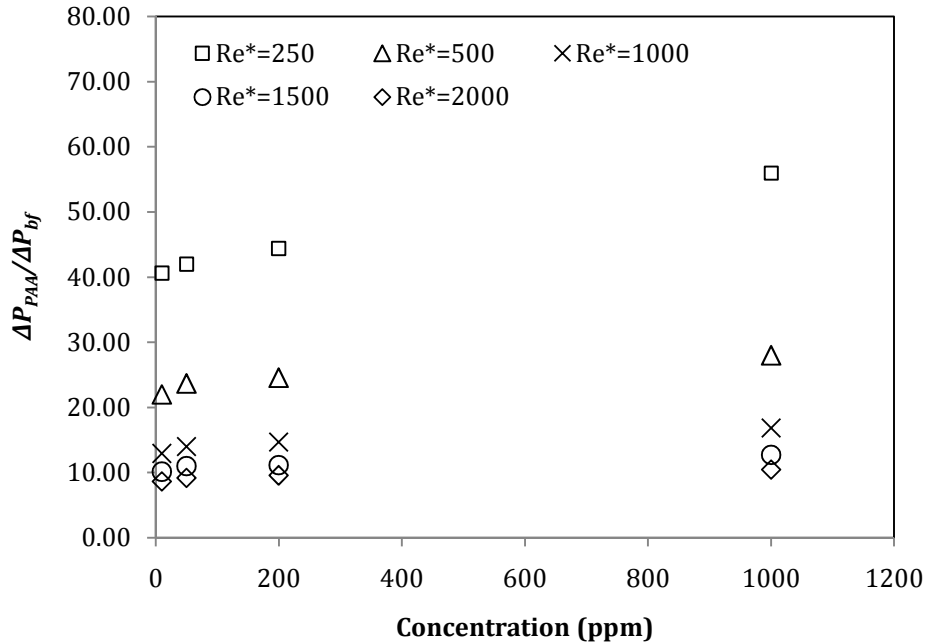
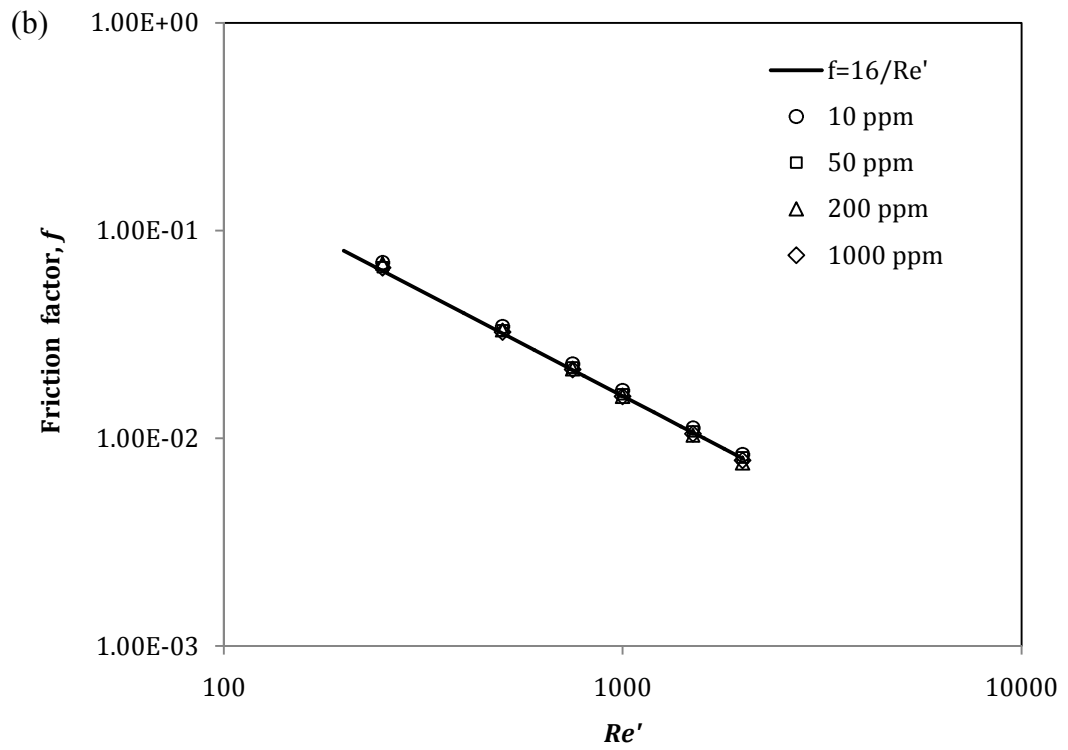
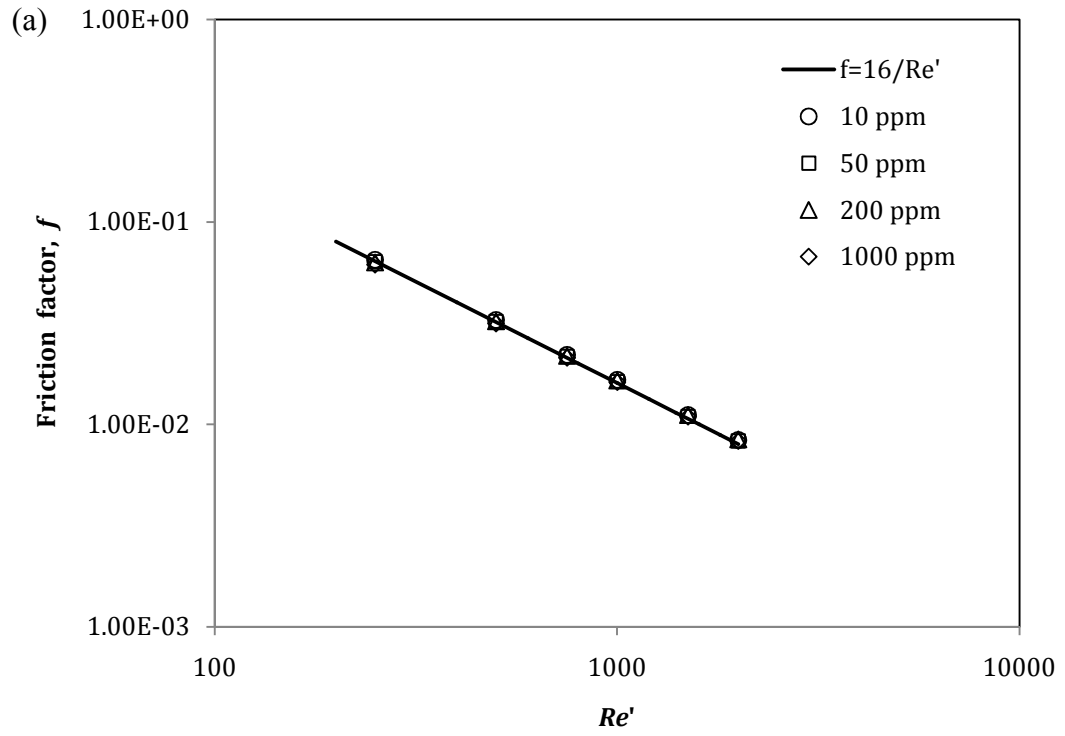


Figure 6.24: Pressure drop ratio of PAA solution to that of water for square duct.

6.4.3 Friction factor for different geometries

Figure 6.25 shows the friction factor of PAA solution in the double pipe heat exchanger, circular and square ducts. The friction factor of PAA solution in the 2:1 and 4:1 rectangular ducts are given in Appendix I (Figure I.13). The result indicates that the friction factor values estimated numerically for the PAA solution in different geometries are in reasonable agreement with the power law prediction. The maximum deviations from the power law prediction are approximately 6.05, 8.00 and 6.61% for the double pipe heat exchanger, circular and non-circular ducts, respectively. This implies that for the non-circular flow, the elasticity of PAA solution does not affect the friction factor (Cho and Harnett 1982; Hartnett 1992). The elastic property is not manifested in the PAA circular flow, thus the friction factor conforms well to that of the value calculated from the non-Newtonian power law model. This current finding of the friction factor is consistent with the results reported by other researchers (Oliver 1969; Mena et al. 1978; Cho and Harnett 1982; Hartnett and Kostic 1985, 1989; Rao 1989; Xie and Hartnett 1992; Kostic 1994) that the friction factor of PAA solution resembles that of the power law fluid.



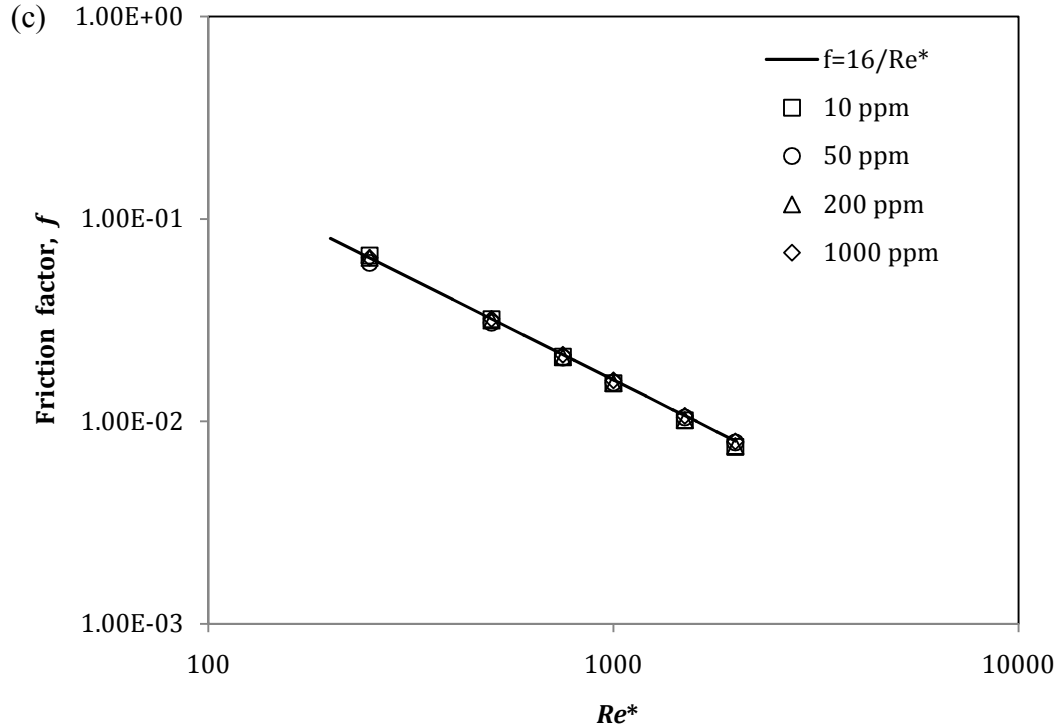


Figure 6.25: Friction factor of PAA solution in (a) double pipe heat exchanger (hot inlet temperature of 313.15 K), (b) circular and (c) square ducts.

6.5 Flow feature of poly-nanofluid

6.5.1 Pressure drop in double pipe heat exchanger

The pressure drop of poly-nanofluid at the hot inlet temperature of 313.15 K for the double pipe heat exchanger is illustrated in Figure 6.26 and Figure 6.27. It is indicated from Figure 6.26 that when the same amount of PAA additives is added into nanofluid with different concentrations, the pressure drop of the poly-nanofluid increases with the increasing nanoparticle loading. In addition, according to Figure 6.27, when different concentrations of PAA are added into nanofluid with the same concentration, the pressure drop increases as the PAA concentration increases. As mentioned in Chapter 4 Section 4.3, the viscosity of poly-nanofluid gets larger when the concentration of either the PAA or nanofluid is raised. Therefore, the concentration increment results in higher pressure drop of poly-nanofluid across the heat exchanger.

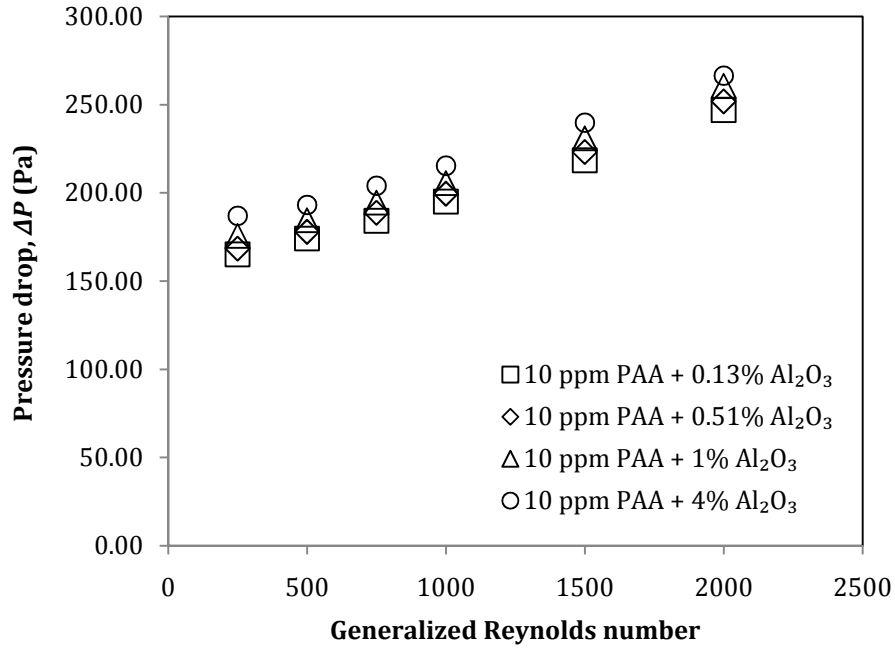


Figure 6.26: Pressure drop of 10 ppm PAA in nanofluid for double pipe heat exchanger at hot inlet temperature of 313.15 K.

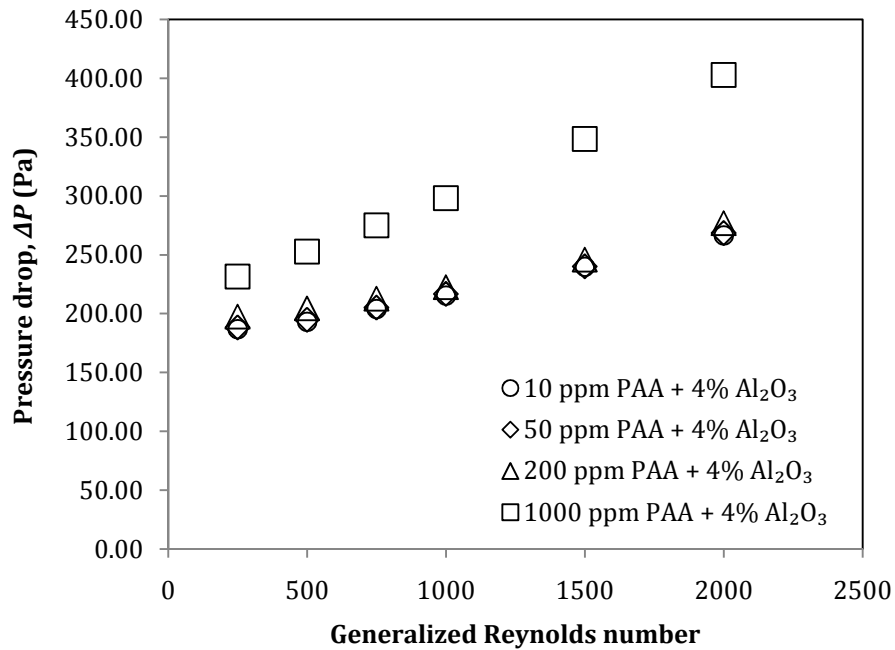


Figure 6.27: Pressure drop of PAA in 4% Al₂O₃ nanofluid for double pipe heat exchanger at hot inlet temperature of 313.15 K.

The pressure drop of poly-nanofluid is far larger compared to that of the nanofluid. Figure 6.28 depicts the pressure drop ratio of 1000 ppm PAA in 4% nanofluid to 4%

nanofluid, $\Delta P_{poly-nf}/\Delta P_{nf}$. For the double pipe heat exchanger, the $\Delta P_{poly-nf}/\Delta P_{nf}$ is approximately 44.45, 50.20 and 53.57 for the hot inlet temperatures of 313.15, 318.15 and 323.15 K, respectively ($Re'=500$). This shows that when the temperature increases, the pressure drop of poly-nanofluid increases more than that of nanofluid.

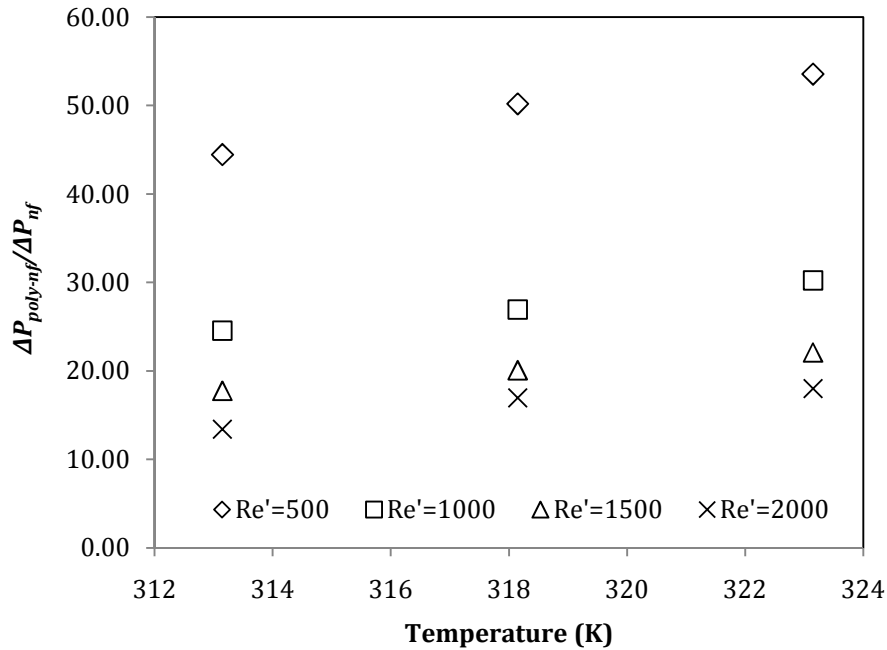


Figure 6.28: Pressure drop ratio of 1000 ppm PAA in 4% nanofluid to 4% nanofluid for double pipe heat exchanger.

6.5.2 Pressure drop in circular and non-circular ducts

The effect of the addition of PAA additives on the pressure drop of nanofluid in the circular and square ducts is illustrated in Figure 6.29 and Figure 6.30. The pressure drop of poly-nanofluid in the other non-circular ducts is depicted in Appendix I (Figure I.16 and Figure I.17). According to Figure 6.29, for a fixed amount of PAA additives added into nanofluid with different concentrations, the pressure drop of poly-nanofluid increases with the increasing of nanofluid concentration. Similarly, the pressure drop of poly-nanofluid increases when the concentration of PAA added to a fixed amount of nanofluid is increased (Figure 6.30). This is similar to the case of double pipe heat exchanger. Besides, it is indicated from Figure 6.30 that the effect of PAA on the

pressure drop of poly-nanofluid is more substantial when PAA concentration is high, especially at 1000 ppm.

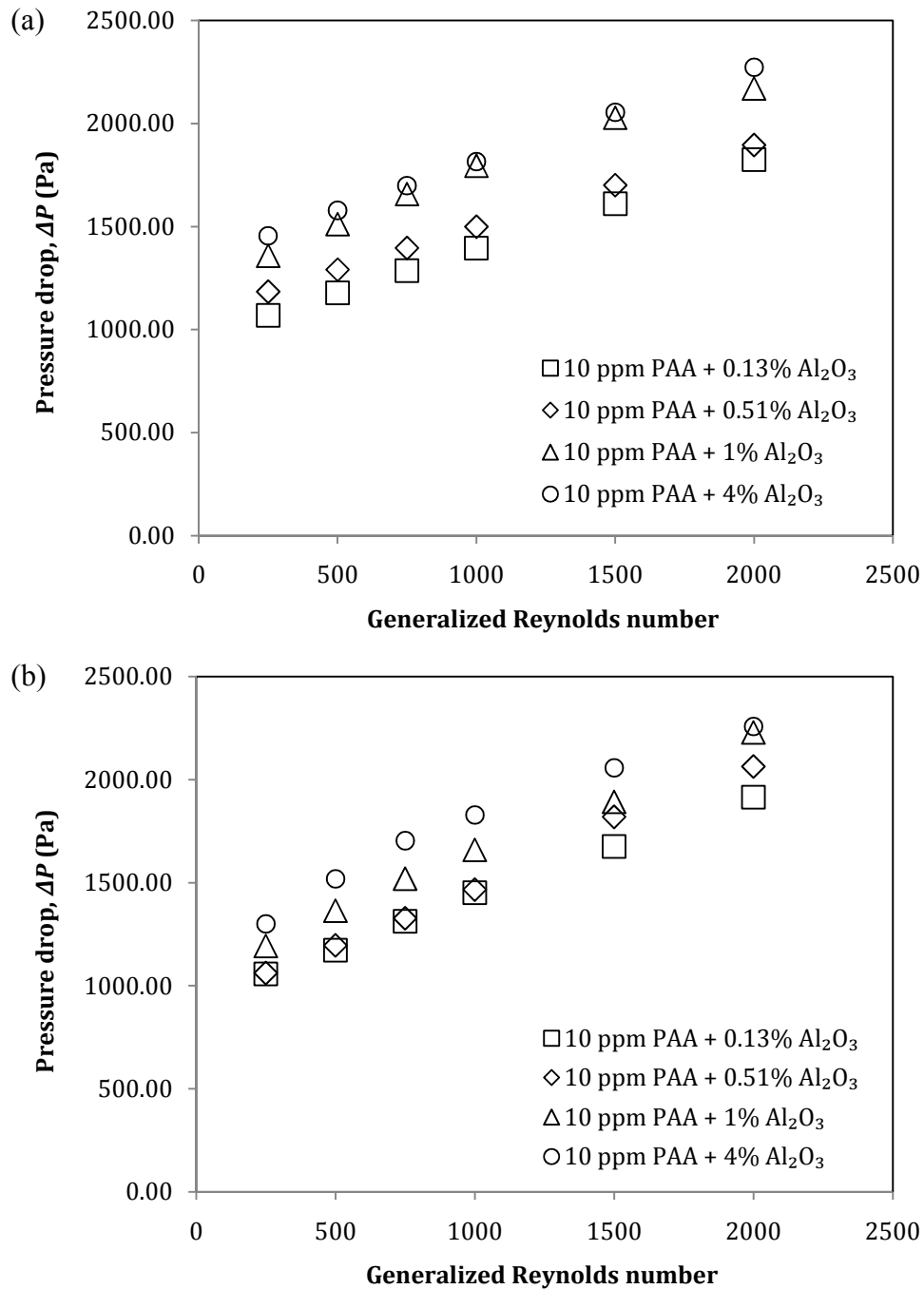


Figure 6.29: Pressure drop of 10 ppm PAA in nanofluid for (a) circular and (b) square ducts.

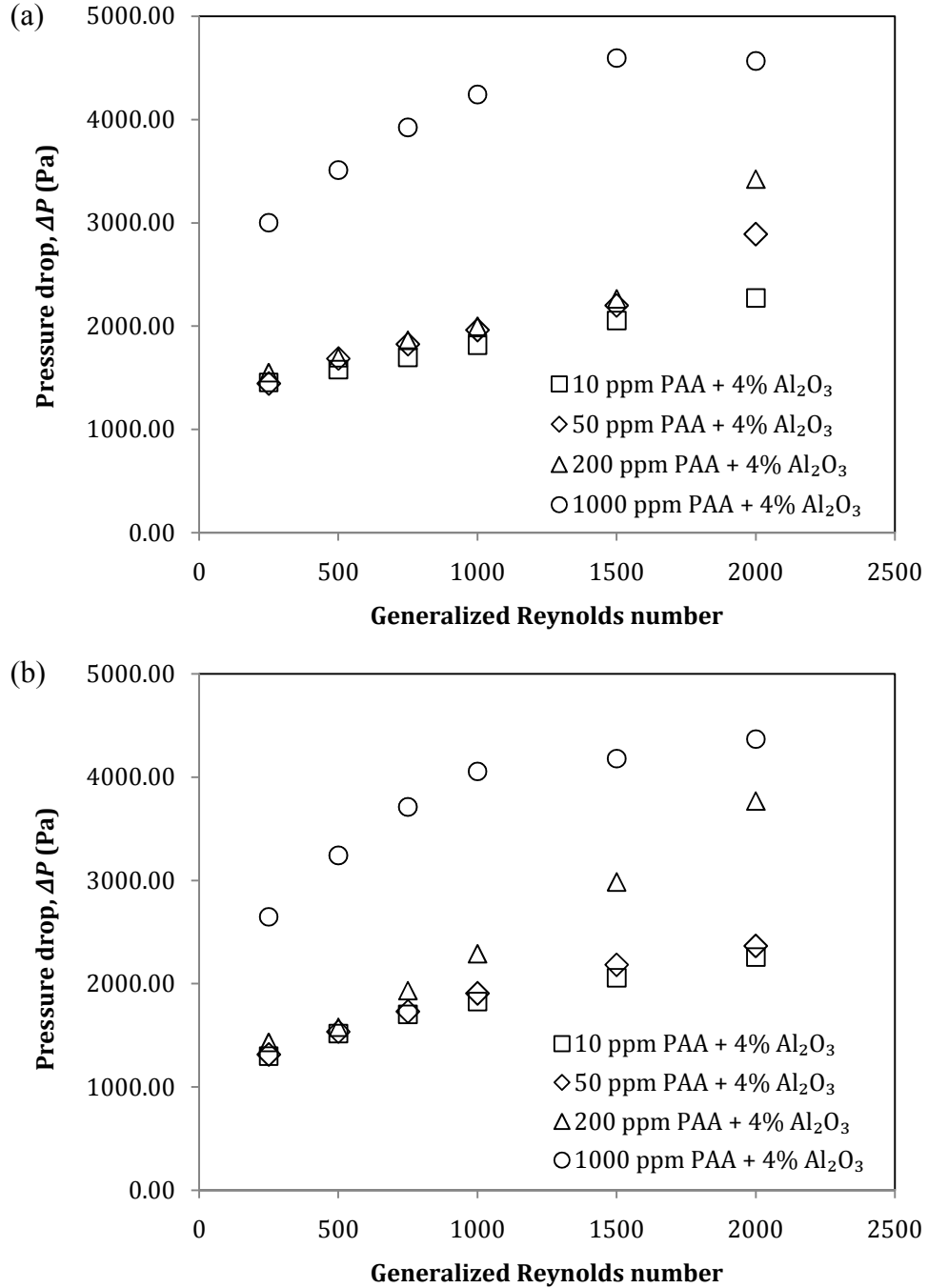


Figure 6.30: Pressure drop of PAA in 4% Al_2O_3 nanofluid for (a) circular and (b) square ducts.

In addition, Table 6.3 and Table 6.4 show the pressure drop ratio of poly-nanofluid to nanofluid, $\Delta P_{poly-nf}/\Delta P_{nf}$ in the circular and square ducts, respectively. The maximum $\Delta P_{poly-nf}/\Delta P_{nf}$ for the circular, square, 2:1 and 4:1 rectangular pipes are

approximately 49.64, 54.80, 51.68 and 45.99, respectively. Besides, the $\Delta P_{poly-nf}/\Delta P_{nf}$ is greater when the Reynolds number is lower. This is because when the Reynolds number is small, the pressure drop of nanofluid is low. As the Reynolds number increases, the pressure drop of nanofluid also increases, thus resulting in smaller $\Delta P_{poly-nf}/\Delta P_{nf}$.

 Table 6.3: $\Delta P_{poly-nf}/\Delta P_{nf}$ for circular pipe.

Concentration of poly-nanofluid		Generalized Reynolds number				
PAA (ppm)	Nanofluid (vol%)	250	500	1000	1500	2000
10	0.13	28.53	15.41	8.97	6.87	5.83
	0.51	31.95	17.04	9.71	7.31	6.10
	1.00	36.05	19.63	11.47	8.60	6.88
	4.00	22.83	12.13	6.87	5.16	4.27
50	0.13	32.24	17.19	9.78	7.35	6.12
	0.51	34.17	18.26	10.45	7.88	6.59
	1.00	36.98	21.06	12.11	8.92	7.58
	4.00	22.67	12.96	7.43	5.53	5.44
200	0.13	33.16	17.72	10.05	7.47	6.13
	0.51	38.52	20.64	11.85	8.96	7.50
	1.00	39.90	21.69	12.62	9.51	7.84
	4.00	24.30	13.02	7.56	5.69	6.44
1000	0.13	36.32	21.17	13.48	10.78	8.72
	0.51	39.17	22.04	13.53	10.68	9.19
	1.00	49.64	26.41	14.81	10.82	9.23
	4.00	47.11	26.98	16.06	11.55	8.59

 Table 6.4: $\Delta P_{poly-nf}/\Delta P_{nf}$ for square duct.

Concentration of poly-nanofluid		Generalized Reynolds number				
PAA (ppm)	Nanofluid (vol%)	250	500	1000	1500	2000
10	0.13	32.15	17.43	10.57	8.09	6.91
	0.51	32.68	17.95	10.77	8.85	7.51
	1.00	36.14	20.16	12.00	9.07	7.99
	4.00	23.24	13.6	7.84	5.85	4.80
50	0.13	34.59	19.28	11.14	8.62	7.52
	0.51	36.57	20.24	12.56	9.56	7.91
	1.00	37.62	20.84	13.38	9.99	8.16
	4.00	23.50	13.41	8.17	6.21	5.03
200	0.13	38.10	20.72	12.05	9.11	7.56
	0.51	42.13	23.58	13.66	10.27	8.48
	1.00	43.37	23.38	14.00	11.15	9.34
	4.00	25.62	13.79	9.81	8.49	8.02
1000	0.13	40.66	22.38	13.98	11.10	9.41
	0.51	43.94	23.61	14.35	11.32	9.79
	1.00	54.80	29.08	16.20	11.76	9.68
	4.00	47.36	28.32	17.38	11.89	9.29

Conversely, from the pressure drop ratio of poly-nanofluid to PAA, $\Delta P_{poly-nf}/\Delta P_{PAA}$ given in Table 6.5 and Table 6.6 for circular and square channels, it is obvious that the $\Delta P_{poly-nf}/\Delta P_{PAA}$ is not as considerable as $\Delta P_{poly-nf}/\Delta P_{nf}$. The maximum $\Delta P_{poly-nf}/\Delta P_{PAA}$ is 2.48 for the circular pipe while it is approximately 2.25 for the square duct. The $\Delta P_{poly-nf}/\Delta P_{nf}$ and $\Delta P_{poly-nf}/\Delta P_{PAA}$ for the 2:1 and 4:1 rectangular ducts are given in Appendix I Table I.16 to Table I.19.

By observing both the $\Delta P_{poly-nf}/\Delta P_{nf}$ and $\Delta P_{poly-nf}/\Delta P_{PAA}$, the PAA additives have the predominant influence over the nanofluid on the pressure drop of poly-nanofluid. This is attributed to the fact that the viscosity of the poly-nanofluid resembles that of the pure PAA solution. Therefore, the high pressure drop of poly-nanofluid is caused primarily by the presence of PAA additives in the nanofluid. The nanofluid becomes more viscous with PAA in it. Higher flow rate is required for the poly-nanofluid to achieve the same Reynolds number as the pure nanofluid, hence the penalty of pressure drop is larger.

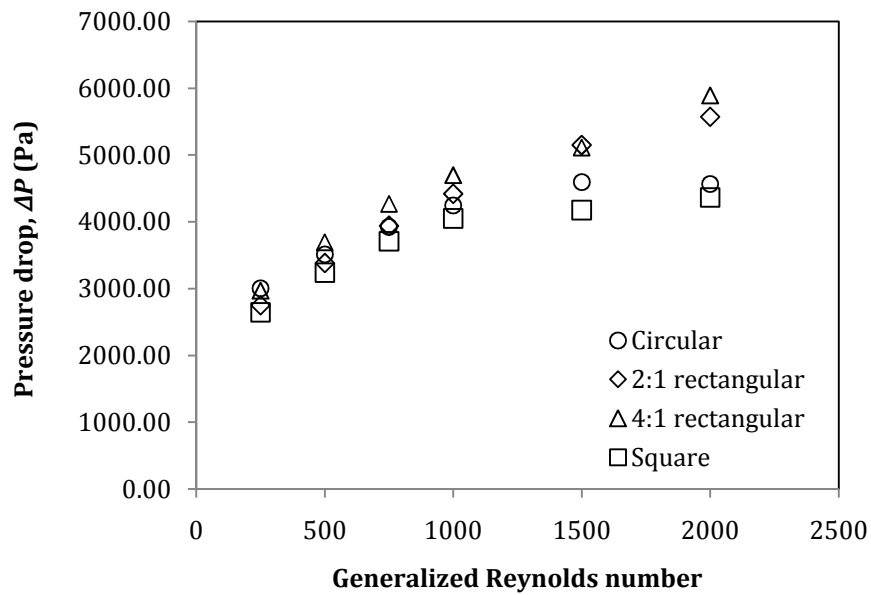
Table 6.5: $\Delta P_{poly-nf}/\Delta P_{PAA}$ for circular pipe.

Concentration of poly-nanofluid		Generalized Reynolds number				
PAA (ppm)	Nanofluid (vol%)	250	500	1000	1500	2000
10	0.13	1.01	1.02	1.03	1.03	1.04
	0.51	1.12	1.11	1.10	1.09	1.08
	1.00	1.29	1.30	1.32	1.30	1.24
	4.00	1.38	1.36	1.33	1.32	1.30
50	0.13	1.07	1.06	1.05	1.04	1.04
	0.51	1.12	1.11	1.11	1.11	1.11
	1.00	1.25	1.30	1.31	1.28	1.30
	4.00	1.27	1.36	1.35	1.34	1.57
200	0.13	1.09	1.08	1.05	1.03	1.01
	0.51	1.25	1.25	1.23	1.22	1.21
	1.00	1.32	1.33	1.33	1.32	1.29
	4.00	1.36	1.35	1.35	1.33	1.79
1000	0.13	1.02	1.10	1.22	1.31	1.28
	0.51	1.08	1.14	1.22	1.28	1.34
	1.00	1.40	1.39	1.35	1.32	1.36
	4.00	2.24	2.39	2.48	2.34	2.14

Table 6.6: $\Delta P_{poly-nf}/\Delta P_{PAA}$ for square duct.

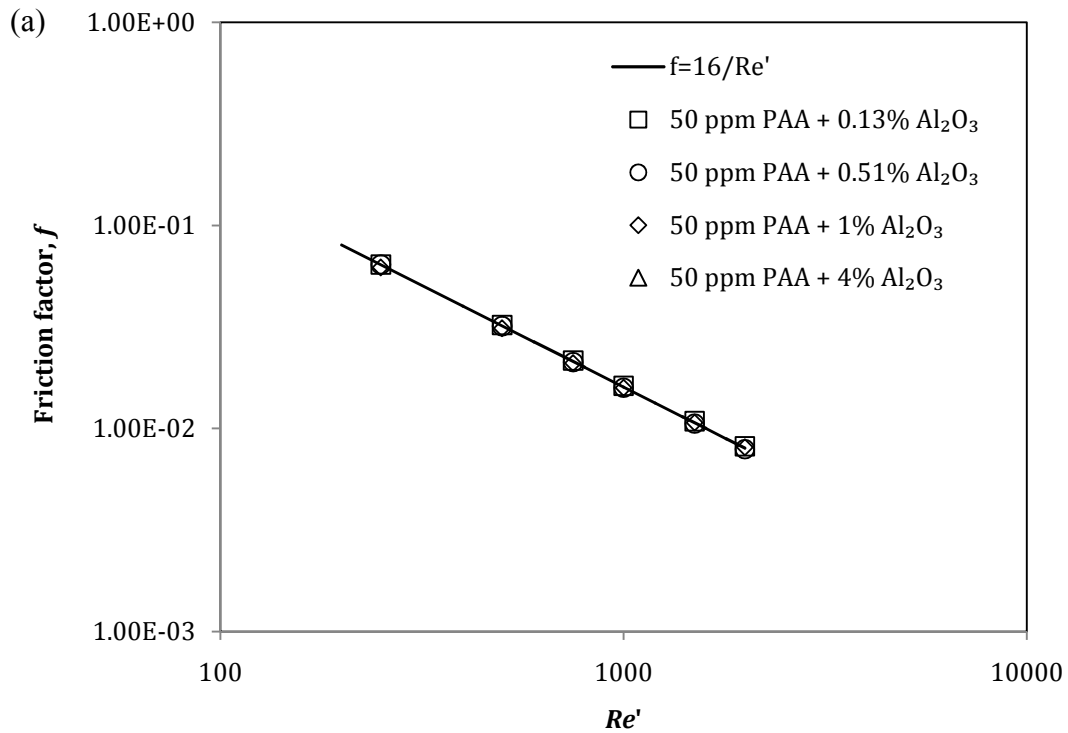
Concentration of poly-nanofluid		Generalized Reynolds number				
PAA (ppm)	Nanofluid (vol%)	250	500	1000	1500	2000
10	0.13	1.01	1.01	1.04	1.02	1.02
	0.51	1.01	1.03	1.06	1.11	1.10
	1.00	1.14	1.17	1.19	1.15	1.19
	4.00	1.24	1.30	1.32	1.26	1.21
50	0.13	1.05	1.04	1.02	1.01	1.05
	0.51	1.10	1.08	1.14	1.10	1.09
	1.00	1.15	1.13	1.23	1.17	1.15
	4.00	1.21	1.23	1.27	1.23	1.19
200	0.13	1.10	1.07	1.05	1.05	1.01
	0.51	1.20	1.21	1.18	1.17	1.13
	1.00	1.25	1.22	1.23	1.29	1.26
	4.00	1.25	1.22	1.45	1.65	1.83
1000	0.13	1.07	1.02	1.06	1.12	1.15
	0.51	1.14	1.06	1.08	1.13	1.19
	1.00	1.44	1.33	1.24	1.19	1.19
	4.00	2.11	2.19	2.25	2.03	1.93

Furthermore, as displayed in Figure 6.31, the pressure drop of poly-nanofluid in the non-circular ducts is similar to the cases of nanofluid and PAA solution that the pressure drop is the highest in the 4:1 rectangular pipe, followed by the 2:1 rectangular and square ducts. The flow in 4:1 rectangular duct experiences the highest shear stress as its aspect ratio is the lowest, leading to high pressure drop.

Figure 6.31: Pressure drop of 1000 ppm PAA in 4% Al_2O_3 nanofluid.

6.5.3 Friction factor for different geometries

Figure 6.32 depicts the friction factor of poly-nanofluid in the double pipe heat exchanger, circular and square ducts. The friction factor in the 2:1 and 4:1 rectangular ducts are shown in Appendix I (Figure I.18). It can be observed that the friction factor of all the poly-nanofluid studied in the double pipe heat exchanger, circular and non-circular ducts agree to the values estimated using the power law non-Newtonian model. This is similar to the case of the PAA solution. The agreement of the numerical friction factor obtained with that of the power law prediction is within 5.57%, 6.05% and 6.42% for the double pipe heat exchanger, circular and non-circular ducts, respectively. It is confirmed from the friction factor results that the addition of PAA additives into the nanofluid changes the friction factor of nanofluid to resemble that of the PAA solution. This is due to the similar rheology behaviour of the PAA solution and poly-nanofluid. Moreover, for the double pipe heat exchanger, it is noticed that the temperature of poly-nanofluid has negligible effect on the friction factor.



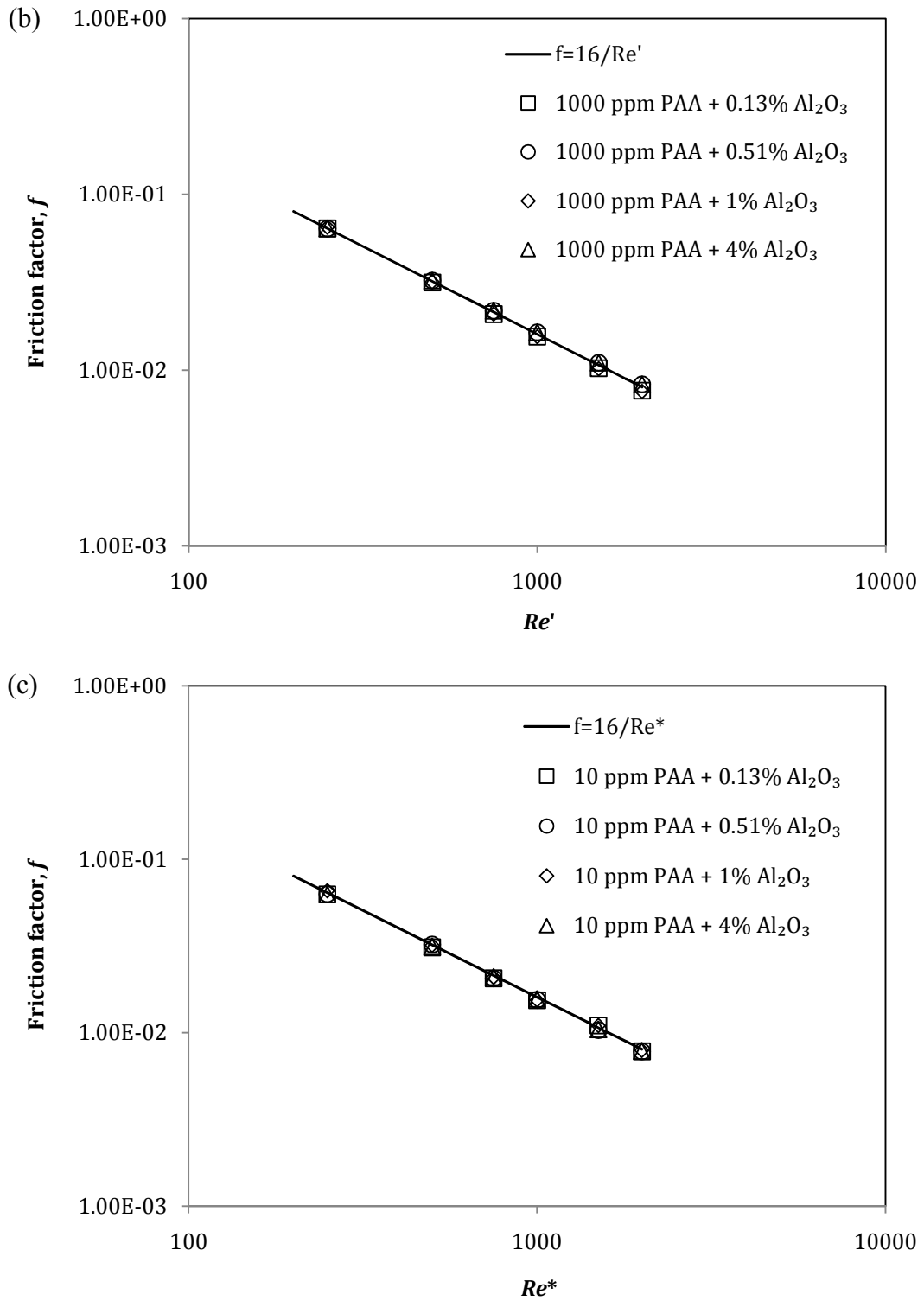


Figure 6.32: Friction factor of poly-nanofluid in (a) double pipe heat exchanger (temperature of 313.15 K), (b) circular and (c) square ducts.

6.6 Correlation to predict the friction factor of poly-nanofluid

The following correlation is introduced to predict the friction factor of poly-nanofluid in different geometries. It is obtained using the multiple regression method.

$$f = 15.645(Re^*)^{-0.9982}(\varphi_{nf})^{0.000886}(\varphi_{PAA})^{-0.0018} \quad R^2 = 0.9985 \quad (6.1)$$

The proposed friction factor correlation is functions of generalized Reynolds number, nanofluid volume fraction and PAA concentration (in fraction). The variation of predicted friction factor (from Equation 6.1) versus the numerical friction factor is shown in Figure 6.33. There is a reasonable agreement between the values of numerical and predicted friction factor, with a maximum deviation of +7% and -8%. Therefore, the correlation proposed in this study helps to predict the friction factor of poly-nanofluid in the circular, square, 2:1 rectangular and 4:1 rectangular ducts for the laminar regime. This correlation is valid for $250 \leq Re^*$ or $Re' \leq 2000$, $0.13\% \leq \varphi_{nf} \leq 4\%$ and $10 \text{ ppm} \leq \varphi_{PAA} \leq 1000 \text{ ppm}$.

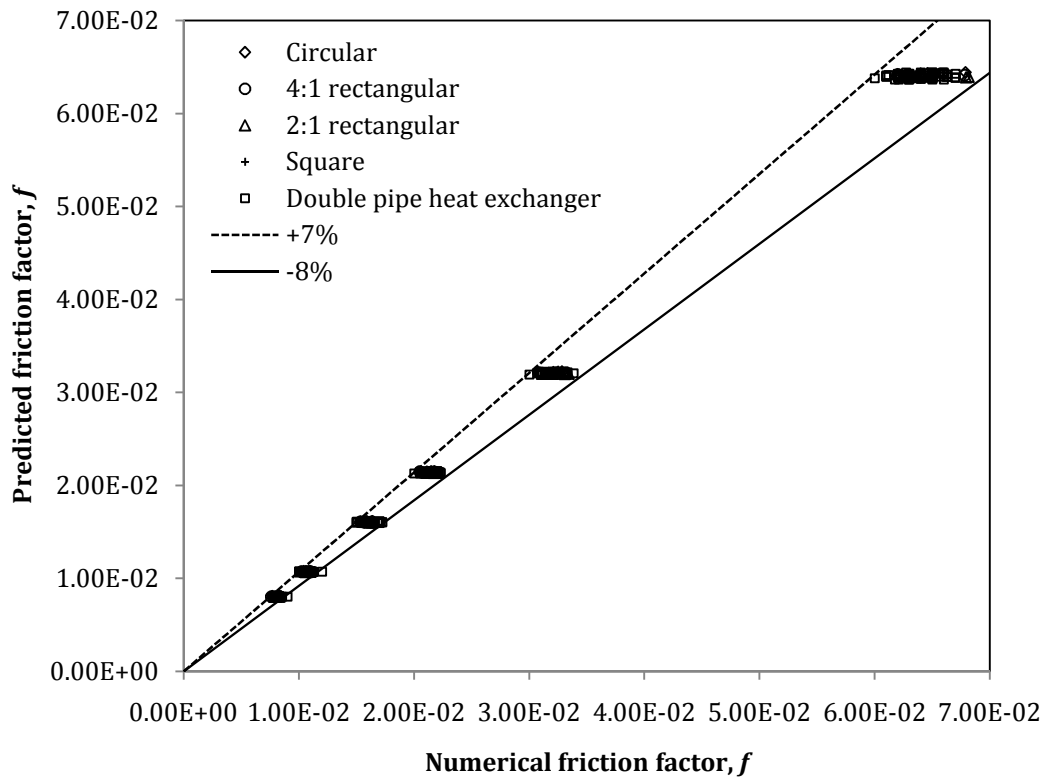


Figure 6.33: Comparison of numerical and predicted friction factor of poly-nanofluid based on the new correlation (Equation 6.1).

6.7 Summary

The study of flow feature reveals that:

1. The pressure drop of nanofluid is found to be higher than the value of water.
 - The increased pressure drop is due to the increased viscosity of nanofluid. Besides, the near-wall velocity gradient of nanofluid is higher than that of water, thus leading to higher wall shear stress.
 - The maximum pressure drop increment occurs at the highest nanofluid concentration considered, which is 4%. The maximum increments obtained in the cases of single-phase temperature-independent and temperature-dependent approaches are 945.69% and 117.75%, respectively.
2. It is ascertained that the temperature effect must be taken into consideration where there is a heat transfer.
 - The temperature-independent approach predicts higher pressure drop compared to the temperature-dependent approach. The maximum deviation between the results of these two approaches is 400% for circular pipe. This is because for the temperature-independent approach, the variation of viscosity with temperature is not considered, so the estimated pressure drop is always higher even at higher temperature.
3. The pressure drop estimated from the two-phase mixture, Eulerian and VOF models is similar at a particular nanofluid concentration and Reynolds number.
4. The pressure drop from the two-phase models is lower than the value obtained from the single-phase model when the nanofluid concentration is above 1%.
 - This is because the viscosity of nanofluid computed from the two-phase model is lower than the value of the single-phase model.
5. The single-phase model is found to be adequate in modelling the flow behaviour of nanofluid. Therefore, only the single-phase model is used for the poly-nanofluid modelling.
6. The maximum pressure drop increment of 1000 ppm PAA solution is approximately 56 times relative to that of water. This large pressure drop increment is due to the high viscosity of PAA solution.

7. The pressure drop of nanofluid is further increased when PAA additives are added into it.
 - The maximum pressure drop increment of 54.80 times higher than the value of pure nanofluid is encountered in the square duct.
 - Nanofluid becomes more viscous with PAA additives in it. Therefore, higher velocity is required for poly-nanofluid to achieve the same Reynolds number as the pure nanofluid, thus resulting in a higher pressure drop.
 - Similar to the cases of pure nanofluid and PAA solution, the pressure drop of poly-nanofluid is highest in the 4:1 rectangular duct. This is because higher wall shear stress is experienced in the duct with lower aspect ratio.
8. Since the pressure drop of poly-nanofluid in the non-circular ducts is comparable to the pressure drop in the circular pipe, it is deduced that the elasticity of poly-nanofluid solution does not change the flow behaviour in the non-circular ducts, similar to PAA solution.
9. The friction factor of poly-nanofluid is not similar to that of water at a particular Reynolds number like in the case of nanofluid, instead, its friction factor agrees reasonably with the value predicted from the Kozicki's correlation ($f=16/Re'$ or $f=16/Re^*$). This is similar to that of the PAA solution.
10. A correlation has been proposed to predict the friction factor of poly-nanofluid in circular and non-circular ducts, with maximum deviation of +7% and -8%.

CHAPTER 7: THERMAL-HYDRAULIC EFFICIENCY OF NANOFLUID, POLYMER AND POLY-NANOFLUID

7.1 Introduction

This study indicates that the heat transfer of nanofluid, PAA solution and poly-nanofluid are better relative to that of water. However, the HTE is acquired at the penalty of substantial pressure drop increment. This increased pressure drop might reduce the promising benefit of HTE. Therefore, a performance index, known as thermal-hydraulic efficiency, must be evaluated with respect to the heat transfer performance and pressure drop. The thermal-hydraulic efficiency is calculated using Equation 3.92 (Chapter 3). Efficiency greater than one shows improved thermal-hydraulic performance compared to water. The efficiency of nanofluid, PAA solution and poly-nanofluid are discussed and compared in this chapter. An optimum concentration of poly-nanofluid is found based on the best average thermal-hydraulic efficiency.

7.2 Thermal-hydraulic efficiency of Al₂O₃ nanofluid

7.2.1 Double pipe heat exchanger

Table 7.1 shows the thermal-hydraulic efficiency of Al₂O₃ nanofluid (based on the temperature-dependent properties) in the double pipe heat exchanger. It can be deduced from Table 7.1 that the thermal-hydraulic efficiency of nanofluid is mostly below one for the double pipe heat exchanger. Lower thermal-hydraulic efficiency of nanofluid is ascribed to the larger increment in the pressure drop than the heat transfer augmentation. Although for 1% and 4% nanofluid, their thermal-hydraulic performance at certain Reynolds number are above one, their thermal-hydraulic performance are still comparable to that of pure water. Based on the analysis of the thermal-hydraulic performance, the Al₂O₃ nanofluid does not show a considerable advantage over pure water.

Table 7.1: Thermal-hydraulic efficiency of nanofluid in double pipe heat exchanger.

Reynolds number	Nanoparticles volume concentration (%)						
	0.01	0.09	0.13	0.25	0.51	1.00	4.00
<i>Temperature of 313.15 K</i>							
250	0.862	0.859	0.860	0.866	0.875	0.888	0.868
500	0.960	0.963	0.965	0.970	0.979	0.994	0.984
1000	0.970	0.973	0.974	0.979	0.989	1.004	1.011
1500	0.958	0.961	0.963	0.968	0.977	0.992	0.964
2000	0.949	0.953	0.955	0.960	0.971	0.985	0.875
<i>Temperature of 318.15 K</i>							
250	0.879	0.883	0.884	0.891	0.901	0.914	0.871
500	0.959	0.962	0.964	0.969	0.979	0.994	0.988
1000	0.970	0.973	0.975	0.980	0.989	1.004	1.011
1500	0.962	0.965	0.967	0.972	0.981	0.996	0.984
2000	0.953	0.957	0.959	0.964	0.974	0.989	0.937
<i>Temperature of 323.15 K</i>							
250	0.954	0.958	0.959	0.964	0.976	0.990	0.970
500	0.963	0.966	0.968	0.973	0.982	0.997	0.995
1000	0.968	0.972	0.973	0.978	0.987	1.002	1.009
1500	0.966	0.970	0.971	0.976	0.985	1.001	0.997
2000	0.960	0.963	0.965	0.970	0.979	0.995	0.968

7.2.2 Circular and non-circular ducts

Table 7.2 presents the thermal-hydraulic efficiency of nanofluid in the circular pipe. The efficiency of nanofluid in the square, 2:1 rectangular and 4:1 rectangular ducts are given in Appendix I (Table I.20 to Table I.22). From Table 7.2, it can be discovered that the thermal-hydraulic efficiency of nanofluid is lower when compared to the base fluid for both the temperature-independent and temperature-dependent models. The efficiency of nanofluid in the other non-circular channels is also below one. In the case of temperature-independent properties, the thermal-hydraulic efficiency of 4% nanofluid in the circular pipe is the lowest with the value of 0.625 (occurring at $Re=250$). Following the trend that the heat transfer and pressure drop increases with the increasing volume fraction, it is concluded that the pressure drop increment of 4% nanofluid is far greater than the heat transfer augmentation. The lowest thermal-hydraulic efficiency of 0.910 for the temperature-dependent model is also obtained by 4% Al_2O_3 nanofluid in the circular pipe at the Reynolds number of 250.

Table 7.2: Thermal-hydraulic efficiency of nanofluid in circular pipe.

Reynolds number	Nanoparticles volume concentration (%)						
	0.01	0.09	0.13	0.25	0.51	1.00	4.00
<i>Temperature-independent properties</i>							
250	0.998	0.985	0.979	0.959	0.922	0.858	0.625
750	0.998	0.987	0.982	0.965	0.932	0.878	0.684
1000	0.998	0.988	0.983	0.967	0.937	0.886	0.703
1500	0.998	0.989	0.985	0.970	0.943	0.897	0.730
2000	0.999	0.990	0.986	0.973	0.947	0.904	0.745
<i>Temperature-dependent properties</i>							
250	0.928	0.932	0.934	0.940	0.952	0.971	0.910
750	0.932	0.936	0.938	0.944	0.954	0.971	0.927
1000	0.935	0.938	0.940	0.946	0.956	0.973	0.932
1500	0.940	0.943	0.945	0.950	0.960	0.974	0.942
2000	0.943	0.946	0.948	0.953	0.963	0.977	0.948

The thermal-hydraulic efficiency of 4% nanofluid (temperature-independent properties) in the square, 2:1 rectangular and 4:1 rectangular ducts are 0.638, 0.659 and 0.702, respectively, at the Reynolds number of 250. At this Reynolds number, the h_{nf}/h_{bf} ratio for the circular, square, 2:1 rectangular and 4:1 rectangular ducts are 1.367, 1.394, 1.441 and 1.534, respectively (refer to Table 5.2, Table I.1, Table I.3 and Table I.5); while for the $\Delta P_{nf}/\Delta P_{bf}$ ratio, their values are comparable which are between 10.444–10.458 (refer to Table 6.2 and Table I.8 to Table I.10). This indicates that at a particular Reynolds number and concentration, the pressure drop increment is similar but the HTE is different for different geometries. Therefore, it is noticed that the degree of heat transfer coefficient enhancement at a particular Reynolds number plays a major role in determining the thermal-hydraulic efficiency of nanofluid in different geometries.

Mashaei, Hosseinalipour, and Bahiraei (2012), Mashaei, Hosseinalipour, and Muslmani (2014) and Eastman et al. (1996) also studied the thermal-hydraulic performance factor of nanofluids in parallel plates channel with discrete heat source, serpentine microchannel and square duct, respectively. The results of Mashaei, Hosseinalipour, and Bahiraei (2012) demonstrated a best thermal-hydraulic performance index of 1.16 at the Reynolds number of 1000 and the concentration of 4%. Similarly, Eastman et al. (1996) also obtained efficiency greater than one in all the cases studied. Mashaei, Hosseinalipour, and Muslmani (2014) considered 2, 4 and 8% Al_2O_3 nanofluid. They reported that only the thermal-hydraulic efficiency of 8% nanofluid was below one.

Their best thermal-hydraulic performance was obtained by 4% nanofluid at the low Reynolds number of 10. On the other hand, Heris et al. (2015) who assessed the laminar thermal-hydraulic index of Al_2O_3 nanofluid pointed out that the minimum performance index achieved was 1.31 in the case of 0.5% Al_2O_3 nanofluid ($Re=1600$).

The difference between this present results and those of Mashaei, Hosseinalipour, and Bahiraei (2012) and Mashaei, Hosseinalipour, and Muslmani (2014) is due to the difference in the channel studied. Conversely, for Eastman et al. (1996) and Heris et al. (2015), they were using a shorter square duct (1 m). Besides, Heris et al. (2015) also utilized a 1 m triangular duct. Their flow is developed hydrodynamically but not thermally. Hence, their heat transfer coefficient enhancement is higher. For this present study, the flow is developed both hydrodynamically and thermally. Moreover, the channels considered in this present study are longer, hence, leading to greater pressure drop.

Zhao et al. (2016) also evaluated the thermal-hydraulic performance of nanofluid under the constant heat transfer rate condition and concluded that the nanofluid had no benefit over the base fluid when the concentration was beyond 3%. By examining the thermal-hydraulic efficiency of nanofluid in this study, it is deduced that water-based Al_2O_3 nanofluid has no advantage over pure water, especially for high nanofluid volume fraction. To make the best use of the nanofluid in the heat transfer applications, it is necessary to increase the thermal-hydraulic efficiency of nanofluid by either further improving the HTE or reducing the pressure drop increment.

7.3 Thermal-hydraulic efficiency of PAA solution

7.3.1 Double pipe heat exchanger

The thermal-hydraulic performance of PAA solution in the double pipe heat exchanger is shown in Table 7.3. Generally, it can be seen from this table that the thermal-hydraulic efficiency of PAA solution increases with the increase of Reynolds number but it decreases when the concentration increases. At a higher Reynolds number, the $\Delta P_{PAA}/\Delta P_{bf}$ will decrease, leading to a higher thermal-hydraulic efficiency. In contrast,

when the PAA concentration increases, the $\Delta P_{PAA}/\Delta P_{bf}$ will increase as well. Hence, at larger PAA concentration, the thermal-hydraulic performance index of the solution decreases. Therefore, it is inferred that the $\Delta P_{PAA}/\Delta P_{bf}$ has more a dominant effect on the performance index over the Nu_{PAA}/Nu_{bf} .

In addition, it is perceived that the temperature of the PAA solution has minor influence on the thermal-hydraulic performance. The performance index obtained for the three different temperatures studied are similar. This is because the pressure drop and the Nusselt number ratio of the PAA solution to that of the base fluid do not vary significantly with the temperature as the temperature range considered is not too big.

Overall, the thermal-hydraulic efficiency of PAA solution in the double pipe heat exchanger is not as good as that of the water, particularly at lower Reynolds number. The best performance index is found to be at the generalized Reynolds number of 2000 and for 10 ppm PAA solution, which is 1.108, 1.106 and 1.105 at the temperature of 313.15 K, 318.15 K and 323.15 K, respectively.

Table 7.3: Thermal-hydraulic efficiency of PAA solution in double pipe heat exchanger.

PAA concentration (ppm)	Generalized Reynolds number					
	250	500	750	1000	1500	2000
<i>Temperature of 313.15 K</i>						
10	0.521	0.738	0.843	0.922	1.042	1.108
50	0.514	0.729	0.842	0.918	1.039	1.103
200	0.504	0.729	0.832	0.910	1.035	1.103
1000	0.494	0.693	0.782	0.846	0.944	0.997
<i>Temperature of 318.15 K</i>						
10	0.521	0.725	0.833	0.911	1.031	1.106
50	0.516	0.721	0.829	0.907	1.030	1.099
200	0.515	0.718	0.825	0.905	1.022	1.097
1000	0.495	0.683	0.772	0.837	0.937	1.005
<i>Temperature of 323.15 K</i>						
10	0.596	0.730	0.826	0.906	1.020	1.105
50	0.595	0.725	0.824	0.902	1.019	1.092
200	0.587	0.723	0.817	0.894	1.018	1.090
1000	0.567	0.698	0.803	0.883	0.985	1.020

7.3.2 Circular and non-circular ducts

Table 7.4 presents the thermal-hydraulic efficiency of PAA solution in different geometries. It is found out that the circular pipe has the lowest thermal-hydraulic performance index among all the ducts studied. This is attributed to the weaker HTE of the PAA solution in the circular pipe compared to that of the non-circular ducts. Moreover, the pressure drop of the solution in the circular duct is comparatively high relative to that of water. Therefore, the thermal-hydraulic efficiency of PAA solution is below one in the circular pipe. It is realized that there is no benefit over water for the laminar flow of PAA solution in the circular duct.

For the non-circular ducts, it is observed that the thermal-hydraulic efficiency improves when the Reynolds number and PAA concentration increase. For a particular concentration, both the Nu_{PAA}/Nu_{bf} and $\Delta P_{PAA}/\Delta P_{bf}$ decrease with the increasing of Reynolds number, so the latter has a major influence on the thermal-hydraulic performance over the former when the Reynolds number is varied. Conversely, when the Reynolds number is constant, both the Nu_{PAA}/Nu_{bf} and $\Delta P_{PAA}/\Delta P_{bf}$ increase with the increase of PAA concentration. However, the former is larger than the latter. Therefore, the Nu_{PAA}/Nu_{bf} has a major effect on the thermal-hydraulic efficiency.

Overall, the flow of PAA solution in the non-circular ducts is efficient thermally and hydrodynamically. The best thermal-hydraulic efficiency is 1.901, 1.787 and 1.469 for the square, 2:1 rectangular and 4:1 rectangular ducts, respectively (obtained by 1000 ppm PAA solution at $Re^*=2000$). Between the non-circular ducts, the square duct has the best thermal-hydraulic performance. This is because the square duct has the largest Nu_{PAA}/Nu_{bf} while its $\Delta P_{PAA}/\Delta P_{bf}$ is comparable to that of the other geometries.

Table 7.4: Thermal-hydraulic efficiency of PAA solution in different geometries.

PAA concentration (ppm)	Generalized Reynolds number					
	250	500	750	1000	1500	2000
<i>Circular</i>						
10	0.427	0.533	0.603	0.653	0.709	0.741
50	0.427	0.529	0.595	0.648	0.709	0.740
200	0.425	0.529	0.593	0.645	0.705	0.734
1000	0.410	0.515	0.583	0.627	0.681	0.712

Table 7.4: (Continued)

PAA concentration (ppm)	Generalized Reynolds number					
	250	500	750	1000	1500	2000
<i>2:1 rectangular</i>						
10	1.091	1.273	1.394	1.479	1.515	1.524
50	1.165	1.350	1.413	1.523	1.579	1.598
200	1.215	1.383	1.480	1.548	1.636	1.680
1000	1.243	1.405	1.508	1.591	1.674	1.787
<i>4:1 rectangular</i>						
10	0.974	1.145	1.223	1.257	1.253	1.263
50	0.999	1.165	1.237	1.267	1.277	1.285
200	1.039	1.207	1.283	1.319	1.332	1.342
1000	1.089	1.295	1.396	1.449	1.450	1.469
<i>Square</i>						
10	1.164	1.422	1.540	1.629	1.707	1.710
50	1.167	1.431	1.563	1.641	1.709	1.713
200	1.214	1.435	1.586	1.647	1.727	1.734
1000	1.228	1.456	1.589	1.655	1.762	1.901

7.4 Thermal-hydraulic efficiency of poly-nanofluid

7.4.1 Double pipe heat exchanger

Generally, the thermal-hydraulic performance index of poly-nanofluid increases when the nanoparticle loading in the solution and the Reynolds number increase (Table 7.5). This is due to the reduction of the pressure drop ratio of poly-nanofluid to water as the Reynolds number increases. Besides, the HTE of poly-nanofluid with higher nanoparticle loading is larger when compared to that of water. Therefore, the efficiency increases when the nanoparticle loading increases.

Overall, the thermal-hydraulic efficiency of poly-nanofluid in the double pipe heat exchanger is below one except for the generalized Reynolds number range of 1500–2000. The efficiency of poly-nanofluid is comparable to that of PAA solution in the double pipe heat exchanger. However, it is not as good as the efficiency of pure nanofluid when the Reynolds number is and below 1000. Therefore, it is not beneficial to add PAA into nanofluid for the double pipe heat exchanger when the Reynolds number is below and 1000. The maximum thermal-hydraulic performance factor of 1.166 is obtained at 313.15 K ($Re'=2000$), where the concentration is 200 ppm PAA in 4% nanofluid.

Table 7.5: Thermal-hydraulic efficiency of poly-nanofluid in double pipe heat exchanger at hot inlet temperature of 313.15 K.

Concentration of poly-nanofluid		Generalized Reynolds number				
PAA (ppm)	Nanofluid (vol%)	250	500	1000	1500	2000
10	0.13	0.527	0.739	0.923	1.043	1.104
	0.51	0.525	0.736	0.916	1.042	1.118
	1.00	0.533	0.749	0.925	1.050	1.116
	4.00	0.539	0.769	0.948	1.070	1.146
50	0.13	0.524	0.736	0.924	1.041	1.109
	0.51	0.519	0.732	0.921	1.048	1.113
	1.00	0.535	0.753	0.940	1.062	1.126
	4.00	0.541	0.768	0.952	1.077	1.160
200	0.13	0.520	0.734	0.917	1.039	1.110
	0.51	0.520	0.734	0.930	1.052	1.108
	1.00	0.535	0.749	0.930	1.047	1.122
	4.00	0.545	0.756	0.959	1.097	1.166
1000	0.13	0.487	0.685	0.841	0.942	0.993
	0.51	0.491	0.689	0.880	0.986	1.011
	1.00	0.503	0.712	0.915	1.008	1.017
	4.00	0.519	0.750	0.938	1.063	1.125

The thermal-hydraulic efficiency of poly-nanofluid at the hot inlet temperature of 318.15 and 323.15 K are given in Appendix I Table I.23 and Table I.24, respectively. The average thermal-hydraulic efficiency of poly-nanofluid at 313.15, 318.15 and 323.15 K are similar, especially when the Reynolds number is higher.

7.4.2 Circular and non-circular ducts

The thermal-hydraulic efficiency of poly-nanofluid in the circular and square ducts are given in Table 7.6 and Table 7.7, respectively. The performance index for 4:1 and 2:1 rectangular ducts are tabulated in Appendix I Table I.25 to Table I.26. According to Table 7.6, the thermal-hydraulic efficiency of poly-nanofluid in the circular pipe is below one and is lower compared to that of the non-circular ducts. This is as a result of a lower HTE but comparable pressure drop increment of poly-nanofluid in the circular pipe relative to that of the non-circular ducts. Furthermore, the efficiency of poly-nanofluid in the circular pipe is poorer than the efficiency of pure nanofluid. Hence, it is inferred that it is not useful to add PAA additives into nanofluid for heat transfer purposes in the circular pipe. The pressure drop increment tends to diminish the benefit of HTE achieved by adding the PAA additives into nanofluid.

Table 7.6: Thermal-hydraulic efficiency of poly-nanofluid in circular pipe.

Concentration of poly-nanofluid		Generalized Reynolds number				
PAA (ppm)	Nanofluid (vol%)	250	500	1000	1500	2000
10	0.13	0.433	0.538	0.653	0.710	0.741
	0.51	0.425	0.530	0.643	0.702	0.733
	1.00	0.408	0.509	0.642	0.700	0.728
	4.00	0.402	0.506	0.624	0.689	0.725
50	0.13	0.424	0.529	0.642	0.700	0.733
	0.51	0.418	0.524	0.640	0.690	0.718
	1.00	0.406	0.514	0.630	0.687	0.707
	4.00	0.406	0.501	0.618	0.684	0.673
200	0.13	0.427	0.529	0.641	0.705	0.735
	0.51	0.425	0.529	0.638	0.702	0.709
	1.00	0.411	0.517	0.633	0.689	0.702
	4.00	0.409	0.505	0.606	0.666	0.670
1000	0.13	0.414	0.504	0.621	0.680	0.682
	0.51	0.408	0.499	0.592	0.642	0.666
	1.00	0.398	0.499	0.591	0.633	0.666
	4.00	0.392	0.469	0.538	0.591	0.651

Table 7.7: Thermal-hydraulic efficiency of poly-nanofluid in square duct.

Concentration of poly-nanofluid		Generalized Reynolds number				
PAA (ppm)	Nanofluid (vol%)	250	500	1000	1500	2000
10	0.13	1.178	1.453	1.691	1.763	1.770
	0.51	1.228	1.481	1.689	1.725	1.748
	1.00	1.190	1.427	1.647	1.708	1.726
	4.00	1.229	1.417	1.717	1.842	1.921
50	0.13	1.214	1.451	1.662	1.719	1.728
	0.51	1.234	1.462	1.625	1.698	1.748
	1.00	1.286	1.521	1.675	1.772	1.844
	4.00	1.266	1.542	1.764	1.880	1.905
200	0.13	1.225	1.460	1.651	1.707	1.730
	0.51	1.193	1.395	1.588	1.677	1.749
	1.00	1.295	1.523	1.677	1.711	1.770
	4.00	1.331	1.528	1.694	1.756	1.785
1000	0.13	1.235	1.479	1.674	1.759	1.825
	0.51	1.317	1.564	1.734	1.780	1.807
	1.00	1.226	1.487	1.721	1.786	1.810
	4.00	1.142	1.299	1.434	1.710	2.216

Looking at the non-circular ducts, the pressure drop increment of poly-nanofluid is also far larger than that of the nanofluid. This is undesirable. Nonetheless, in terms of the heat transfer performance, it is much better than the nanofluid. The thermal-hydraulic performance of poly-nanofluid is efficient as the efficiency is above one, which is better than that of water. Besides, the thermal-hydraulic performance index of poly-nanofluid

is superior than the value of pure nanofluid because the HTE of poly-nanofluid is higher. However, some thermal-hydraulic efficiency of poly-nanofluid are slightly lower than that of the pure PAA solution due to the higher pressure drop increment of poly-nanofluid. The pressure drop of poly-nanofluid is higher relative to that of the pure PAA solution because the viscosity of poly-nanofluid is higher.

The best thermal-hydraulic efficiency is achieved by 1000 ppm PAA in 4% nanofluid at $Re^*=2000$. These values are 2.216, 2.033 and 1.908 for the square, 2:1 and 4:1 rectangular ducts, respectively. The efficiency is the best in the square duct because its HTE is the greatest while its pressure drop increment is the smallest among the non-circular ducts.

7.5 Optimum concentration

In order to obtain the optimum concentration of poly-nanofluid, the average thermal-hydraulic efficiency is assessed over the Reynolds number range studied. The average efficiency is given in Table 7.8. The best average thermal-hydraulic efficiency for different geometries is highlighted in this table. For the double pipe heat exchanger, the best average thermal-hydraulic efficiency occurs when 200 ppm PAA is added into 4% nanofluid. It is 10 ppm PAA in 0.13% nanofluid for the case of circular pipe. For all the three non-circular ducts, the largest average performance index is acquired by 50 ppm PAA in 4% nanofluid.

Since the thermal-hydraulic performance index of poly-nanofluid obtained for the double pipe heat exchanger and circular pipe is not superior than those of water and nanofluid, the optimum concentration is chosen based on the average efficiency in the non-circular ducts. Therefore, after evaluating the heat transfer performance and pressure drop of poly-nanofluid in the non-circular ducts, the optimum concentration chosen is 50 ppm PAA in 4% Al_2O_3 nanofluid. The average performance index obtained at this optimum concentration for the double pipe heat exchanger, circular, square, 2:1 and 4:1 rectangular ducts are 0.894, 0.586, 1.667, 1.586 and 1.404 , respectively.

Table 7.8: Average thermal-hydraulic efficiency of poly-nanofluid.

Concentration of poly-nanofluid		Efficiency in:				
PAA (ppm)	Nanofluid (vol%)	Double pipe heat exchanger	Circular	Square	2:1 rectangular	4:1 rectangular
10	0.13	0.862	0.613	1.576	1.419	1.198
	0.51	0.863	0.604	1.580	1.421	1.196
	1.00	0.885	0.589	1.543	1.295	1.362
	4.00	0.890	0.593	1.632	1.561	1.388
50	0.13	0.860	0.603	1.560	1.475	1.273
	0.51	0.864	0.594	1.563	1.536	1.338
	1.00	0.876	0.581	1.623	1.561	1.359
	4.00	0.894	0.586	1.667	1.586	1.404
200	0.13	0.858	0.605	1.559	1.533	1.331
	0.51	0.863	0.575	1.519	1.516	1.338
	1.00	0.870	0.591	1.602	1.537	1.340
	4.00	0.900	0.594	1.622	1.558	1.345
1000	0.13	0.808	0.560	1.596	1.531	1.304
	0.51	0.813	0.560	1.646	1.548	1.334
	1.00	0.840	0.574	1.610	1.507	1.337
	4.00	0.876	0.526	1.529	1.481	1.377

7.6 Summary

It is observed from the evaluation of the thermal-hydraulic efficiency that:

- The thermal-hydraulic efficiency of nanofluid is generally below one for the double pipe heat exchanger, circular and non-circular ducts.
 - This poor efficiency of nanofluid is due to the larger pressure drop increment than the heat transfer augmentation.
 - Therefore, nanofluid does not show significant advantage over water. It is crucial to improve the thermal-hydraulic efficiency to make the application of nanofluid beneficial.
- For PAA solution, the flow in the double pipe heat exchanger is efficient only when the Reynolds number is above 1000. However, the efficiency of PAA solution obtained in the circular pipe is below one because the pressure drop encountered is high.
- Although the pressure drop of PAA solution in the non-circular ducts is also high, the high heat transfer enhancement improves the thermal-hydraulic efficiency of PAA solution to be better than that of water.

- The maximum thermal-hydraulic efficiency of 1.901 is obtained by 1000 ppm PAA in the square duct.
4. Even though the heat transfer is further enhanced when PAA additives are added into nanofluid, the heat transfer enhancement in the circular pipe is not attractive because the efficiency is poor. In addition, the flow of poly-nanofluid in the double pipe heat exchanger is only efficient when the Reynolds number is above 1000. As a result, it is not beneficial to add PAA into nanofluid for the heat exchanger when the Reynolds number is and below 1000.
 5. The efficiency of poly-nanofluid in the non-circular ducts is found to be better than those of water and pure nanofluid.
 6. The optimum concentration of poly-nanofluid chosen is 50 ppm PAA added to 4% Al_2O_3 nanofluid, with the best average thermal-hydraulic efficiency of 1.667 obtained in the square duct.
 7. The square duct has the best efficiency as the HTE is the highest with the lowest pressure drop increment.

CHAPTER 8: CONCLUSIONS AND RECOMMENDATIONS

8.1 Conclusions

In this present study, some important conclusions were drawn as follows:

1. PAA solution is found to be non-Newtonian shear-thinning. The addition of PAA additives changes the rheology of nanofluid from Newtonian to resemble that of the PAA solution. The poly-nanofluid is also determined to be non-Newtonian shear-thinning.
2. The viscosity of poly-nanofluid is higher compared to the value of pure PAA solution. The viscosity of PAA solution and poly-nanofluid was well-fitted with the Carreau model, which was functions of shear rate and temperature, with the errors of less than $\pm 10\%$.
3. Al_2O_3 nanofluid enhances the heat transfer in the double pipe heat exchanger, circular and non-circular ducts.
 - This HTE was attributed to the increased thermal-conductivity of nanofluid.
 - Although the Nusselt number of nanofluid was the highest in the circular pipe, the nanofluid improved the thermal performance in the non-circular ducts more than the circular duct.
 - At the Reynolds number of 2000, the Nusselt number of 4% nanofluid was approximately 5.12% higher relative to that of water in the square duct (obtained from the single-phase temperature-dependent approach).
4. Higher viscosity of nanofluid results in a higher pressure drop compared to the case of water.
 - The maximum pressure drop increment computed from the temperature-dependent approach was 117.75% for 4% nanofluid.
 - The pressure drop of nanofluid was the highest in the 4:1 rectangular duct because the flow experienced higher shear stress when the aspect ratio of the duct decreased.

5. The friction factor of nanofluid was similar to that of water at a particular Reynolds number.
6. The heat transfer and pressure drop of nanofluid estimated from the single-phase temperature-independent approach were higher compared to those of the temperature-dependent approach.
 - This was because the variation of thermal-conductivity and viscosity with temperature were not considered in the case of temperature-independent approach. As a result, the heat transfer was always higher even the temperature was lower; while the pressure drop was higher even at higher temperature. Therefore, it was concluded in this present study that it was crucial to consider the temperature effect on the thermo-physical properties for heat transfer study.
7. The heat transfer and pressure drop results estimated from the two-phase mixture, Eulerian and VOF models were similar at a particular Reynolds number and concentration.
8. When compared to the case of single-phase model, the heat transfer predicted from the two-phase model was higher, while the pressure drop estimated was lower as the nanofluid concentration increased. Nonetheless, the results obtained from the single-phase and two-phase models were close and comparable when the nanofluid concentration was low. Therefore, the use of single-phase model was found to be adequate for nanofluid modelling. Besides this reason, the single-phase model was applied for poly-nanofluid due to its simplicity.
9. The use of nanofluid did not show advantages over water.
 - The flow of nanofluid in all the geometries studied was not efficient owing to higher pressure drop increment compared to the HTE.
 - Therefore, it was crucial to improve the thermal-hydraulic efficiency of nanofluid to make the use of nanofluid beneficial.
10. The PAA solution is also discovered to enhance heat transfer.
 - The heat transfer augmentation of PAA solution in the circular pipe (including double pipe heat exchanger) was weaker compared to that achieved in the non-circular ducts.

- The HTE in the circular pipe was attributed to the purely viscous shear-thinning behaviour of PAA solution. In contrast, the presence of secondary flow induced from the elasticity of PAA solution was the main reason of HTE in the non-circular pipes.
 - The magnitude of the HTE was the highest in the square duct because the intensity of the secondary flow was higher in duct with higher aspect ratio. The maximum Nusselt number enhancement of 5.40 times larger than the value of water was obtained in the square duct.
11. The pressure drop of 1000 ppm PAA solution was 56 times higher than the pressure drop of water. This was caused by the viscosity increment of the solution.
 12. The efficiency of PAA solution was generally poor in the circular pipe. For the heat exchanger, the flow was only efficient when the Reynolds number was above 1000. However, the flow of PAA solution in the non-circular ducts was efficient thermally and hydraulically. The maximum thermal-hydraulic efficiency of 1.901 was achieved by using 1000 ppm PAA in the square pipe.
 13. When PAA additives are added into nanofluid, the heat transfer is further augmented.
 - The HTE of poly-nanofluid in the circular pipe (including double pipe heat exchanger) was ascribed to the increased thermal-conductivity and shear-thinning behaviour of the solution, where the latter had the dominant effect.
 - The secondary flow induced in the non-circular pipes helped to enhance heat transfer in the non-circular ducts more than that of the circular pipe.
 - Similar to PAA solution, the magnitude of Nusselt number enhancement was the largest in the square duct. The HTE of poly-nanofluid in the square duct was maximum with the Nusselt number of 5.95 times the value of pure nanofluid.
 14. The addition of PAA also increase the pressure drop of nanofluid as the solution becomes more viscous with PAA additives in it.
 - The maximum pressure drop increment of poly-nanofluid in the square duct was 54.80 times higher than the value of pure nanofluid.
 - Like the PAA solution, it was deduced that the elasticity of poly-nanofluid did not affect the flow behaviour of the solution in the non-circular ducts.
 - The pressure drop of poly-nanofluid was the highest in the 4:1 rectangular duct.

15. The friction factor of poly-nanofluid agreed reasonably with the value estimated from the Kozicki's correlation ($f=16/Re'$ or $f=16/Re^*$).
16. The high pressure drop increment had diminished the advantage of HTE achieved by adding PAA into nanofluid in the circular pipe and double pipe heat exchanger. By analyzing the average thermal-hydraulic performance index, the efficiency of poly-nanofluid in the circular pipe was poor. The flow of poly-nanofluid in the double pipe heat exchanger is only efficient when the Reynolds number is above 1000. Therefore, it was not attractive to add PAA additives to nanofluid in these two geometries.
17. The large HTE achieved by adding PAA additives to nanofluid improved the efficiency of the flow in the non-circular ducts even though the pressure drop encountered was also high.
18. The optimum concentration was chosen to be 50 ppm PAA added to 4% Al_2O_3 nanofluid. The best thermal-hydraulic efficiency of 1.667 was obtained in the square duct at this optimum concentration. Square duct had the best efficiency because the HTE was the greatest, but the pressure drop increment was the lowest.
19. Correlations were proposed to predict the Nusselt number and friction factor of poly-nanofluid in the circular and non-circular pipe. These correlations were valid for $250 \leq Re^*$ or $Re' \leq 2000$, $Pr > 50$, $13\% \leq \varphi_{nf} \leq 4\%$ and $10 \text{ ppm} \leq \varphi_{PAA} \leq 1000$ ppm. They are given as below:

Circular pipe:

$$Nu = 2.011(Re')^{0.1160}(Pr)^{0.1384}(\varphi_{nf})^{0.0002}(\varphi_{PAA})^{0.0056} \quad \pm 6.80\%$$

Square duct:

$$Nu = 9.198(Re^*)^{0.0626}(Pr)^{0.0821}(\varphi_{nf})^{0.0004}(\varphi_{PAA})^{0.0213} \quad \pm 7.30\%$$

2:1 rectangular duct:

$$Nu = 11.409(Re^*)^{0.0560}(Pr)^{0.0591}(\varphi_{nf})^{0.0004}(\varphi_{PAA})^{0.0271} \quad \pm 7.60\%$$

4:1 rectangular duct:

$$Nu = 7.134(Re^*)^{0.0706}(Pr)^{0.1603}(\varphi_{nf})^{0.0223}(\varphi_{PAA})^{0.0242} \quad \pm 8.40\%$$

All geometries:

$$f = 15.645(Re^*)^{-0.9982}(\varphi_{nf})^{0.000886}(\varphi_{PAA})^{-0.0018} \quad \pm 8.00\%$$

8.2 Recommendations

The focus of this present study is on the laminar regime. It is recommended to study the effect of the addition of PAA additives to nanofluid for different geometries in the turbulent regime. It is interesting to know if the high pressure drop encountered by the poly-nanofluid in the laminar regime is reduced when the flow is extended to the turbulent regime. Besides, it is also worthwhile to study the turbulent thermal-hydraulic efficiency of poly-nanofluid. Although the PAA solution is reported to reduce the heat transfer in the turbulent flow (Gupta, Metzner, and Hartnett 1967; Poreh and Paz 1968; Kwack and Hartnett 1983; Hartnett and Kwack 1986), the nanoparticles in poly-nanofluid might still have the HTE ability. More investigations are needed.

In this research, the thermal conductivity and heat capacity of poly-nanofluid are taken to be the same as the nanofluid. Moreover, the first normal stress difference of poly-nanofluid is calculated based on the existing correlation. It is proposed to include the measurement of thermal properties and first normal stress difference for the poly-nanofluid. This is necessary for establishing the applications of poly-nanofluid in the future.

It is also suggested to perform the numerical investigation on the heat transfer and flow feature of poly-nanofluid using the two-phase approach. The two-phase approach might aid to better understand the behaviour of nanoparticles in poly-nanofluid. It is also important to examine the HTE mechanism of poly-nanofluid more thoroughly. More studies are required to find out the chemical interactions of polymer chains with the nanoparticles in the poly-nanofluid.

Moreover, different available equations of thermal conductivity and viscosity can be applied for nanofluid and poly-nanofluid. For example, the aspect of Brownian motion can be taken into considerable in computing the thermal conductivity of nanofluid and poly-nanofluid for future study. Comparison of the heat transfer results obtained using these different equations with that of this present study can be done.

Furthermore, the effect of nanoparticle size, nanoparticle material, type of additive, pipe length and diameter on the heat transfer and flow behaviour of poly-nanofluid can be examined. For the double pipe heat exchanger, a wider temperature range for research can be considered. These works will help to find out the effect of different parameters on the heat transfer and flow behaviour of poly-nanofluid.

In addition, different constitutive equations can be applied to model the viscoelastic property of poly-nanofluid. The results obtained from these different constitutive equations can be used to compare with the results of this present study. This investigation helps to address the benefits and limitations of each constitutive equation in modelling the poly-nanofluid.

REFERENCES

- Abubakar, A., T. Al-Wahaibi, Y. Al-Wahaibi, A. R. Al-Hashmi, and A. Al-Ajmi. 2014. "Roles of Drag Reducing Polymers in Single- and Multi-Phase Flows." *Chem. Eng. Res. Design* 92 (11): 2153-2181.
- Ahmad, U. K., M. Hasreen, N. A. Yahaya, and B. Rosnadiyah. 2017. "Comparative Study of Heat Transfer and Friction Factor Characteristics of Nanofluids in Rectangular Channel." *Procedia Engineering* 170: 541-546.
- Akbari, M., N. Galanis, and A. Behzadmehr. 2011. "Comparative Analysis of Single and Two-Phase Models for Cfd Studies of Nanofluid Heat Transfer." *Int. J. Therm. Sci.* 50 (8): 1343-1354.
- Akindoyo, Edward Oluwasoga, Hayder A. Abdulbari, and Zainab Yousif. 2015. "A Dual Mechanism of the Drag Reduction by Rigid Polymers and Cationic Surfactant: Complex and Nanofluids of Xanthan Gum and Hexadecyl Trimethyl Ammonium Chloride." *International Journal of Research in Engineering and Technology* 4 (2): 84-93.
- Aladag, Bahadir, Salma Halelfadl, Nimeti Doner, Thierry Mare, Steven Duret, and Patrice Estelle. 2012. "Experimental Investigations of the Viscosity of Nanofluids at Low Temperatures." *Appl. Energy* 97: 876-880.
- Anoop, K. B., T. Sundararajan, and Sarit K. Das. 2009. "Effect of Particle Size on the Convective Heat Transfer in Nanofluid in the Developing Region." *Int. J. Heat Mass Transfer* 52 (9–10): 2189-2195.
- Ansys Fluent 15.0 Theory Guide*. 2013. USA: ANSYS Inc.
- Ansys Fluent 15.0 User's Guide*. 2013. USA: ANSYS Inc.
- Ar 500/1000 Rheometers Hardware Manual*. 2000. New Castle: TA Instruments.
- Azari, A., M. Kalbasi, and M. Rahimi. 2014. "Cfd and Experimental Investigation on the Heat Transfer Characteristics of Alumina Nanofluids under the Laminar Flow Regime." *Braz. J. Chem. Eng.* 31: 469-481.
- Azmi, W. H., K. V. Sharma, Rizalman Mamat, G. Najafi, and M. S. Mohamad. 2016. "The Enhancement of Effective Thermal Conductivity and Effective Dynamic Viscosity of Nanofluids – a Review." *Renewable and Sustainable Energy Reviews* 53: 1046-1058.
- Barnes, Howard A., John Fletcher Hutton, and Kenneth Walters. 1989. *An Introduction to Rheology*. Amsterdam, Netherlands: Elsevier.
- Batill, Stephen M. 1994. *Experimental Uncertainty and Drag Measurements in the National Transonic Facility*. Virginia, USA.
- Berman, N. S. 1978. "Drag Reduction by Polymers." *Annu. Rev. Fluid Mech.* 10 (1): 47-64.
- Bianco, Vincenzo, F. Chiacchio, Oronzio Manca, and Sergio Nardini. 2009. "Numerical Investigation of Nanofluids Forced Convection in Circular Tubes." *Appl. Therm. Eng.* 29 (17–18): 3632-3642.
- Bianco, Vincenzo, Oronzio Manca, Ferdinando Marzano, Sergio Nardini, Salvatore Tamburrino, and Antonio Vitale. 2008. "Numerical Investigation of Forced Convection of Nanofluids in Channels." In *Proceedings of 2008 ASME International Mechanical Engineering Congress and Exposition*, 929-938. New York: American Society of Mechanical Engineers.

- Bianco, Vincenzo, Oronzio Manca, and Sergio Nardini. 2011. "Numerical Investigation on Nanofluids Turbulent Convection Heat Transfer inside a Circular Tube." *Int. J. Therm. Sci.* 50 (3): 341-349.
- Bird, R. B., R. C. Armstrong, and O. Hassager. 1987. *Dynamics of Polymeric Liquids*. New York: Wiley.
- Bodnar, T., A. Sequeira, and M. Prosi. 2011. "On the Shear-Thinning and Viscoelastic Effects of Blood Flow under Various Flow Rates." *Applied Mathematics and Computation* 217 (11): 5055-5067.
- Bonn, Daniel, Amarouchene Yacine, Wagner Christian, Douady Stephane, and Cadot Olivier. 2005. "Turbulent Drag Reduction by Polymers." *J. Phys.: Condens. Matter* 17 (14): 1195.
- Bschorer, Sabine, and Peter O. Brunn. 1996. "Numerical Simulation of Contraction Flow of a Dilute Polymer Solution." *Chem. Eng. Technol.* 19 (4): 386-389.
- Chandrasekar, M., S. Suresh, and A. Chandra Bose. 2010. "Experimental Investigations and Theoretical Determination of Thermal Conductivity and Viscosity of Al₂O₃/Water Nanofluid." *Exp. Therm. Fluid Sci.* 34 (2): 210-216.
- Chen, Hai Sheng, Sanjeeva Witharana, Yi Jin, Chong Youp Kim, and Yu Long Ding. 2009. "Predicting Thermal Conductivity of Liquid Suspensions of Nanoparticles (Nanofluids) Based on Rheology." *Particuology* 7 (2): 151-157.
- Chevalier, J., O. Tillement, and F. Ayela. 2007. "Rheological Properties of Nanofluids Flowing through Microchannels." *Appl. Phys. Lett.* 91 (23): 233103-3.
- Chinnaraj, Anand Natchimuthu. 2011. "Thermal Conductivity Enhancement in Nanofluids- Mathematical Model." Master's thesis. Southern Illinois University Carbondale.
- Cho, Young I., and James P. Harnett. 1982. "Non-Newtonian Fluids in Circular Pipe Flow." In *Adv. Heat Transfer*, eds. James P. Harnett and F. Irvine Thomas, 59-141. USA: Elsevier.
- Choi, Stephen U. S., and J. A. Eastman. 1995. "Enhancing Thermal Conductivity of Fluids with Nanoparticles." Paper presented at *ASME International Mechanical Engineering Congress & Exposition, San Francisco, California, November 12-17*.
- Chun, Byung Hee, Hyun Uk Kang, and Sung Hyun Kim. 2008. "Effect of Alumina Nanoparticles in the Fluid on Heat Transfer in Double-Pipe Heat Exchanger System." *Korean J. Chem. Eng.* 25 (5): 966-971.
- Das, Pritam Kumar. 2017. "A Review Based on the Effect and Mechanism of Thermal Conductivity of Normal Nanofluids and Hybrid Nanofluids." *J. Mol. Liq.* 240: 420-446.
- Dawood, H. K., H. A. Mohammed, and K. M. Munisamy. 2014. "Heat Transfer Augmentation Using Nanofluids in an Elliptic Annulus with Constant Heat Flux Boundary Condition." *Case Studies in Thermal Engineering* 4: 32-41.
- Dealy, John M., and Jian Wang. 2013. "Viscosity and Normal Stress Differences." In *Melt Rheology and Its Applications in the Plastics Industry*, 19-47. Dordrecht: Springer.
- Debrule, Paul M., and Rolf H. Sabersky. 1974. "Heat Transfer and Friction Coefficients in Smooth and Rough Tubes with Dilute Polymer Solutions." *Int. J. Heat Mass Transfer* 17 (5): 529-540.

- Dharaiya, V. V., and S. G. Kandlikar. 2012. "Numerical Investigation of Heat Transfer in Rectangular Microchannels under H₂ Boundary Condition During Developing and Fully Developed Laminar Flow." *J. Heat Transfer* 134 (2): 020911.
- Dimitropoulos, Costas D., R. Sureshkumar, and Antony N. Beris. 1998. "Direct Numerical Simulation of Viscoelastic Turbulent Channel Flow Exhibiting Drag Reduction: Effect of the Variation of Rheological Parameters." *J. Non-Newton. Fluid Mech.* 79 (2): 433-468.
- Drew, D. A., and R. T. Lahey. 1993. *In Particulate Two-Phase Flow*. Boston: Butterworth-Heinemann.
- Drzazga, Michal, Andrzej Gierczycki, Grzegorz Dzido, and Marcin Lemanowicz. 2013. "Influence of Nonionic Surfactant Addition on Drag Reduction of Water Based Nanofluid in a Small Diameter Pipe." *Chinese J. Chem. Eng.* 21 (1): 104-108.
- Duangthongsuk, Weerapun, and Somchai Wongwises. 2009a. "Heat Transfer Enhancement and Pressure Drop Characteristics of TiO₂-Water Nanofluid in a Double-Tube Counter Flow Heat Exchanger." *Int. J. Heat Mass Transfer* 52 (7-8): 2059-2067.
- Duangthongsuk, Weerapun, and Somchai Wongwises. 2009b. "Measurement of Temperature-Dependent Thermal Conductivity and Viscosity of TiO₂-Water Nanofluids." *Exp. Therm. Fluid Sci.* 33 (4): 706-714.
- Duangthongsuk, Weerapun, and Somchai Wongwises. 2010. "An Experimental Study on the Heat Transfer Performance and Pressure Drop of TiO₂-Water Nanofluids Flowing under a Turbulent Flow Regime." *Int. J. Heat Mass Trans.* 53 (1-3): 334-344.
- Eastman, J. A., Stephen U. S. Choi, S. Li, L. J. Thompson, and S. Lee. 1996. "Enhanced Thermal Conductivity through the Development of Nanofluids." In *MRS Online Proceedings Library Archive*, 3. UK: Cambridge University Press.
- Escudier, M. P., F. Presti, and S. Smith. 1998. "Drag Reduction in the Turbulent Pipe Flow of Polymers." *J. Non-Newton. Fluid Mech.* 81 (3): 197-213.
- Escudier, M. P., and S. Smith. 2001. "Fully Developed Turbulent Flow of Non-Newtonian Liquids through a Square Duct." *Proceedings of the Royal Society of London. Series A: Mathematical, Physical and Engineering Sciences* 457 (2008): 911-936.
- Esfandiary, M, A Habibzadeh, and H Sayehvand. 2016. "Numerical Study of Single Phase/Two-Phase Models for Nanofluid Forced Convection and Pressure Drop in a Turbulence Pipe Flow." *Transp. Phenom. Nano Micro Scales* 4 (1): 11-18.
- Esf, Mohammad Hemmat, Seyfolah Saedodin, Omid Mahian, and Somchai Wongwises. 2014. "Thermophysical Properties, Heat Transfer and Pressure Drop of Cooh-Functionalized Multi Walled Carbon Nanotubes/Water Nanofluids." *Int. Commun. Heat Mass Transfer* 58: 176-183.
- Fard, M. Haghshenas, M. Nasr Esfahany, and M. R. Talaie. 2010. "Numerical Study of Convective Heat Transfer of Nanofluids in a Circular Tube Two-Phase Model Versus Single-Phase Model." *Int. Commun. Heat Mass Transfer* 37 (1): 91-97.
- Fiveland, Annbjorg. 2015. "Effect of Nano-Silica and Salts on Xanthan Gum Polymer-Bentonite Solution." Master's thesis. University of Stavanger.
- Fleming, Don J. 1999. "Capillary Rheometry: Elongational Viscosity and Beyond." *Progress in Rubber and Plastics Technology* 15 (4): 215-233.

- Fotukian, S. M., and M. Nasr Esfahany. 2010. "Experimental Study of Turbulent Convective Heat Transfer and Pressure Drop of Dilute CuO/Water Nanofluid inside a Circular Tube." *Int. Commun. Heat Mass Transfer* 37 (2): 214-219.
- Ganvir, R. B., P. V. Walke, and V. M. Kriplani. 2017. "Heat Transfer Characteristics in Nanofluid—a Review." *Renewable and Sustainable Energy Reviews* 75: 451-460.
- Gao, Shi Xiang. 1993. "Flow and Heat Transfer Behavior of Non-Newtonian Fluids in Rectangular Ducts." PhD diss. University of Illinois at Chicago.
- Gao, Shi Xiang, and James P. Hartnett. 1992. "Non-Newtonian Fluid Laminar Flow and Forced Convection Heat Transfer in Rectangular Ducts." *Int. Commun. Heat Mass Transfer* 19 (5): 673-686.
- Gao, Shi Xiang, and James P. Hartnett. 1993. "Steady Flow of Non-Newtonian Fluids through Rectangular Ducts." *Int. Commun. Heat Mass Transfer* 20 (2): 197-210.
- Gao, Shi Xiang, and James P. Hartnett. 1996. "Heat Transfer Behavior of Reiner-Rivlin Fluids in Rectangular Ducts." *Int. J. Heat Mass Transfer* 39 (6): 1317-1324.
- Gervang, Bo Groht. 1989. "Numerical Simulation of 3-Dimensional Flow in Straight and Curved Ducts of Rectangular Cross Section." PhD diss. Technical University of Denmark.
- Gervang, Bo Groht, and P. S. Larsen. 1991. "Secondary Flows in Straight Ducts of Rectangular Cross Section." *J. Non-Newton. Fluid Mech.* 39 (3): 217-237.
- Ghanbarpour, M., E. Bitaraf Haghighi, and R. Khodabandeh. 2014. "Thermal Properties and Rheological Behavior of Water Based Al₂O₃ Nanofluid as a Heat Transfer Fluid." *Exp. Therm. Fluid Sci.* 53: 227-235.
- Gierczycki, Andrzej, Michal Drzazga, Marcin Lemanowicz, and Grzegorz Dzido. 2015. "Drag Reduction in the Flow of CuO Based Nanofluid." *Inzynieria i Aparatura Chemiczna* 54 (1): 8-9.
- Gillissen, J. J. J. 2008. "Polymer Flexibility and Turbulent Drag Reduction." *Phys. Rev. E* 78 (4): 046311.
- Gingrich, William K., Young I. Cho, and Wei Shyy. 1992a. "Effect of Aspect Ratio on Laminar Heat Transfer Behavior of a Non-Newtonian Fluid in an Electronics Coldplate." *Int. Commun. Heat Mass Transfer* 19 (3): 311-325.
- Gingrich, William K., Young I. Cho, and Wei Shyy. 1992b. "Effects of Shear Thinning on Laminar Heat Transfer Behavior in a Rectangular Duct." *Int. J. Heat Mass Transfer* 35 (11): 2823-2836.
- Goktepe, Sinan, Kunt Atalik, and Hakan Erturk. 2014. "Comparison of Single and Two-Phase Models for Nanofluid Convection at the Entrance of a Uniformly Heated Tube." *Int. J. Therm. Sci.* 80: 83-92.
- Green, A. E., and R. S. Rivlin. 1956. "Steady Flow of Non-Newtonian Fluids through Tubes." *Quarterly of Appl. Mathematics* 14 (3): 299-308.
- Green, Don W., and Robert H. Perry. 2008. *Perry's Chemical Engineers' Handbook, Eighth Edition*. New York: McGraw-Hill.
- Gupta, M. K., A. B. Metzner, and James P. Hartnett. 1967. "Turbulent Heat-Transfer Characteristics of Viscoelastic Fluids." *Int. J. Heat Mass Transfer* 10 (9): 1211-1224.
- Halefadi, Salma, Patrice Estelle, and Thierry Mare. 2014. "Heat Transfer Properties of Aqueous Carbon Nanotubes Nanofluids in Coaxial Heat Exchanger under Laminar Regime." *Exp. Therm. Fluid Sci.* 55: 174-180.

- Hartnett, James P. 1992. "1990 Max Jakob Memorial Award Lecture: Viscoelastic Fluids: A New Challenge in Heat Transfer." *J. Heat Transfer* 114 (2): 296-303.
- Hartnett, James P., and Milivoje Kostic. 1985. "Heat Transfer to a Viscoelastic Fluid in Laminar Flow through a Rectangular Channel." *Int. J. Heat Mass Transfer* 28 (6): 1147-1155.
- Hartnett, James P., and Milivoje Kostic. 1989. "Heat Transfer to Newtonian and Non-Newtonian Fluids in Rectangular Ducts." In *Advances in Heat Transfer*, eds. J. P. Hartnett and Jr. T. F. Irvine, 247-356. USA: Academic Press, Inc.
- Hartnett, James P., and E. Y. Kwack. 1986. "Prediction of Friction and Heat Transfer for Viscoelastic Fluids in Turbulent Pipe Flow." *Int. J. Thermophys.* 7 (1): 53-63.
- Haynes, W. M. 2015. *Handbook of Chemistry and Physics*. USA: CRC Press.
- He, Yurong, Yi Jin, Haisheng Chen, Yulong Ding, Daqiang Cang, and Huilin Lu. 2007. "Heat Transfer and Flow Behaviour of Aqueous Suspensions of TiO₂ Nanoparticles (Nanofluids) Flowing Upward through a Vertical Pipe." *Int. J. Heat Mass Trans.* 50 (11-12): 2272-2281.
- Heris, Zeinali Saeed, S. Gh Etamad, and N. M. Esfahany. 2006. "Experimental Investigation of Oxide Nanofluids Laminar Flow Convective Heat Transfer." *Int. Commun. Heat Mass Transfer* 33 (4): 529-535.
- Heris, Zeinali Saeed, Beydokhti Kazemi, A., S. H. Noie, and S. Rezvan. 2012. "Numerical Study on Convective Heat Transfer of Al₂O₃/Water, CuO/Water and Cu/Water Nanofluids through Square Cross-Section Duct in Laminar Flow." *Eng. Appl. Comp. Fluid* 6 (1): 1-14.
- Heris, Zeinali Saeed, Taofik H. Nassan, and S. H. Noie. 2011. "CuO/Water Nanofluid Convective Heat Transfer through Square Duct under Uniform Heat Flux." *Int. J. Nanosci. Nanotechnol.* 7 (3): 111-120.
- Heris, Zeinali Saeed, Taofik H. Nassan, S. H. Noie, H. Sardarabadi, and M. Sardarabadi. 2013. "Laminar Convective Heat Transfer of Al₂O₃/Water Nanofluid through Square Cross-Sectional Duct." *Int. J. Heat Fluid Flow* 44: 375-382.
- Heris, Zeinali Saeed, F. Oghazian, M. Khademi, and Effat Saeedi. 2015. "Simulation of Convective Heat Transfer and Pressure Drop in Laminar Flow of Al₂O₃/Water and CuO/Water Nanofluids through Square and Triangular Cross-Sectional Ducts." *Journal of Renewable Energy and Environment* 2 (1): 7-20.
- Heyhat, M. M., F. Kowsary, A. M. Rashidi, M. H. Momenpour, and A. Amrollahi. 2013. "Experimental Investigation of Laminar Convective Heat Transfer and Pressure Drop of Water-Based Al₂O₃ Nanofluids in Fully Developed Flow Regime." *Exp. Therm. Fluid Sci.* 44: 483-489.
- Hwang, Kyo Sik, Seok Pil Jang, and Stephen U. S. Choi. 2009. "Flow and Convective Heat Transfer Characteristics of Water-Based Al₂O₃ Nanofluids in Fully Developed Laminar Flow Regime." *Int. J. Heat Mass Transfer* 52 (1-2): 193-199.
- Hwang, Y. J., Y. C. Ahn, H. S. Shin, C. G. Lee, G. T. Kim, H. S. Park, and J. K. Lee. 2006. "Investigation on Characteristics of Thermal Conductivity Enhancement of Nanofluids." *Curr. Appl. Phys.* 6 (6): 1068-1071.
- Incropera, Frank P., and David P. Dewitt. 1996. *Introduction to Heat Transfer*. New York, USA: John Wiley & Sons, Inc.
- Incropera, Frank P., David P. Dewitt, Theodore L. Bergman, and Adrienne S. Lavine. 2011. *Fundamentals of Heat and Mass Transfer*. USA: John Wiley & Sons.

- Kakac, Sadik, and Anchasa Pramuanjaroenkij. 2016. "Single-Phase and Two-Phase Treatments of Convective Heat Transfer Enhancement with Nanofluids – a State-of-the-Art Review." *Int. J. Therm. Sci.* 100: 75-97.
- Keblinski, Pawel, Jeffrey A. Eastman, and David G. Cahill. 2005. "Nanofluids for Thermal Transport." *Mater. Today* 8 (6): 36-44.
- Khairul, M. A., Elham Doroodchi, Reza Azizian, and Behdad Moghtaderi. 2017. "The Influence of Different Flow Regimes on Heat Transfer Performance and Exergy Loss of Al₂O₃/Di-Water and CuO/Di-Water Nanofluids." *Appl. Therm. Eng.* 122: 566-578.
- Khambhampati, Tejasvi Krishna. 2013. "A Comparative Study between Newtonian and Non-Newtonian Models in a Stenosis of a Carotid Artery." Master's thesis. Texas A&M University.
- Kim, Doohyun, Younghwan Kwon, Yonghyeon Cho, Chengguo Li, Seongir Cheong, Yujin Hwang, Jaekeun Lee, Daeseung Hong, and Seongyong Moon. 2009. "Convective Heat Transfer Characteristics of Nanofluids under Laminar and Turbulent Flow Conditions." *Curr. Appl. Phys.* 9 (2): 119-123.
- Kim, Nam Jin, Sin Kim, Sang Hoon Lim, Kuan Chen, and Wongee Chun. 2009. "Measurement of Drag Reduction in Polymer Added Turbulent Flow." *Int. Commun. Heat Mass Transfer* 36 (10): 1014-1019.
- Kole, Madhusree, and T. K. Dey. 2010. "Viscosity of Alumina Nanoparticles Dispersed in Car Engine Coolant." *Exp. Therm. Fluid Sci.* 34 (6): 677-683.
- Kostic, Milivoje M. 1994. "On Turbulent Drag and Heat Transfer Reduction Phenomena and Laminar Heat Transfer Enhancement in Non-Circular Duct Flow of Certain Non-Newtonian Fluids." *Int. J. Heat Mass Trans.* 37 (Supplement 1): 133-147.
- Kostic, Milivoje M. . 2013. "Critical Issues in Nanofluids Research and Application Potentials " In *Nanofluids: Research, Development and Applications*, ed. Yuwen Zhang, 1-54. New York, USA: Nova Science Pub. Inc.
- Kostic, Milivoje M., and James P. Hartnett. 1985. "Heat Transfer Performance of Aqueous Polyacrylamide Solutions in Turbulent Flow through a Rectangular Channel." *Int. Commun. Heat Mass Transfer* 12 (4): 483-490.
- Kumar, Nishant, and B. P. Puranik. 2016. "Assessment of Single Phase Model of a Nanofluid for Numerical Prediction of Forced Convection Heat Transfer." *J. Nanofluids* 5 (1): 94-100.
- Kumar, Perumal, and Rajamohan Ganesan. 2012. "A Cfd Study of Turbulent Convective Heat Transfer Enhancement in Circular Pipeflow." *Int. J. Civil Environmental Eng.* 6: 385-392.
- Kwack, E. Y., and James P. Hartnett. 1983. "Empirical Correlations of Turbulent Friction Factors and Heat Transfer Coefficients for Viscoelastic Fluids." *Int. Commun. Heat Mass Transfer* 10 (5): 451-461.
- Kwack, E. Y., James P. Hartnett, and Young I. Cho. 1982. "Turbulent Heat Transfer in Circular Tube Flows of Viscoelastic Fluids." *Warme- und Stoffubertragung* 16 (1): 35-44.
- Lee, J., R. D. Flynn, K. E. Goodson, and J. K. Eaton. 2007. "Convective Heat Transfer of Nanofluids (Di Water-Al₂O₃) in Microchannels." In *Proceedings of HT2007*, 843-850. USA: ASME.

- Lee, S., Stephen U. S. Choi, S. Li, and J. A. Eastman. 1999. "Measuring Thermal Conductivity of Fluids Containing Oxide Nanoparticles." *J. Heat Transfer* 121 (2): 280-289.
- Lee, Seung Won, Sung Dae Park, Sarah Kang, In Cheol Bang, and Ji Hyun Kim. 2011. "Investigation of Viscosity and Thermal Conductivity of Sic Nanofluids for Heat Transfer Applications." *Int. J. Heat Mass Transfer* 54 (1-3): 433-438.
- Lelea, Dorin, and Catalin Nisulescu. 2011. "The Micro-Tube Heat Transfer and Fluid Flow of Water Based Al₂O₃ Nanofluid with Viscous Dissipation." *Int. Commun. Heat Mass Transfer* 38 (6): 704-710.
- Leong, K. Y., K. Z. Ku Ahmad, Hwai Chyuan Ong, M. J. Ghazali, and Azizah Baharum. 2017. "Synthesis and Thermal Conductivity Characteristic of Hybrid Nanofluids – a Review." *Renewable and Sustainable Energy Reviews* 75: 868-878.
- Li, Feng Chen, Juan Cheng Yang, Wen Wu Zhou, Yu Rong He, Yi Min Huang, and Bao Cheng Jiang. 2013. "Experimental Study on the Characteristics of Thermal Conductivity and Shear Viscosity of Viscoelastic-Fluid-Based Nanofluids Containing Multiwalled Carbon Nanotubes." *Thermochim. Acta* 556: 47-53.
- Lin, Cheng Xian, Shao Yen Ko, and F. K. Tsou. 1996. "Laminar Heat Transfer in Square Duct Flow of Aqueous Cmc Solutions." *Int. J. Heat Mass Trans.* 39 (3): 503-510.
- Liu, Zhen Hua, and Liang Liao. 2010. "Forced Convective Flow and Heat Transfer Characteristics of Aqueous Drag-Reducing Fluid with Carbon Nanotubes Added." *Int. J. Therm. Sci.* 49 (12): 2331-2338.
- Lotfi, R., Y. Saboohi, and A. M. Rashidi. 2010. "Numerical Study of Forced Convective Heat Transfer of Nanofluids: Comparison of Different Approaches." *Int. Commun. Heat Mass Transfer* 37 (1): 74-78.
- Lumley, J. L. 1969. "Drag Reduction by Additives." *Annu. Rev. Fluid Mech.* 1 (1): 367-384.
- Maiga, Sidi El Becaye, Samy Joseph Palm, Cong Tam Nguyen, Gilles Roy, and Nicolas Galanis. 2005. "Heat Transfer Enhancement by Using Nanofluids in Forced Convection Flows." *Int. J. Heat Fluid Flow* 26 (4): 530-546.
- Manninen, Mikko, Veikko Taivassalo, and Sirpa Kallio. 1996. *On the Mixture Model for Multiphase Flow*. Finland: Julkaisija-Utgivare Publisher.
- Mare, Thierry, Salma Halelfadl, Ousmane Sow, Patrice Estelle, Steven Duret, and Frederic Bazantay. 2011. "Comparison of the Thermal Performances of Two Nanofluids at Low Temperature in a Plate Heat Exchanger." *Exp. Therm. Fluid Sci.* 35 (8): 1535-1543.
- Mashaie, Payam Rahim, Seyed Mostafa Hosseinalipour, and Mehdi Bahiraei. 2012. "Numerical Investigation of Nanofluid Forced Convection in Channels with Discrete Heat Sources." *J. Appl. Math.* 2012: 1-18.
- Mashaie, Rahim P., S. M. Hosseinalipour, and El Jawad M. Muslmani. 2014. "The Impact of Nanoparticles on Forced Convection in a Serpentine Microchannel." *Transp. Phenom. Nano Micro Scales* 2 (2): 86-99.
- McComb, W. D., and L. H. Rabie. 1982. "Local Drag Reduction Due to Injection of Polymer Solutions into Turbulent Flow in a Pipe. Part I: Dependence on Local Polymer Concentration." *AIChE J.* 28 (4): 547-557.
- Mena, B., G. Best, P. Bautista, and T. Sanchez. 1978. "Heat Transfer in Non-Newtonian Flow through Pipes." *Rheol. Acta* 17 (4): 454-457.

- Meybodi, Mahdi Kalantari, Amin Daryasafar, Mehran Moradi Koochi, Jamshid Moghadasi, Roohollah Babaei Meybodi, and Ali Khorram Ghahfarokhi. 2016. "A Novel Correlation Approach for Viscosity Prediction of Water Based Nanofluids of Al₂O₃, TiO₂, SiO₂ and CuO." *J. Taiwan Inst. Chem. Eng.* 58: 19-27.
- Mirmasoumi, S., and A. Behzadmehr. 2008. "Numerical Study of Laminar Mixed Convection of a Nanofluid in a Horizontal Tube Using Two-Phase Mixture Model." *Appl. Therm. Eng.* 28 (7): 717-727.
- Mohsenipour, Ali Asghar, and Rajinder Pal. 2013. "Drag Reduction in Turbulent Pipeline Flow of Mixed Nonionic Polymer and Cationic Surfactant Systems." *Canadian J. Chem. Eng.* 91 (1): 190-201.
- Moraveji, Keshavarz Mostafa, and Elahe Esmaeili. 2012. "Comparison between Single-Phase and Two-Phases Cfd Modeling of Laminar Forced Convection Flow of Nanofluids in a Circular Tube under Constant Heat Flux." *Int. Commun. Heat Mass Transfer* 39 (8): 1297-1302.
- Murshed, S. M. S., K. C. Leong, and C. Yang. 2008. "Investigations of Thermal Conductivity and Viscosity of Nanofluids." *Int. J. Therm. Sci.* 47 (5): 560-568.
- Naccache, Monica F., and Paulo R. Souza Mendes. 1996. "Heat Transfer to Non-Newtonian Fluids in Laminar Flow through Rectangular Ducts." *Int. J. Heat Fluid Flow* 17 (6): 613-620.
- Namburu, Praveen K., Debendra K. Das, Krishna M. Tanguturi, and Ravikanth S. Vajjha. 2009. "Numerical Study of Turbulent Flow and Heat Transfer Characteristics of Nanofluids Considering Variable Properties." *Int. J. Therm. Sci.* 48 (2): 290-302.
- Namburu, Praveen K., Devdatta P. Kulkarni, Debendra K. Das, and Debasmita Misra. 2007. "Viscosity of Copper Oxide Nanoparticles Dispersed in Ethylene Glycol and Water Mixture." *Exp. Therm. Fluid Sci.* 32 (2): 397-402.
- Nassan, Taofik H., S. Zeinali Heris, and S. H. Noie. 2010. "A Comparison of Experimental Heat Transfer Characteristics for Al₂O₃/Water and CuO/Water Nanofluids in Square Cross-Section Duct." *Int. Commun. Heat Mass Transfer* 37 (7): 924-928.
- Nguyen, C. T., F. Desgranges, N. Galanis, G. Roy, T. Mare, S. Boucher, and H. Angue Mintsa. 2008. "Viscosity Data for Al₂O₃-Water Nanofluid—Hysteresis: Is Heat Transfer Enhancement Using Nanofluids Reliable?" *Int. J. Therm. Sci.* 47 (2): 103-111.
- Nguyen, C. T., F. Desgranges, G. Roy, N. Galanis, T. Mare, S. Boucher, and H. Angue Mintsa. 2007. "Temperature and Particle-Size Dependent Viscosity Data for Water-Based Nanofluids – Hysteresis Phenomenon." *Int. J. Heat Fluid Flow* 28 (6): 1492-1506.
- Norouzi, M., M. H. Kayhani, and M. R. H. Nobari. 2009. "Mixed and Forced Convection of Viscoelastic Materials in Straight Duct with Rectangular Cross Section." *World Appl. Sci, J.* 7 (3): 285-296.
- Oliver, D. R. 1969. "Non-Newtonian Heat Transfer- an Interesting Effect Observed in Non-Circular Tubes " *Trans. Inst. Chem. Eng.* 47 (1): T18.
- Oliver, D. R., and R. B. Karim. 1971. "Laminar-Flow Non-Newtonian Heat Transfer in Flattened Tubes." *Canadian J. Chem. Eng.* 49 (2): 236-240.
- Ozerinc, Sezer. 2010. "Heat Transfer Enhancement with Nanofluids." Master's thesis. Middle East Technical University.

- Pak, Bock Choon, and Young I. Cho. 1998. "Hydrodynamic and Heat Transfer Study of Dispersed Fluids with Submicron Metallic Oxide Particles." *Exp. Heat Transfer* 11 (2): 151-170.
- Pathipakka, Govarthan, and P. Sivashanmugam. 2010. "Heat Transfer Behaviour of Nanofluids in a Uniformly Heated Circular Tube Fitted with Helical Inserts in Laminar Flow." *Superlattices and Microstructures* 47 (2): 349-360.
- Payvar, Parviz. 1997. "Heat Transfer Enhancement in Laminar Flow of Viscoelastic Fluids through Rectangular Ducts." *Int. J. Heat Mass Transfer* 40 (3): 745-756.
- Peres, N., A. M. Afonso, M. A. Alves, and F. T. Pinho. 2009. "Heat Transfer Enhancement in Laminar Flow of Viscoelastic Fluids through a Rectangular Duct." Paper presented at *Congreso de Metodos Numericos en Ingenieria, Barcelona, Spain, June 29-July 2*.
- Peysers, Paul. 1973. "The Drag Reduction of Chrysotile Asbestos Dispersions." *J. Appl. Polym. Sci.* 17 (2): 421-431.
- Phuoc, Tran X., Mehrdad Massoudi, and Ruey Hung Chen. 2011. "Viscosity and Thermal Conductivity of Nanofluids Containing Multi-Walled Carbon Nanotubes Stabilized by Chitosan." *Int. J. Therm. Sci.* 50 (1): 12-18.
- Poreh, M., and U. Paz. 1968. "Turbulent Heat Transfer to Dilute Polymer Solutions." *Int. J. Heat Mass Transfer* 11 (5): 805-818.
- Ptasinski, P. K., B. J. Boersma, F. T. M. Nieuwstadt, M. A. Hulsen, B. H. A. A. Van Den Brule, and J. C. R. Hunt. 2003. "Turbulent Channel Flow near Maximum Drag Reduction: Simulations, Experiments and Mechanisms." *J. Fluid Mech.* 490: 251-291.
- Purnode, B., and M. J. Crochet. 1998. "Polymer Solution Characterization with the Fene-P Model." *J. Non-Newton. Fluid Mech.* 77 (1-2): 1-20.
- Ranz, W. E., and W. R. Marshall. 1952. "Evaporation from Drops. Part I." *Chem. Eng. Prog.* 48 (3): 141-146.
- Rao, Bhamidipaty Kameswara 1988. "Heat Transfer to Viscoelastic Fluids in a 5:1 Rectangular Duct." PhD diss. University of Illinois at Chicago.
- Rao, Bhamidipaty Kameswara 1989. "Laminar Mixed Convection Heat Transfer to Viscoelastic Fluids in a 5:1 Rectangular Channel." *Int. J. Heat Fluid Flow* 10 (4): 334-338.
- Rashin, M. Nabeel, and J. Hemalatha. 2013. "Viscosity Studies on Novel Copper Oxide-Coconut Oil Nanofluid." *Exp. Therm. Fluid Sci.* 48: 67-72.
- Rashmi, W., M. Khalid, A. F. Ismail, R. Saidur, and A. K. Rashid. 2013. "Experimental and Numerical Investigation of Heat Transfer in Cnt Nanofluids." *J. Exp. Nanosci.*: 1-19.
- Rea, Ulzie, Tom McKrell, Lin Wen Hu, and Jacopo Buongiorno. 2009. "Laminar Convective Heat Transfer and Viscous Pressure Loss of Alumina-Water and Zirconia-Water Nanofluids." *Int. J. Heat Mass Transfer* 52 (7-8): 2042-2048.
- Reddy, M. Chandra Sekhara, and Veeredhi Vasudeva Rao. 2014. "Experimental Investigation of Heat Transfer Coefficient and Friction Factor of Ethylene Glycol Water Based Tio₂ Nanofluid in Double Pipe Heat Exchanger with and without Helical Coil Inserts." *Int. Commun. Heat Mass Transfer* 50: 68-76.
- Sahin, Ahmet Z. 1998. "Irreversibilities in Various Duct Geometries with Constant Wall Heat Flux and Laminar Flow." *Energy* 23 (6): 465-473.

- Schiller, L., and A. Naumann. 1935. "A Drag Coefficient Correlation." *Z. Ver. Deutsch. Ing* 77: 318-320.
- Sellin, R. H. J., J. W. Hoyt, and O. Scrivener. 1982. "The Effect of Drag-Reducing Additives on Fluid Flows and Their Industrial Applications Part 1: Basic Aspects" *J. Hydraulic Res.* 20 (1): 29-68.
- Semjonow, V. V. 1967. "Pressure Effect of Viscosity for Polymer Fluids." *Rheol. Acta* 6 (2): 171.
- Shah, R. K., and A. L. London. 1971. *Laminar Flow Forced Convection Heat Transfer and Flow Friction in Straight and Curved Ducts- a Summary of Analytical Solutions*. Stanford, California.
- Shah, Ramesh K., and Dusan P. Sekulic. 2003. *Fundamentals of Heat Exchanger Design*. USA: John Wiley and Sons.
- Shahmohammadi, Ali, and Arezou Jafari. 2014. "Application of Different Cfd Multiphase Models to Investigate Effects of Baffles and Nanoparticles on Heat Transfer Enhancement." *Front. Chem. Sci. Eng.* 8 (3): 320-329.
- Sharma, Tushar, Stefan Iglauer, and Jitendra S. Sangwai. 2016. "Silica Nanofluids in an Oilfield Polymer Polyacrylamide: Interfacial Properties, Wettability Alteration, and Applications for Chemical Enhanced Oil Recovery." *Ind. Eng. Chem. Res.* 55 (48): 12387-12397.
- Shin, Sehyun, and Young I. Cho. 1993. "Temperature Effect on the Non-Newtonian Viscosity of an Aqueous Polyacrylamide Solution." *Int. Commun. Heat Mass Transfer* 20 (6): 831-844.
- Shin, Sehyun, and Young I. Cho. 1998. "The Effect of Thermal Degradation on the Non-Newtonian Viscosity of an Aqueous Polyacrylamide Solution." *KSME Int. J.* 12 (2): 267-273.
- Shin, Sehyun, and Young I. Cho. 1994. "Laminar Heat Transfer in a Rectangular Duct with a Non-Newtonian Fluid with Temperature-Dependent Viscosity." *Int. J. Heat Mass Transfer* 37 (Supplement 1): 19-30.
- Singh, Ram Prakash. 2002. "Drag Reduction." In *Encyclopedia of Polymer Science and Technology*, ed. Jacqueline I. Kroschwitz, 519-563. New Jersey: John Wiley & Sons, Inc.
- Singh, Ram Prakash. 2011. "Drag Reduction." In *Properties and Behavior of Polymers*, eds. Janet Bailey, Azra Seidel, Erin Arndt, Shirley Thomas, Kristen Parrish and Dean Gonzalez, 254-297. New Jersey: John Wiley & Sons, Inc.
- Sonawane, Shriram S., Rohit S. Khedkar, and Kailas L. Wasewar. 2013. "Study on Concentric Tube Heat Exchanger Heat Transfer Performance Using Al₂O₃ – Water Based Nanofluids." *Int. Commun. Heat Mass Transfer* 49: 60-68.
- Steller, Ryszard. 2016. "Determination of the First Normal Stress Difference from Viscometric Data for Shear Flows of Polymer Liquids." *Rheol. Acta* 55 (8): 649-656.
- Stern, Fred, Marian Muste, Maria Laura Beninati, and W. E. Eichinger. 1999. *Summary of Experimental Uncertainty Assessment Methodology with Example*. Iowa, USA.
- Stroder, Simon. 2011. "Convective Heat Transfer with Nanofluids." Master's thesis. Kungliga Tekniska Hogskolan (Royal Institute of Technology).
- Sundar, L. Syam, Manoj K. Singh, and Antonio C. M. Sousa. 2013. "Investigation of Thermal Conductivity and Viscosity of Fe₃O₄ Nanofluid for Heat Transfer Applications." *Int. Commun. Heat Mass Transfer* 44: 7-14.

- Sundar, L. Syam, and K. V. Sharma. 2010. "Turbulent Heat Transfer and Friction Factor of Al₂O₃ Nanofluid in Circular Tube with Twisted Tape Inserts." *Int. J. Heat Mass Trans.* 53 (7–8): 1409-1416.
- Sundar, L. Syam, K. V. Sharma, M. T. Naik, and Manoj K. Singh. 2013. "Empirical and Theoretical Correlations on Viscosity of Nanofluids: A Review." *Renewable and Sustainable Energy Reviews* 25: 670-686.
- Syrjala, Seppo. 1998. "Laminar Flow of Viscoelastic Fluids in Rectangular Ducts with Heat Transfer: A Finite Element Analysis." *Int. Commun. Heat Mass Transfer* 25 (2): 191-204.
- Teng, Tun Ping, Yi Hsuan Hung, Tun Chien Teng, and Jyun Hong chen. 2011. "Performance Evaluation on an Air-Cooled Heat Exchanger for Alumina Nanofluid under Laminar Flow." *Nanoscale Res. Lett.* 6:488.
- Tiong, Angnes Ngieng Tze, Perumal Kumar, and Agus Saptoro. 2015. "Reviews on Drag Reducing Polymers." *Korean J. Chem. Eng.* 32 (8): 1455-1476.
- Toh, Ken H., and Afshin J. Ghajar. 1988. "Heat Transfer in the Thermal Entrance Region for Viscoelastic Fluids in Turbulent Pipe Flows." *Int. J. Heat Mass Transfer* 31 (6): 1261-1267.
- Tokit, E. Mat, M. Z. Yusoff, and H. Mohammed. 2013. "Investigation on Nanoparticle Velocity in Two Phase Approach." *World Academy of Science, Engineering and Technology, International Journal of Mechanical, Aerospace, Industrial, Mechatronic and Manufacturing Engineering* 7 (10): 2037-2043.
- Toms, B. A. 1949. "Some Observations on the Flow of Linear Polymer Solutions through Straight Tubes at Large Reynolds Numbers." In *Proceedings of the First International Congress on Rheology*, 135-141. Netherlands.
- Toonder, J. M. J. Den, M. A. Hulsen, G. D. C. Kuiken, and F. T. M. Nieuwstadt. 1997. "Drag Reduction by Polymer Additives in a Turbulent Pipe Flow: Numerical and Laboratory Experiments." *J. Fluid Mech.* 337: 193-231.
- Townsend, P., K. Walters, and W. M. Waterhouse. 1976. "Secondary Flows in Pipes of Square Cross-Section and the Measurement of the Second Normal Stress Difference." *J. Non-Newton. Fluid Mech.* 1 (2): 107-123.
- Vajjha, Ravikanth S., Debendra K. Das, and D. P. Kulkarni. 2010. "Development of New Correlations for Convective Heat Transfer and Friction Factor in Turbulent Regime for Nanofluids." *Int. J. Heat Mass Transfer* 53 (21–22): 4607-4618.
- Walleck, Casey J. 2009. "Development of Steady-State, Parallel-Plate Thermal Conductivity Apparatus for Poly-Nanofluids and Comparative Measurements with Transient Hwte Apparatus." Master's thesis. Northern Illinois University.
- Wang, Jian Li, Jian Jun Zhu, Xing Zhang, and Yun Fei Chen. 2013. "Heat Transfer and Pressure Drop of Nanofluids Containing Carbon Nanotubes in Laminar Flows." *Exp. Therm. Fluid Sci.* 44: 716-721.
- Wang, Xiang Qi, and Arun S. Mujumdar. 2007. "Heat Transfer Characteristics of Nanofluids: A Review." *Int. J. Therm. Sci.* 46 (1): 1-19.
- Wang, Xin Wei, Xian Fan Xu, and Stephen U. S. Choi. 1999. "Thermal Conductivity of Nanoparticle - Fluid Mixture." *J. Thermophys. Heat Transfer* 13 (4): 474-480.
- Wang, Yi, Bo Yu, Jacques L. Zakin, and Hai Feng Shi. 2011. "Review on Drag Reduction and Its Heat Transfer by Additives." *Advances in Mechanical Engineering* 2011: 1-17.

- Wen, Dong Sheng, and Yu Long Ding. 2004. "Experimental Investigation into Convective Heat Transfer of Nanofluids at the Entrance Region under Laminar Flow Conditions." *Int. J. Heat Mass Transfer* 47 (24): 5181-5188.
- Wheeler, John A., and Eugene H. Wissler. 1966. "Steady Flow of Non - Newtonian Fluids in a Square Duct." *Trans. Soc. Rheol.* 10 (1): 353-367.
- Xie, Chun Bo, and James P. Hartnett. 1992. "Influence of Rheology on Laminar Heat Transfer to Viscoelastic Fluids in a Rectangular Channel." *Ind. Eng. Chem. Res.* 31 (3): 727-732.
- Xuan, Yi Min, and Qiang Li. 2003. "Investigation on Convective Heat Transfer and Flow Features of Nanofluids." *J. Heat Transfer* 125 (1): 151-155.
- Xue, S. C., N. Phan Thien, and R. I. Tanner. 1995. "Numerical Study of Secondary Flows of Viscoelastic Fluid in Straight Pipes by an Implicit Finite Volume Method." *J. Non-Newton. Fluid Mech.* 59 (2): 191-213.
- Yang, Juan Cheng, Feng Chen Li, Yu Rong He, Yi Min Huang, and Bao Cheng Jiang. 2013. "Experimental Study on the Characteristics of Heat Transfer and Flow Resistance in Turbulent Pipe Flows of Viscoelastic-Fluid-Based Cu Nanofluid." *Int. J. Heat Mass Transfer* 62: 303-313.
- Yang, Juan Cheng, Feng Chen Li, Wen Wu Zhou, Yu Rong He, and Bao Cheng Jiang. 2012. "Experimental Investigation on the Thermal Conductivity and Shear Viscosity of Viscoelastic-Fluid-Based Nanofluids." *Int. J. Heat Mass Transfer* 55 (11-12): 3160-3166.
- Yang, C., W. Li, and A. Nakayama. 2013. "Convective Heat Transfer of Nanofluids in a Concentric Annulus." *Int. J. Therm. Sci.* 71: 249-257.
- Yang, Liu, J. Y. Xu, K. Du, and X. S. Zhang. 2017. "Recent Developments on Viscosity and Thermal Conductivity of Nanofluids." *Powder Technol.* 317: 348-369.
- Yang, Mu Hoe. 2001. "The Rheological Behavior of Polyacrylamide Solution Ii. Yield Stress." *Polym. Test.* 20 (6): 635-642.
- Yiamsawas, Thaklaew, Omid Mahian, Ahmet Selim Dalkilic, Suthep Kaewnai, and Somchai Wongwises. 2013. "Experimental Studies on the Viscosity of Tio₂ and Al₂O₃ Nanoparticles Suspended in a Mixture of Ethylene Glycol and Water for High Temperature Applications." *Appl. Energy* 111: 40-45.
- Yue, Peng Tao, Joseph Dooley, and James J. Feng. 2008. "A General Criterion for Viscoelastic Secondary Flow in Pipes of Noncircular Cross Section." *J. Rheol.* 52 (1): 315-332.
- Zhang, Hong Xia, De Zhong Wang, and Han Ping Chen. 2009. "Experimental Study on the Effects of Shear Induced Structure in a Drag-Reducing Surfactant Solution Flow." *Arch. Appl. Mech.* 79 (8): 773-778.
- Zhao, Ning Bo, J. L. Yang, S. Y. Li, and Qiang Wang. 2016. "Numerical Investigation of Laminar Thermal-Hydraulic Performance of Al₂O₃-Water Nanofluids in Offset Strip Fins Channel." *Int. Commun. Heat Mass Transfer* 75: 42-51.

Every reasonable effort has been made to acknowledge the owners of copyright material. I would be pleased to hear from any copyright owner who has been omitted or incorrectly acknowledged.

APPENDICES

Appendix A

The accuracy of a measurement relies on how closely the experimental result agrees with its true value. The difference between the experimentally measured quantity with its actual value is termed as an error. Errors can be classified into bias and precision errors. The bias errors are fixed errors which induce the deviation between the mean value of a measured variable and its true value. This type of error can be reduced by calibration of the instruments used. Conversely, the precision errors are random errors that cause the reading to be different for every measurement. They are observed as the scatter of the readings taken during multiple measurements. They can be minimized by repeating the measurements.

Uncertainty is the estimation of errors. Uncertainty analysis is performed to determine the uncertainty propagation from each measured variable into the final desired results through the data reduction equations (Figure A.1). The uncertainty estimate for the bias and precision errors are called the bias and precision limits, correspondingly.

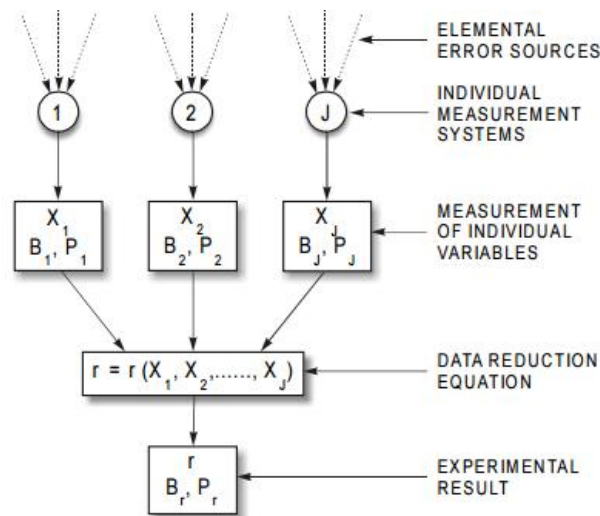


Figure A.1: Error propagation into the experimental results (Stern et al. 1999).

Table A.1: Values of variables in Equation 3.7.

Q_h (L/min)	Q_c (L/min)	T_{hi} (K)	$S_{\bar{U}}$ (W/m ² K)	$P_{\bar{U}}$ (W/m ² K)	$B_{\Delta T_{LMTD}}$ (K)	$B_{A_t} \times 10^3$ (m ²)	B_Q (J/s)	$B_{\bar{U}}$ (W/m ² K)	$U_{\bar{U}}$ (W/m ² K)	Total uncertainty (%)
<i>water</i>										
0.22	5.00	313.40	2.18	2.51	0.01	3.35	4.29	7.05	7.48	5.71
0.36	5.00	313.38	4.01	4.63	0.01	3.35	3.66	6.51	7.99	5.34
0.62	4.93	313.27	2.91	3.36	0.01	3.35	3.07	6.20	7.05	4.44
0.77	5.03	313.23	2.00	2.31	0.01	3.35	3.01	6.86	7.24	3.96
1.02	5.02	313.15	2.58	2.98	0.01	3.35	2.84	7.16	7.75	3.96
0.20	4.99	318.29	2.69	3.10	0.01	3.35	5.28	6.41	7.12	5.67
0.40	4.95	318.15	1.30	1.50	0.01	3.35	4.10	5.73	5.93	4.14
0.60	5.01	318.10	2.90	3.35	0.01	3.35	3.62	5.82	6.72	4.31
0.80	4.95	318.20	1.40	1.61	0.01	3.35	3.37	6.12	6.33	3.74
1.02	4.98	318.17	3.73	4.31	0.01	3.35	3.17	6.57	7.85	4.23
0.20	5.01	323.08	2.79	3.22	0.01	3.35	6.17	5.87	6.69	5.73
0.38	5.05	322.76	9.97	1.15	0.01	3.35	4.85	5.52	5.64	4.06
0.60	4.97	322.83	3.61	4.17	0.01	3.35	4.17	5.84	7.18	4.48
0.78	4.95	322.99	4.02	4.64	0.01	3.35	3.94	6.25	7.79	4.42
1.03	5.02	322.67	3.64	4.21	0.01	3.35	3.55	6.37	7.63	4.19
<i>0.10% Al₂O₃ nanofluid</i>										
0.21	4.94	313.24	3.43	3.96	0.01	3.35	4.17	5.84	7.18	4.48
0.40	4.95	313.55	1.38	1.59	0.01	3.35	3.43	6.08	6.28	4.39
0.57	5.00	313.47	4.15	4.79	0.01	3.35	3.22	6.57	8.13	4.85
0.81	5.01	312.87	4.15	4.79	0.01	3.35	2.86	6.68	8.22	4.63
0.96	4.97	313.01	3.38	0.39	0.01	3.35	2.89	7.16	7.17	3.73
0.20	5.02	317.99	2.74	3.16	0.01	3.35	5.07	6.11	6.88	5.98
0.37	5.05	317.82	2.28	2.63	0.01	3.35	4.19	5.96	6.51	4.46
0.56	5.06	317.79	3.32	3.84	0.01	3.35	3.83	6.01	7.13	4.55
0.80	5.01	318.06	2.60	3.01	0.01	3.35	3.31	6.20	6.89	4.02
1.00	5.02	317.88	3.91	4.52	0.01	3.35	3.14	6.59	7.99	4.30
0.20	5.02	322.92	2.91	3.36	0.01	3.35	6.17	6.19	7.05	5.68
0.50	5.05	322.52	3.10	3.58	0.01	3.35	4.49	5.93	6.93	4.39
0.60	5.05	322.80	2.91	3.36	0.01	3.35	4.18	6.04	6.91	4.17
0.80	4.98	323.20	3.33	3.84	0.01	3.35	3.80	6.19	7.29	4.17
1.00	5.00	322.98	3.97	4.58	0.01	3.35	3.54	6.31	7.80	4.32

Table A.1: (Continued)

Q_h (L/min)	Q_c (L/min)	T_{hi} (K)	$S_{\bar{U}}$ (W/m ² K)	$P_{\bar{U}}$ (W/m ² K)	$B_{\Delta T_{LMTD}}$ (K)	$B_{A_t} \times 10^3$ (m ²)	B_Q (J/s)	$B_{\bar{U}}$ (W/m ² K)	$U_{\bar{U}}$ (W/m ² K)	Total uncertainty (%)
<i>1000 ppm PAA</i>										
2.02	5.02	313.15	1.42	1.64	0.01	3.35	2.95	10.25	10.38	3.52
3.03	5.01	312.86	6.36	7.34	0.01	3.35	3.06	13.09	15.01	3.92
4.04	5.02	312.94	1.09	12.57	0.01	3.35	3.33	14.58	19.25	4.50
5.03	4.98	313.50	2.41	2.78	0.01	3.35	3.64	16.16	16.40	3.45
2.00	5.02	318.05	1.59	1.84	0.01	3.35	3.32	11.31	11.46	3.44
2.99	5.00	318.25	2.66	3.07	0.01	3.35	3.37	14.01	14.34	3.46
4.01	5.01	318.38	1.21	1.40	0.01	3.35	3.58	16.14	16.20	3.38
4.99	5.05	317.97	3.43	3.96	0.01	3.35	3.82	17.36	17.81	3.46
2.00	5.00	322.81	1.50	1.73	0.01	3.35	3.78	12.25	12.37	3.41
3.00	5.00	323.00	3.49	4.03	0.01	3.35	3.76	15.20	15.73	3.48
3.99	4.95	323.10	2.53	2.92	0.01	3.35	3.63	10.80	11.19	3.52
4.99	4.92	323.08	3.99	4.60	0.01	3.35	4.06	18.52	19.09	3.46
<i>1000 ppm PAA in 0.10% Al₂O₃ nanofluid</i>										
2.04	5.00	313.35	2.38	2.75	0.01	3.35	2.89	9.64	10.03	3.67
3.00	5.00	313.05	6.33	7.31	0.01	3.35	3.04	11.77	13.85	4.06
4.02	5.00	313.38	6.25	7.22	0.01	3.35	3.32	13.70	15.49	3.87
5.04	5.00	313.68	7.73	8.92	0.01	3.35	3.61	15.47	17.86	3.95
2.00	5.00	318.15	2.02	2.33	0.01	3.35	3.23	10.71	10.96	3.50
300	5.00	318.25	2.52	2.92	0.01	3.35	3.26	10.00	10.42	3.61
4.00	5.00	317.55	1.88	2.17	0.01	3.35	3.44	14.67	14.83	3.42
5.01	5.00	317.75	4.23	4.89	0.01	3.35	3.72	16.04	16.77	3.53
2.00	5.00	323.15	2.27	2.62	0.01	3.35	3.80	11.59	11.88	3.47
2.98	5.00	323.13	2.58	2.98	0.01	3.35	3.64	13.82	14.13	3.44
3.98	5.00	323.89	2.09	2.41	0.01	3.35	3.90	16.24	16.42	3.39
4.97	5.00	323.05	7.86	0.91	0.01	3.35	3.98	17.41	17.44	3.36
<i>10 ppm PAA in 0.10% Al₂O₃ nanofluid</i>										
1.02	4.94	313.15	5.71	6.59	0.01	3.35	3.21	8.01	10.37	4.76
1.98	5.00	312.85	5.93	6.85	0.01	3.35	3.00	11.01	12.96	4.08
2.92	4.92	313.14	3.28	3.79	0.01	3.35	3.07	12.91	13.45	3.56
4.01	5.02	312.99	3.93	4.53	0.01	3.35	3.29	14.30	15.00	3.60
5.00	4.97	313.10	4.00	4.62	0.01	3.35	3.58	15.69	16.36	3.57

Table A.1: (Continued)

Q_h (L/min)	Q_c (L/min)	T_{hi} (K)	$S_{\bar{U}}$ (W/m ² K)	$P_{\bar{U}}$ (W/m ² K)	$B_{\Delta T_{LMTD}}$ (K)	$B_{A_t} \times 10^3$ (m ²)	B_Q (J/s)	$B_{\bar{U}}$ (W/m ² K)	$U_{\bar{U}}$ (W/m ² K)	Total uncertainty (%)
<i>10 ppm PAA in 0.10% Al₂O₃ nanofluid</i>										
1.00	4.99	317.95	2.65	3.06	0.01	3.35	3.72	8.57	9.10	3.75
2.00	5.00	317.96	1.21	1.40	0.01	3.35	3.39	12.68	12.76	3.42
3.00	4.94	318.60	3.17	3.66	0.01	3.35	3.38	14.66	15.11	3.48
4.03	5.02	317.85	4.18	4.83	0.01	3.35	3.54	16.74	17.43	3.51
5.05	5.03	318.15	6.17	7.13	0.01	3.35	3.82	18.21	19.55	3.62
1.00	4.94	322.65	1.08	0.12	0.01	3.35	4.44	9.29	9.29	3.47
1.90	4.98	322.97	2.84	3.28	0.01	3.35	3.91	12.93	13.34	3.49
3.02	5.00	323.15	3.24	3.74	0.01	3.35	3.84	16.42	16.84	3.45
3.98	4.94	323.33	2.75	3.18	0.01	3.35	3.83	17.35	17.64	3.41
4.95	4.97	323.11	7.60	0.88	0.01	3.35	4.05	19.15	19.17	3.36

Table A.2: Values of variables in Equation 3.8.

Q_h (L/min)	Q_c (L/min)	T_{hi} (K)	S_{Re}	P_{Re}	$B_\rho \times 10^3$ (kg/m ³)	$B_v \times 10^5$ (m/s)	$B_D \times 10^6$ (m)	$B_\mu \times 10^7$ (Pa s)	B_{Re}	U_{Re}	Total uncertainty (%)
<i>water</i>											
0.22	5.00	313.40	17.60	20.30	3.55	1.86	5.00	1.36	0.47	20.30	5.24
0.36	5.00	313.38	31.40	36.27	3.62	3.04	5.00	1.32	0.79	36.28	5.63
0.62	4.93	313.27	11.00	12.65	3.67	5.27	5.00	1.29	1.38	12.73	1.12
0.77	5.03	313.23	17.80	20.56	3.68	6.51	5.00	1.29	1.71	20.63	1.47
1.02	5.02	313.15	64.20	74.08	3.70	8.60	5.00	1.28	2.26	74.12	3.99
0.20	4.99	318.29	11.00	12.65	3.81	1.72	5.00	1.22	0.47	12.66	3.32
0.40	4.95	318.15	0.32	0.37	3.92	3.38	5.00	1.16	0.94	1.01	0.13
0.60	5.01	318.10	38.00	43.89	3.97	5.07	5.00	1.13	1.43	43.92	3.74
0.80	4.95	318.20	1.83	2.11	4.00	6.77	5.00	1.12	1.92	2.85	0.18
1.02	4.98	318.17	51.90	59.89	4.02	8.63	5.00	1.11	2.46	59.94	2.97
0.20	5.01	323.08	18.70	21.58	4.06	1.69	5.00	1.09	0.49	21.58	5.40
0.38	5.05	322.76	21.50	24.82	4.18	3.21	5.00	1.04	0.95	24.84	3.18
0.60	4.97	322.83	53.40	61.60	4.25	5.10	5.00	1.01	1.53	61.62	4.88
0.78	4.95	322.99	42.30	48.90	4.28	6.57	5.00	9.93	1.99	48.94	2.99
1.03	5.02	322.67	36.80	42.47	4.30	8.68	5.00	9.83	2.65	42.55	1.95
<i>0.10% Al₂O₃ nanofluid</i>											
0.21	4.94	313.24	10.60	12.18	3.53	1.75	5.00	1.62	0.40	12.19	3.71
0.40	4.95	313.55	25.70	29.73	3.62	3.36	5.00	1.55	0.79	29.74	4.59
0.57	5.00	313.47	14.90	17.19	3.64	4.82	5.00	1.54	1.14	17.23	1.84
0.81	5.01	312.87	29.70	34.31	3.63	6.85	5.00	1.54	1.62	34.34	2.58
0.96	4.97	313.01	9.32	10.76	3.64	8.15	5.00	1.54	1.93	10.93	0.69
0.20	5.02	317.99	49.60	0.57	3.76	1.69	5.00	1.45	0.42	0.71	0.21
0.37	5.05	317.82	10.20	11.82	3.83	3.16	5.00	1.40	0.79	11.84	1.82
0.56	5.06	317.79	26.90	31.01	3.87	4.71	5.00	1.37	1.19	31.04	3.17
0.80	5.01	318.06	26.10	30.17	3.94	6.74	5.00	1.33	1.74	30.22	2.12
1.00	5.02	317.88	3.69	4.27	3.94	8.46	5.00	1.32	2.19	4.79	0.27
0.20	5.02	322.92	4.84	5.59	3.98	1.71	5.00	1.30	0.45	5.61	1.53
0.50	5.05	322.52	2.97	3.42	4.12	4.23	5.00	1.21	1.15	3.61	0.38
0.60	5.05	322.80	88.70	1.02	4.17	5.07	5.00	1.18	1.40	1.73	0.15
0.80	4.98	323.20	50.90	58.78	4.23	6.79	5.00	1.15	1.90	58.81	3.77
1.00	5.00	322.98	2.48	2.87	4.25	8.46	5.00	1.14	2.37	3.72	0.19

Table A.3: Values of variables in Equation 3.9.

Q_h (L/min)	Q_c (L/min)	T_{hi} (K)	$S_{Re'}$ $\times 10^1$	$P_{Re'}$	$B_\rho \times 10^3$ (kg/m ³)	$B_v \times 10^4$ (m/s)	$B_D \times 10^6$ (m)	$B_n \times 10^5$	$B_K \times 10^5$ (Pa s ⁿ)	$B_{Re'}$	$U_{Re'}$	Total uncertainty (%)
<i>1000 ppm PAA</i>												
2.02	5.02	313.15	177.00	20.39	3.70	1.71	5.00	4.01	4.08	0.38	20.40	3.47
3.03	5.01	312.86	104.00	12.00	3.70	2.56	5.00	2.85	2.16	0.72	12.03	0.96
4.04	5.02	312.94	117.00	13.55	3.72	3.41	5.00	2.21	1.23	1.12	13.59	0.68
5.03	4.98	313.50	204.00	23.53	3.77	4.25	5.00	1.84	0.78	1.54	23.58	0.86
2.00	5.02	318.05	0.18	0.02	4.02	1.69	5.00	4.07	4.42	0.38	0.38	0.07
2.99	5.00	318.25	103.00	11.86	4.06	2.53	5.00	2.90	2.37	0.71	11.88	0.97
4.01	5.01	318.38	119.00	13.74	4.08	3.39	5.00	2.24	1.35	1.12	13.79	0.69
4.99	5.05	317.97	172.00	19.85	4.07	4.22	5.00	1.86	0.84	1.54	19.91	0.72
2.00	5.00	322.81	0.22	0.03	4.31	1.69	5.00	4.14	4.77	0.39	0.39	0.07
3.00	5.00	323.00	0.14	0.02	4.35	2.54	5.00	2.95	2.58	0.73	0.73	0.06
3.99	4.95	323.10	199.00	22.96	4.38	3.38	5.00	2.28	1.48	1.12	22.99	1.15
4.99	4.92	323.08	169.00	19.48	4.39	4.22	5.00	1.89	0.92	1.55	19.54	0.70
<i>1000 ppm PAA in 0.10% Al₂O₃ nanofluid</i>												
2.04	5.00	313.35	103.00	11.85	3.72	1.73	5.00	4.23	4.15	0.39	11.86	1.96
3.00	5.00	313.05	0.60	0.07	3.72	2.54	5.00	2.95	2.16	0.71	0.72	0.06
4.02	5.00	313.38	44.00	5.08	3.75	3.40	5.00	2.27	1.24	1.11	5.00	0.26
5.04	5.00	313.68	123.00	14.15	3.78	4.26	5.00	1.85	0.75	1.54	14.23	0.52
2.00	5.00	318.15	0.16	0.02	4.03	1.69	5.00	4.25	4.40	0.39	0.39	0.07
3.00	5.00	318.25	0.45	0.05	4.06	2.54	5.00	2.95	2.31	0.72	0.73	0.06
4.00	5.00	317.55	0.19	0.02	4.03	3.38	5.00	2.27	1.31	1.11	1.11	0.06
5.01	5.00	317.75	125.00	14.46	4.06	4.24	5.00	1.86	0.79	1.55	14.54	0.53
2.00	5.00	323.15	0.21	0.02	4.33	1.69	5.00	4.21	4.57	0.39	0.39	0.07
2.98	5.00	323.13	104.00	12.02	4.37	2.52	5.00	2.94	2.41	0.73	12.04	0.97
3.98	5.00	323.89	90.80	10.49	4.43	3.37	5.00	2.22	1.30	1.12	10.55	0.53
4.97	5.00	323.05	48.10	5.55	4.39	4.21	5.00	1.85	0.83	1.55	5.76	0.21
<i>10 ppm PAA in 0.10% Al₂O₃ nanofluid</i>												
1.02	4.94	313.15	20.70	2.39	3.65	0.87	5.00	3.22	4.05	0.15	2.39	1.15
1.98	5.00	312.85	97.60	11.27	3.67	1.68	5.00	2.42	2.24	0.45	11.28	1.50
2.92	4.92	313.14	165.00	19.10	3.71	2.47	5.00	2.10	1.59	0.85	19.12	1.29

Table A.3: (Continued)

Q_h (L/min)	Q_c (L/min)	T_{hi} (K)	$S_{Re'}$ $\times 10^1$	$P_{Re'}$	$B_\rho \times 10^3$ (kg/m ³)	$B_\nu \times 10^4$ (m/s)	$B_D \times 10^6$ (m)	$B_n \times 10^5$	$B_K \times 10^5$ (Pa s ⁿ)	$B_{Re'}$	$U_{Re'}$	Total uncertainty (%)
<i>10 ppm PAA in 0.10% Al₂O₃ nanofluid</i>												
4.01	5.02	312.99	148.00	17.13	3.73	3.39	5.00	1.73	0.94	1.40	17.19	0.68
5.00	4.97	313.10	0.27	0.03	3.74	4.23	5.00	1.50	0.60	1.98	1.98	0.06
1.00	4.99	317.95	0.14	0.02	3.95	8.46	5.00	3.12	4.02	0.14	0.14	0.07
2.00	5.00	317.96	0.40	0.05	4.00	1.69	5.00	2.38	2.30	0.45	0.45	0.06
3.00	4.94	318.60	0.57	0.07	4.07	2.54	5.00	2.13	1.76	0.87	0.88	0.06
4.03	5.02	317.85	97.10	11.22	4.05	3.41	5.00	1.79	1.09	1.39	11.30	0.45
5.05	5.03	318.15	121.00	13.99	4.08	4.27	5.00	1.53	0.69	1.98	14.13	0.40
1.00	4.94	322.65	0.13	0.01	4.31	1.60	5.00	2.45	2.58	0.41	0.14	0.07
1.90	4.98	322.97	34.10	3.93	4.31	1.60	5.00	2.45	2.58	0.40	3.95	0.61
3.02	5.00	323.15	124.00	14.31	4.35	2.55	5.00	2.26	2.15	0.88	14.34	0.98
3.98	4.94	323.33	95.90	11.08	4.39	3.37	5.00	1.90	1.39	1.35	11.16	0.47
4.95	4.97	323.11	106.00	12.20	4.39	4.19	5.00	1.65	0.92	1.90	12.35	0.36

Appendix B

The velocity gradient, ∇v is represented by:

$$\nabla v = \begin{pmatrix} \frac{\partial u}{\partial x} & \frac{\partial v}{\partial x} & \frac{\partial w}{\partial x} \\ \frac{\partial u}{\partial y} & \frac{\partial v}{\partial y} & \frac{\partial w}{\partial y} \\ \frac{\partial u}{\partial z} & \frac{\partial v}{\partial z} & \frac{\partial w}{\partial z} \end{pmatrix}$$

The rate-of-deformation tensor, $\underline{\dot{\gamma}}$ is defined by:

$$\nabla v + (\nabla v)^T = \begin{pmatrix} 2\frac{\partial u}{\partial x} & \frac{\partial v}{\partial x} + \frac{\partial u}{\partial y} & \frac{\partial w}{\partial x} + \frac{\partial u}{\partial z} \\ \frac{\partial u}{\partial y} + \frac{\partial v}{\partial x} & 2\frac{\partial v}{\partial y} & \frac{\partial w}{\partial y} + \frac{\partial v}{\partial z} \\ \frac{\partial u}{\partial z} + \frac{\partial w}{\partial x} & \frac{\partial v}{\partial z} + \frac{\partial w}{\partial y} & 2\frac{\partial w}{\partial z} \end{pmatrix}$$

Each component of the second and third terms of the CEF model outlined in Equation 3.52 takes the form of:

$$\begin{aligned} \bar{\tau}_{11}^P &= \frac{1}{2} \psi_1 \left\{ 2u \frac{\partial^2 u}{\partial x \partial x} + 2v \frac{\partial^2 u}{\partial y \partial x} + 2w \frac{\partial^2 u}{\partial z \partial x} + 4 \frac{\partial u}{\partial x} \frac{\partial u}{\partial x} + 2 \frac{\partial v}{\partial x} \frac{\partial v}{\partial x} + 2 \frac{\partial w}{\partial x} \frac{\partial w}{\partial x} \right. \\ &\quad \left. + 2 \frac{\partial v}{\partial x} \frac{\partial u}{\partial y} + 2 \frac{\partial w}{\partial x} \frac{\partial u}{\partial z} \right\} \\ &\quad + \psi_2 \left\{ 4 \frac{\partial u}{\partial x} \frac{\partial u}{\partial x} + 2 \frac{\partial v}{\partial x} \frac{\partial u}{\partial y} + 2 \frac{\partial w}{\partial x} \frac{\partial u}{\partial z} + \frac{\partial u}{\partial y} \frac{\partial u}{\partial y} + \frac{\partial u}{\partial z} \frac{\partial u}{\partial z} + \frac{\partial v}{\partial x} \frac{\partial v}{\partial x} \right. \\ &\quad \left. + \frac{\partial w}{\partial x} \frac{\partial w}{\partial x} \right\} \\ \bar{\tau}_{12}^P &= \frac{1}{2} \psi_1 \left\{ u \left[\frac{\partial^2 u}{\partial x \partial y} + \frac{\partial^2 v}{\partial x \partial x} \right] + v \left[\frac{\partial^2 u}{\partial y \partial y} + \frac{\partial^2 v}{\partial y \partial x} \right] + w \left[\frac{\partial^2 u}{\partial z \partial y} + \frac{\partial^2 v}{\partial z \partial x} \right] + 3 \frac{\partial u}{\partial y} \frac{\partial u}{\partial x} \right. \\ &\quad \left. + 3 \frac{\partial v}{\partial y} \frac{\partial v}{\partial x} + 2 \frac{\partial w}{\partial y} \frac{\partial w}{\partial x} + \frac{\partial u}{\partial x} \frac{\partial v}{\partial x} + \frac{\partial w}{\partial x} \frac{\partial v}{\partial z} + \frac{\partial v}{\partial y} \frac{\partial u}{\partial y} + \frac{\partial w}{\partial y} \frac{\partial u}{\partial z} \right\} \\ &\quad + \psi_2 \left\{ 2 \frac{\partial u}{\partial y} \frac{\partial u}{\partial x} + 2 \frac{\partial v}{\partial y} \frac{\partial u}{\partial y} + \frac{\partial w}{\partial y} \frac{\partial u}{\partial z} + 2 \frac{\partial u}{\partial x} \frac{\partial v}{\partial x} + \frac{\partial u}{\partial z} \frac{\partial v}{\partial z} + 2 \frac{\partial v}{\partial y} \frac{\partial v}{\partial x} \right. \\ &\quad \left. + \frac{\partial w}{\partial y} \frac{\partial w}{\partial x} + \frac{\partial w}{\partial x} \frac{\partial v}{\partial z} \right\} \end{aligned}$$

$$\begin{aligned}
 \bar{\tau}^P_{13} = & \frac{1}{2} \psi_1 \left\{ u \left[\frac{\partial^2 u}{\partial x \partial z} + \frac{\partial^2 w}{\partial x \partial x} \right] + v \left[\frac{\partial^2 u}{\partial y \partial z} + \frac{\partial^2 w}{\partial y \partial x} \right] + w \left[\frac{\partial^2 u}{\partial z \partial z} + \frac{\partial^2 w}{\partial z \partial x} \right] + 3 \frac{\partial u}{\partial z} \frac{\partial u}{\partial x} \right. \\
 & + 2 \frac{\partial v}{\partial z} \frac{\partial v}{\partial x} + 3 \frac{\partial w}{\partial z} \frac{\partial w}{\partial x} + \frac{\partial u}{\partial x} \frac{\partial z}{\partial x} + \frac{\partial v}{\partial x} \frac{\partial w}{\partial y} + \frac{\partial v}{\partial z} \frac{\partial u}{\partial y} + \left. \frac{\partial w}{\partial z} \frac{\partial u}{\partial z} \right\} \\
 & + \psi_2 \left\{ 2 \frac{\partial u}{\partial z} \frac{\partial u}{\partial x} + \frac{\partial v}{\partial z} \frac{\partial u}{\partial y} + 2 \frac{\partial w}{\partial z} \frac{\partial u}{\partial z} + 2 \frac{\partial u}{\partial x} \frac{\partial w}{\partial x} + \frac{\partial u}{\partial y} \frac{\partial w}{\partial y} + \frac{\partial v}{\partial z} \frac{\partial v}{\partial x} \right. \\
 & \left. + 2 \frac{\partial w}{\partial z} \frac{\partial w}{\partial x} + \frac{\partial v}{\partial x} \frac{\partial w}{\partial y} \right\}
 \end{aligned}$$

$$\bar{\tau}^P_{21} = \tau^P_{12}$$

$$\begin{aligned}
 \bar{\tau}^P_{22} = & \frac{1}{2} \psi_1 \left\{ 2u \frac{\partial^2 v}{\partial x \partial y} + 2v \frac{\partial^2 v}{\partial y \partial y} + 2w \frac{\partial^2 v}{\partial z \partial y} + 2 \frac{\partial u}{\partial y} \frac{\partial u}{\partial y} + 4 \frac{\partial v}{\partial y} \frac{\partial v}{\partial y} + 2 \frac{\partial w}{\partial y} \frac{\partial w}{\partial y} \right. \\
 & \left. + 2 \frac{\partial u}{\partial y} \frac{\partial v}{\partial x} + 2 \frac{\partial w}{\partial y} \frac{\partial v}{\partial z} \right\} \\
 & + \psi_2 \left\{ 2 \frac{\partial u}{\partial y} \frac{\partial v}{\partial x} + 4 \frac{\partial v}{\partial y} \frac{\partial v}{\partial y} + 2 \frac{\partial w}{\partial y} \frac{\partial v}{\partial z} + \frac{\partial v}{\partial x} \frac{\partial v}{\partial x} + \frac{\partial v}{\partial z} \frac{\partial v}{\partial z} + \frac{\partial u}{\partial y} \frac{\partial u}{\partial y} \right. \\
 & \left. + \frac{\partial w}{\partial y} \frac{\partial w}{\partial y} \right\}
 \end{aligned}$$

$$\begin{aligned}
 \bar{\tau}^P_{23} = & \frac{1}{2} \psi_1 \left\{ u \left[\frac{\partial^2 v}{\partial x \partial z} + \frac{\partial^2 w}{\partial x \partial y} \right] + v \left[\frac{\partial^2 v}{\partial y \partial z} + \frac{\partial^2 w}{\partial y \partial y} \right] + w \left[\frac{\partial^2 v}{\partial z \partial z} + \frac{\partial^2 w}{\partial z \partial y} \right] + 2 \frac{\partial u}{\partial z} \frac{\partial u}{\partial y} \right. \\
 & + 3 \frac{\partial v}{\partial z} \frac{\partial v}{\partial y} + 3 \frac{\partial w}{\partial z} \frac{\partial w}{\partial y} + \frac{\partial u}{\partial y} \frac{\partial w}{\partial x} + \frac{\partial v}{\partial y} \frac{\partial w}{\partial y} + \frac{\partial u}{\partial z} \frac{\partial v}{\partial x} + \left. \frac{\partial w}{\partial z} \frac{\partial v}{\partial z} \right\} \\
 & + \psi_2 \left\{ \frac{\partial u}{\partial z} \frac{\partial v}{\partial x} + 2 \frac{\partial v}{\partial z} \frac{\partial v}{\partial y} + 2 \frac{\partial w}{\partial z} \frac{\partial v}{\partial z} + \frac{\partial v}{\partial x} \frac{\partial w}{\partial x} + 2 \frac{\partial v}{\partial y} \frac{\partial w}{\partial y} + \frac{\partial u}{\partial z} \frac{\partial u}{\partial y} \right. \\
 & \left. + 2 \frac{\partial w}{\partial z} \frac{\partial w}{\partial y} + \frac{\partial u}{\partial y} \frac{\partial w}{\partial x} \right\}
 \end{aligned}$$

$$\bar{\tau}^P_{31} = \tau^P_{13}$$

$$\bar{\tau}^P_{32} = \tau^P_{23}$$

$$\begin{aligned}
 \bar{\tau}^P_{33} = & \frac{1}{2} \psi_1 \left\{ 2u \frac{\partial^2 w}{\partial x \partial z} + 2v \frac{\partial^2 w}{\partial y \partial z} + 2w \frac{\partial^2 w}{\partial z \partial z} + 2 \frac{\partial u}{\partial z} \frac{\partial u}{\partial z} + 2 \frac{\partial v}{\partial z} \frac{\partial v}{\partial z} + 4 \frac{\partial w}{\partial z} \frac{\partial w}{\partial z} \right. \\
 & \left. + 2 \frac{\partial u}{\partial z} \frac{\partial w}{\partial x} + 2 \frac{\partial y}{\partial z} \frac{\partial w}{\partial y} \right\} \\
 & + \psi_2 \left\{ 2 \frac{\partial u}{\partial z} \frac{\partial w}{\partial x} + 2 \frac{\partial v}{\partial z} \frac{\partial w}{\partial y} + 4 \frac{\partial w}{\partial z} \frac{\partial w}{\partial z} + \frac{\partial w}{\partial x} \frac{\partial w}{\partial x} + \frac{\partial w}{\partial y} \frac{\partial w}{\partial y} + \frac{\partial u}{\partial z} \frac{\partial u}{\partial z} \right. \\
 & \left. + \frac{\partial v}{\partial z} \frac{\partial v}{\partial z} \right\}
 \end{aligned}$$

Appendix C

The UDF and source terms written for 1000 ppm PAA flow in the 2:1 rectangular duct using the rheological data from Hartnett and Kostic (1985):

```
#include "udf.h"

DEFINE_PROPERTY(cell_viscosity,c,t) /*Defining the viscosity of PAA solution*/
{
double shear_rate;
double mu; /*Declaring the variable for viscosity of PAA*/

mu=0.00385+(0.282-0.00385)*(pow((1+(pow((4.74*shear_rate),0.942))),(-
0.506/0.942))); /*Defining the Carreau-Yasuda model*/
return mu;
}

DEFINE_SOURCE(Tx_source,c,t,dS,eqn) /*Defining the x-momentum source term*/
{
float T11_source,T21_source;
double shear_rate,NSC2;

shear_rate=C_STRAIN_RATE_MAG(c,t);
NSC2=-0.10*(0.168159159*pow(shear_rate, -1.50053648));
T11_source=(NSC2)*(C_W_G(c,t)[0]*C_W_G(c,t)[0]);
T21_source=(NSC2)*(C_W_G(c,t)[0]*C_W_G(c,t)[1]);

C_UDSI(c,t,0)=T11_source;
C_UDSI(c,t,1)=T21_source;
dS[eqn]=0;
return C_UDSI_G(c,t,0)[0]+C_UDSI_G(c,t,1)[1];
}
```

```
DEFINE_SOURCE(Ty_source,c,t,dS,eqn) /*Defining the y-momentum source term*/
{
float T12_source,T22_source;
double shear_rate,NSC2;

shear_rate=C_STRAIN_RATE_MAG(c,t);
NSC2=-0.10*(0.168159159*pow(shear_rate, -1.50053648));
T12_source=(NSC2)*(C_W_G(c,t)[0]*C_W_G(c,t)[1]);
T22_source=(NSC2)*(C_W_G(c,t)[1]*C_W_G(c,t)[1]);

C_UDSI(c,t,2)=T12_source;
C_UDSI(c,t,3)=T22_source;
dS[eqn]=0;
return C_UDSI_G(c,t,2)[0]+C_UDSI_G(c,t,3)[1];
}
```

The UDF and source terms written for 1000 ppm PAA flow in the non-circular ducts:

```

#include "udf.h"

/*Defining the viscosity for 1000 ppm PAA using the Carreau model*/
DEFINE_PROPERTY(cell_viscosity,cell,thread)
{
float shear_rate,K,n,ZSV,ISV;
double mu,temp1,temp2,temp3,temp4;

shear_rate=C_STRAIN_RATE_MAG(cell,thread);
temp1=C_T(cell,thread);
temp2=C_T(cell,thread);
temp3=C_T(cell,thread);
temp4=C_T(cell,thread);

K=(81168.8235*(pow((1/temp1),2)))-(492.5144*(1/temp1))+0.7805;
n=(-371379.5433*(pow((1/temp2),2)))+(1787.3878*(1/temp2))-0.3457;
ISV=(0.0002066)*(exp(760.9637*(1/temp3)));
ZSV=(56951.6662*(pow((1/temp4),2)))-(350.6373*(1/temp4))+0.5653;
mu=ISV+(ZSV-ISV)*(1/(pow((1+(pow((K*shear_rate),2))),(n/2))));
return mu;
}

DEFINE_SOURCE(Tx_source,c,t,dS,eqn) /*Defining the x-momentum source term*/
{
float T11_source,T21_source;
double NSC2,shear_rate;

shear_rate=C_STRAIN_RATE_MAG(c,t);
NSC2=-0.10*(31.7649189*(pow(shear_rate,-2.61679604)));
T11_source=(NSC2)*(C_W_G(c,t)[0]*C_W_G(c,t)[0]);

```

```
T21_source=(NSC2)*(C_W_G(c,t)[0]*C_W_G(c,t)[1]);
```

```
C_UDSI(c,t,0)=T11_source;
```

```
C_UDSI(c,t,1)=T21_source;
```

```
dS[eqn]=0;
```

```
return C_UDSI_G(c,t,0)[0]+C_UDSI_G(c,t,1)[1];
```

```
}
```

```
DEFINE_SOURCE(Ty_source,c,t,dS,eqn) /*Defining the y-momentum source term*/
```

```
{
```

```
float T12_source,T22_source;
```

```
double NSC2,shear_rate;
```

```
shear_rate=C_STRAIN_RATE_MAG(c,t);
```

```
NSC2=-0.10*(31.7649189*(pow(shear_rate,-2.61679604)));
```

```
T12_source=(NSC2)*(C_W_G(c,t)[0]*C_W_G(c,t)[1]);
```

```
T22_source=(NSC2)*(C_W_G(c,t)[1]*C_W_G(c,t)[1]);
```

```
C_UDSI(c,t,2)=T12_source;
```

```
C_UDSI(c,t,3)=T22_source;
```

```
dS[eqn]=0;
```

```
return C_UDSI_G(c,t,2)[0]+C_UDSI_G(c,t,3)[1];
```

```
}
```

The UDF written for the Carreau model used for 1000 ppm PAA flow in the circular pipe and double pipe heat exchanger:

```
#include "udf.h"

/*Defining the viscosity for 1000 ppm PAA using the Carreau model*/
DEFINE_PROPERTY(cell_viscosity,cell,thread)
{
float shear_rate,K,n,ZSV,ISV;
double mu; /*Declaring the variable for viscosity of PAA*/
double temp1,temp2,temp3,temp4;

shear_rate=C_STRAIN_RATE_MAG(cell,thread);
temp1=C_T(cell,thread);
temp2=C_T(cell,thread);
temp3=C_T(cell,thread);
temp4=C_T(cell,thread);

K=(81168.8235*(pow((1/temp1),2)))-(492.5144*(1/temp1))+0.7805;
n=(-371379.5433*(pow((1/temp2),2)))+(1787.3878*(1/temp2))-0.3457;
ISV=(0.0002066)*(exp(760.9637*(1/temp3)));
ZSV=(56951.6662*(pow((1/temp4),2)))-(350.6373*(1/temp4))+0.5653;
mu=ISV+(ZSV-ISV)*(1/(pow((1+(pow((K*shear_rate),2))),(n/2))));
return mu;
}
```

Not all the UDFs written are shown because the only difference in the UDFs for other concentrations of PAA solution and poly-nanofluid is on the values of the parameters of Carreau model and second normal stress coefficient. These values are given in (Appendix G) Table G.1 to Table G.4, and Table G.9.

Appendix D

The two algorithms available for the pressure-based solver are depicted in Figure D.1. The segregated algorithm solves the momentum and continuity equations sequentially while the coupled algorithm solves the continuity and momentum equations simultaneously.

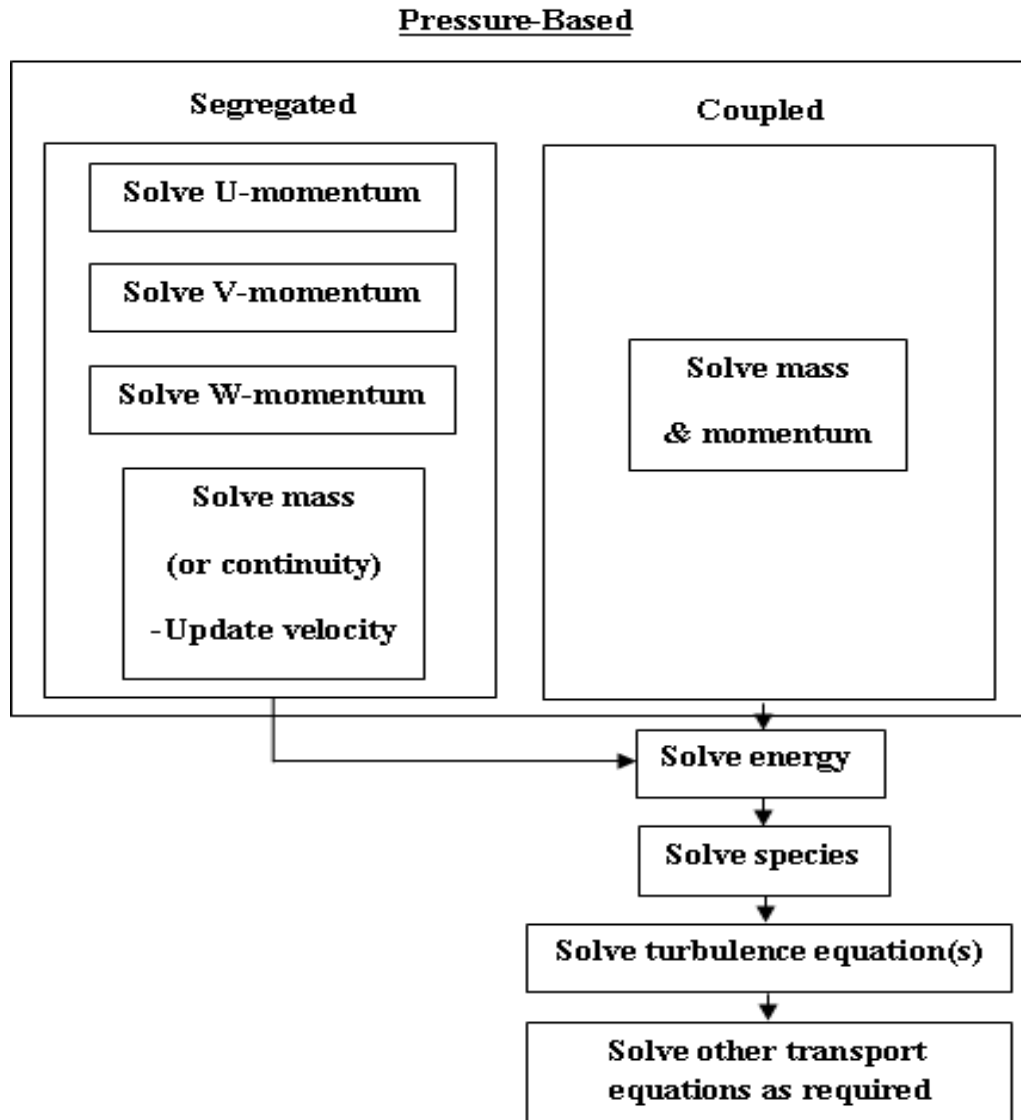


Figure D.1: Two algorithms available for the pressure-based solver
(*Ansys Fluent 15.0 User's Guide* 2013).

Appendix E

Table E.1: Solution method for the modelling of test fluids in circular and non-circular ducts (except for two-phase nanofluid modelling).

Solution method	
Pressure-velocity coupling	: SIMPLE scheme
<u>Spatial Discretization:</u>	
Gradient	: Least square cell based gradient
Pressure	: Second order
Momentum & energy	: Second order upwind

Table E.2: Solution method for the modelling of nanofluid in circular and non-circular ducts under the mixture and VOF models.

Solution method	
Pressure-velocity coupling	: Coupled scheme
<u>Spatial Discretization:</u>	
Gradient	: Least square cell based gradient
Pressure	: PRESTO
Momentum & energy	: Second order upwind
Volume fraction	: First order upwind

Table E.3: Solution method for the modelling of nanofluid in circular and non-circular ducts under the Eulerian model.

Solution method	
Pressure-velocity coupling	: Phase Coupled SIMPLE scheme
<u>Spatial Discretization:</u>	
Gradient	: Least square cell based gradient
Momentum & energy	: Second order upwind
Volume fraction	: First order upwind

Table E.4: Solution method for the modelling of test fluids in double pipe heat exchanger (except for two-phase nanofluid modelling).

Solution method	
Pressure-velocity coupling	: SIMPLE scheme
<u>Spatial Discretization:</u>	
Gradient	: Least square cell based gradient
Pressure	: Second order
Momentum & energy	: Second order upwind

Table E.5: Solution method for the modelling of nanofluid in double pipe heat exchanger under the mixture model.

Solution method	
Pressure-velocity coupling	: Coupled scheme
<u>Spatial Discretization:</u>	
Gradient	: Least square cell based gradient
Pressure	: PRESTO
Momentum & energy	: Second order upwind
Volume fraction	: First order upwind

Table E.6: Under-relaxation factors for numerical studies of water and nanofluid in circular and non-circular ducts (except for the two-phase nanofluid modelling).

Under-relaxation factors	
Pressure	: 0.3
Density	: 1
Body Forces	: 1
Momentum	: 0.7
Energy	: 1

Table E.7: Under-relaxation factors for numerical studies of nanofluid in circular and non-circular ducts under the mixture model.

Values	
Flow courant number	: 4
<u>Explicit relaxation factors:</u>	
Pressure	: 0.75
Momentum	: 0.75
<u>Under-relaxation factors:</u>	
Density	: 1
Body Forces	: 1
Slip velocity	: 0.1
Volume fraction	: 0.5
Energy	: 1

Table E.8: Under-relaxation factors for numerical studies of nanofluid in circular and non-circular ducts under the Eulerian model.

Under-relaxation factors	
Pressure	: 0.3
Density	: 1
Body Forces	: 1
Momentum	: 0.7
Volume fraction	: 0.5
Energy	: 1

Table E.9: Under-relaxation factors for numerical studies of nanofluid in circular and non-circular ducts under the VOF model.

		Values
Flow courant number	:	4
<u>Explicit relaxation factors:</u>		
Pressure	:	0.75
Momentum	:	0.75
<u>Under-relaxation factors:</u>		
Density	:	1
Body Forces	:	1
Volume fraction	:	0.5
Energy	:	1

Table E.10: Under-relaxation factors for numerical studies of PAA solution and poly-nanofluid in circular pipe.

		Under-relaxation factors
Pressure	:	0.3
Density	:	1
Body Forces	:	1
Momentum	:	0.7
Energy	:	1

Table E.11: Under-relaxation factors for numerical studies of PAA solution and poly-nanofluid in non-circular ducts.

		Under-relaxation factors
Pressure	:	0.3
Density	:	1
Body Forces	:	1
Momentum	:	0.7
Energy	:	1
User Scalars	:	1

Table E.12: Under-relaxation factors for numerical studies of test fluids in double pipe heat exchanger (except for two-phase nanofluid modelling).

		Under-relaxation factors
Pressure	:	0.3
Density	:	1
Body Forces	:	1
Momentum	:	0.7
Energy	:	1

Table E.13: Under-relaxation factors for numerical studies of nanofluid in double pipe heat exchanger under the mixture model.

Under-relaxation factors		
Pressure	:	0.3
Density	:	1
Body Forces	:	1
Momentum	:	0.7
Slip velocity	:	0.1
Volume fraction	:	0.5
Energy	:	1

Appendix F

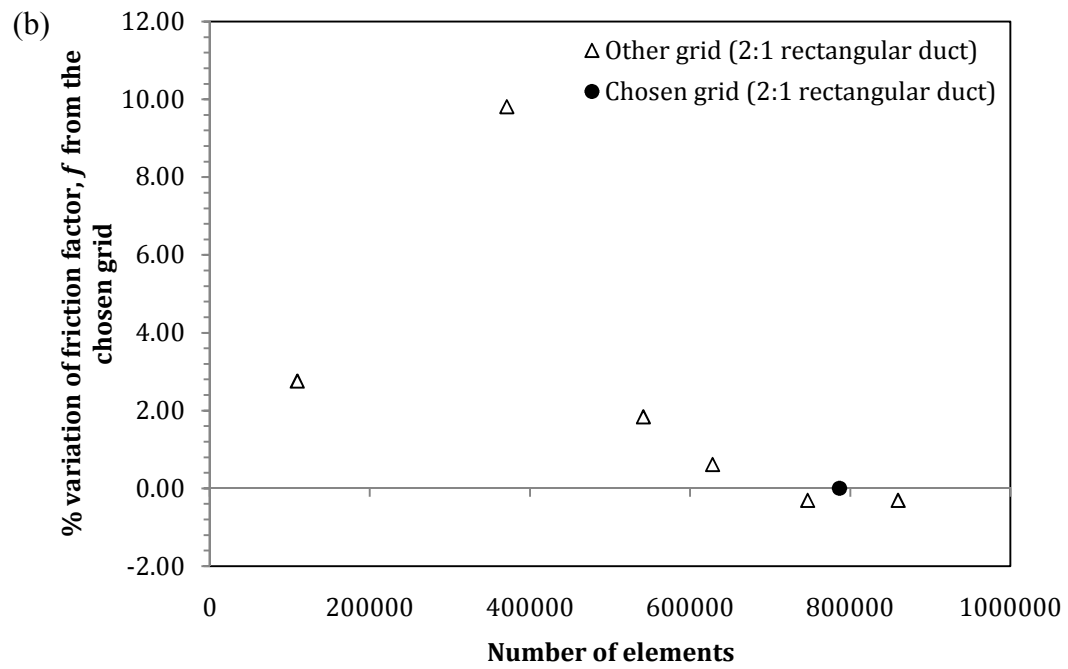
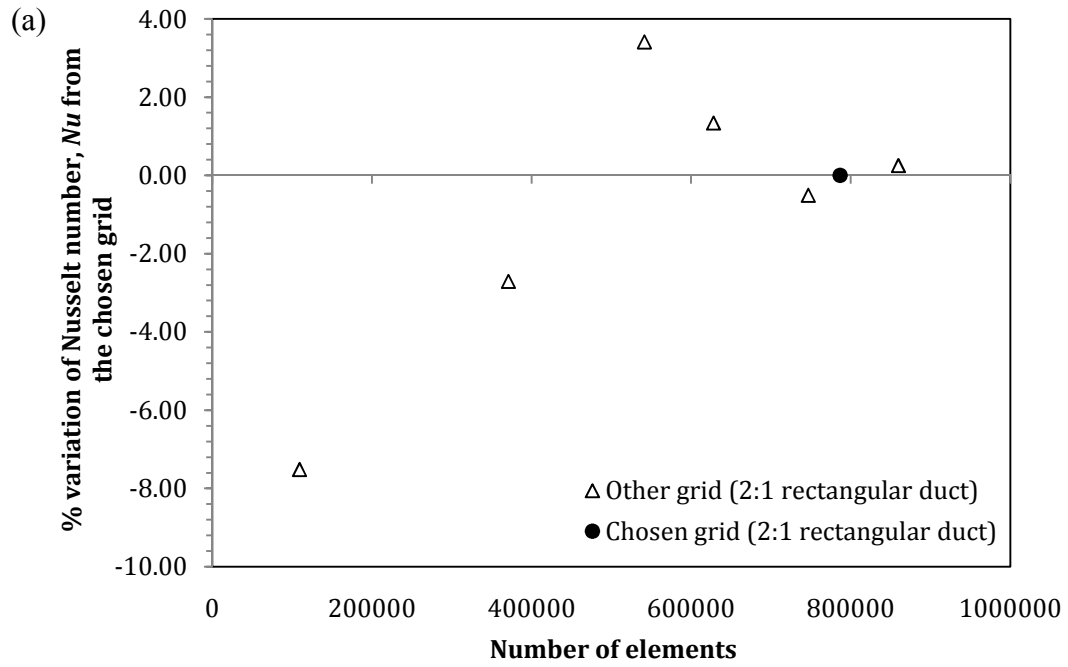


Figure F.1: Variations of (a) Nusselt number and (b) friction factor of the grids from the chosen grid (%) for 2:1 rectangular duct.

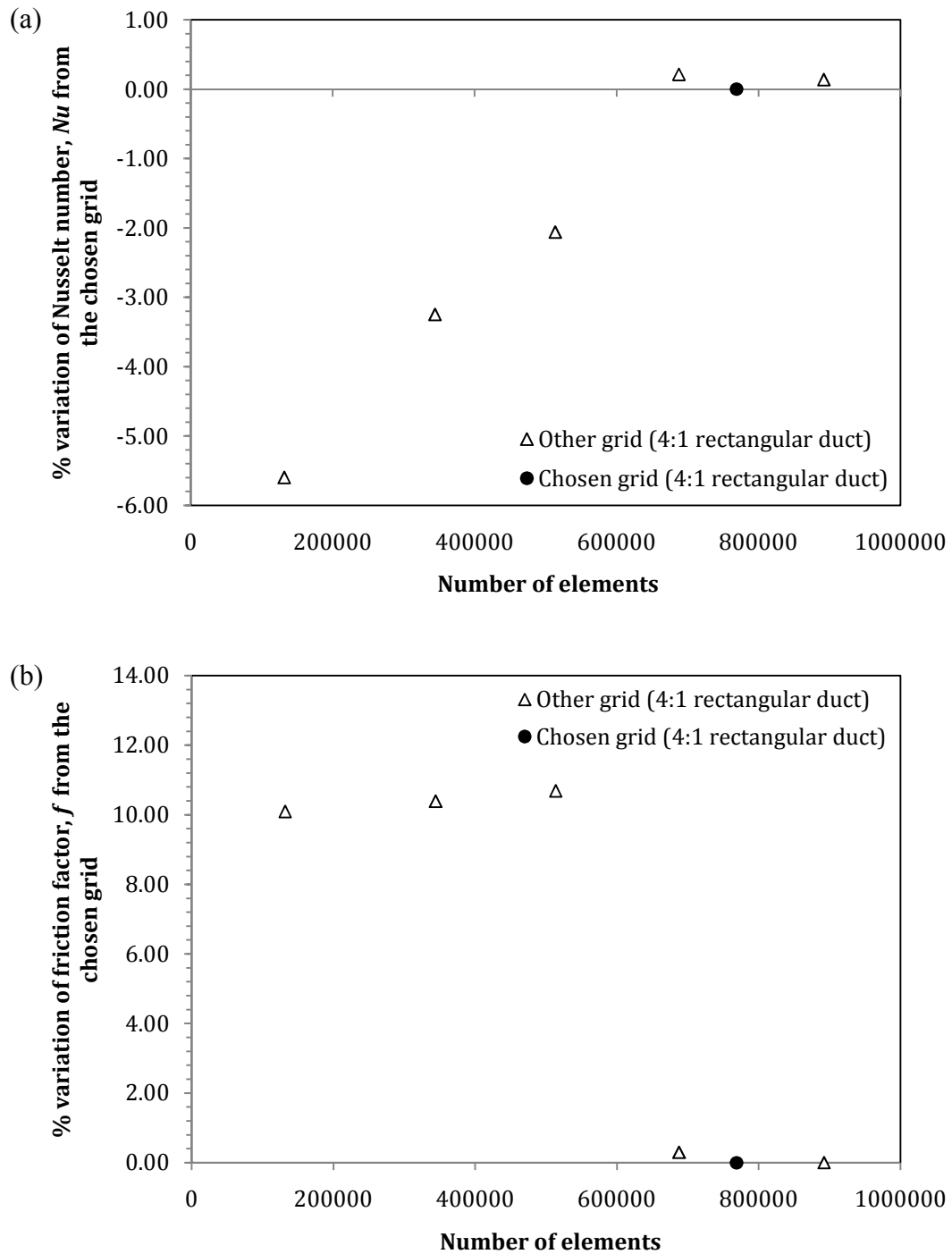


Figure F.2: Variations of (a) Nusselt number and (b) friction factor of the grids from the chosen grid (%) for 4:1 rectangular duct.

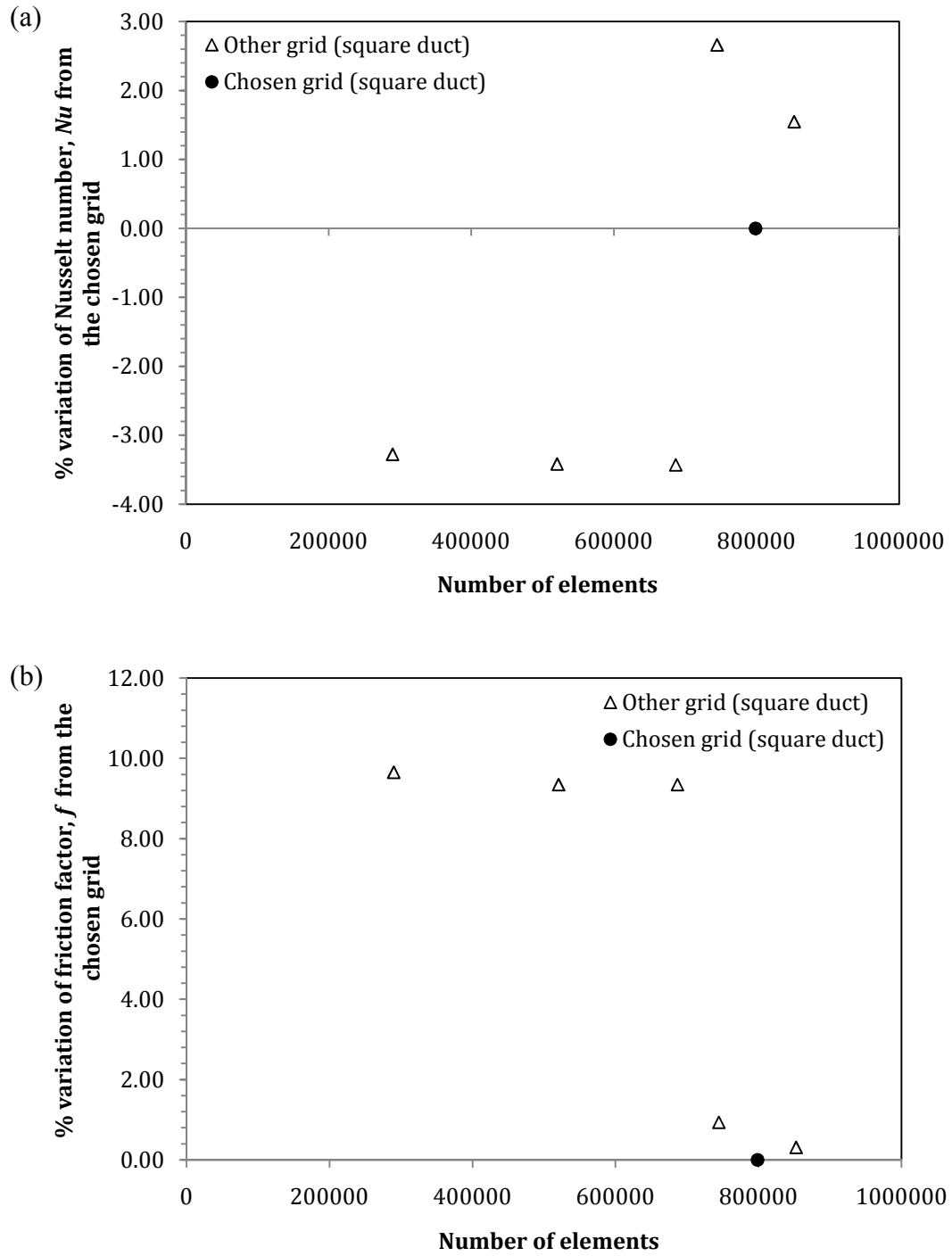


Figure F.3: Variations of (a) Nusselt number and (b) friction factor of the grids from the chosen grid (%) for square duct.

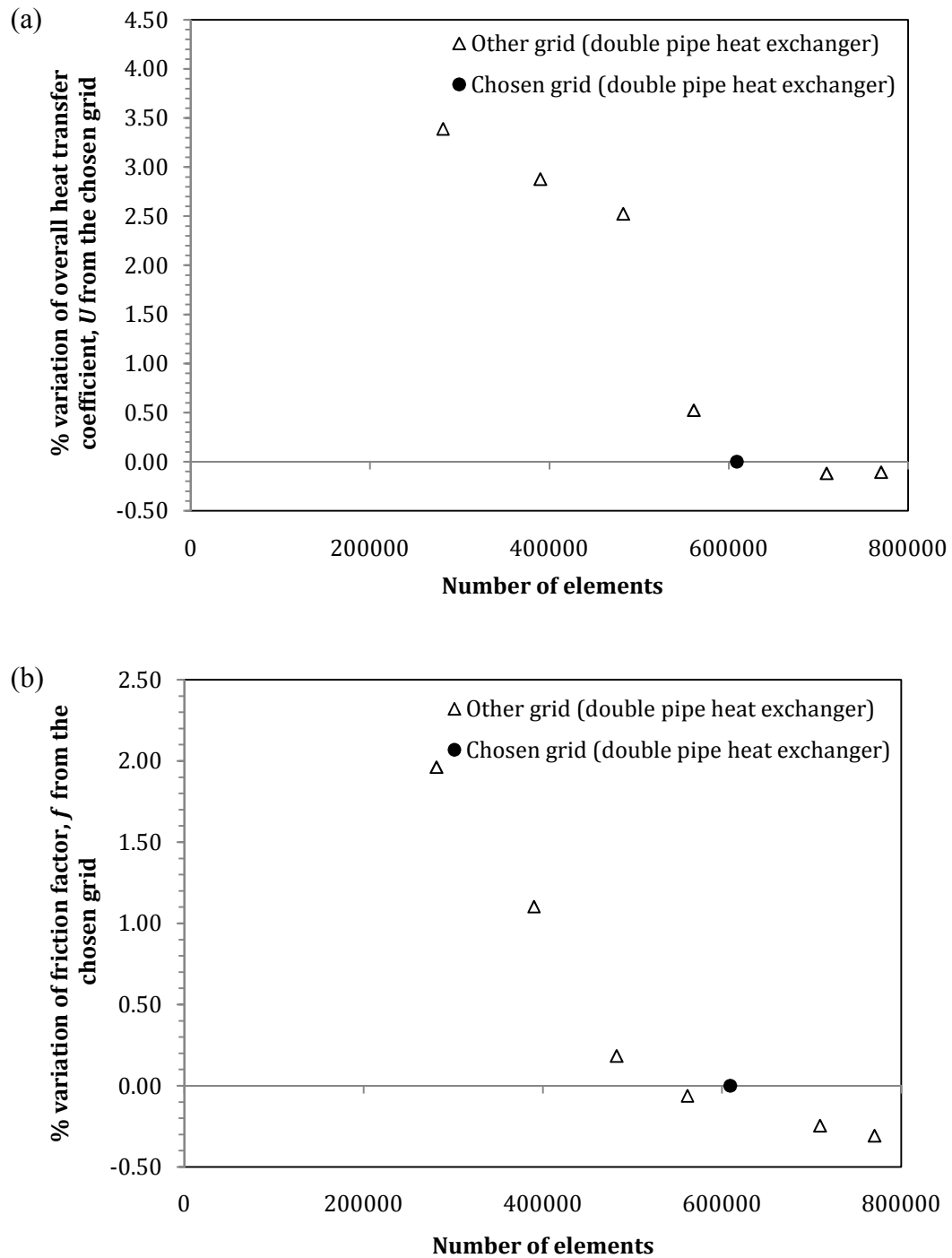


Figure F.4: Variations of (a) Nusselt number and (b) friction factor of the grids from the chosen grid (%) for double pipe heat exchanger.

Appendix G

Table G.1: The values of constants for η_∞ in Equation 4.1.

Concentration		A_1	A_2	A_3	A_4
PAA (ppm)	Al ₂ O ₃ (vol%)				
10	0.00	-4.61×10^1	4.30×10^4	-1.33×10^7	1.38×10^9
50	0.00	1.02×10^0	-1.63×10^3	7.29×10^5	-9.84×10^7
200	0.00	3.24×10^1	-2.94×10^4	8.91×10^6	-8.99×10^8
1000	0.00	5.65×10^{-1}	-3.51×10^2	5.70×10^4	-
10	0.13	1.83×10^1	-1.67×10^4	5.06×10^6	-5.13×10^8
10	0.51	6.04×10^1	-5.62×10^4	1.74×10^7	-1.80×10^9
10	1.00	7.92×10^1	-7.37×10^4	2.29×10^7	-2.36×10^9
10	4.00	1.81×10^1	-1.64×10^4	4.95×10^6	-4.98×10^8
50	0.13	1.48×10^2	-1.39×10^5	4.32×10^7	-4.48×10^9
50	0.51	-4.94×10^1	4.63×10^4	-1.45×10^7	1.50×10^9
50	1.00	-5.98×10^1	5.54×10^4	-1.72×10^7	1.76×10^9
50	4.00	7.17×10^1	-6.66×10^4	2.06×10^7	-2.13×10^9
200	0.13	-7.40×10^0	6.28×10^3	-1.76×10^6	1.62×10^8
200	0.51	-1.04×10^2	9.60×10^4	-2.98×10^7	3.08×10^9
200	1.00	-7.26×10^1	6.73×10^4	-2.08×10^7	2.14×10^9
200	4.00	4.61×10^2	-4.30×10^5	1.33×10^8	-1.38×10^{10}
1000	0.13	-6.72×10^1	6.23×10^4	-1.92×10^7	1.98×10^9
1000	0.51	1.07×10^1	-9.83×10^3	3.02×10^6	-3.10×10^8
1000	1.00	2.30×10^1	-2.20×10^4	6.99×10^6	-7.39×10^8
1000	4.00	-4.87×10^1	4.46×10^4	-1.36×10^7	1.38×10^9

Table G.2: The values of constants for η_o in Equation 4.2.

Concentration		B_1	B_2
PAA (ppm)	Al ₂ O ₃ (vol%)		
10	0.00	1.43×10^{-4}	7.83×10^2
50	0.00	3.30×10^{-4}	5.30×10^2
200	0.00	1.64×10^{-4}	7.58×10^2
1000	0.00	2.07×10^{-4}	7.61×10^2
10	0.13	1.31×10^{-4}	8.08×10^2
10	0.51	1.88×10^{-4}	6.99×10^2
10	1.00	9.16×10^{-5}	9.29×10^2
10	4.00	1.43×10^{-4}	7.89×10^2
50	0.13	1.19×10^{-4}	8.38×10^2
50	0.51	1.88×10^{-4}	7.01×10^2
50	1.00	1.98×10^{-4}	6.79×10^2
50	4.00	1.42×10^{-4}	8.28×10^2
200	0.13	1.56×10^{-4}	7.74×10^2
200	0.51	1.85×10^{-4}	7.19×10^2
200	1.00	1.55×10^{-4}	7.80×10^2
200	4.00	2.19×10^{-5}	1.56×10^3
1000	0.13	1.66×10^{-4}	8.32×10^2
1000	0.51	1.70×10^{-4}	7.30×10^2
1000	1.00	2.00×10^{-4}	7.98×10^2
1000	4.00	1.79×10^{-4}	8.28×10^2

Table G.3: The values of constants for λ in Equation 4.3.

Concentration		C_1	C_2	C_3	C_4
PAA (ppm)	Al ₂ O ₃ (vol%)				
10	0.00	-4.20×10^1	3.95×10^4	-1.23×10^7	1.28×10^9
50	0.00	-4.89×10^0	3.66×10^3	-8.45×10^5	5.70×10^7
200	0.00	1.19×10^2	-1.10×10^5	3.40×10^7	-3.50×10^9
1000	0.00	7.80×10^{-1}	-4.93×10^2	8.12×10^4	-
10	0.13	5.26×10^1	-4.88×10^4	1.51×10^7	-1.56×10^9
10	0.51	2.21×10^1	-1.99×10^4	5.98×10^6	-5.97×10^8
10	1.00	8.08×10^1	-7.50×10^4	2.32×10^7	-2.39×10^9
10	4.00	8.69×10^1	-8.03×10^4	2.47×10^7	-2.53×10^9
50	0.13	1.88×10^2	-1.76×10^5	5.47×10^7	-5.67×10^9
50	0.51	-1.10×10^2	1.03×10^5	-3.21×10^7	3.34×10^9
50	1.00	2.94×10^1	-2.79×10^4	8.80×10^6	-9.27×10^8
50	4.00	-8.38×10^1	7.87×10^4	-2.46×10^7	2.56×10^9
200	0.13	-4.51×10^1	4.14×10^4	-1.26×10^7	1.28×10^9
200	0.51	-1.56×10^2	1.45×10^5	-4.51×10^7	4.66×10^9
200	1.00	-6.30×10^1	5.82×10^4	-1.79×10^7	1.84×10^9
200	4.00	-1.38×10^2	1.29×10^5	-4.02×10^7	4.17×10^9
1000	0.13	-1.67×10^2	1.57×10^5	-4.90×10^7	5.11×10^9
1000	0.51	8.38×10^0	-7.65×10^3	2.34×10^6	-2.37×10^8
1000	1.00	-4.25×10^1	3.89×10^4	-1.19×10^7	1.21×10^9
1000	4.00	-3.81×10^1	3.35×10^4	-9.75×10^6	9.40×10^8

Table G.4: The values of constants for n' in Equation 4.4.

Concentration		D_1	D_2	D_3	D_4
PAA (ppm)	Al ₂ O ₃ (vol%)				
10	0.00	8.32×10^2	-7.83×10^5	2.46×10^8	-2.57×10^{10}
50	0.00	1.97×10^2	-1.73×10^5	5.10×10^7	-5.00×10^9
200	0.00	-5.60×10^2	5.17×10^5	-1.58×10^8	1.62×10^{10}
1000	0.00	-3.46×10^{-1}	1.79×10^3	-3.71×10^5	-
10	0.13	9.65×10^1	-8.80×10^4	2.71×10^7	-2.76×10^9
10	0.51	-4.53×10^2	4.09×10^5	-1.23×10^8	1.22×10^{10}
10	1.00	1.44×10^3	-1.35×10^6	4.22×10^8	-4.39×10^{10}
10	4.00	4.48×10^2	-4.24×10^5	1.34×10^8	-1.41×10^{10}
50	0.13	-9.62×10^2	9.04×10^5	-2.83×10^8	2.95×10^{10}
50	0.51	-5.69×10^2	5.19×10^5	-1.57×10^8	1.58×10^{10}
50	1.00	1.54×10^3	-1.44×10^6	4.49×10^8	-4.66×10^{10}
50	4.00	2.87×10^3	-2.68×10^6	8.35×10^8	-8.66×10^{10}
200	0.13	-7.39×10^2	6.90×10^5	-2.14×10^8	2.22×10^{10}
200	0.51	1.10×10^3	-1.02×10^6	3.16×10^8	-3.25×10^{10}
200	1.00	1.05×10^3	-9.84×10^5	3.07×10^8	-3.20×10^{10}
200	4.00	-7.36×10^3	6.84×10^6	-2.12×10^9	2.18×10^{11}
1000	0.13	5.45×10^2	-5.22×10^5	1.68×10^8	-1.79×10^{10}
1000	0.51	1.05×10^3	-9.84×10^5	3.08×10^8	-3.22×10^{10}
1000	1.00	5.95×10^1	-4.33×10^4	1.03×10^7	-7.70×10^8
1000	4.00	1.39×10^3	-1.28×10^6	3.97×10^8	-4.10×10^{10}

Table G.5: Constants for a in Equation 4.6.

Concentration		a_o	a_1	a_2
PAA (ppm)	Al ₂ O ₃ (vol%)			
10	0.00	7.50×10^0	-4.91×10^{-2}	8.25×10^{-5}
50	0.00	-1.54×10^{-1}	9.15×10^{-4}	6.30×10^{-7}
200	0.00	-6.05×10^0	3.97×10^{-2}	-6.32×10^{-5}
1000	0.00	4.02×10^0	-2.68×10^{-2}	4.61×10^{-5}
10	0.13	7.59×10^{-1}	-4.56×10^{-3}	8.96×10^{-6}
10	0.51	8.56×10^{-1}	-5.40×10^{-3}	1.06×10^{-5}
10	1.00	-2.73×10^{-1}	2.46×10^{-3}	-2.99×10^{-6}
10	4.00	1.38×10^0	-8.33×10^{-3}	1.46×10^{-5}
50	0.13	1.80×10^1	-1.13×10^{-1}	1.79×10^{-4}
50	0.51	-2.41×10^0	1.61×10^{-2}	-2.48×10^{-5}
50	1.00	1.56×10^1	-9.82×10^{-2}	1.56×10^{-4}
50	4.00	-6.22×10^0	4.02×10^{-2}	-6.30×10^{-5}
200	0.13	-2.02×10^0	1.32×10^{-2}	-1.94×10^{-5}
200	0.51	-1.47×10^0	9.05×10^{-3}	-1.19×10^{-5}
200	1.00	1.13×10^1	-7.18×10^{-2}	1.16×10^{-4}
200	4.00	-7.23×10^0	4.27×10^{-2}	-6.24×10^{-5}
1000	0.13	-1.32×10^1	9.34×10^{-2}	-1.70×10^{-4}
1000	0.51	-7.01×10^{-1}	4.67×10^{-3}	-5.68×10^{-6}
1000	1.00	4.20×10^0	-2.80×10^{-2}	4.81×10^{-5}
1000	4.00	6.65×10^1	-4.21×10^{-1}	6.69×10^{-4}

Table G.6: Constants for b in Equation 4.7.

Concentration		b_o	b_1	b_2
PAA (ppm)	Al ₂ O ₃ (vol%)			
10	0.00	-5.89×10^1	3.89×10^{-1}	-6.51×10^{-4}
50	0.00	-8.36×10^0	5.67×10^{-2}	-1.05×10^{-4}
200	0.00	4.16×10^1	-2.71×10^{-1}	4.31×10^{-4}
1000	0.00	-2.76×10^1	1.85×10^{-1}	-3.15×10^{-4}
10	0.13	-4.65×10^0	3.07×10^{-2}	-6.11×10^{-5}
10	0.51	4.00×10^0	-2.38×10^{-2}	2.54×10^{-5}
10	1.00	1.43×10^0	-1.11×10^{-2}	1.10×10^{-5}
10	4.00	-1.22×10^1	7.75×10^{-2}	-1.33×10^{-4}
50	0.13	-1.32×10^2	8.28×10^{-1}	-1.31×10^{-3}
50	0.51	1.50×10^1	-9.76×10^{-2}	1.49×10^{-4}
50	1.00	-1.16×10^2	7.34×10^{-1}	-1.17×10^{-3}
50	4.00	3.99×10^1	-2.55×10^{-1}	4.00×10^{-4}
200	0.13	6.75×10^0	-4.22×10^{-2}	5.60×10^{-5}
200	0.51	1.03×10^1	-6.10×10^{-2}	8.00×10^{-5}
200	1.00	-8.23×10^1	5.24×10^{-1}	-8.42×10^{-4}
200	4.00	3.36×10^1	-1.91×10^{-1}	2.70×10^{-4}
1000	0.13	5.46×10^1	-3.65×10^{-1}	6.17×10^{-4}
1000	0.51	4.00×10^0	-2.38×10^{-2}	2.54×10^{-5}
1000	1.00	-3.26×10^1	2.18×10^{-1}	-3.69×10^{-4}
1000	4.00	-4.60×10^2	2.92×10^0	-4.63×10^{-3}

Table G.7: Constants for c in Equation 4.8.

Concentration		c_o	c_1	c_2
PAA (ppm)	Al ₂ O ₃ (vol%)			
10	0.00	1.54×10^2	-1.02×10^0	1.69×10^{-3}
50	0.00	3.60×10^1	-2.40×10^{-1}	4.13×10^{-4}
200	0.00	-8.98×10^1	5.85×10^{-1}	-9.38×10^{-4}
1000	0.00	6.39×10^1	-4.25×10^{-1}	7.16×10^{-4}
10	0.13	1.13×10^1	-7.69×10^{-2}	1.47×10^{-4}
10	0.51	-5.77×10^0	3.05×10^{-2}	-2.28×10^{-5}
10	1.00	-2.53×10^0	1.87×10^{-2}	-1.80×10^{-5}
10	4.00	3.50×10^1	-2.24×10^{-1}	3.75×10^{-4}
50	0.13	3.19×10^2	-2.01×10^0	3.18×10^{-3}
50	0.51	-2.76×10^1	1.79×10^{-1}	-2.72×10^{-4}
50	1.00	2.87×10^2	-1.82×10^0	2.88×10^{-3}
50	4.00	-7.95×10^1	5.08×10^{-1}	-7.96×10^{-4}
200	0.13	1.07×10^1	-7.30×10^{-2}	1.40×10^{-4}
200	0.51	-2.00×10^1	1.15×10^{-1}	-1.48×10^{-4}
200	1.00	1.99×10^2	-1.26×10^0	2.03×10^{-3}
200	4.00	-5.21×10^1	2.89×10^{-1}	-3.97×10^{-4}
1000	0.13	5.46×10^1	-3.65×10^{-1}	6.17×10^{-4}
1000	0.51	-5.77×10^0	3.05×10^{-2}	-2.28×10^{-5}
1000	1.00	8.33×10^1	-5.50×10^{-1}	9.17×10^{-4}
1000	4.00	1.03×10^3	-6.54×10^0	1.04×10^{-2}

Table G.8: Constants for d in Equation 4.9.

Concentration		d_o	d_1	d_2
PAA (ppm)	Al ₂ O ₃ (vol%)			
10	0.00	-1.31×10^2	8.61×10^{-1}	-1.43×10^{-3}
50	0.00	-3.19×10^1	2.10×10^{-1}	-3.58×10^{-4}
200	0.00	6.32×10^1	-4.16×10^{-1}	6.71×10^{-4}
1000	0.00	-4.50×10^1	2.96×10^{-1}	-4.95×10^{-4}
10	0.13	-8.84×10^0	5.81×10^{-2}	-1.09×10^{-4}
10	0.51	-2.03×10^1	1.34×10^{-1}	-2.35×10^{-4}
10	1.00	5.04×10^0	-3.64×10^{-2}	5.20×10^{-5}
10	4.00	-2.88×10^1	1.82×10^{-1}	-3.00×10^{-4}
50	0.13	-2.53×10^2	1.59×10^0	-2.52×10^{-3}
50	0.51	1.79×10^1	-1.18×10^{-1}	1.80×10^{-4}
50	1.00	-2.32×10^2	1.46×10^0	-2.32×10^{-3}
50	4.00	5.01×10^1	-3.22×10^{-1}	5.05×10^{-4}
200	0.13	-3.07×10^1	1.98×10^{-1}	-3.32×10^{-4}
200	0.51	1.30×10^1	-7.50×10^{-2}	9.48×10^{-5}
200	1.00	-1.54×10^2	9.79×10^{-1}	-1.56×10^{-3}
200	4.00	4.29×10^1	-2.50×10^{-1}	3.61×10^{-4}
1000	0.13	-6.16×10^1	4.00×10^{-1}	-6.57×10^{-4}
1000	0.51	3.88×10^0	-2.19×10^{-2}	1.78×10^{-5}
1000	1.00	-6.27×10^1	4.09×10^{-1}	-6.77×10^{-4}
1000	4.00	-7.37×10^2	4.66×10^0	-7.39×10^{-3}

Table G.9: Constants for Equation 4.10.

Concentration		e	f
PAA (ppm)	Al ₂ O ₃ (vol%)		
10	0.00	7.91×10^1	-2.81
50	0.00	2.68×10^2	-3.00
200	0.00	6.91×10^1	-2.78
1000	0.00	3.18×10^1	-2.62
10	0.13	7.27×10^1	-2.78
10	0.51	7.74×10^1	-2.79
10	1.00	6.72×10^1	-2.78
10	4.00	6.24×10^1	-2.75
50	0.13	1.39×10^2	-2.89
50	0.51	7.44×10^1	-2.78
50	1.00	2.36×10^1	-2.58
50	4.00	8.89×10^1	-2.83
200	0.13	5.60×10^1	-2.73
200	0.51	1.02×10^2	-2.84
200	1.00	3.49×10^1	-2.65
200	4.00	1.35×10^1	-2.44
1000	0.13	2.60×10^1	-2.58
1000	0.51	7.74×10^1	-2.79
1000	1.00	2.94×10^1	-2.60
1000	4.00	7.04×10^1	-2.65

Appendix H

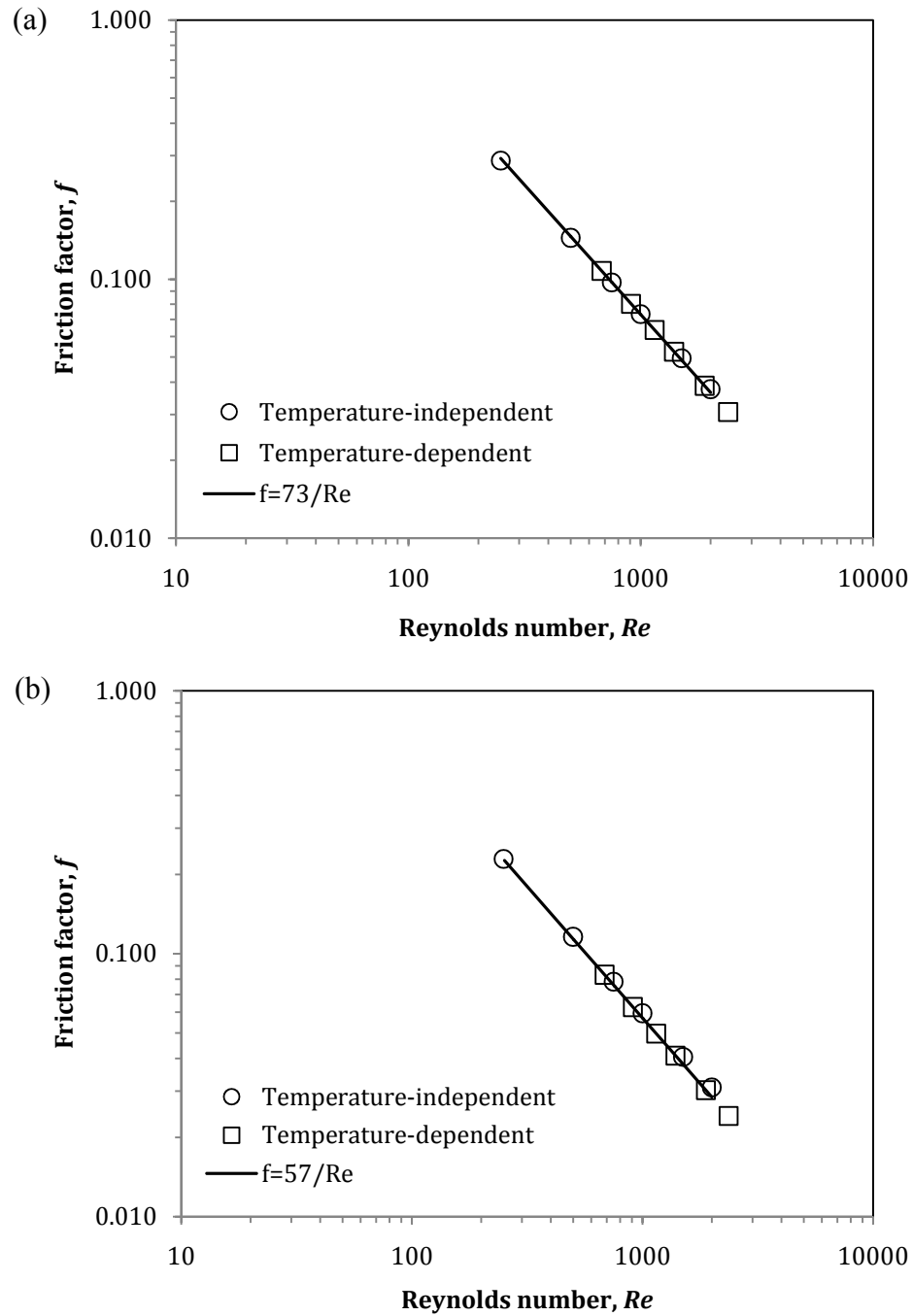


Figure H.1: Friction factor for water in (a) 4:1 rectangular and (b) square ducts for temperature-independent and temperature-dependent properties.

Appendix I

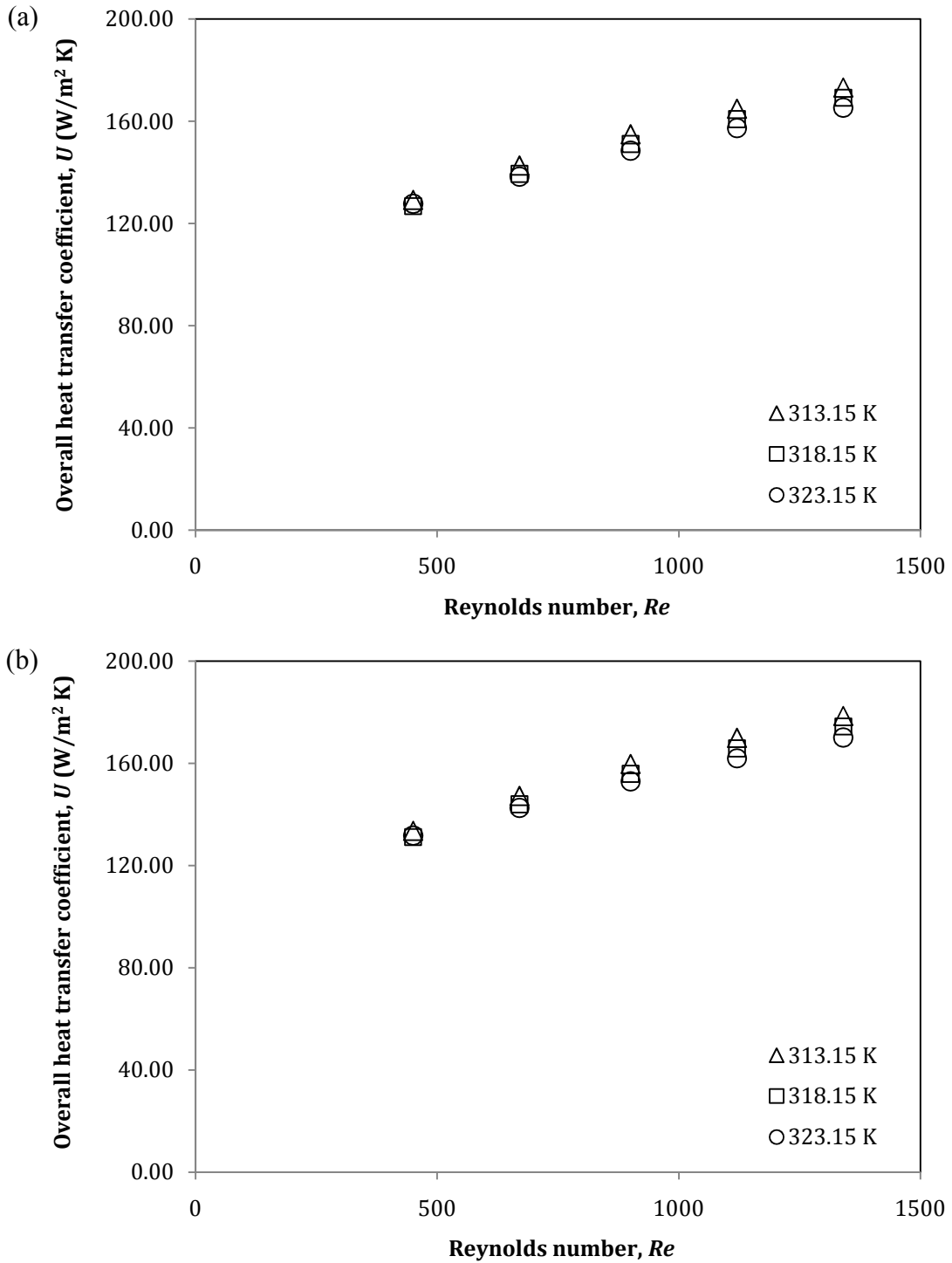


Figure I.1: Overall heat transfer coefficient of (a) 0.01% and (b) 1% Al₂O₃ nanofluid at different hot inlet temperatures.

Table I.1: h enhancement (%) of nanofluid in 2:1 rectangular duct.

Reynolds number	Nanoparticles volume concentration (%)						
	0.01	0.09	0.13	0.25	0.51	1.00	4.00
<u>Temperature-independent properties</u>							
250	0.12	0.85	1.22	2.48	5.04	10.05	44.10
750	0.16	1.12	1.60	3.24	6.61	13.19	57.62
1000	0.17	1.18	1.70	3.43	7.00	13.97	61.00
1500	0.18	1.25	1.81	3.67	7.51	15.00	65.46
2000	0.19	1.33	1.91	3.86	7.88	15.72	68.38
<u>Temperature-dependent properties</u>							
250	1.84	2.30	2.34	2.73	3.47	5.56	19.23
750	2.37	2.71	2.91	3.18	3.73	5.76	21.88
1000	2.49	2.75	2.86	3.28	4.39	6.22	22.69
1500	2.90	3.13	3.24	3.63	4.49	6.50	23.10
2000	3.21	3.42	3.54	3.91	4.75	6.73	23.89

Table I.2: Nu enhancement (%) of nanofluid in 2:1 rectangular duct.

Reynolds number	Nanoparticles volume concentration (%)						
	0.01	0.09	0.13	0.25	0.51	1.00	4.00
<u>Temperature-independent properties</u>							
250	0.03	0.20	0.28	0.57	1.18	2.40	10.95
750	0.07	0.46	0.66	1.32	2.69	5.32	21.35
1000	0.07	0.53	0.75	1.51	3.06	6.05	23.95
1500	0.07	0.60	0.86	1.75	3.55	7.01	27.39
2000	0.10	0.67	0.96	1.93	3.91	7.67	29.64
<u>Temperature-dependent properties</u>							
250	0.56	0.53	0.53	0.44	0.40	0.37	1.62
750	1.49	1.49	1.47	1.47	1.20	1.33	3.52
1000	2.85	2.86	2.91	2.91	2.91	3.38	4.09
1500	3.03	3.03	3.03	3.03	3.03	3.25	4.55
2000	3.38	3.34	3.34	3.32	3.30	3.30	5.01

Table I.3: h enhancement (%) of nanofluid in 4:1 rectangular duct.

Reynolds number	Nanoparticles volume concentration (%)						
	0.01	0.09	0.13	0.25	0.51	1.00	4.00
<u>Temperature-independent properties</u>							
250	0.15	1.09	1.56	3.14	6.38	12.65	53.41
750	0.16	1.19	1.71	3.46	7.02	13.88	58.31
1000	0.17	1.21	1.74	3.52	7.14	14.14	59.87
1500	0.18	1.25	1.79	3.62	7.36	14.62	62.71
2000	0.18	1.29	1.84	3.73	7.58	15.08	65.06
<u>Temperature-dependent properties</u>							
250	1.84	2.34	2.56	2.95	3.55	5.74	20.31
750	2.42	2.83	3.26	3.37	3.82	6.26	21.90
1000	2.33	2.58	2.70	3.13	4.05	6.09	22.34
1500	2.55	2.80	2.91	3.33	4.22	6.26	22.52
2000	2.81	3.04	3.16	3.56	4.44	6.46	23.00

Table I.4: *Nu* enhancement (%) of nanofluid in 4:1 rectangular duct.

Reynolds number	Nanoparticles volume concentration (%)						
	0.01	0.09	0.13	0.25	0.51	1.00	4.00
<u>Temperature-independent properties</u>							
250	0.20	0.56	0.74	1.35	2.59	4.95	18.26
750	0.05	0.51	0.74	1.51	3.06	5.94	21.86
1000	0.19	0.67	0.91	1.70	3.31	6.32	23.22
1500	0.16	0.67	0.92	1.78	3.49	6.73	25.37
2000	0.06	0.60	0.87	1.77	3.59	7.05	27.05
<u>Temperature-dependent properties</u>							
250	0.89	0.87	0.84	0.84	0.76	0.76	2.29
750	1.69	1.58	1.48	1.48	1.48	1.39	3.59
1000	2.76	2.76	2.56	2.36	2.16	1.75	4.01
1500	2.89	2.71	2.71	2.52	2.15	1.77	4.44
2000	3.17	3.00	3.00	2.82	2.47	2.12	4.88

Table I.5: *h* enhancement (%) of nanofluid in square duct.

Reynolds number	Nanoparticles volume concentration (%)						
	0.01	0.09	0.13	0.25	0.51	1.00	4.00
<u>Temperature-independent properties</u>							
250	0.12	0.78	1.12	2.26	4.59	9.11	39.45
750	0.14	1.02	1.47	2.99	6.12	12.28	55.14
1000	0.16	1.12	1.61	3.27	6.68	13.40	59.71
1500	0.18	1.25	1.79	3.63	7.41	14.85	65.39
2000	0.19	1.24	1.82	3.76	7.77	15.62	68.62
<u>Temperature-dependent properties</u>							
250	0.61	0.95	1.15	1.83	2.89	5.17	18.79
750	1.44	1.83	2.16	2.56	3.57	5.79	21.15
1000	2.31	2.56	2.67	3.10	4.02	6.06	21.86
1500	2.92	3.15	3.26	3.72	4.51	6.51	23.29
2000	3.50	3.70	3.82	4.19	5.02	7.00	24.40

Table I.6: *Nu* enhancement (%) of nanofluid in square duct.

Reynolds number	Nanoparticles volume concentration (%)						
	0.01	0.09	0.13	0.25	0.51	1.00	4.00
<u>Temperature-independent properties</u>							
250	0.03	0.14	0.19	0.37	0.76	1.53	7.37
750	0.05	0.37	0.53	1.08	2.22	4.49	19.46
1000	0.07	0.47	0.67	1.35	2.76	5.52	22.97
1500	0.09	0.60	0.85	1.71	3.47	6.87	27.35
2000	0.58	0.58	0.87	1.83	3.80	7.58	29.82
<u>Temperature-dependent properties</u>							
250	0.39	0.39	0.36	0.29	0.29	0.29	1.53
750	1.22	1.22	1.17	1.09	1.07	1.04	3.26
1000	2.63	2.51	2.51	2.26	2.26	2.26	3.83
1500	3.21	3.21	3.21	2.98	2.75	2.75	4.59
2000	3.47	3.45	3.45	3.43	3.41	3.41	5.12

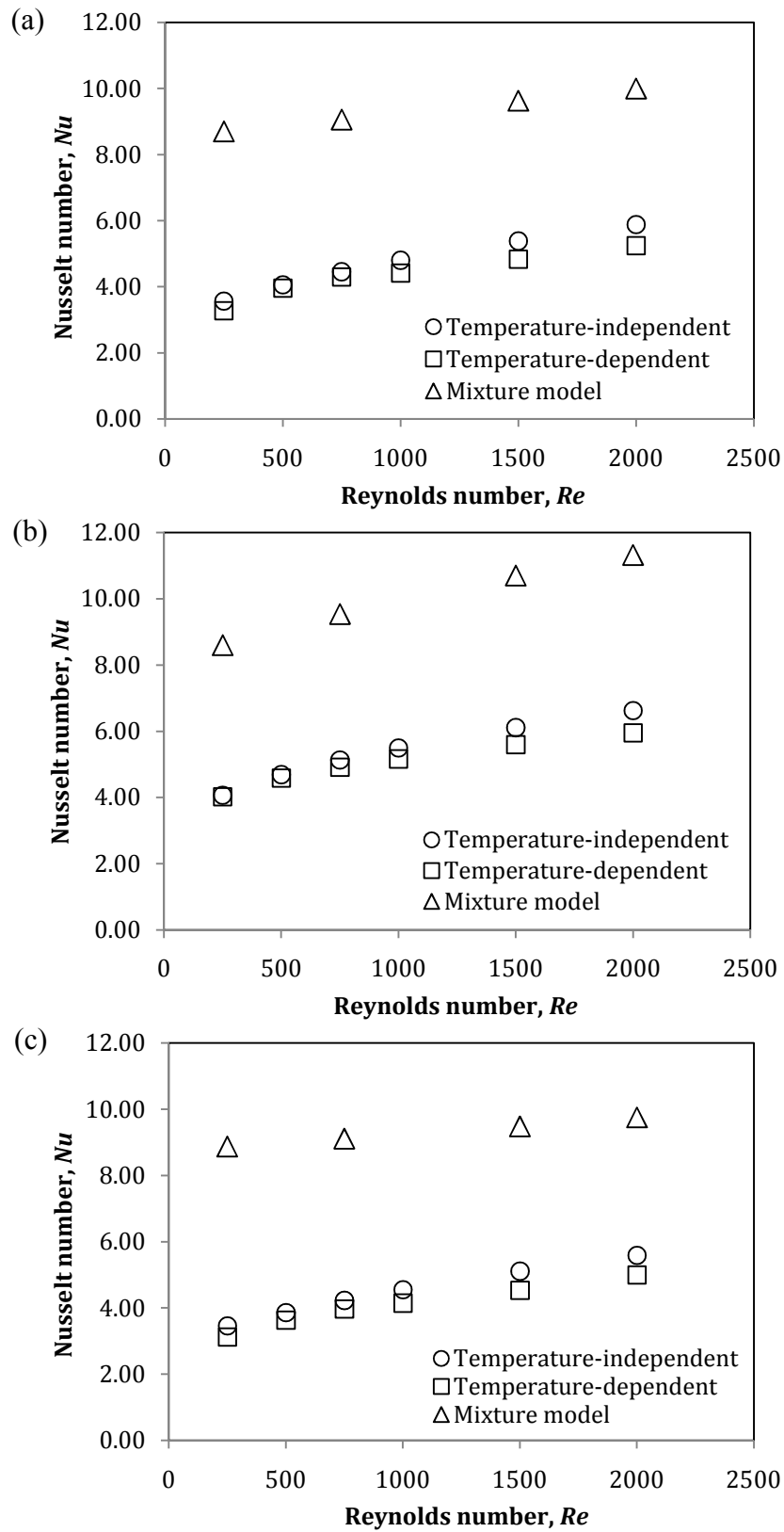


Figure I.2: Comparison of Nusselt number obtained from different models for 4% Al_2O_3 nanofluid in (a) 2:1 rectangular, (b) 4:1 rectangular and (c) square ducts.

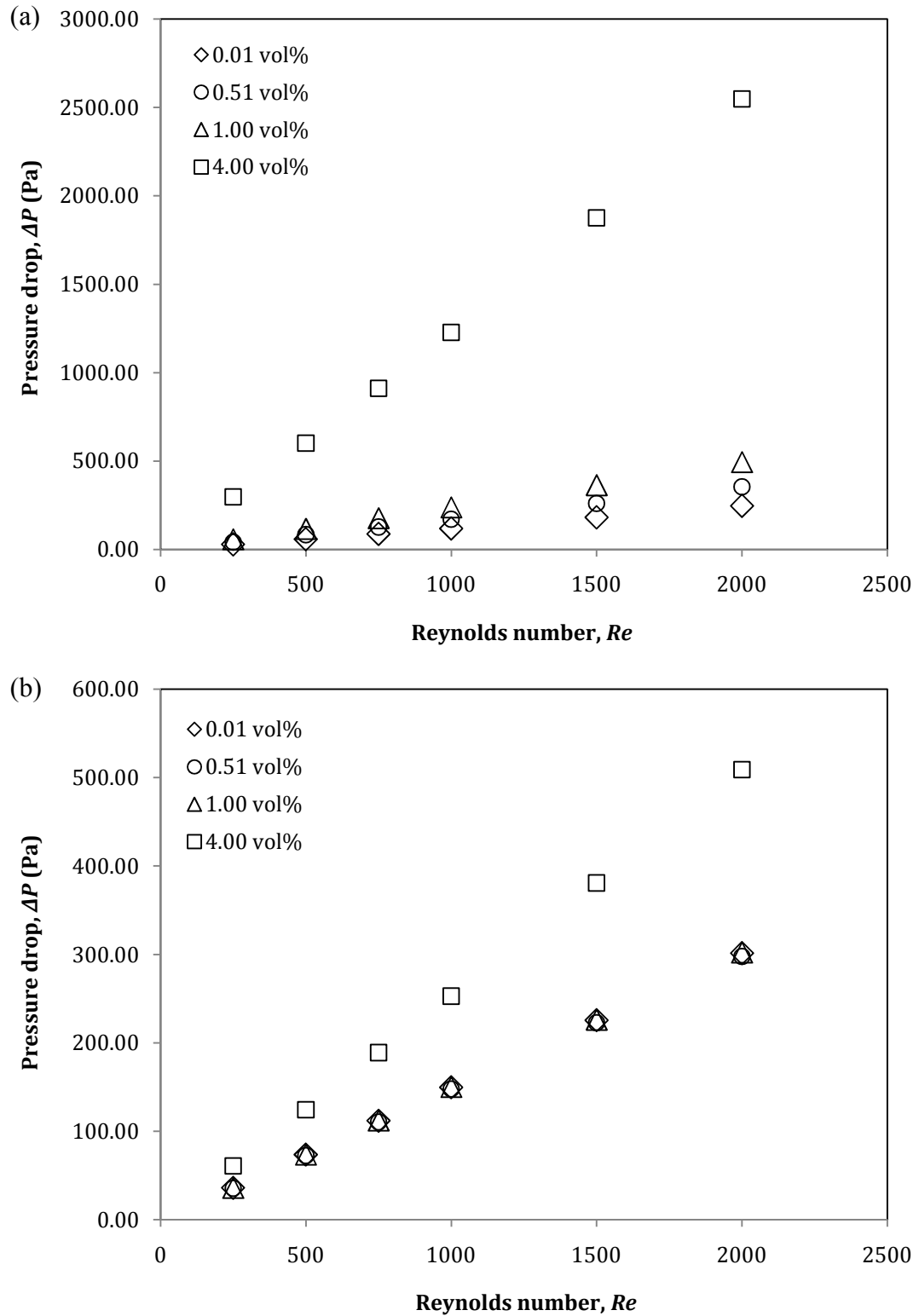


Figure I.3: Pressure drop of nanofluid in 2:1 rectangular duct for the cases of (a) temperature-independent and (b) temperature-dependent properties.

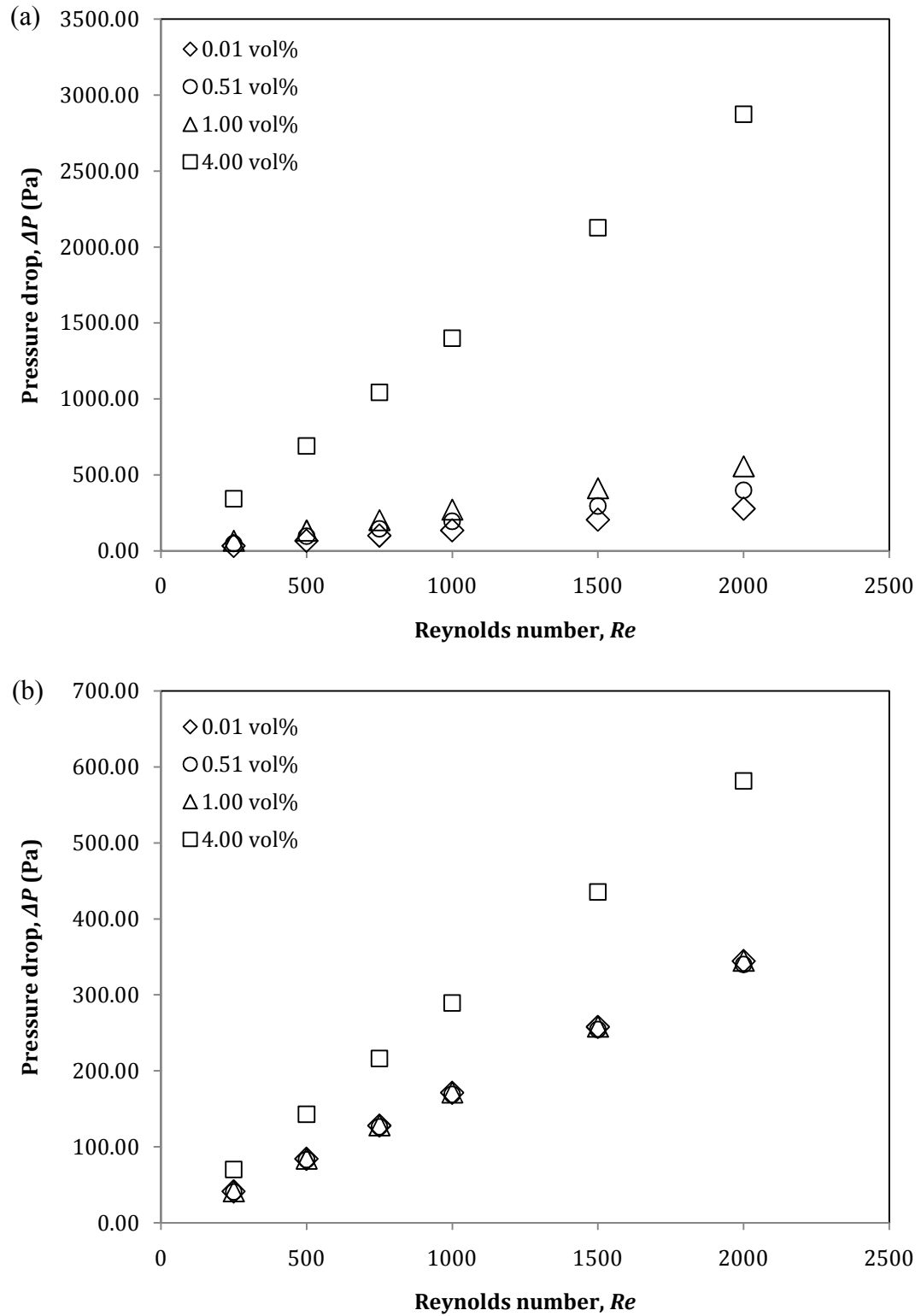


Figure I.4: Pressure drop of nanofluid in 4:1 rectangular duct for the cases of (a) temperature-independent and (b) temperature-dependent properties.

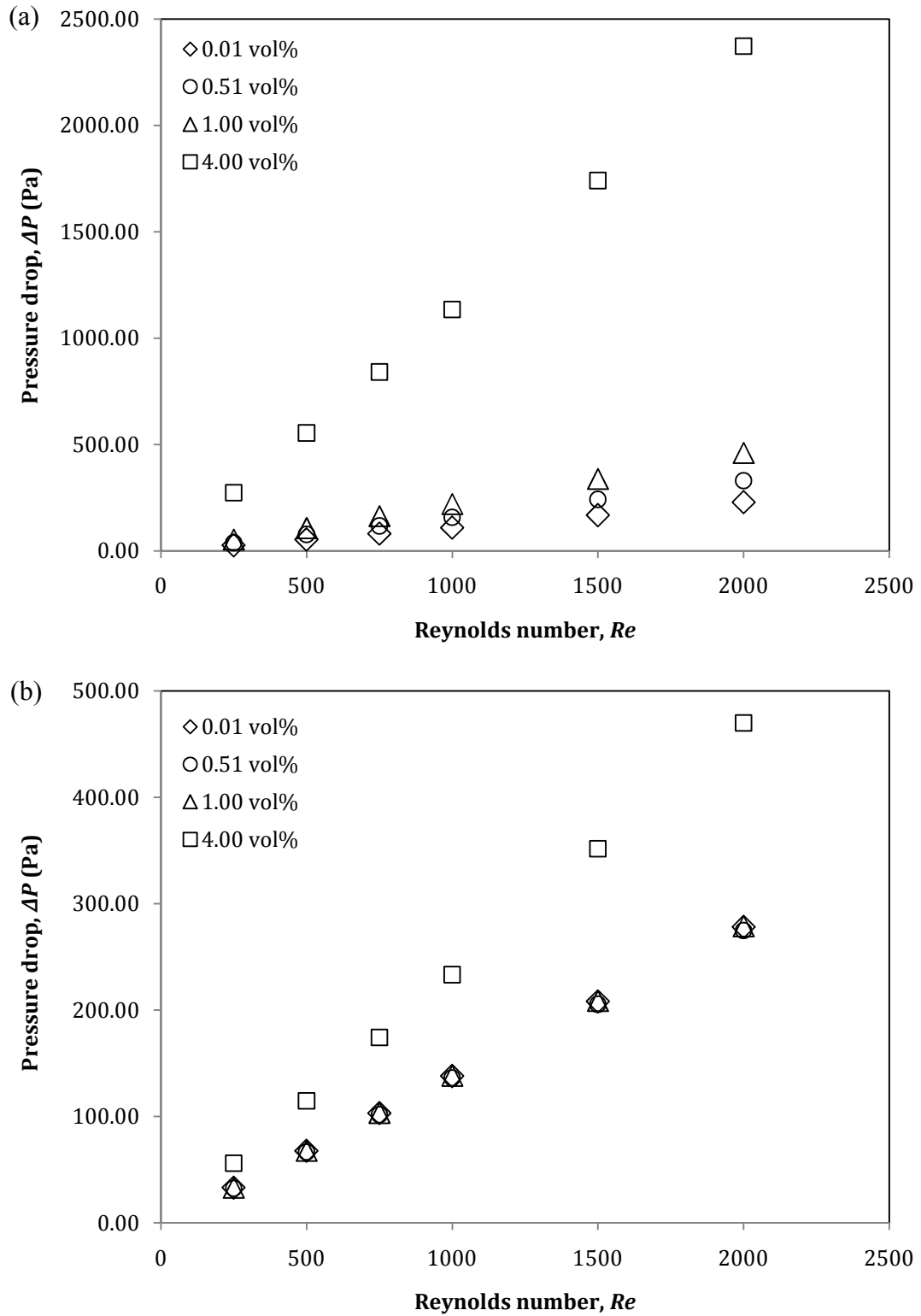


Figure I.5: Pressure drop of nanofluid in square duct for the cases of (a) temperature-independent and (b) temperature-dependent properties.

Table I.7: τ_w increment (%) of Al₂O₃ nanofluid in 2:1 rectangular duct.

<i>Reynolds number</i>	<i>Nanoparticles volume concentration (%)</i>						
	0.01	0.09	0.13	0.25	0.51	1.00	4.00
<i><u>Temperature-independent properties</u></i>							
250	0.96	6.86	9.90	20.67	45.06	102.57	944.43
750	0.96	6.86	9.90	20.66	45.06	102.57	944.43
1000	0.96	6.86	9.90	20.66	45.06	102.57	944.43
1500	0.96	6.86	9.90	20.66	45.06	102.57	944.43
2000	0.96	6.86	9.89	20.66	45.06	102.57	944.43
<i><u>Temperature-dependent properties</u></i>							
250	28.31	27.54	27.54	26.78	26.02	28.31	116.95
750	28.92	28.42	28.17	27.42	27.18	28.92	117.69
1000	28.82	28.39	28.08	27.39	27.15	28.89	117.57
1500	28.96	28.54	28.21	27.51	27.35	29.00	118.24
2000	29.02	28.62	28.28	27.57	27.44	29.05	117.82

Table I.8: ΔP increment (%) of Al₂O₃ nanofluid in 2:1 rectangular duct.

<i>Reynolds number</i>	<i>Nanoparticles volume concentration (%)</i>						
	0.01	0.09	0.13	0.25	0.51	1.00	4.00
<i><u>Temperature-independent properties</u></i>							
250	0.96	6.86	9.90	20.66	45.06	102.57	944.43
750	0.96	6.86	9.90	20.66	45.06	102.57	944.43
1000	0.96	6.86	9.89	20.66	45.06	102.57	944.43
1500	0.96	6.86	9.89	20.66	45.06	102.57	944.43
2000	0.96	6.86	9.89	20.66	45.06	102.57	944.43
<i><u>Temperature-dependent properties</u></i>							
250	28.02	27.59	27.55	26.95	26.10	28.19	116.93
750	28.83	28.39	28.17	27.57	27.09	29.06	117.67
1000	26.00	25.58	25.32	24.73	24.30	26.22	112.85
1500	27.06	26.64	26.36	25.77	25.38	27.30	114.56
2000	27.60	27.17	26.89	26.29	25.92	27.84	115.42

Table I.9: ΔP increment (%) of Al₂O₃ nanofluid in 4:1 rectangular duct.

<i>Reynolds number</i>	<i>Nanoparticles volume concentration (%)</i>						
	0.01	0.09	0.13	0.25	0.51	1.00	4.00
<i><u>Temperature-independent properties</u></i>							
250	1.08	6.99	10.03	20.81	45.24	102.81	945.69
750	0.92	6.81	9.85	20.61	45.00	102.49	943.99
1000	0.96	6.86	9.89	20.66	45.06	102.57	944.42
1500	0.96	6.86	9.89	20.66	45.06	102.57	944.43
2000	0.96	6.86	9.89	20.66	45.06	102.57	944.42
<i><u>Temperature-dependent properties</u></i>							
250	28.03	27.60	27.57	26.98	26.11	28.09	116.92
750	28.81	28.37	28.15	27.55	27.07	28.96	117.59
1000	28.77	28.34	28.07	27.47	27.03	28.92	117.48
1500	28.91	28.48	28.19	27.59	27.20	29.07	117.63
2000	28.98	28.54	28.25	27.65	27.28	29.15	117.70

Table I.10: ΔP increment (%) of Al_2O_3 nanofluid in square duct.

Reynolds number	Nanoparticles volume concentration (%)						
	0.01	0.09	0.13	0.25	0.51	1.00	4.00
<i>Temperature-independent properties</i>							
250	1.09	7.00	10.04	20.82	45.25	102.83	945.79
750	0.91	6.81	9.85	20.61	45.00	102.48	943.96
1000	0.96	6.86	9.90	20.67	45.07	102.58	944.47
1500	0.96	6.86	9.90	20.67	45.07	102.58	944.44
2000	0.96	6.86	9.89	20.66	45.06	102.58	944.43
<i>Temperature-dependent properties</i>							
250	28.02	27.59	27.59	26.97	26.12	28.09	117.00
750	28.83	28.39	28.18	27.58	27.10	29.07	117.70
1000	28.80	28.36	28.10	27.50	27.06	29.03	117.59
1500	28.94	28.50	28.22	27.63	27.23	29.19	117.74
2000	29.01	28.57	28.28	27.69	27.31	29.28	117.82

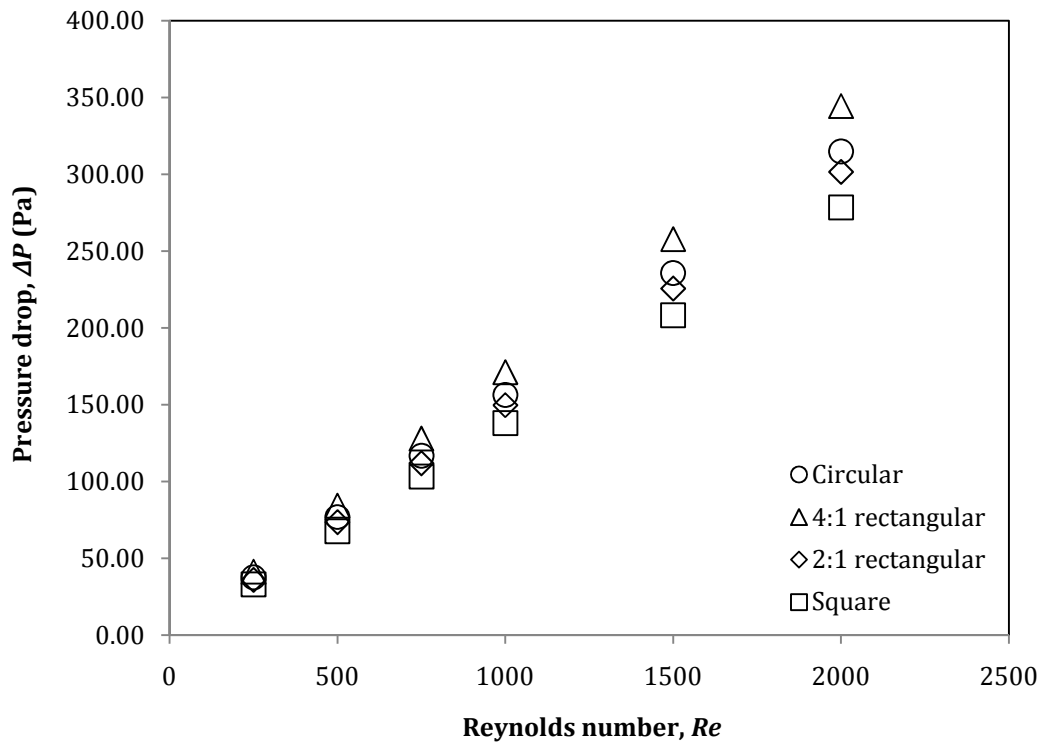


Figure I.6: Pressure drop of 0.10% Al_2O_3 nanofluid for temperature-dependent approach.

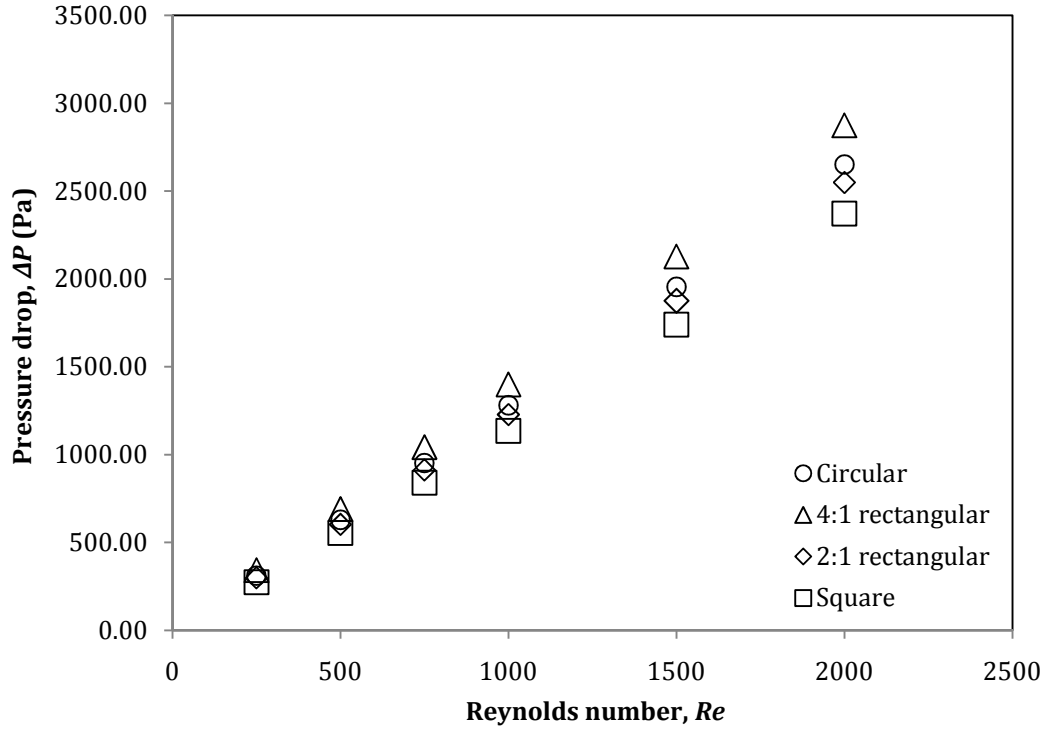


Figure I.7: Pressure drop of 4% Al_2O_3 nanofluid for temperature-independent approach.

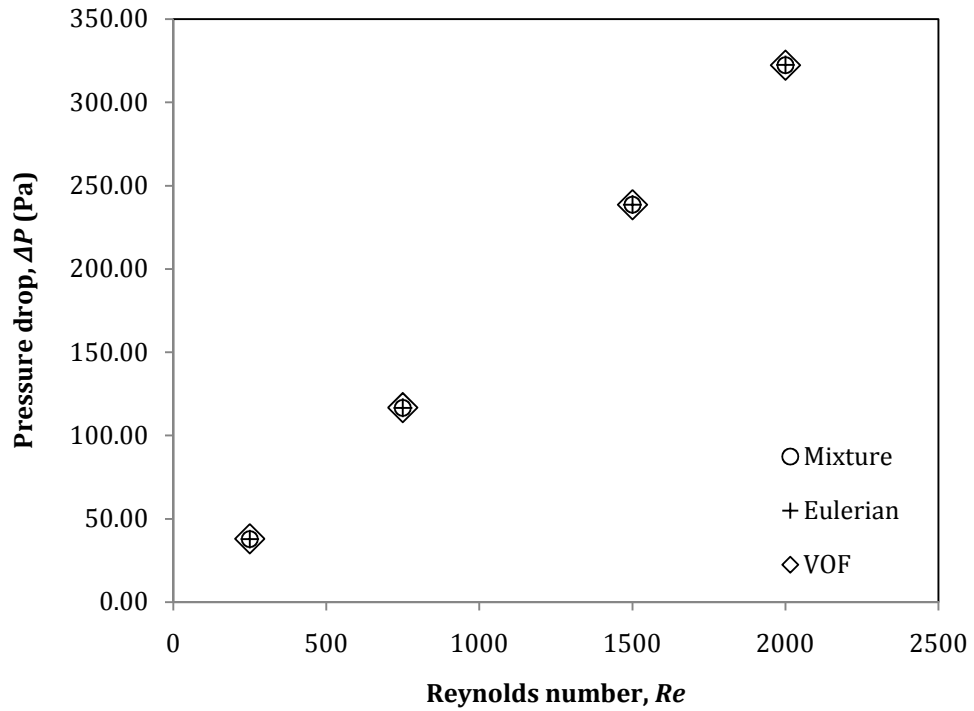


Figure I.8: Pressure drop of 1% nanofluid obtained from two-phase models for circular pipe.

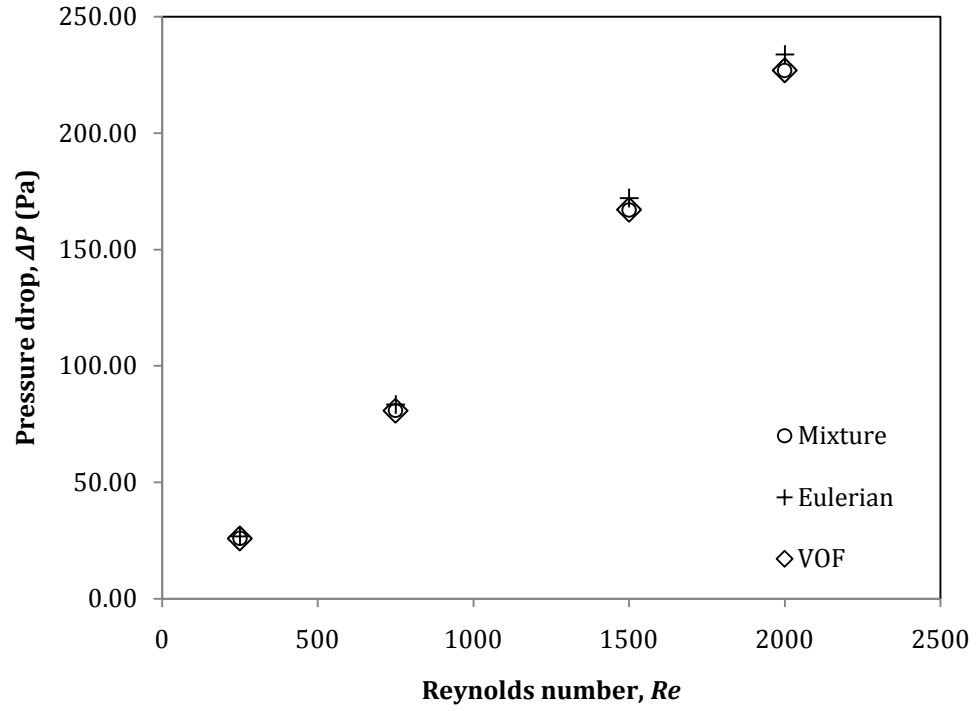


Figure I.9: Pressure drop of 4% nanofluid obtained from two-phase models for 2:1 rectangular duct.

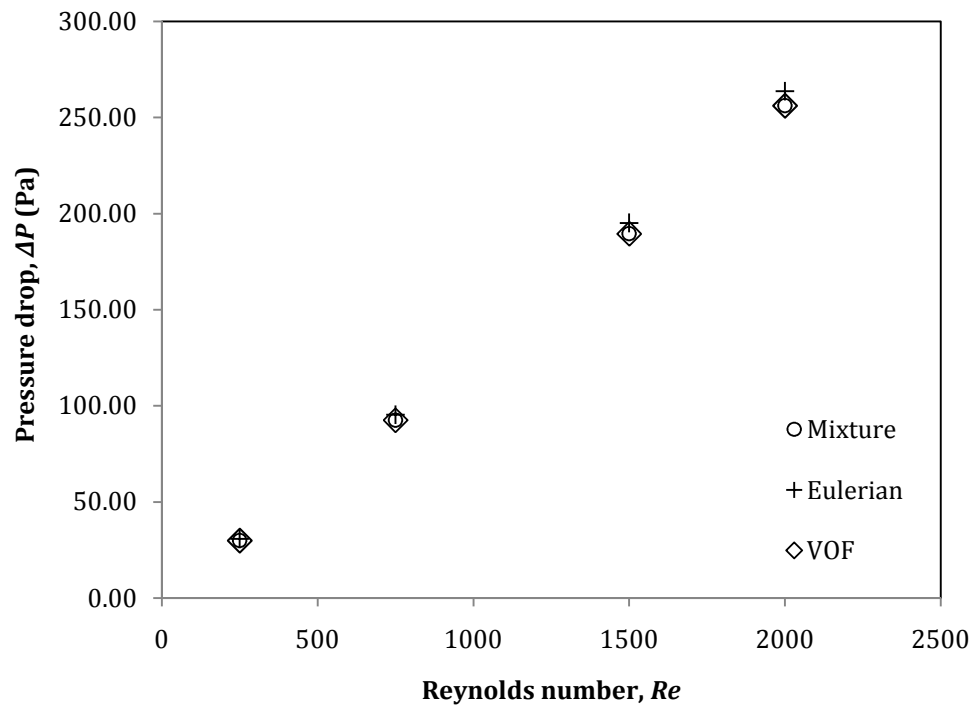


Figure I.10: Pressure drop of 4% nanofluid obtained from two-phase models for 4:1 rectangular duct.

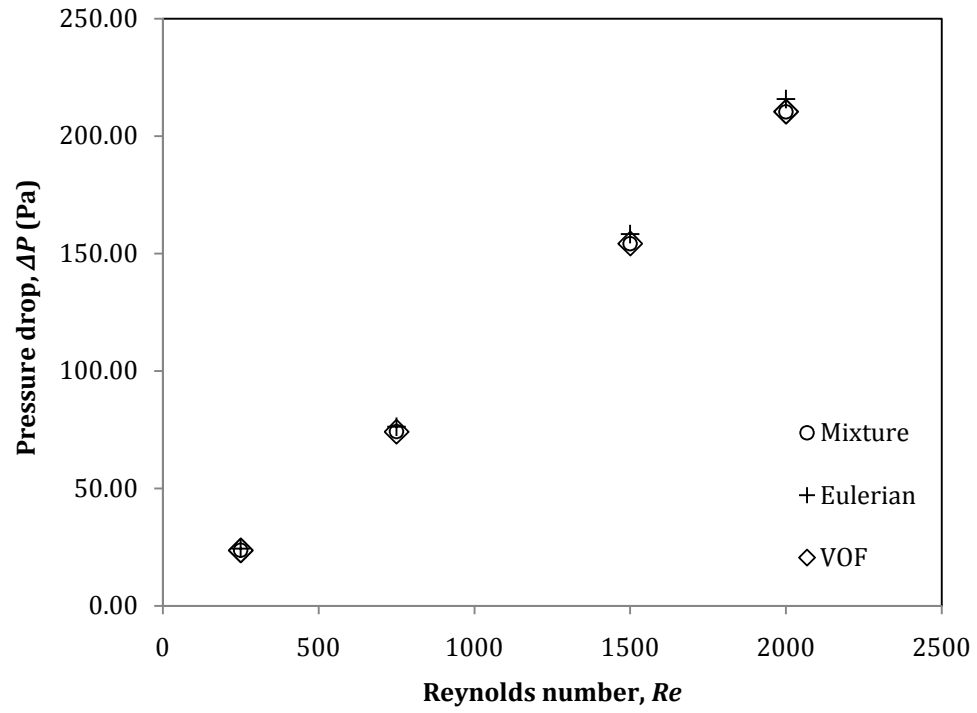


Figure I.11: Pressure drop of 4% nanofluid obtained from two-phase models for square duct.

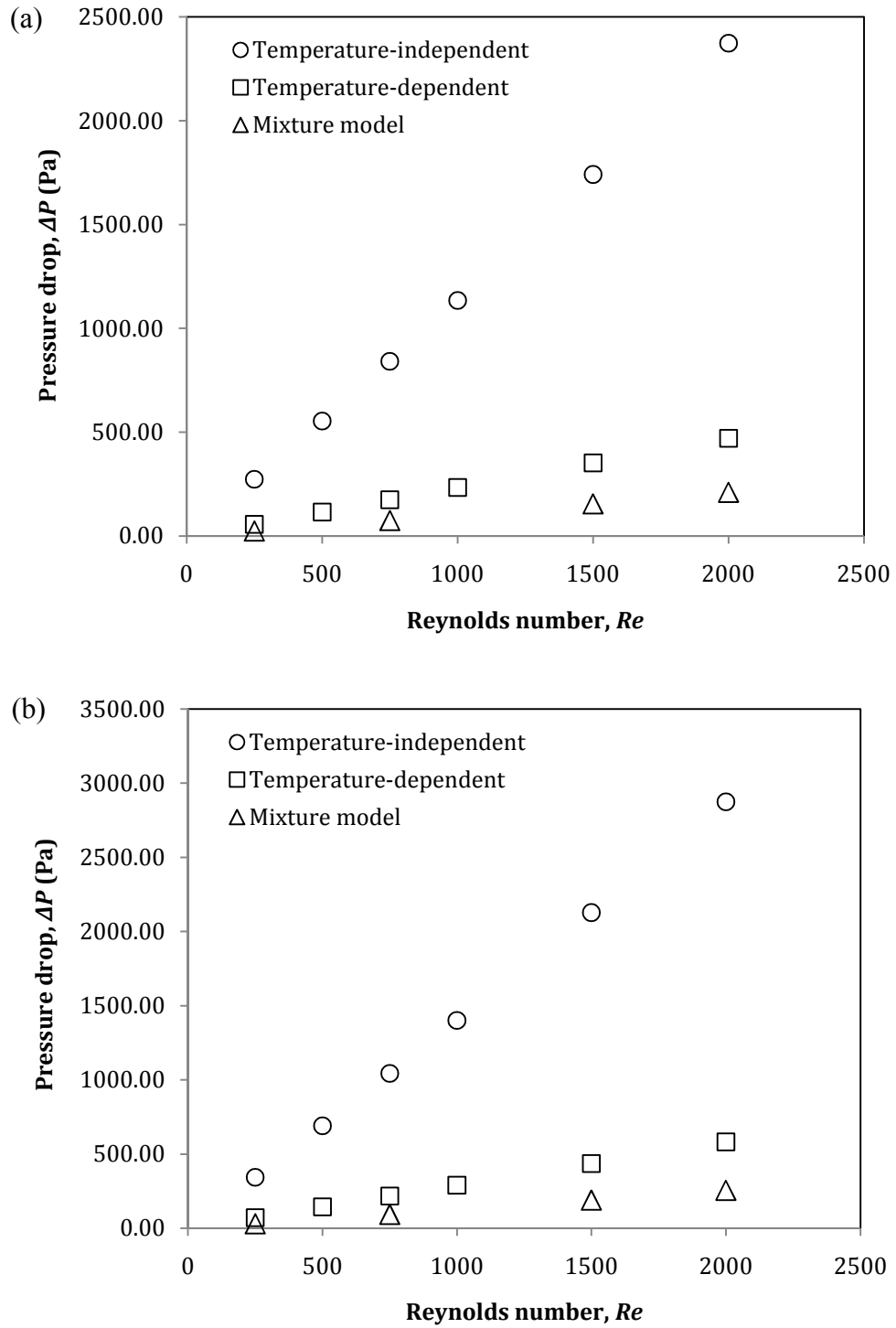


Figure I.12: Comparison of pressure drop obtained from different models for 4% Al_2O_3 nanofluid in (a) square and (b) 4:1 rectangular ducts.

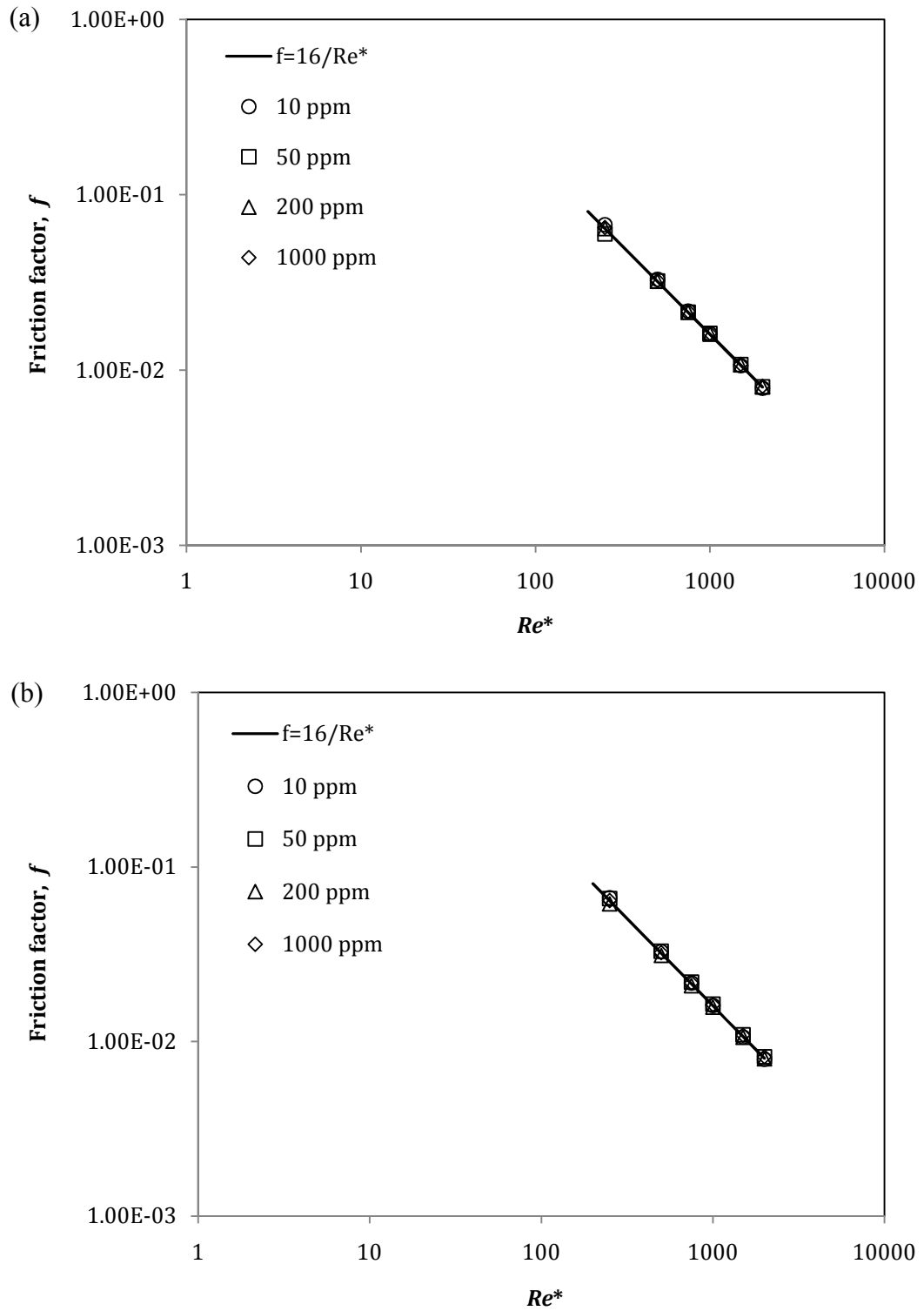


Figure I.13: Friction factor of PAA solution in (a) 2:1 and (b) 4:1 rectangular ducts.

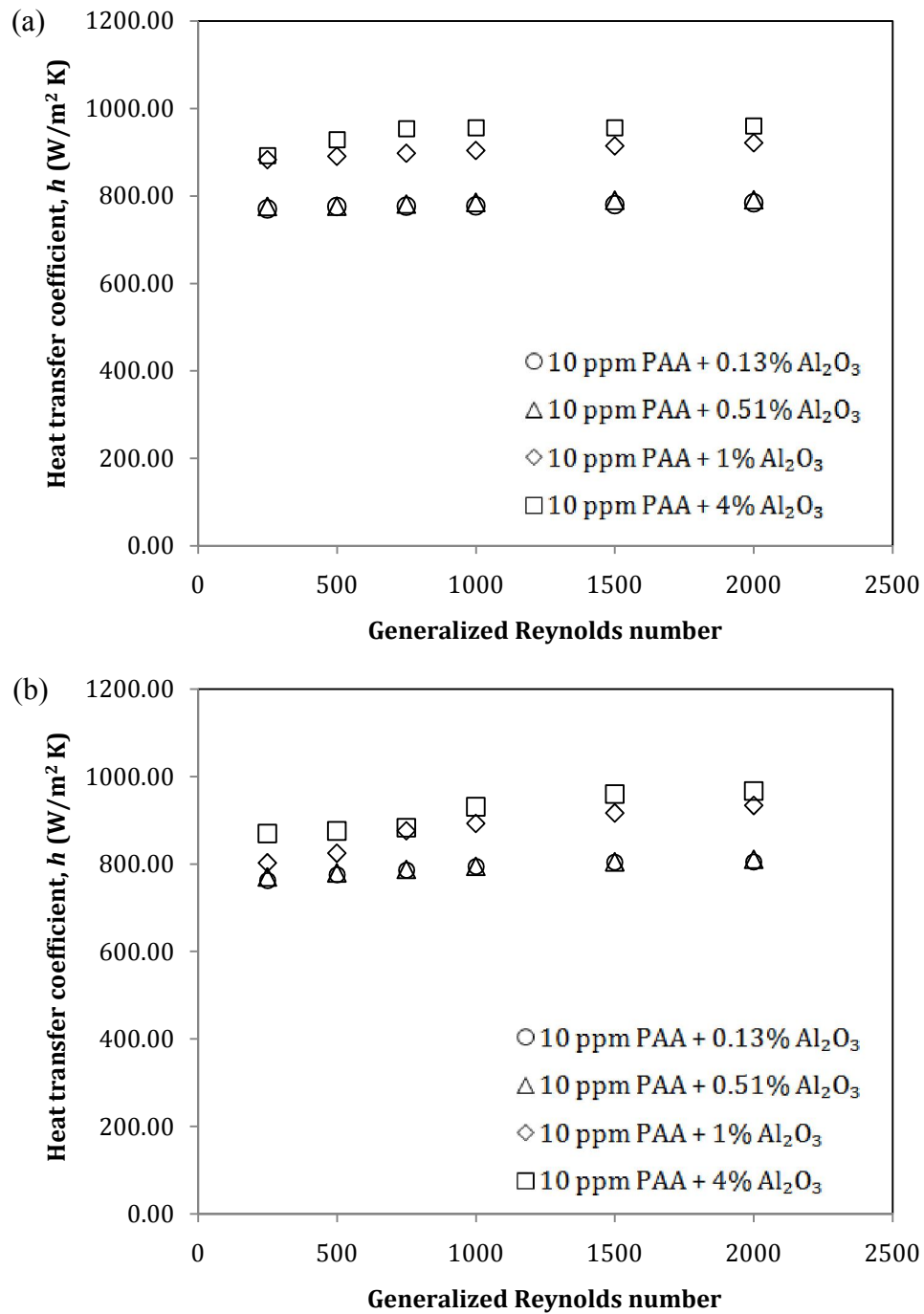


Figure I.14: Heat transfer coefficient of 10 ppm PAA in nanofluid in (a) 4:1 and (b) 2:1 rectangular ducts.

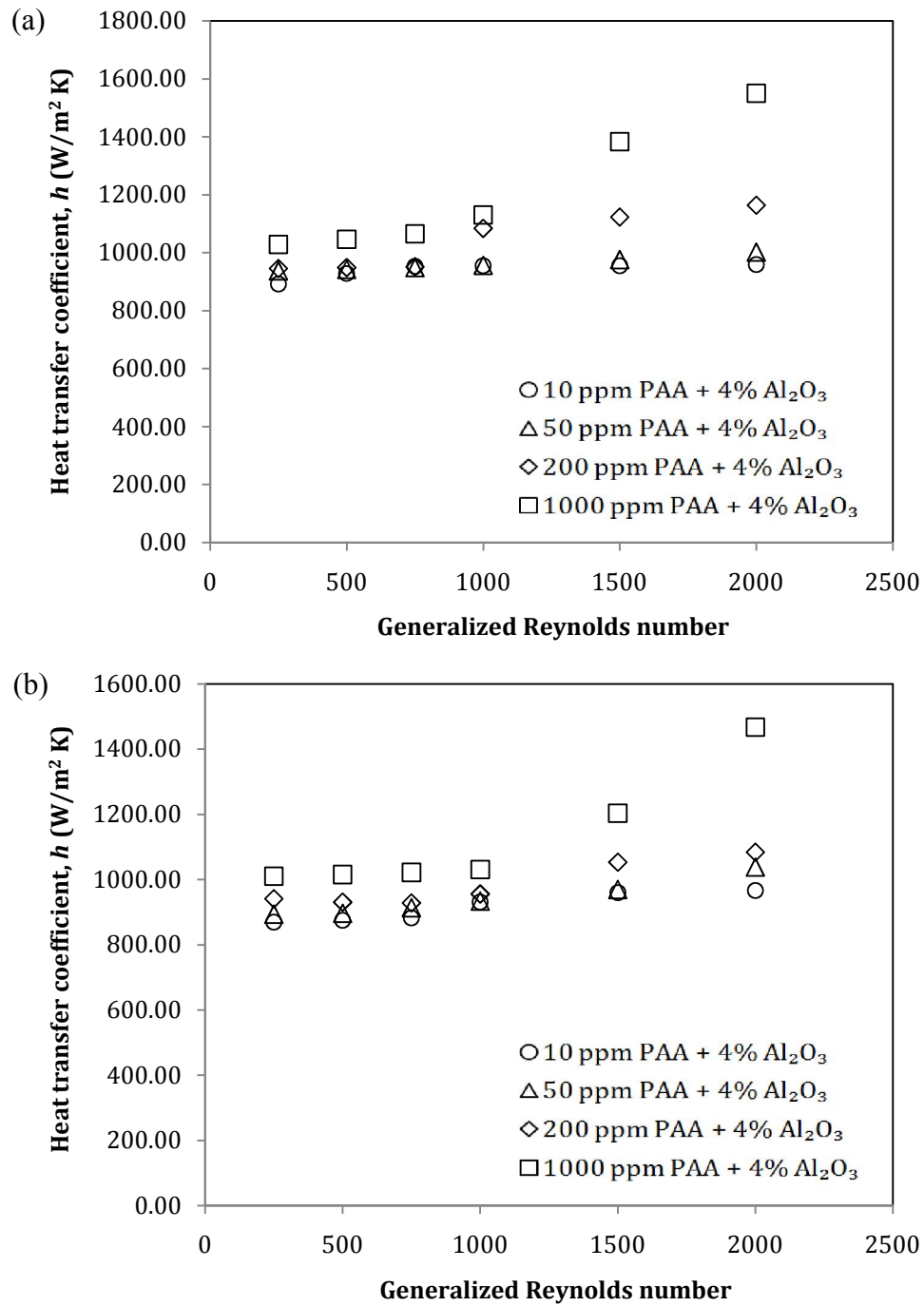


Figure I.15: Heat transfer coefficient of PAA in 4% Al₂O₃ nanofluid in (a) 4:1 and (b) 2:1 rectangular ducts.

Table I.11: $Nu_{poly-nf}/Nu_{nf}$ for circular pipe.

Concentration of poly-nanofluid		Generalized Reynolds number				
PAA (ppm)	Nanofluid (vol%)	250	500	1000	1500	2000
10	0.13	1.65	1.54	1.50	1.47	1.44
	0.51	1.65	1.54	1.50	1.46	1.42
	1.00	1.60	1.51	1.50	1.48	1.43
	4.00	1.42	1.34	1.34	1.31	1.25
50	0.13	1.68	1.57	1.52	1.48	1.45
	0.51	1.65	1.56	1.50	1.47	1.43
	1.00	1.61	1.52	1.51	1.48	1.43
	4.00	1.43	1.39	1.38	1.32	1.26
200	0.13	1.71	1.59	1.52	1.49	1.45
	0.51	1.68	1.57	1.51	1.49	1.45
	1.00	1.67	1.59	1.57	1.53	1.45
	4.00	1.54	1.43	1.39	1.36	1.33
1000	0.13	1.69	1.60	1.56	1.52	1.48
	0.51	1.71	1.58	1.54	1.52	1.48
	1.00	1.71	1.64	1.62	1.57	1.47
	4.00	1.80	1.62	1.50	1.44	1.42

Table I.12: $Nu_{poly-nf}/Nu_{nf}$ for 4:1 rectangular duct.

Concentration of poly-nanofluid		Generalized Reynolds number				
PAA (ppm)	Nanofluid (vol%)	250	500	1000	1500	2000
10	0.13	3.89	3.45	3.06	2.84	2.69
	0.51	3.85	3.40	3.05	2.84	2.68
	1.00	4.25	3.78	3.41	3.20	3.03
	4.00	3.75	3.43	3.13	2.89	2.73
50	0.13	4.08	3.60	3.23	3.11	3.10
	0.51	4.31	3.80	3.41	3.29	3.20
	1.00	4.28	3.88	3.57	3.37	3.18
	4.00	3.94	3.48	3.13	2.95	2.85
200	0.13	4.32	3.85	3.47	3.27	3.11
	0.51	4.35	3.93	3.56	3.35	3.22
	1.00	4.39	3.92	3.57	3.38	3.21
	4.00	3.98	3.50	3.55	3.39	3.31
1000	0.13	4.56	4.05	3.63	3.39	3.32
	0.51	4.55	4.08	3.70	3.51	3.43
	1.00	4.51	4.02	3.68	3.53	3.48
	4.00	4.33	3.86	3.70	4.18	4.40

Table I.13: $Nu_{poly-nf}/Nu_{nf}$ for 2:1 rectangular duct.

Concentration of poly-nanofluid		Generalized Reynolds number				
PAA (ppm)	Nanofluid (vol%)	250	500	1000	1500	2000
10	0.13	4.71	3.98	3.64	3.38	3.12
	0.51	4.69	3.95	3.58	3.33	3.09
	1.00	4.73	4.05	3.88	3.66	3.45
	4.00	4.50	3.74	3.57	3.36	3.12
50	0.13	4.96	4.22	3.80	3.54	3.41
	0.51	4.99	4.38	3.98	3.76	3.52
	1.00	5.07	4.41	3.98	3.71	3.50
	4.00	4.62	3.83	3.58	3.39	3.34
200	0.13	5.26	4.38	3.97	3.75	3.62
	0.51	5.26	4.39	3.98	3.83	3.66
	1.00	5.30	4.45	4.01	3.75	3.57
	4.00	4.86	3.98	3.66	3.69	3.49
1000	0.13	5.50	4.59	4.16	3.92	3.86
	0.51	5.60	4.68	4.17	3.93	3.80
	1.00	5.48	4.57	4.09	3.84	3.71
	4.00	5.22	4.34	3.95	4.21	4.73

Table I.14: $Nu_{poly-nf}/Nu_{PAA}$ for 4:1 rectangular duct.

Concentration of poly-nanofluid		Generalized Reynolds number				
PAA (ppm)	Nanofluid (vol%)	250	500	1000	1500	2000
10	0.13	1.03	1.03	1.02	1.02	1.03
	0.51	1.02	1.01	1.01	1.02	1.02
	1.00	1.13	1.13	1.13	1.14	1.15
	4.00	1.01	1.04	1.06	1.06	1.06
50	0.13	1.05	1.05	1.06	1.09	1.15
	0.51	1.11	1.11	1.12	1.15	1.19
	1.00	1.10	1.13	1.16	1.18	1.17
	4.00	1.03	1.03	1.04	1.06	1.08
200	0.13	1.05	1.06	1.08	1.09	1.09
	0.51	1.06	1.08	1.10	1.11	1.12
	1.00	1.07	1.08	1.10	1.12	1.12
	4.00	0.98	0.98	1.12	1.15	1.18
1000	0.13	1.00	1.00	1.00	1.01	1.05
	0.51	1.00	1.01	1.02	1.04	1.07
	1.00	0.99	0.99	1.01	1.04	1.09
	4.00	0.96	0.97	1.04	1.26	1.41

Table I.15: $Nu_{poly-nf}/Nu_{PAA}$ for 2:1 rectangular duct.

Concentration of poly-nanofluid		Generalized Reynolds number				
PAA (ppm)	Nanofluid (vol%)	250	500	1000	1500	2000
10	0.13	1.08	1.05	1.02	1.01	1.00
	0.51	1.08	1.04	1.00	1.00	0.99
	1.00	1.09	1.07	1.09	1.10	1.11
	4.00	1.04	1.01	1.01	1.02	1.02
50	0.13	1.07	1.06	1.02	1.01	1.04
	0.51	1.07	1.10	1.07	1.07	1.08
	1.00	1.09	1.10	1.08	1.06	1.07
	4.00	1.00	0.98	0.98	0.98	1.04
200	0.13	1.05	1.04	1.04	1.02	1.04
	0.51	1.05	1.04	1.04	1.04	1.05
	1.00	1.05	1.05	1.05	1.02	1.02
	4.00	0.98	0.96	0.97	1.01	1.02
1000	0.13	1.04	1.03	1.02	1.00	1.01
	0.51	1.05	1.05	1.02	1.00	0.99
	1.00	1.03	1.02	1.00	0.98	0.97
	4.00	1.00	0.99	0.98	1.09	1.26

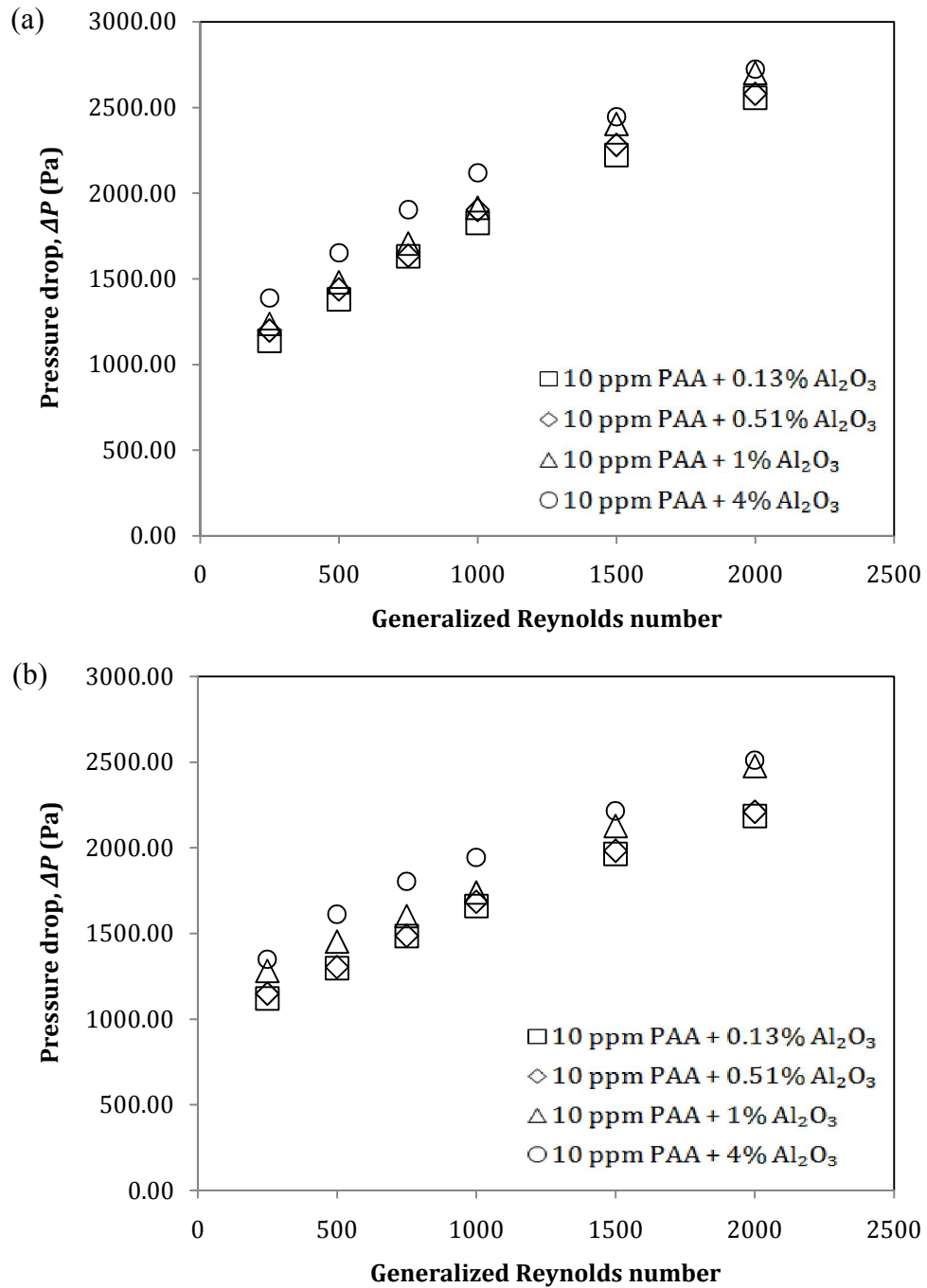


Figure I.16: Pressure drop of 10 ppm PAA in nanofluid for (a) 4:1 and (b) 2:1 rectangular ducts.

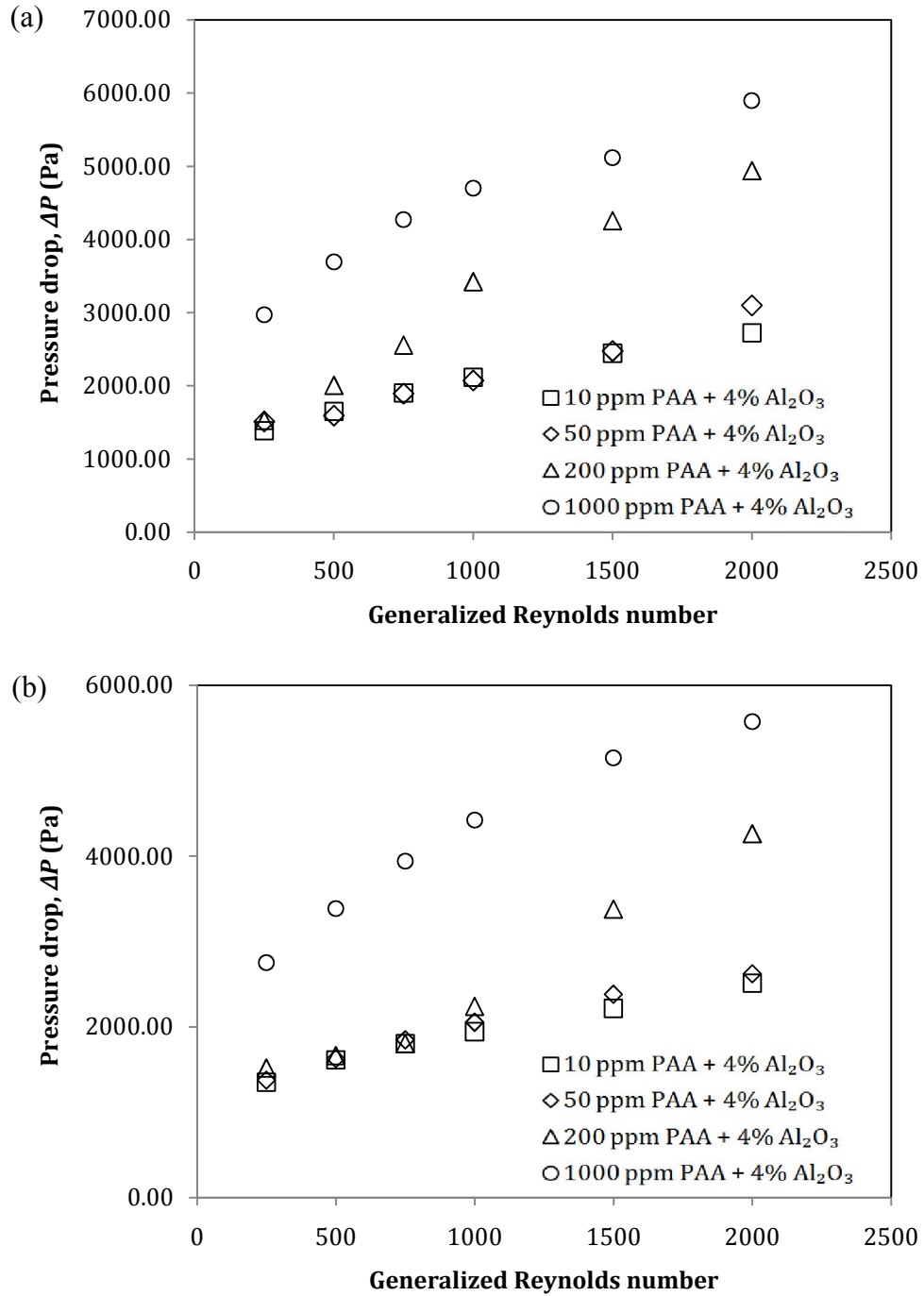


Figure I.17: Pressure drop of PAA in 4% Al_2O_3 nanofluid for (a) 4:1 and (b) 2:1 rectangular ducts.

Table I.16: $\Delta P_{poly-nf} / \Delta P_{nf}$ for 2:1 rectangular duct.

Concentration of poly-nanofluid		Generalized Reynolds number				
PAA (ppm)	Nanofluid (vol%)	250	500	1000	1500	2000
10	0.13	31.32	17.75	11.14	8.75	7.28
	0.51	32.46	18.01	11.41	8.91	7.43
	1.00	35.64	19.74	11.60	9.42	8.20
	4.00	22.18	12.96	7.69	5.81	4.93
50	0.13	33.51	18.79	11.94	9.10	7.45
	0.51	35.09	19.87	12.57	9.64	7.94
	1.00	35.98	20.27	13.06	9.94	8.59
	4.00	22.59	13.08	8.12	6.25	5.15
200	0.13	36.06	20.12	12.03	9.18	7.69
	0.51	41.61	22.46	13.15	10.20	8.77
	1.00	40.96	22.31	14.14	11.49	9.07
	4.00	24.92	13.36	8.86	8.87	8.37
1000	0.13	37.57	21.92	14.12	11.24	9.78
	0.51	41.72	23.11	14.28	11.61	10.18
	1.00	51.68	27.86	15.79	11.50	10.15
	4.00	45.22	27.22	17.49	13.52	10.95

Table I.17: $\Delta P_{poly-nf} / \Delta P_{nf}$ for 4:1 rectangular duct.

Concentration of poly-nanofluid		Generalized Reynolds number				
PAA (ppm)	Nanofluid (vol%)	250	500	1000	1500	2000
10	0.13	27.59	16.45	10.72	8.67	7.46
	0.51	29.40	17.31	11.26	8.97	7.59
	1.00	29.89	17.54	11.17	9.31	7.83
	4.00	19.81	11.57	7.33	5.62	4.68
50	0.13	30.28	17.33	11.04	8.69	7.67
	0.51	32.44	18.68	11.67	9.17	7.76
	1.00	35.32	20.63	12.51	10.03	8.57
	4.00	21.58	11.16	7.17	5.69	5.33
200	0.13	32.14	18.05	11.20	8.91	7.77
	0.51	37.02	20.59	12.43	9.68	8.24
	1.00	37.07	21.29	14.24	10.82	8.66
	4.00	21.81	14.06	11.84	9.78	8.50
1000	0.13	34.83	21.37	14.13	11.47	10.02
	0.51	37.61	22.06	14.53	11.96	10.48
	1.00	45.99	25.31	14.70	11.80	10.49
	4.00	42.38	25.87	16.25	11.75	10.14

Table I.18: $\Delta P_{poly-nf}/\Delta P_{PAA}$ for 2:1 rectangular duct.

Concentration of poly-nanofluid		Generalized Reynolds number				
PAA (ppm)	Nanofluid (vol%)	250	500	1000	1500	2000
10	0.13	1.03	1.01	1.02	1.03	1.02
	0.51	1.05	1.01	1.04	1.04	1.03
	1.00	1.17	1.12	1.07	1.12	1.16
	4.00	1.24	1.24	1.20	1.17	1.17
50	0.13	1.08	1.06	1.05	1.04	1.02
	0.51	1.12	1.11	1.10	1.10	1.08
	1.00	1.16	1.16	1.16	1.15	1.19
	4.00	1.24	1.26	1.22	1.22	1.20
200	0.13	1.06	1.05	1.02	1.01	1.01
	0.51	1.21	1.16	1.11	1.11	1.15
	1.00	1.21	1.17	1.21	1.27	1.20
	4.00	1.25	1.18	1.28	1.65	1.87
1000	0.13	1.01	1.02	1.08	1.12	1.19
	0.51	1.10	1.07	1.08	1.15	1.23
	1.00	1.39	1.31	1.21	1.16	1.24
	4.00	2.06	2.16	2.27	2.29	2.26

Table I.19: $\Delta P_{poly-nf}/\Delta P_{PAA}$ for 4:1 rectangular duct.

Concentration of poly-nanofluid		Generalized Reynolds number				
PAA (ppm)	Nanofluid (vol%)	250	500	1000	1500	2000
10	0.13	1.03	1.06	1.08	1.07	1.04
	0.51	1.08	1.11	1.12	1.10	1.05
	1.00	1.12	1.14	1.13	1.15	1.10
	4.00	1.26	1.27	1.25	1.17	1.11
50	0.13	1.11	1.10	1.08	1.03	1.06
	0.51	1.18	1.18	1.14	1.08	1.07
	1.00	1.30	1.32	1.24	1.20	1.20
	4.00	1.35	1.21	1.19	1.14	1.25
200	0.13	1.12	1.08	1.05	1.05	1.03
	0.51	1.27	1.22	1.16	1.13	1.08
	1.00	1.30	1.28	1.35	1.28	1.16
	4.00	1.29	1.43	1.89	1.95	1.91
1000	0.13	1.02	1.14	1.24	1.24	1.21
	0.51	1.09	1.17	1.26	1.29	1.26
	1.00	1.36	1.36	1.29	1.29	1.28
	4.00	2.12	2.35	2.41	2.16	2.08

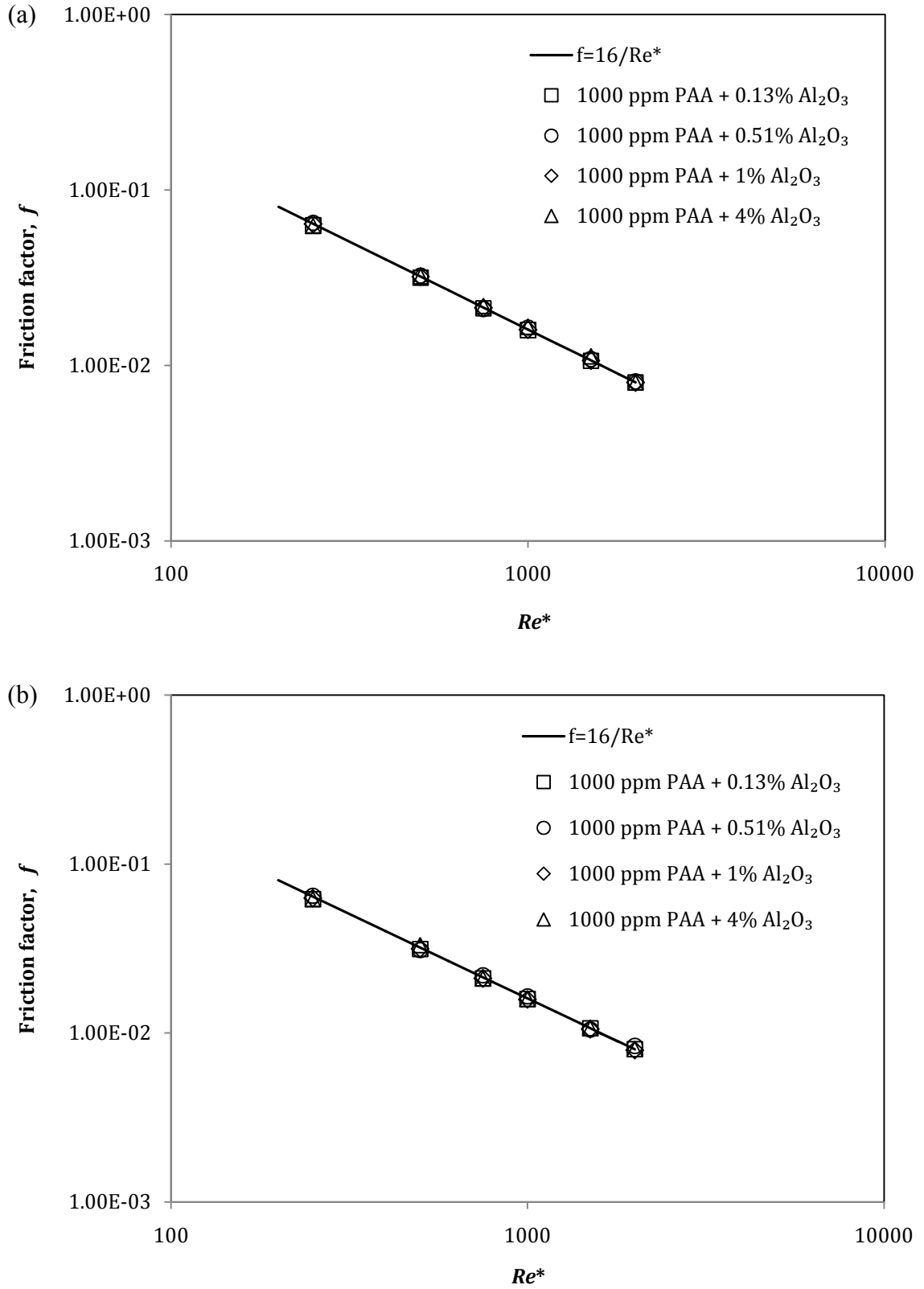


Figure I.18: Friction factor of poly-nanofluid in (a) 2:1 and (b) 4:1 rectangular ducts.

Table I.20: Thermal-hydraulic efficiency of nanofluid in square duct.

Reynolds number	Nanoparticles volume concentration (%)						
	0.01	0.09	0.13	0.25	0.51	1.00	4.00
<i>Temperature-independent properties</i>							
250	0.998	0.985	0.979	0.960	0.924	0.862	0.638
750	0.998	0.987	0.981	0.964	0.931	0.876	0.680
1000	0.998	0.989	0.985	0.970	0.942	0.896	0.731
1500	0.999	0.990	0.986	0.973	0.949	0.908	0.757
2000	0.999	0.990	0.987	0.975	0.952	0.914	0.771
<i>Temperature-dependent properties</i>							
250	0.927	0.931	0.933	0.940	0.952	0.968	0.918
750	0.931	0.935	0.940	0.945	0.956	0.972	0.930
1000	0.940	0.944	0.945	0.951	0.960	0.974	0.940
1500	0.946	0.949	0.951	0.956	0.964	0.978	0.951
2000	0.951	0.954	0.956	0.960	0.969	0.982	0.960

Table I.21: Thermal-hydraulic efficiency of nanofluid in 2:1 rectangular duct.

Reynolds number	Nanoparticles volume concentration (%)						
	0.01	0.09	0.13	0.25	0.51	1.00	4.00
<i>Temperature-independent properties</i>							
250	0.998	0.986	0.981	0.963	0.928	0.870	0.659
750	0.998	0.988	0.983	0.967	0.937	0.885	0.698
1000	0.999	0.990	0.985	0.972	0.945	0.895	0.721
1500	0.999	0.990	0.987	0.974	0.950	0.909	0.757
2000	0.999	0.991	0.988	0.976	0.953	0.915	0.770
<i>Temperature-dependent properties</i>							
250	0.938	0.943	0.944	0.949	0.958	0.972	0.921
750	0.941	0.946	0.947	0.952	0.960	0.972	0.935
1000	0.949	0.952	0.954	0.959	0.971	0.983	0.954
1500	0.950	0.953	0.955	0.960	0.969	0.983	0.954
2000	0.952	0.955	0.956	0.961	0.970	0.983	0.959

Table I.22: Thermal-hydraulic efficiency of nanofluid in 4:1 rectangular duct.

Reynolds number	Nanoparticles volume concentration (%)						
	0.01	0.09	0.13	0.25	0.51	1.00	4.00
<i>Temperature-independent properties</i>							
250	0.998	0.988	0.984	0.968	0.939	0.890	0.702
750	0.998	0.989	0.985	0.971	0.944	0.897	0.716
1000	0.999	0.990	0.986	0.972	0.946	0.902	0.731
1500	0.999	0.990	0.986	0.973	0.948	0.906	0.744
2000	0.999	0.991	0.987	0.974	0.950	0.909	0.755
<i>Temperature-dependent properties</i>							
250	0.938	0.944	0.946	0.951	0.958	0.974	0.929
750	0.941	0.946	0.950	0.954	0.961	0.977	0.939
1000	0.941	0.944	0.946	0.951	0.961	0.975	0.944
1500	0.942	0.946	0.947	0.953	0.962	0.976	0.945
2000	0.944	0.948	0.950	0.955	0.964	0.978	0.949

Table I.23: Thermal-hydraulic efficiency of poly-nanofluid in double pipe heat exchanger at hot inlet temperature of 318.15 K.

Concentration of poly-nanofluid		Generalized Reynolds number				
PAA (ppm)	Nanofluid (vol%)	250	500	1000	1500	2000
10	0.13	0.528	0.728	0.908	1.027	1.106
	0.51	0.526	1.728	0.916	1.042	1.115
	1.00	0.533	0.737	0.915	1.034	1.110
	4.00	0.548	0.756	0.940	1.065	1.141
50	0.13	0.524	0.724	0.908	1.028	1.106
	0.51	0.519	0.727	0.915	1.037	1.108
	1.00	0.541	0.742	0.925	1.044	1.114
	4.00	0.548	0.754	0.944	1.067	1.157
200	0.13	0.519	0.722	0.911	1.030	1.099
	0.51	0.521	0.724	0.921	1.039	1.106
	1.00	0.535	0.737	0.920	1.033	1.115
	4.00	0.549	0.752	0.951	1.089	1.168
1000	0.13	0.493	0.687	0.876	0.987	1.024
	0.51	0.494	0.696	0.873	0.974	1.010
	1.00	0.507	0.713	0.916	1.005	1.019
	4.00	0.521	0.735	0.937	1.058	1.121

Table I.24: Thermal-hydraulic efficiency of poly-nanofluid in double pipe heat exchanger at hot inlet temperature of 323.15 K.

Concentration of poly-nanofluid		Generalized Reynolds number				
PAA (ppm)	Nanofluid (vol%)	250	500	1000	1500	2000
10	0.13	0.595	0.731	0.910	1.029	1.106
	0.51	0.594	0.728	0.903	1.031	1.109
	1.00	0.667	0.807	0.976	1.072	1.118
	4.00	0.627	0.758	0.935	1.058	1.134
50	0.13	0.592	0.730	0.912	1.021	1.102
	0.51	0.590	0.733	0.928	1.045	1.104
	1.00	0.614	0.748	0.925	1.045	1.103
	4.00	0.628	0.758	0.940	1.062	1.149
200	0.13	0.587	0.727	0.906	1.020	1.099
	0.51	0.589	0.727	0.914	1.028	1.102
	1.00	0.617	0.743	0.918	1.029	1.102
	4.00	0.622	0.753	0.954	1.077	1.163
1000	0.13	0.560	0.710	0.875	0.977	1.015
	0.51	0.562	0.704	0.882	0.973	1.000
	1.00	0.573	0.717	0.941	1.034	1.040
	4.00	0.589	0.738	0.935	1.060	1.129

Table I.25: Thermal-hydraulic efficiency of poly-nanofluid in 4:1 rectangular duct.

Concentration of poly-nanofluid		Generalized Reynolds number				
PAA (ppm)	Nanofluid (vol%)	250	500	1000	1500	2000
10	0.13	1.000	1.162	1.258	1.272	1.273
	0.51	1.000	1.146	1.253	1.277	1.283
	1.00	1.114	1.303	1.439	1.452	1.472
	4.00	1.084	1.309	1.470	1.509	1.529
50	0.13	1.017	1.189	1.316	1.391	1.459
	0.51	1.071	1.247	1.387	1.466	1.524
	1.00	1.062	1.264	1.451	1.494	1.497
	4.00	1.107	1.345	1.484	1.537	1.530
200	0.13	1.055	1.256	1.409	1.451	1.460
	0.51	1.035	1.248	1.417	1.467	1.502
	1.00	1.072	1.264	1.391	1.462	1.508
	4.00	1.112	1.253	1.422	1.474	1.520
1000	0.13	1.085	1.247	1.362	1.386	1.429
	0.51	1.077	1.268	1.396	1.433	1.474
	1.00	1.024	1.226	1.417	1.484	1.531
	4.00	1.000	1.129	1.334	1.708	1.908

Table I.26: Thermal-hydraulic efficiency of poly-nanofluid in 2:1 rectangular duct.

Concentration of poly-nanofluid		Generalized Reynolds number				
PAA (ppm)	Nanofluid (vol%)	250	500	1000	1500	2000
10	0.13	1.176	1.348	1.504	1.523	1.523
	0.51	1.180	1.353	1.497	1.521	1.529
	1.00	1.000	1.178	1.390	1.457	1.474
	4.00	1.263	1.416	1.673	1.748	1.748
50	0.13	1.212	1.400	1.532	1.575	1.653
	0.51	1.224	1.451	1.611	1.674	1.705
	1.00	1.267	1.489	1.640	1.684	1.694
	4.00	1.290	1.446	1.648	1.724	1.850
200	0.13	1.253	1.422	1.599	1.666	1.736
	0.51	1.217	1.396	1.587	1.675	1.715
	1.00	1.267	1.456	1.608	1.623	1.700
	4.00	1.314	1.490	1.638	1.667	1.643
1000	0.13	1.292	1.446	1.587	1.626	1.708
	0.51	1.296	1.472	1.618	1.646	1.693
	1.00	1.213	1.390	1.580	1.659	1.700
	4.00	1.157	1.282	1.408	1.654	2.033